The Pennsylvania State University

The Graduate School

College of Earth and Mineral Sciences

MODELING OF PLASMA AND THERMO-FLUID TRANSPORT IN HYBRID WELDING

A Dissertation in

Materials Science and Engineering

by

Brandon D. Ribic

Submitted in Partial Fulfillment
of the Requirements
for the Degree of

Doctor of Philosophy

December 2011

The dissertation of Brandon D. Ribic was reviewed and approved* by the following:

Joan M. Redwing
Professor of Materials Science and Engineering, Chemical Engineering & Electrical Engineering
Chair, Intercollege Graduate Degree Program in Materials Science and Engineering

Tarasankar DebRoy
Professor of Materials Science and Engineering
Dissertation Adviser
Chair of Committee

Todd Palmer
Assistant Professor of Materials Science and Engineering
Research Associate

Christopher Muhlstein
Associate Professor of Materials Science and Engineering

Long-Qing Chen
Professor of Materials Science and Engineering

Jian Xu
Associate Professor of Engineering Science and Mechanics

*Signatures are on file in the Graduate School.

ABSTRACT

Hybrid welding combines a laser beam and electrical arc in order to join metals within a single pass at welding speeds on the order of 1 m min^{-1}. Neither autonomous laser nor arc welding can achieve the weld geometry obtained from hybrid welding for the same process parameters. Depending upon the process parameters, hybrid weld depth and width can each be on the order of 5 mm. The ability to produce a wide weld bead increases gap tolerance for square joints which can reduce machining costs and joint fitting difficulty. The weld geometry and fast welding speed of hybrid welding make it a good choice for application in ship, pipeline, and aerospace welding.

Heat transfer and fluid flow influence weld metal mixing, cooling rates, and weld bead geometry. Cooling rate affects weld microstructure and subsequent weld mechanical properties. Fluid flow and heat transfer in the liquid weld pool are affected by laser and arc energy absorption. The laser and arc generate plasmas which can influence arc and laser energy absorption. Metal vapors introduced from the keyhole, a vapor filled cavity formed near the laser focal point, influence arc plasma light emission and energy absorption. However, hybrid welding plasma properties near the opening of the keyhole are not known nor is the influence of arc power and heat source separation understood. A sound understanding of these processes is important to consistently achieving sound weldments.

By varying process parameters during welding, it is possible to better understand their influence on temperature profiles, weld metal mixing, cooling rates, and plasma properties. The current literature has shown that important process parameters for hybrid welding include: arc power, laser power, and heat source separation distance. However, their influence on weld temperatures, fluid flow, cooling rates, and plasma properties are not well understood. Modeling has shown to be a successful means of better understanding the influence of processes parameters on heat transfer, fluid flow, and plasma characteristics for arc and laser welding. However, numerical modeling of laser/GTA hybrid welding is just beginning.

Arc and laser welding plasmas have been previously analyzed successfully using optical emission spectroscopy in order to better understand arc and laser plasma

properties as a function of plasma radius. Variation of hybrid welding plasma properties with radial distance is not known. Since plasma properties can affect arc and laser energy absorption and weld integrity, a better understanding of the change in hybrid welding plasma properties as a function of plasma radius is important and necessary.

Material composition influences welding plasma properties, arc and laser energy absorption, heat transfer, and fluid flow. The presence of surface active elements such as oxygen and sulfur can affect weld pool fluid flow and bead geometry depending upon the significance of heat transfer by convection. Easily vaporized and ionized alloying elements can influence arc plasma characteristics and arc energy absorption. The effects of surface active elements on heat transfer and fluid flow are well understood in the case of arc and conduction mode laser welding. However, the influence of surface active elements on heat transfer and fluid flow during keyhole mode laser welding and laser/arc hybrid welding are not well known. Modeling has been used to successfully analyze the influence of surface active elements during arc and conduction mode laser welding in the past and offers promise in the case of laser/arc hybrid welding.

A critical review of the literature revealed several important areas for further research and unanswered questions. (1) The understanding of heat transfer and fluid flow during hybrid welding is still beginning and further research is necessary. (2) Why hybrid welding weld bead width is greater than that of laser or arc welding is not well understood. (3) The influence of arc power and heat source separation distance on cooling rates during hybrid welding are not known. (4) Convection during hybrid welding is not well understood despite its importance to weld integrity. (5) The influence of surface active elements on weld geometry, weld pool temperatures, and fluid flow during high power density laser and laser/arc hybrid welding are not known. (6) Although the arc power and heat source separation distance have been experimentally shown to influence arc stability and plasma light emission during hybrid welding, the influence of these parameters on plasma properties is unknown. (7) The electrical conductivity of hybrid welding plasmas is not known, despite its importance to arc stability and weld integrity.

In this study, heat transfer and fluid flow are analyzed for laser, gas tungsten arc (GTA), and laser/GTA hybrid welding using an experimentally validated three dimensional phenomenological model. By evaluating arc and laser welding using similar process parameters, a better understanding of the hybrid welding process is expected. The role of arc power and heat source separation distance on weld depth, weld pool centerline cooling rates, and fluid flow profiles during CO_2 laser/GTA hybrid welding of 321 stainless steel are analyzed. Laser power is varied for a constant heat source separation distance to evaluate its influence on weld temperatures, weld geometry, and fluid flow during Nd:YAG laser/GTA hybrid welding of A131 structural steel. The influence of oxygen and sulfur on keyhole and weld bead geometry, weld temperatures, and fluid flow are analyzed for high power density Yb doped fiber laser welding of (0.16 %C, 1.46 %Mn) mild steel.

Optical emission spectroscopy was performed on GTA, Nd:YAG laser, and Nd:YAG laser/GTA hybrid welding plasmas for welding of 304L stainless steel. Emission spectroscopy provides a means of determining plasma temperatures and species densities using deconvoluted measured spectral intensities, which can then be used to calculate plasma electrical conductivity. In this study, hybrid welding plasma temperatures, species densities, and electrical conductivities were determined using various heat source separation distances and arc currents using an analytical method coupled calculated plasma compositions.

As a result of these studies heat transfer by convection was determined to be dominant during hybrid welding of steels. The primary driving forces affecting hybrid welding fluid flow are the surface tension gradient and electromagnetic force. Fiber laser weld depth showed a negligible change when increasing the (0.16 %C, 1.46 %Mn) mild steel sulfur concentration from 0.006 wt% to 0.15 wt%. Increasing the dissolved oxygen content in weld pool from 0.0038 wt% to 0.0257 wt% increased the experimental weld depth from 9.3 mm to 10.8 mm. Calculated partial pressure of carbon monoxide increased from 0.1 atm to 0.75 atm with the 0.0219 wt% increase in dissolved oxygen in the weld metal and may explain the increase in weld depth. Nd:YAG laser/GTA hybrid welding plasma temperatures were calculated to be approximately between 7927 K and 9357 K. Increasing the Nd:YAG laser/GTA hybrid welding heat source separation distance from 4 mm to 6 mm reduced plasma temperatures between 500 K and 900 K.

Hybrid welding plasma total electron densities and electrical conductivities were on the order of 1 x 10^{22} m^{-3} and 3000 S m^{-1}, respectively.

TABLE OF CONTENTS

LIST OF FIGURES ix

LIST OF TABLES xvi

ACKNOWLEDGEMENTS xix

Chapter 1 INTRODUCTION 1
- 1.1 General Background 1
- 1.2 Research Objectives 5
- 1.3 Connections between various investigations reported in the thesis 5
- 1.4 Thesis structure 6
- 1.5 References 8

Chapter 2 BACKGROUND 12
- 2.1 Energy absorption during arc and laser welding 12
  - 2.1.1 Energy absorption during hybrid welding 18
- 2.2 Keyhole formation 21
- 2.3 Driving forces affecting weld pool fluid flow 24
  - 2.3.1 Role of surface active elements during hybrid welding 28
  - 2.3.2 Fluid flow and hybrid weld pool geometry 30
- 2.4 Plasma formation 32
  - 2.4.1 Plasma formation during hybrid welding 39
- 2.5 Role of laser-arc separation on hybrid welding plasma and weld attributes 41
- 2.6 Defect formation 43
- 2.7 Microstructure and properties 45
  - 2.7.1 Role of heat input and power density 45
  - 2.7.2 Steel hybrid welds 46
  - 2.7.3 Magnesium and aluminum hybrid welds 49
- 2.8 Summary 58
- 2.9 References 60

Chapter 3 HEAT TRASNFER AND FLUID FLOW IN LASER/GTA HYBRID WELDING 67
- 3.1 Introduction 67
- 3.2 Mathematical model 72
  - 3.2.1 Model capabilities 72
  - 3.2.2 Special features of the program 72
  - 3.2.3 Input file 73
  - 3.2.4 Output file 76
  - 3.2.5 Calculation procedure 78
  - 3.2.6 Major components of the code 81
    - 3.2.6.1 Calculation of keyhole geometry 81
      - 3.2.6.1.1 Initial keyhole shape from energy and pressure balance 81

3.2.6.1.2 Adjustment of keyhole heat input 88
3.2.6.2 Turbulence model... 89
3.2.6.3 EMF field calculation... 90
3.2.6.4 Enthalpy calculation... 93
3.2.6.5 Calculation of boundary conditions for enthalpy............................. 97
3.2.6.6 Three dimensional fluid flow and heat transfer 100
3.2.6.6.1 Governing equations 100
3.4.6.7 Boundary conditions 105
3.2.6.7.1 Top surface... 105
3.2.6.7.1.1 Input heat flux 105
3.2.6.7.1.2 Radiation heat loss 107
3.2.6.7.1.3 Convective heat loss.. 107
3.2.6.7.1.4 Evaporative heat loss... 108
3.2.6.8 Solution methodology 109
3.2.7 Convergence criteria 110
3.2.8 Remarks about the code 110
3.3 Experimental Procedure 112
3.3.1 Role of laser-arc spacing on weld geometry and cooling rate 112
3.3.2 Role of laser power on weld pool geometry and fluid flow................... 112
3.3.3 Role of surface active elements on fluid flow and weld geometry 114
3.3.4 Data Analysis 116
3.4 Results and Discussion... 117
3.4.1 Role of laser-arc spacing on weld geometry and cooling rate 117
3.4.2 Role of laser power on weld pool geometry and fluid flow................... 122
3.4.3 Influence of sulfur 132
3.4.3.1 Statistical analysis of effect of base metal sulfur concentration 132
3.4.3.2 Effect of sulfur: experimental and computational study 132
3.4.4 Influence of oxygen... 140
3.4.4.1 Statistical analysis of the effect of ambient oxygen 140
3.4.4.2 Effect of oxygen: experimental and computational study............. 140
3.5 Summary and conclusions.. 146
3.6 References 149

Chapter 4 HYBRID WELDING PLASMA CHARACTERISTICS........................... 153
4.1 Introduction 153
4.2 Experimental procedures... 154
4.3 Data analysis 156
4.3.1 Time-average plasma electron temperatures... 156
4.3.2 Atom, ion, and electron densities 159
4.3.3 Electrical conductivity... 162
4.4 Results and discussion... 163
4.4.1 Temperature and velocity fields and alloying element vaporization 163
4.4.2 Time-average plasma electron temperatures... 167
4.4.3 Atom, ion, and electron densities 171
4.4.4 Electrical conductivity... 177
4.5 Summary and conclusions.. 178

4.6 References 180

Chapter 5 SUMMARY AND CONCLUSIONS 183
5.1 Summary and conclusions 183
5.2 Future work 189
5.3 References 190

Appendix A ANAYLSIS OF VARIANCE (ANOVA) CALCULATION 191
A.1 ANOVA calculation 191
A.2 References 193

Appendix B SOURCE CODE FOR ABEL TRANSFORM AND ELECTRON TEMPERATURE CALCULATION 194
B.1 Source code 194
B.2 References 198

Appendix C SOURCE CODE FOR CALCULATION OF IONIC AND ATOMIC PURE SPECIES DENSITIES 199
C.1 Source code 199
C.2 References 209

LIST OF FIGURES

Fig. 1.1: Thesis research component relationships 8

Fig. 2.1: Power density as a function of horizontal position relative to the heat source symmetry axis with varying distribution factors for a 3 kW heat source. The effect of distribution factor on energy distribution shape and the size of the area affected by the heat source are shown. Laser heat sources tend to have energy distributions similar to the solid line (f =3), while electrical arc energy distributions are similar to the dashed line (f =1) 13

Fig. 2.2: (a) Temperature dependence of absorptivity for pure Al, Ag, Au, Cu, Pb, and W at a laser wavelength of 10.6 μm and (b) temperature dependence of absorptivity for mild steel, AISI 304 stainless steel, and iron at a laser wavelength of 10.6 μm 15

Fig. 2.3: Heat transfer efficiency as a function of welding power when the (laser + arc) arc and laser welding are performing separately or during (laser/arc) Nd:YAG laser/GTA hybrid welding of mild steel 20

Fig. 2.4: Melting efficiency as a function of the heat transfer rate. The two data sets show the arc and laser welding (laser + arc) performed separately and (laser/arc) hybrid welding of mild steel 21

Fig. 2.5: Micrographs of (a) keyhole (4500 W) and (b) conduction (800 W) mode laser welds performed on A131 structural steel. The welding speed was 8.5 mm s^{-1} 22

Fig. 2.6: Change in weld pool width and depth for increasing (a) shielding gas oxygen content and (b) alloy sulfur content for 7 kW laser welding of mild carbon steel at a welding speed of 16.7 mm s^{-1}. The material in Fig. 2.6 (a) contained 0.006 wt% sulfur 29

Fig. 2.7: Micrographs of laser welded mild steel for various concentrations of oxygen in the shielding gas and sulfur in the base metal. The laser power and welding speed were 7 kW and 16.7 mm s^{-1} 30

Fig. 2.8: Temperature distribution in the arc column under GTA welding conditions for an arc current of 100 A. The welded material was mild steel. The temperatures in the arc column were calculated using electrostatic probes 35

Fig. 2.9: Gas tungsten arc welding plasma. The shielding gas was helium and welded material was SUS304 stainless steel. The arc current and welding speed were 150 A and 0.5 mm s^{-1}, respectively 36

Fig. 2.10: Laser welding plasma spectrum during welding of AISI 201 stainless steel using argon shielding gas. The laser power, beam radius, pulse duration, pulse frequency, and welding speed were 2462 W, 140 μm, 3 ms, 100 Hz, and 5 mm s^{-1}, respectively 37

Fig. 2.11: Ion and total electron density as a function of electron temperature for various pure species for pulsed laser welded AISI 201 stainless steel. The laser power and welding speed were 2462 W and 5 mm s^{-1}, respectively. 38

Fig. 2.12: Characteristics of current and voltage during GTA and CO_2 laser/GTA hybrid welding of mild steel. (a) Arc electrical resistance decreasing due to the presence of the laser, and (b) laser stabilization of fluctuations in arc voltage and current. The laser power was 1870 W 40

Fig. 2.13: Effect of the distance between the gas metal arc root and CO_2 laser focal point (D_{LA}) on hybrid weld pool penetration depth. In addition, the effect of defocusing (df) on penetration depth is shown for hybrid welding. The base metal was low carbon steel. The laser power, arc current, and welding speed were 2 kW, 200 A, and 10 mm s^{-1}, respectively 42

Fig. 2.14: Schematic of the effect of heat source separation distance on weld geometry and penetration depth during CO_2 laser/GMA hybrid welding. A, B, C, D, and E indicate the change in relative position of the arc and laser in the weld pool (images above workpiece) and their corresponding weld bead geometry. The base metal was low carbon steel. The laser power, arc current, and welding speed were 2 kW, 200 A, and 10 mm s^{-1}, respectively 43

Fig 2.15: Micrographs of mild steel (a) base metal, (b) laser, (c) GMA, and (d) hybrid weld microstructures. The laser and hybrid weld laser power was 4.5 kW. The GMA and hybrid welds' arc current was 180 A. The welding speed for all welds was 13.3 mm s^{-1} 47

Fig. 2.16: Microhardness as a function of distance from the weld centerline for GMA, CO_2 laser, and laser/GMA hybrid welds made on mild steel samples. The hybrid weld is represented by two microhardness profiles. The arc zone is located closer to the surface of the weld pool, while the laser zone of the hybrid weld is located closer to the weld root. The arc and laser weld microhardness samples were taken relatively close to the weld pool surface 49

Fig. 2.17: Fusion zone (FZ), heat affected zone (HZ), and base metal (BZ) microstructures for (a) Nd:YAG laser, (b) GTA, and (c) hybrid welded AZ31B magnesium alloy. The laser power was 400 W for the laser and hybrid welds. The arc current for the arc and hybrid welds is approximately 70 A 50

Fig. 2.18: Fusion zone microstructures of (a) Nd:YAG laser/GMAW hybrid welded AA7075(T6) aluminum alloy and (b) fiber laser welded (with filler metal) 7xxx series aluminum alloy........ 55

Fig. 2.19: Microhardness profiles of (a) post welding heat treated Yb fiber laser and Yb laser/GMAW hybrid, (b) aged Nd:YAG laser, and (c) as-welded Nd:YAG laser/GMAW hybrid welds based upon the work of Hu and Richardson. The welds were made on (a) 7xxx series and (b and c) AA7075(T6) aluminum alloys. The hybrid weld was evaluated close to the top surface of the weld (hybrid top) and at the mid depth of the weld (hybrid mid) in Fig. 2.19 (a). The hardness profiles are functions of the distance across the weld fusion zone and distance from the weld centerline........ 56

Fig. 3.1: Outline of calculation procedure........ 80

Fig. 3.2: Co-ordinate system for keyhole profile calculation........ 82

Fig. 3.3: The effect of the Lorentz force on fluid motion in the weld pool 90

Fig. 3.4: Flow chart of the EMF calculation subroutine 92

Fig. 3.5: Control volume in three dimensions........ 93

Fig. 3.6: Scalar control volume 95

Fig. 3.7: Stepwise profile assumption for Γ 96

Fig. 3.8: Plot of enthalpy as a function of temperature 97

Fig. 3.9: Schematic of control volume in liquid weld pool used for calculating equations of change 101

Fig. 3.10: Mass fluxes entering and leaving control volume in the x-direction........ 102

Fig. 3.11: Boundary conditions and calculation domain........ 105

Fig. 3.12: Schematic of the boundary conditions of the weld pool........ 109

Fig. 3.13: Penetration depth of the hybrid welding of AISI 321 stainless steel samples as a function of the distance between the laser beam and arc electrode and the current of the arc heat source. The laser power level was 900 W for all welding cases. The welding velocity was 16.7 mm s^{-1} for all welds. The arc current levels were 60, 120, and 180 A. The dashed horizontal line is the penetration depth achieved by lone laser welding. The calculated result (a) and experimental measured result (b) are both depicted........ 119

Fig. 3.14: Temperature and velocity profiles for hybrid welded AISI 321 stainless steel when the separation between the heat sources is (a) 3.5 mm and (b) 7.6 mm. All of the temperature values are in units of Kelvin. In figure 3.14 (a), the arc and laser are located at approximately x = 3 mm and in figure 3.2 (b) the laser is location at x = 3 mm and the arc is located at x = 10.6 mm. 120

Fig. 3.15: Cooling rate from 1073 K to 773 K along the weld centerline as a function of the horizontal distance between the arc electrode tip and laser beam focal point for hybrid welded AISI 321 stainless steel using a 60, 120, and 180 A arc and 900 W laser beam 121

Fig. 3.16: Weld cross sections of (a) laser, (b) arc, and (c) hybrid welded A131 structural steel. For the laser and hybrid welds, the laser power is 4.5 kW. The arc current and voltage are 191 A and 11 V for the arc weld, and 190 A and 12.3 V for the hybrid weld, respectively. The welding velocity was 8.5 mm s^{-1} for all welds.. 123

Fig. 3.17: Measured weld pool depth (a) and width (b) as a function of laser power for hybrid and lone laser welding of A131 structural steel. The travel speed was 8.5 mm s^{-1}. The dashed line is the weld pool depth and width achievable by lone GTAW 124

Fig. 3.18: (a) Arc, (b) laser, and (c) hybrid weld geometry and fluid flow calculated using the three-dimensional heat transfer and fluid flow model. The welded material was A131 structural steel. The welding direction is towards the origin of the coordinate axes.. 125

Fig. 3.19: GTA (a), laser (b), and hybrid welded (c) A131 structural steel cross sections with the calculated cross section overlaid on top of the experimental result. The dashed isotherm is the 3100K isotherm, i.e. the location of the keyhole 130

Fig. 3.20: Comparison of calculated and measured laser and hybrid A131 structural steel welds depth (a) and width (b) as a function of laser power............................. 131

Fig. 3.21: Plots comparing the experimental and calculated laser weld (a) depths and (b) widths as a function of the sulfur concentration in the base metal for 7 kW laser welds on mild steel (0.16 %C, 1.46 %Mn) at 16.7 mm s^{-1}. Standard error bars are shown for the measured weld dimensions 134

Fig. 3.22: Calculated three-dimensional temperature and fluid flow profiles during 7 kW laser welding of mild steel (0.16 %C, 1.46 %Mn) containing (a) 0.015 wt%, (b) 0.056 wt%, and (c) 0.101 wt% sulfur at a welding speed of 16.7 mm s^{-1} 135

Fig. 3.23: Comparison of calculated and measured 7 kW laser weld cross sections when the base metal (0.16 %C, 1.46 %Mn) contained (a) 0.006 wt%, (b) 0.015 wt%, (c) 0.056 wt%, (d) 0.077 wt%, (e) 0.101 wt%, and (f) 0.150 wt% sulfur. The dotted line in the cross sections is the 1000 K isotherm and the solid line outlining the fusion zones is the 1745 K solidus isotherm. The welding speed was 16.7 mm s^{-1} 137

Fig. 3.24: Comparison of the experimental and calculated 7 kW laser welds (a) depths and (b) widths as a function of shielding gas O_2 percentage. Standard error bars are shown for measured weld dimensions. The base metal was 0.16 %C, 1.46 %Mn mild steel and welding speed was 16.7 mm s^{-1} 143

Fig. 3.25: Comparison of experimental and calculated 7 kW laser weld cross sections when welding with shielding gas containing (a) 0%, (b) 5%, (c) 10%, and (d) 15% O_2 on mild steel (0.16 %C, 1.46 %Mn) at 16.7 mm s^{-1} travel speed. The dotted lines in the cross sections are the 1000 K isotherm and the solid line outlining the fusion zones is the 1745 K solidus isotherm.......... 145

Fig. 3.26: Temperature and fluid velocity profiles during 7 kW laser welding of mild steel when (a) 0% and (b) 10% O_2 is introduced to the shielding gas 146

Fig. 4.1: A schematic diagram of the spectroscopy and high speed camera experimental setup. The rotation of the cylindrical workpiece is indicated in the figure 156

Fig. 4.2: A schematic diagram of the spectrometer line of sight data collection arrangement. The welding direction is perpendicular to the spectrometer line of sight 157

Fig. 4.3: Hybrid welding plasma circular cross section (a) close to keyhole opening and weld pool top surface and (b) circular symmetric plasma shape along the plasma vertical axis above weld pool top surface. The arc current and heat source separation distance are 101 A and 4mm, respectively. The arrows indicate the proximity of the laser focal point and the welding direction.......... 158

Fig. 4.4: Calculated (a) arc, (b) laser, and (c) hybrid welding three dimensional temperature and fluid flow profiles used for determining plasma composition. The arc current and laser power were 141 A and 1700 W. The hybrid welding heat source separation distance was 4 mm. All welds were performed at 8.5 mm s^{-1} on 304L stainless steel. The 1727 K and 1697 K isotherms are the alloy liquidus and solidus temperatures 164

Fig. 4.5: (a) Laser, (b) arc, and (c) hybrid welding calculated weld bead cross sections overlaid on top of experimental weld bead cross sections. The laser power and arc current were 1700 W and 141 A. The heat source separation distance during hybrid welding was 6 mm. All welds were performed at 8.5 mm s^{-1} on 304L stainless steel. The solid isotherm indicates the 1697 K solidus. The dashed isotherm is the keyhole boundary, 3034 K 165

Fig. 4.6: Measured intensity versus wavelength plot for plasma formed during hybrid welding with several spectral lines identified by wavelength and species type. The laser power and arc current were 1700 W and 141 A, respectively. The heat source separation distance was 4 mm. The spectral data were taken from 0.75 mm above the laser focal point 168

Fig. 4.7: Time-average electron temperatures calculated from spectral measurements as a function of arc current for hybrid welding plasmas when the heat source separation distance is 4 mm and 6 mm. The laser power was 1700 W. The data were obtained from 0.75 mm above the laser focal point. The laser was focused at the workpiece surface 169

Fig. 4.8: Time-average electron temperatures calculated from spectral measurements for arc, laser, and hybrid welding plasmas as a function of arc current. The data were obtained from the laser beam symmetry axis during laser and hybrid welding and the arc symmetry axis during arc welding. The dashed line is the calculated laser welding plasma time-average electron temperature. Heat source separation distances were 4 mm and 6 mm during hybrid welding. The error bars are based on a 2% standard deviation in the data... 170

Fig. 4.9: Calculated arc, laser, and hybrid welding plasma electron temperatures from spectral measurements as a function of horizontal location relative to the laser focal point. The laser symmetry axis is at 0 mm and the arc symmetry axis is at – 4 mm. The hybrid welding was performed with a 1700 W laser and 101 A or 141 A arc current. The hybrid welding heat source separation distance was varied from 4 mm to 6 mm using a constant arc current... 171

Fig. 4.10: Calculated atom, ion, and total electron densities for hybrid welding argon plasma containing metal vapors as a function of electron temperature. The arc current and heat source separation distance were 121 A and 4 mm. The data were obtained at the laser beam symmetry axis and the laser power was 1700 W. The total electron density of the plasma is given by N_e 173

Fig. 4.11: Calculated electrical conductivities for arc, laser, and hybrid welding plasmas as a function of arc current. The electrical conductivity values were obtained from the laser beam symmetry axis during laser and hybrid welding and the arc symmetry axis during arc welding. The laser power was 1700 W. The dashed line shows the electrical conductivity of the laser welding plasma....... 178

Fig. B.1: Sample input file for spectral line transition probability, statistical weight, upper energy level potential, and wavelength data 194

Fig. B.2: Sample input file for the Abel transform and electron temperature calculation 194

Fig. B.3: Flow chart for measured line intensity deconvolution and calculation of electron temperatures 195

Fig. C.1: Flow chart of species density source code calculation procedure.................. 200

LIST OF TABLES

Table 2.1: Calculated values of magnetic Reynolds number and surface tension Reynolds number for Nd:YAG laser and GTA welding of A131 structural steel. The laser power was 1900 W, and the arc current and voltage were 191 A and 11 V, respectively.......... 26

Table 2.2: The microstructural features and mechanical properties of AZ31B magnesium alloy arc, laser, and hybrid welds 54

Table 3.1: Partial pressure of various gaseous species reactions considered at the keyhole wall calculated at 3000 K 86

Table 3.2: Typical values of arc efficiency, laser and arc power distribution factors, and arc radius 106

Table 3.3: Chemical composition of the AISI 321 stainless steel.......... 112

Table 3.4: Chemical composition of the A131 structural steel.......... 113

Table 3.5: Measured hybrid welding arc current and voltage values and their corresponding laser power levels for hybrid welding of A131 structural steel. The arc current and voltage were not constant for the various hybrid welding cases. 113

Table 3.6: Material properties used in welding calculations for AISI 321 stainless and A131 structural steels 114

Table 3.7: Chemical composition of mild steel samples.......... 115

Table 3.8: Material properties for the mild steel used in the fiber laser welding calculations.......... 115

Table 3.9: Arc radii used in heat transfer and fluid flow simulations to achieve the measured results of Chen et al. when hybrid welding AISI 321 stainless steel.......... 118

Table 3.10: Dimensionless Peclet number for GTA, laser, and hybrid welding of A131 steel. The laser power was 1900 W, and arc current and voltage were approximately 191 A and 12 V 127

Table 3.11: Separation distance and arc radius values used in the numerical model in order to achieve the experimentally observed hybrid weld pool width and depth. The results are arranged by laser power level.......... 129

Table 3.12: ANOVA results for the influence of sulfur concentration on fiber laser weld bead depth and width. The welded material was mild steel (0.16 %C, 1.46 %Mn) ... 132

Table 3.13: Calculated keyhole dimensions, keyhole wall temperature, and magnitudes of partial pressures acting at keyhole surface 4.5 mm below the top surface of the weld pool for various concentrations of sulfur in the base metal during 7 kW laser welding of mild steel (0.16 %C, 1.46 %Mn) ... 139

Table 3.14: ANOVA results for the influence of weld metal oxygen concentration on laser weld bead depth and width. The weld material was 0.16 %C, 1.46 %Mn mild steel ... 140

Table 3.15: Calculated keyhole dimensions, local keyhole wall temperature, and magnitudes of partial pressures acting at keyhole surface 4.5 mm below the top surface of the weld pool when O_2 content of shielding gas is varied during 7 kW laser welding of 0.16 %C, 1.46 %Mn mild steel ... 142

Table 4.1: 304L Stainless Steel composition ... 154

Table 4.2: Nd:YAG laser, GTA, and laser/GTA hybrid welding process parameters... 155

Table 4.3: 304L stainless steel material properties used for numerical model calculations ... 161

Table 4.4: Calculated arc, laser, and hybrid welding plasma compositions and weld depths for various arc current and heat source separation distances determined by the heat transfer and fluid flow model. The laser power was 1700 W ... 166

Table 4.5: Arc, Arc, laser, and hybrid welding plasma total electron densities calculated via Stark broadening and the analytical method. The data were obtained from the laser beam symmetry axis during laser and hybrid welding and the arc symmetry axis during arc welding for various arc currents and heat source separation distances. The laser power in all cases was 1700 W ... 174

Table 4.6: Analysis of imperfect mixing on hybrid welding plasma total electron density for an arc current and heat source separation of 101 A and 4 mm, respectively. The metal vaporization rates were varied by ± 10%. The percentages in parenthesis are the relative error to the total electron density when perfect mixing is assumed ... 177

Table C.1: Input file sample for species density calculation... 199

Table C.2: Data for atomic and singly charged chromium for calculating the partition function ... 201

Table C.3: Data for atomic and singly charged iron for calculating the partition function....... 201

Table C.4: Data for atomic and singly charged manganese for calculating the partition function....... 202

Table C.5: Data for atomic and singly charged molybdenum for calculating the partition function....... 202

Table C.6: Data for atomic and singly charged nickel for calculating the partition function....... 203

Table C.7: Data for atomic and singly charged argon for calculating the partition function....... 203

ACKNOWLEDGEMENTS

Special thanks to the members of my dissertation and comprehensive committee: Dr. Tarasankar DebRoy, Dr. Todd Palmer, Dr. Long-Qing Chen, Dr. Christopher Muhlstein, and Dr. Jian Xu for reading and evaluating my work. Special thanks to my fellow group members and colleagues Dr. Gour Goplan Roy, Dr. Saurahb Mishra, Dr. Amit Kumar, Dr. Rituraj Nandan, Dr. Rohit Rai, Dr. Amit Arora, and Mr. Ashwin Raghavan for their help, support, and collaboration throughout my graduate school experiences. Sincere thanks to Dr. DebRoy for providing extensive help, support, and guidance throughout my graduate school experience as my advisor. Finally, I would like to thank Dr. Shawn Kelly, Mr. Ed Good, Mr. Bill Rhoads, Mr. Chris Sills, Mr. Jay Tressler, Mr. John Bernal, Dr. Thomas J. Lienert, Dr. Paul Burgardt, Dr. Kendall Hollis, Dr. Patrick Hochanadel, and Dr. Susumu Tsukamoto for their interest, support, and help with experimentation at Penn State ARL, Los Alamos National Lab, and NIMS, Japan.

Chapter 1

INTRODUCTION

1.1 General background

Hybrid welding is the process of joining two materials/workpieces using a laser and electrical arc to produce a structurally sound component. Welding results in heating, subsequent melting, and solidification as the heat sources traverse the workpiece.[1-3] Most of the previous research on hybrid welding has focused on its benefits compared to arc and laser welding. Deep weld penetration, a wide weld pool (can be on the order of 4 to 5 mm given the process parameters) , and a reduced propensity for porosity are a few of the attractive features of hybrid welding.[1] The benefits of hybrid welding arise due to the interaction of the heat source with the workpiece material and with each other.

The interaction of the laser and arc with the welded material results in a number of physical processes including: keyhole formation,[4-6]energy absorption,[2, 4, 6-7] alloying element vaporization,[2-3, 8-9] plasma formation,[2-3, 10-11] heat transfer, and fluid flow.[2, 5, 12-14] However, unlike lone laser or arc welding, hybrid welding involves a synergy between the two heat sources which is caused by metal vapors forming due to the high power density laser beam. A deep and narrow vapor filled cavity called a keyhole forms allowing for a much deeper weld penetration to be obtained as compared to arc welding alone.[2, 6, 13, 15] Depending upon the process parameters, arc weld pool penetration can be on the order of 0.5 to 1 mm compared to 4 to 10 mm for hybrid welding. Metal vapors leaving the laser generated keyhole is the primary source of the laser-arc synergy when the arc and laser beam are in close proximity.[3, 5, 16-17] Arc plasma electrical conductivity, thermal conductivity, and arc stability are enhance by the metal vapors.[5, 16, 18-19] The peak arc power density and melting efficiency increase due to the presence of metal vapors in the arc plasma.[3, 7, 20] In addition, the high local vaporization rates of alloying elements close to the keyhole provide a location of relatively high electrical conductivity. Since the arc travels along the path of least electrical resistance, the arc tends to bend, and the root forms within close proximity of the keyhole.[3] These important processes are dependent upon the welding parameters and plasma characteristics.

The transfer of heat in the weld by conduction and convection determines the weld temperature profile, weld pool shape, and cooling rates. Liquid metal weld pool circulation is influenced by several driving forces: buoyancy, surface tension, electromagnetic, and plasma shear or frictional.[2, 14-15, 21] Previous research[22-25] has shown that when convective heat transport is significant, surface active elements (e.g. sulfur and oxygen) affect the aspect ratio of the transverse weld cross section and the direction of fluid flow in the weld pool. The effect of surface active elements on fluid flow has been analyzed for arc[26-31] and conduction mode laser welding.[22, 32] The influence of surface active elements on weld pool temperatures and fluid flow during high power density laser and hybrid welding are not well understood.[24, 33-35] It has been experimentally observed during laser and hybrid welding[24-25, 36-37] that increasing surface active element concentration in the base metal increases weld depth. The increase in weld depth was not related to the presence of the arc during hybrid welding.[24-25, 36-37] Since surface active elements can be present in steels, the effect of surface active elements during laser and laser-arc hybrid welding is important to understand.

Previous experimental research has analyzed hybrid weld top surface fluid flow using markers (elements whose motion can be traced along the weld surface) via high speed video imaging.[24, 35] These studies have been able to provide an idea of the fluid flow direction at the weld pool top surface. However, high speed video imaging can not provide a three-dimensional fluid velocity profile for the entire weld. The fluid flow direction and magnitudes for the entire weld, not simply at the weld pool top surface, needs to be understood in order to realize the weld cross section shape. Since convection plays an important role in dictating weld shape, it is important to understand the three dimensional fluid flow inside the weld pool. Transport phenomena based models have been successful in the past at evaluating fluid flow in three dimensions for the entire weld pool during arc and laser welding.[13, 22, 38-39]

Weld temperature fields are important to determining alloying element vaporization rates, which can influence plasma characteristics and weldment composition.[8-9, 40] Temperature fields can be used to determine cooling rates and fusion zone geometry. Knowledge of hybrid welding cooling rates is important to microstructure development. A quantitative understanding of the weld pool temperature fields and cooling rates during hybrid welding are not known. High temperatures and the presence of plasma make measuring weld pool temperatures difficult during hybrid welding.[41] To overcome these issues, transport phenomena based numerical models have been successfully utilized for other types of welding in the past. For example, laser and arc welding have been extensively evaluated for a number of important structural materials.[4, 6, 9, 38-39] These studies have provided important data on keyhole stability, weld thermal cycles, and fusion zone geometry. The current transport phenomena based modeling of hybrid welding is lacking validation, applicability, and consideration of the important laser-arc interaction.[42-43] An experimentally validated thermo-fluid model which considers the effects of the laser-arc interaction for analyzing heat transfer and fluid flow during hybrid welding is necessary.

Hybrid welding plasma characteristics near the keyhole opening are not well understood as a function of important process parameters such as laser power, arc current, or heat source separation distance.[44-47] The keyhole is the source of metal vapors which can influence plasma species number densities and electrical conductivity, yet the plasma properties in this region are not known. Heat source separation distance affects the amount of metal vapors entering the plasma near the arc. If the arc is not within close proximity of the keyhole, metal vapors are less likely to enhance arc stability. It has been observed that beyond a critical separation distance, the laser-arc synergy during hybrid welding ceases. Similarly, laser power density influences metal vapor concentrations local to the keyhole and plasma electrical conductivity. Arc current can influence plasma temperature, electrical conductivity, arc stability, and weld integrity.

Heat transfer, fluid flow, and plasma properties are intertwined during hybrid welding.[7, 20, 44] For example, the arc affects weld pool width, melting efficiency, and weld cooling rates during hybrid welding.[1] The arc can not provide these benefits if it lacks stability. Since arc stability is dependent upon plasma characteristics, knowing hybrid welding plasma characteristics as a function of laser power, arc current, and heat source separation distance is necessary for a better understanding of arc stability during hybrid welding.

Optical emission spectroscopy has previously been successfully used to analyze arc[48-52] and laser[8, 10-11, 53] welding plasmas. The current understanding of hybrid welding plasma temperatures is based upon average temperatures for the bulk plasma.[44-46] Since plasma temperatures can vary on the order of several thousand Kelvin over the plasma radius,[17] it is important to understand the variation of plasma temperatures over the plasma radius. Bulk data can not provide information about how temperature varies with location in the plasma. The local plasma temperature determines the extent of ionization of the plasma and the equilibrium number density of atoms, ions, and electrons.[17] These particles affect plasma electrical conductivity, arc stability, and weld integrity. Hence, it is important to realize how plasma temperatures vary radially in the plasma.

Hybrid welding plasma is composed primarily of shielding gas and metal vapors. The concentrations of metal vapors in the plasma are influenced by the vaporization rates of alloying elements from the workpiece. Metal vaporization rates during hybrid welding are not known and are dependent upon temperature profiles. The influence of heat source separation distance and arc current on hybrid weld temperature profiles is not known. Increasing the concentration of metal vapors in arc plasmas has shown to increase plasma electrical conductivity in previous research. However, the influence of metal vapors on hybrid welding plasma temperatures, species densities, and electrical conductivity not known.

In summary, the shape, structure, and composition of hybrid welds are affected by numerous intertwined and simultaneously occurring physical processes. Therefore, it is important to understand the various interconnected physical processes during hybrid welding. Transport phenomena based models have been successful at analyzing temperature profiles, fluid flow, cooling rates, vaporization rates previously for arc and laser welding, and offer a good possibility of the same for hybrid welding. A good understanding of the plasma characteristics relies upon a better understanding of hybrid welding vaporization rates. In order to better understand the mechanisms of improved arc stability and the laser-arc interaction during hybrid welding the plasma characteristics need to be known. Arc current and heat source separation distance are important process parameters which can affect the laser-arc interaction. The effects of important process parameters on plasma properties need to be understood and the influence of the heat transfer and fluid flow on plasma properties must be considered.

1.2 Research objectives

The focus of this research is to quantitatively analyze hybrid weld temperatures, cooling rates, vaporization rates, fluid flow, plasma temperatures, species number densities, and electrical conductivity. In addition, this work aims to provide an explanation of the influence of laser power, heat source separation distance, surface active element compositions, and arc current on the resulting weld temperature profile, bead shape, and fluid flow during hybrid welding. The effects of heat source separation distance and arc current on hybrid weld cooling rates are also analyzed. The thesis research will improve the understanding of the interconnection between plasma characteristics, heat transfer, and fluid flow during hybrid welding. The final goal of the research is to quantify the impact of heat source separation distance and arc current on plasma temperatures, species densities, electrical conductivity, and consequently arc stability during hybrid welding.

1.3 Connections between various investigations reported in the thesis

During hybrid welding, metal vapors entering the plasma from the keyhole affect plasma electrical conductivity and arc stability. Energy absorption, fluid flow, and heat transfer are dependent upon keyhole and arc stability. The heat transfer and fluid flow determine the weld pool temperature profile and local vaporization rates of alloying elements. These metal vapors affect plasma species densities, electrical conductivity, and arc stability. Hence, it is important to understand both the plasma properties and physical processes occurring in the weld pool, their relationships, and the effects of process parameters. Fig. 1.1 shows the relationships between the research components contained in the thesis. Heat transfer, and fluid flow were investigated for gas tungsten arc (GTA), Nd:YAG laser, fiber laser, and Nd:YAG/GTA hybrid welding. The arc and laser welding processes were individually analyzed to better understand hybrid welding.

Laser energy absorption can be influenced by the presence of plasma, depending upon the beam characteristic wavelength. The laser beam high power density results in rapid vaporization of alloying elements. If the laser beam energy can not be transferred to the workpiece surface efficiently, then the vaporization rate decreases. The vaporization rates at the weld top and keyhole surfaces are determined by the heat transfer inside the weld pool. The vaporization of metal vapors affects the plasma species densities, electrical conductivity, and arc stability.

Process parameters, for example heat source separation distance, influence plasma characteristics and consequently the heat transfer and fluid flow during hybrid welding. It is important to realize the importance of process parameters in the interconnection between the properties of the plasma and processes occurring in the weld pool. Arc, laser, and hybrid welding were theoretically and experimentally analyzed using three sets of experimental results. The experimental results were obtained from the literature,[20] performed at Penn State ARL, provided by collaborators from the National Institute for Material Science in Japan, and personally developed and performed at Los Alamos National Laboratory.

1.4 Thesis structure

The thesis analyzes several important issues for hybrid welding, which are likely to have a major impact. The important issues include:

- The physical processes which give rise to a wider weld pool during hybrid welding compared to laser welding
- Arc constriction and bending influence on heat transfer and fluid flow during hybrid welding and the effect of laser power on hybrid weld penetration depth
- The quantitative impact of arc current and heat source separation distance on hybrid weld cooling rates.
- The difference between hybrid and laser weld pool penetration depth
- Role of surface active elements on hybrid weld pool temperatures and fluid flow
- Quantitatively analyzing hybrid welding plasma temperatures, species densities, and electrical conductivity
- Detailing the influence of important process parameters on heat transfer, fluid flow, arc stability

The thesis answers these important issues throughout five chapters to help expand application of the hybrid welding process. Chapter 1 describes the motivation, objectives, and structure of the thesis. To provide a basis for undertaking the research, chapter 2 is a critical assessment of the previous research on hybrid welding energy absorption, keyhole formation, heat transfer, fluid flow, plasma formation, the laser-arc interaction, microstructure, and properties.

Chapter 3 addresses heat transfer and fluid flow during hybrid welding and the influence of important process parameters on weld pool temperatures, fluid flow, and cooling rates. The process parameters include arc current, laser power, and heat source separation distance. These topics are explained via theoretical and experimental analysis of arc, laser, and hybrid welded A131 structural steel and 321 stainless steel. In addition, the role of surface active elements on weld geometry, temperatures, and fluid flow during high power density fiber laser welding of mild steel is evaluated via theoretical and experimental analyses.

Hybrid welding plasma electrical conductivity and the influence of heat source separation distance and arc current on arc stability are evaluated in chapter 4. Arc, laser, and hybrid welding experimental and theoretical studies are performed to quantitatively evaluate plasma temperatures and species densities during welding of 304L stainless steel. Chapter 4 provides values of hybrid welding plasma temperatures, species densities, and electrical conductivities compared to arc and laser welding plasmas. In addition, the chapter details the influence of heat source separation distance and arc current on electrical conductivity and arc stability during hybrid welding.

Chapter 5 summarizes the conclusions of the work. Appendix A details the analysis of variance (ANOVA) calculations. Appendix B is the source code for the Abel transform of the measured spectral line intensities and the calculation of plasma electron temperatures. Appendix C contains the data used to calculate the partition functions and the source code used to calculate the pure element species densities.

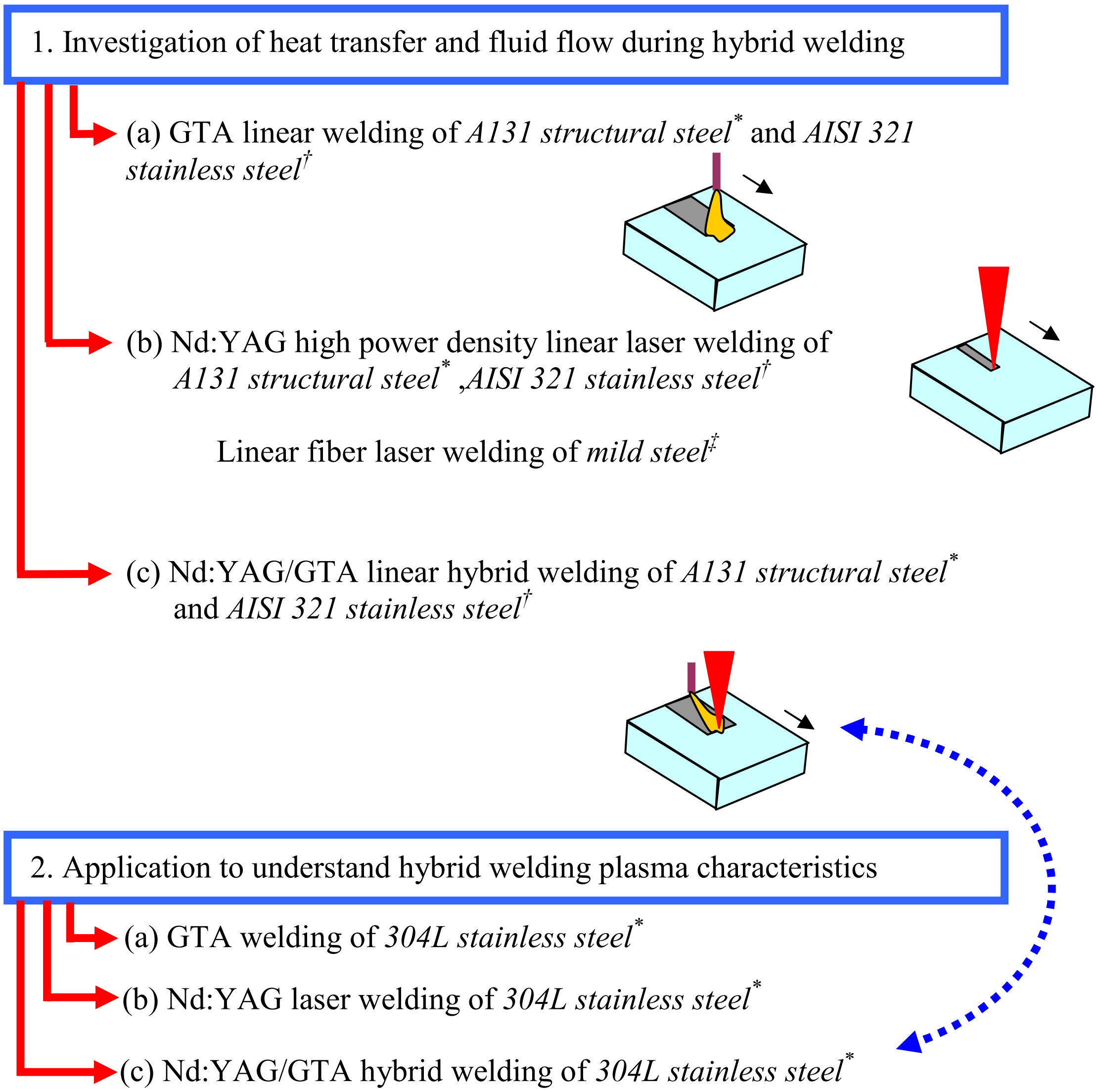

* Experimentation personally developed and performed
† Experimentation obtained from the literature[20]
‡ Experimentation performed by collaborators at Japan National Institute for Material Science[25, 37]

Fig. 1.1: Thesis research component relationships

1.5 References

1. C. Bagger, F. O. Olsen, Journal of Laser Applications **17** (1), 2-14 (2004).
2. B. Ribic, T. Palmer, T. DebRoy, International Materials Reviews **54** (4), 223-244 (2009).
3. W. M. Steen, Journal of Applied Physics **51** (11), 5636-5641 (1980).

4. R. Rai, S. M. Kelly, R. P. Martukanitz, T. DebRoy, Metallurgical and Materials Transactions A-Physical Metallurgy and Materials Science **39A** (1), 98-112 (2008).
5. B. Ribic, R. Rai, T. DebRoy, Science and Technology of Welding and Joining **13** (8), 683-693 (2008).
6. H. Zhao, T. Debroy, Journal of Applied Physics **93** (12), 10089-10096 (2003).
7. B. Hu, and G. Den Ouden, Science and Technology of Welding and Joining **10** (4), 427-431 (2005).
8. M. M. Collur, A. Paul, T. DebRoy, Metallurgical Transactions B-Process Metallurgy **18** (4), 733-740 (1987).
9. X. He, T. DebRoy, P. W. Fuerschbach,, Journal of Physics D- Applied Physics **36** (23), 3079-3088 (2003).
10. M. M. Collur, T. DebRoy Metallurgical Transactions B-Process Metallurgy **20** (2), 277-286 (1989).
11. R. Miller, T. DebRoy, Journal of Metals **40** (7), A71-A71 (1988).
12. K. Mundra, T. DebRoy, K. M. Kelkar, Numerical Heat Transfer Part A-Applications **29** (2), 115-129 (1996).
13. R. Rai, J. W. Elmer, T. A. Palmer, T. DebRoy, Journal of Physics D- Applied Physics **40** (18), 5753-5766 (2007).
14. T. DebRoy, S. A. David, Reviews of Modern Physics **67**, 85-112 (1995).
15. J. F. Lancaster, *The Physics of Welding*. (Pergamon Press, New York, NY, 1986).
16. B. D. Ribic, R. Rai, T. A. Palmer, T. DebRoy, presented at the Trends in Welding Research, Pine Mountain, GA, USA, 2008 (unpublished).
17. H. Terasaki, M. Tanaka, M. Ushio, Metallurgical and Materials Transactions A-Physical Metallurgy and Materials Science **33** (4), 1183-1188 (2002).
18. K. Etemadi, E. Pfender, Plasma Chemistry and Plasma Processing **5** (2), 175-182 (1985).
19. B. Hu, and G. Den Ouden, Science and Technology of Welding and Joining **10** (1), 76-81 (2005).
20. Y. B. Chen, Z. L. Lei, L. Q. Li, L. Wu, Science and Technology of Welding and Joining **11** (4), 403-411 (2006).
21. H. Zhao, D. R. White, T. Debroy, International Materials Reviews **44** (6), 238-266 (1999).
22. W. Pitscheneder, T. DebRoy, K. Mundra, R. Ebner, Welding Journal **75** (3), S71-S80 (1996).
23. P. Sahoo, T. DebRoy, M. J. McNallan, Metallurgical Transactions B-Process Metallurgy **19** (3), 483-491 (1988).
24. Y. Naito, M. Mizutani, S. Katayama, Journal of Laser Applications **18** (1), 21-27 (2006).
25. S. Tsukamoto, (Personal Communication, University Park, PA, 2008), pp. 1-5.
26. S. Mishra, T. J. Lienert, M. Q. Johnson, T. DebRoy, Acta Materialia **56** (9), 2133-2146 (2008).
27. Y. Wang, H. L. Tsai, Metallurgical and Materials Transactions B- Process Metallurgy and Materials Processing Science **32** (3), 501-515 (2001).
28. Y. Wang, Q. Shi, H. L. Tsai, Metallurgical and Materials Transactions B- Process Metallurgy and Materials Processing Science **32** (1), 145-161 (2001).

29. Y. Z. Zhao, Y. P. Lei, Y. W. Shi, Acta Metallurgica Sinica **40** (10), 1085-1092 (2004).
30. Y. Z. Zhao, Y. P. Lei, Y. W. Shi, Journal of Materials Science & Technology **21** (3), 408-414 (2005).
31. Y. Z. Zhao, H. P., Zhou, Y. W. Shi, Modeling and Simulation in Materials Science and Engineering **14** (3), 331-349 (2006).
32. P. Sahoo, M. M. Collur, T. DebRoy, Metallurgical Transactions B-Process Metallurgy **19** (6), 967-972 (1988).
33. D. K. Aidun, S. A. Martin, Journal of Materials Engineering and Performance **6** (4), 496-502 (1997).
34. C. Limmaneevichitr, S. Kou, Welding Journal **79** (8), 231S-237S (2000).
35. L. Zhao, T. Sugino, G. Arakane, S. Tsukamoto, Science and Technology of Welding and Joining **14** (5), 457-467 (2009).
36. T. Fuhrich, P. Berger, H> Hugel, Journal of Laser Applications **13** (5), 178-186 (2001).
37. S. Tsukamoto, (Personal Communication, University Park, PA, 2009), pp. 1-20.
38. A. Kumar, T. DebRoy, Metallurgical and Materials Transactions A-Physical Metallurgy and Materials Science **38A**, 506-519 (2007).
39. S. Mishra, T. DebRoy, Materials Science and Engineering A **454-455**, 477-486 (2007).
40. R. Rai, G. G. Roy, T. DebRoy, Journal of Applied Physics **101** (5), 054909 (2007).
41. J. Slania, Z. Mikno, M. Wojcik, Welding International **21** (8), 589-592 (2007).
42. J. Zhou, W. H. Zhang, H. L. Tsai, S. P. Martin, P. C. Wang, R. Menassa, presented at the ASME International Mechanical Engineering Congress and Exposition, Washington, D.C., 2003 (unpublished).
43. J. Zhou, H. L. Tsai, International Journal of Heat and Mass Transfer **51** (17-18), 4353-4366 (2008).
44. X. Hao, and G. Song, IEEE Transactions of Plasma Science **37** (1), 76-82 (2009).
45. L. M. Liu, R. Huang, G. Song, X. Hao, IEEE Transactions on Plasma Science **36** (4), 1937-1943 (2008).
46. L. M. Liu, X. F. Song, Journal of Physics D- Applied Physics **41** (20), 205202 (2008).
47. G. A. Turichin, A. M. Grigor'ev, E. V. Zemlyakov, E. A. Valdaitseva, U. Dilthey, A. Gumeniuk, High Temperature **44** (5), 647-655 (2006).
48. P. W. J. M. Boumans, *Theory of Spectrochemical Excitation*. (Plenum Press, New York, 1966).
49. G. J. Dunn, T. W. Eager, Metallurgical Transactions A-Physical Metallurgy and Materials Science **17** (10), 1865-1871 (1986).
50. A. E. F. Gick, M. B. C. Quigley, P. H. Richards, Journal of Physics D- Applied Physics **6** (16), 1941-1949 (1973).
51. A. Gleizes, J. J. Gonzales, B. Liani, G. Raynal, Journal of Physics D- Applied Physics **26** (11), 1921-1927 (1993).
52. T. A. Palmer, T. DebRoy, Welding Journal **75** (7), s197-s207 (1996).
53. R. Miller, T. DebRoy, Journal of Applied Physics **68** (5), 2045-2050 (1990).

Chapter 2

BACKGROUND

Although the advantages of the hybrid welding process over those obtained from either arc or laser welding are well established, the fundamental physical processes are less well understood. The physical processes of hybrid welding include energy absorption, keyhole formation, heat transfer, fluid flow, plasma formation, and the laser-arc interaction. Physical processes affect plasma characteristics, temperature profiles, weldment composition, microstructure, and mechanical properties. Much of the existing literature detailing laser-arc hybrid welding is based on empirical studies designed to determine process capabilities, such as weldability, weld bead geometry, and porosity content. In the following sections, the physical processes of laser-arc hybrid welding are examined. In addition, the current understanding of defect formation, microstructure, and mechanical properties are critically reviewed. Areas for further research and knowledge gaps are identified.

2.1 Energy absorption during arc and laser welding

The power density distribution describes the nature of the heat source that interacts with the workpiece and is important in predicting the weld pool geometry. During arc or laser welding, the peak power density is affected by the arc or laser beam radius. In arc welding, the arc radius is dictated by the arc current, length, electrode tip angle, and the angle at which the arc is applied relative to the surface of the workpiece. The minimum achievable laser beam radius at the focal point is controlled by the laser focusing optics, and laser radiation characteristic wavelength.[1]

Power density of a heat source can be represented by a Gaussian distribution: [2]

$$P_d = \frac{fP_t}{\pi r_b^2} \exp^{(-fr^2/r_b^2)} \tag{2.1}$$

where f is the distribution factor, P_t is the total power of the heat source, r_b is the radius of the heat source at the focal point, and r is the radial distance from the axis of the heat source. Fig. 2.1 shows a plot of power density as a function of horizontal position relative to the heat source symmetry axis for various values of distribution factor, f.

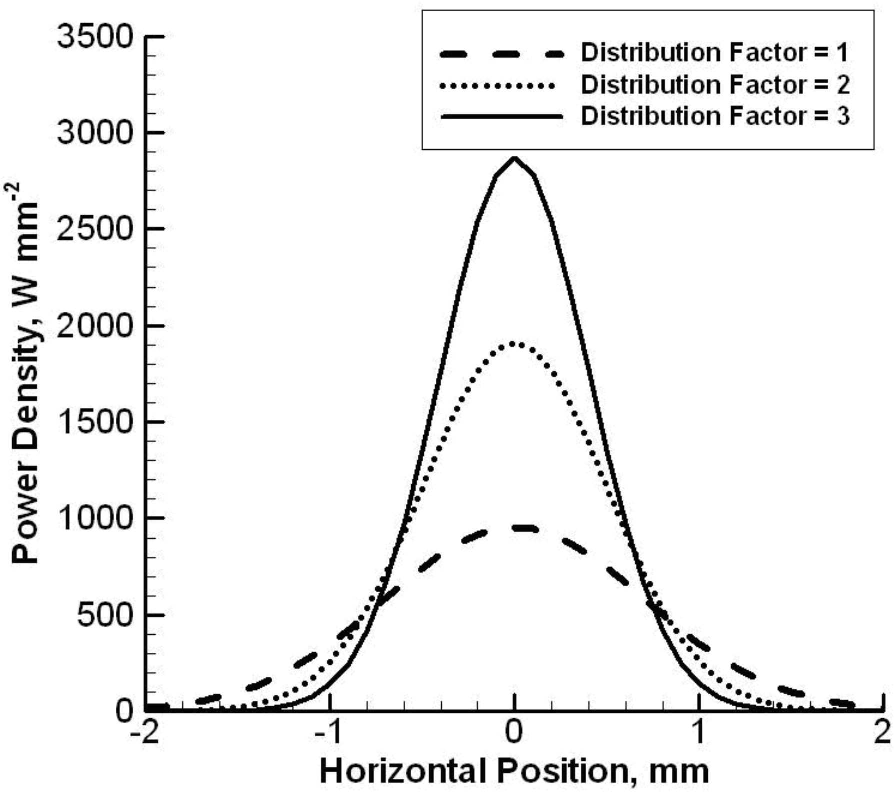

Fig. 2.1: Power density as a function of horizontal position relative to the heat source symmetry axis with varying distribution factors for a 3 kW heat source. The effect of distribution factor on energy distribution shape and the size of the area affected by the heat source are shown. Laser heat sources tend to have energy distributions similar to the solid line (f =3), while electrical arc energy distributions are similar to the dashed line (f =1).[3]

As the distribution factor increases, the energy becomes more focused, resulting in an increase in the peak power density at the center of the laser beam or arc. The typical power density distribution of a laser beam is characterized by a higher distribution factor than that of an arc and is represented in Fig. 2.1 by the solid line (f = 3). With a distribution factor of three, the laser has a higher peak power density than the arc distribution, which is represented by the line with a distribution factor of one.

Narrow and highly intense power density distributions produce sufficiently high power densities that result in high local vaporization rates. These vaporization rates can produce a deep narrow vapor filled cavity called a keyhole. The presence of the keyhole results in deeper weld penetration than low power density conduction mode laser welding (< 10^5 W cm^{-2})[4-8] Keyhole mode laser welds have a martini glass shape and conduction mode welds are hemispherical..[4, 9-10]

The laser beam radius at the workpiece surface can also be altered by defocusing the heat source. Negative defocusing of the laser may increase the penetration depth of the weld pool due to the convergent nature of the laser beam.[11-13] As the convergent laser beam travels into the workpiece, the power density of the laser beam increases. Therefore, increasing the amount of negative defocusing can increase the keyhole depth and weld penetration. However, if the defocusing exceeds a critical value, keyhole formation will be inhibited and the weld penetration will decrease. In the case of positive defocusing, the keyhole depth decreases because the laser beam converges at a location above the workpiece surface, thus hindering keyhole formation and laser beam energy absorption. [14-16]

The type of heat source affects process efficiency through differences in the mechanisms of energy absorption. For an arc, energy absorption by the workpiece is affected by the manner in which the electrical circuit of the arc is arranged,[17] metal transfer mode, shielding gas used, and workpiece material.[2, 4, 18-19] In the case of hybrid welding, the arc welding is typically performed as gas tungsten arc (GTA) or gas metal arc welding (GMAW). GTAW uses a non-consumable tungsten electrode to generate a weld bead blanketed by inert shielding gas to prevent weld oxidation.[2] In the case of GMAW, the welding electrode is a filler material for the weld to improve weld chemistry, properties, and fusion.[2] Electrical arcs can be generated using direct (DC) or alternating current (AC).[2] Depending upon the polarity of the electrical circuit, electrons are emitted or received at the electrode.[17] GMAW most often employs direct current electrode positive (DCEP) to avoid erratic metal transfer, while GTAW can operate using a direct or alternating current.[2]

The absorption of laser energy by the workpiece differs from the energy absorption of arcs and is affected by factors such as the laser wavelength, nature of the workpiece surface, and the size and nature of the plasma present above the weld pool.[20-23] Fig. 2.2 (a) shows the dependence of absorptivity on temperature[21] for several pure materials, and Fig. 2.2 (b) shows the same relationship for important structural steels, based on work by Duley[1] and Boyden et al.[22]

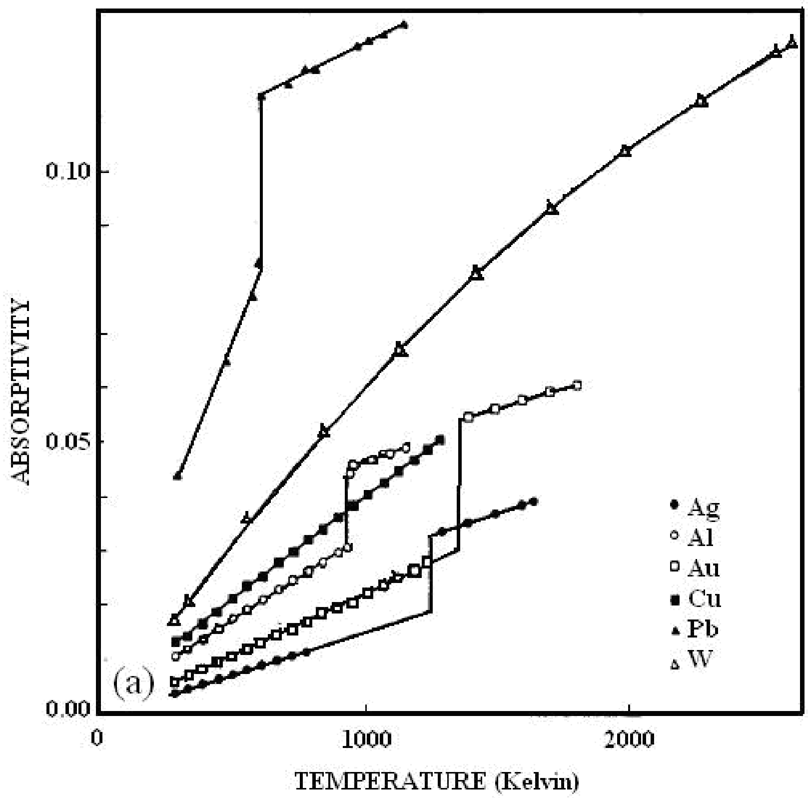

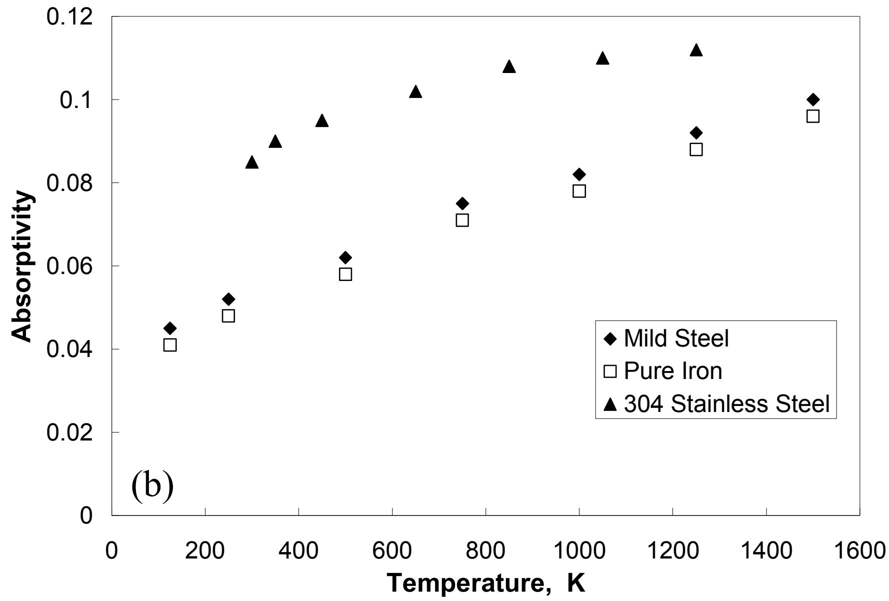

Fig. 2.2: (a) Temperature dependence of absorptivity[21] for pure Al, Ag, Au, Cu, Pb, and W at a laser wavelength of 10.6 μm and (b) temperature dependence of absorptivity for mild steel,[1] AISI 304 stainless steel,[22] and iron[1] at a laser wavelength of 10.6 μm.

As the temperature of solid metallic materials increase, absorptivity will increase. Upon melting, absorptivity increases significantly, resulting in the discontinuities shown in each curve in Fig. 2.2 (a). Upon melting, convection aids in the transport of heat in the molten weld pool. The absorptivity of mild steel is approximately 9% higher than that of iron and varies similarly as a function of temperature (Fig. 2.2 (b)).[1] Absorptivity of solid iron increases with temperature in a manner similar to other pure metals. The 304 stainless steel shows much less variation in absorptivity over the same temperature range. Within the range of temperatures which the steels were evaluated no melting occurs, unlike in Fig. 2.2 (a).

Absorption of infrared energy by metals depends primarily on Fresnel absorption,[4, 24-26] which is defined as conductive absorption by free electrons where a portion of the laser energy is either reflected or absorbed by the workpiece.[27] When a keyhole forms during laser welding, the absorption efficiency of the laser energy increases greatly due to multiple reflections of the laser beam within the keyhole.[6-8, 20] Only about 30% of the laser energy is absorbed during one reflection.[7,24] When the laser is reflected multiple times over the keyhole surface, the sum total of absorbed laser energy can increase to approximately 98%. As a result, the energy from the laser is able to penetrate to a greater depth into the workpiece without changing the weld width, thus increasing the weld aspect ratio.[28-29]

During high power density laser welding ($\geq 10^5$ W cm^{-2}), a laser induced plasma can form and a portion of the laser energy is absorbed by the plasma phase within the keyhole through inverse Bremsstrahlung absorption.[4, 20, 24, 30] Inverse Bremsstrahlung absorption occurs when, "energy of the electric field induced by the laser is absorbed by the plasma via electron-ion collisions."[31] This condition is most often quantitatively described by the Beer-Lambert law given by:[28]

$$I_a = I_o \exp(-\mu_a L_P) \tag{2.2}$$

where I_a and I_o are the attenuated and the incident laser beam intensity, respectively, μ_a is the absorption coefficient, and L_P is the length of the plasma. Often the Beer-Lambert law is empirically modified based upon the size of the particles which comprise the plasma, the nature of the interacting particles in the plasma, and workpiece material. For example, the following relationship is applicable for plasmas containing particles on the order of 20 nm to 50 nm in diameter:[23]

$$E_A = P[1 - \exp^{-(Q_S + Q_A)\pi r_p^2 N z}] \tag{2.3}$$

where E_A is the attenuated incident radiation in watts, P is the incident laser power, r_p is the average radius of the particles, N is the number density of the scattering particles, z is the distance over which attenuation of laser beam energy occurs, Q_S is the amount of attenuation due to scattering, and Q_A is the absorption efficiency.

For a shorter wavelength heat source, scattering will play a larger role in the laser beam attenuation.[23] The amount of attenuation due to scattering (Q_S) is inversely proportional to the fourth power of the wavelength of the laser heat source, as shown by the following relationship:[23]

$$Q_S = \frac{8}{3}\left(\frac{2\pi r_p}{\lambda}\right)^4 \left|\frac{m^2 - 1}{m^2 + 2}\right|^2 \tag{2.4}$$

where m is the complex refractive index ($m = n + k_e i$), i is an imaginary number, n is the refractive index of the material, and λ is the laser wavelength. The extinction coefficient

(k_e) is simply the fraction of incident radiation lost to absorption and scattering per unit distance.

The absorption efficiency is defined by the following relation:[23]

$$Q_A = \frac{-8\pi r_p}{\lambda} I_m \left\{ \frac{m^2 - 1}{m^2 + 2} \right\} \tag{2.5}$$

where I_m is the imaginary portion of the complex refractive index, m. Wavelength plays a major role in defining the amount of attenuation due to scattering and absorption efficiency. Because the characteristic wavelength of Nd:YAG lasers is 1.06 μm, they experience greater energy loss due to scattering compared to 10.6 μm wavelength CO_2 lasers. With a wavelength of 10.6 μm, CO_2 lasers often experience lower efficiency of absorption by the workpiece material[23, 25-26, 32] than Nd:YAG lasers. In addition, CO_2 lasers have higher energy losses due to inverse Bremsstrahlung absorption compared to Nd:YAG lasers because of the relatively greater characteristic laser light wavelength.

2.1.1 Energy absorption during hybrid welding

In arc and laser welding, the workpiece absorbs only a portion of the total energy supplied. The amount of energy absorbed depends on the material, type of heat source, and process parameters.[4, 20, 33-34] During hybrid welding, arc energy absorption is affected by an interaction between the arc and laser due to surface heating interactions, stabilization of the arc cathode spot, and constriction of the arc plasma column.[28, 35-37] The surface heating interaction between the two heat sources provides extra energy for welding and enhances weld pool width.[37-38] Surface heating interactions are explained by the absorption of laser and arc energy by the workpiece and the nature of their power density distributions. Stabilization of the arc cathode spot occurs through the introduction of metal vapors produced by the melting and intense vaporization of the workpiece by the laser.[39-42] A laser generated plasma has a higher electron density than other regions above the surface of the workpiece.[35, 40, 43-44] Therefore, if the arc is close enough to the laser generated plasma, the laser plasma offers a line of least electrical resistance or potential drop[28, 35, 45] coinciding with the Steenbeck effect, which states that the arc will always operate at the lowest possible potential.[35] As a result, the arc root will preferentially move toward the laser focal point, or keyhole opening.[35-36, 46]

The surface heating synergistic effect is the ability to achieve greater energy absorption efficiency and melting efficiency compared to that achieved during lone arc or laser welding. The heat transfer efficiency is defined as the fraction of heat transferred to the workpiece by the heat sources versus the applied welding power, and the melting efficiency is the percentage of heat source energy which actually resulting in melting of the workpiece. The heat transfer and melting efficiencies are given by:[37]

$$\eta_h = Q_i / Q_o \tag{2.6}$$

$$\eta_m = Q_m / Q_i = Av\rho\left(\int_{T_o}^{T_m} C_p dT + H_f\right) / Q_i \tag{2.7}$$

where η_h is the heat transfer efficiency, Q_i is the heat transfer rate, Q_o is the welding power, η_m is the melting efficiency, Q_m is the melting rate, A is the area of the transverse weld cross-section, v is the welding speed, ρ is the density of the material, C_p is the heat capacity of the material, T is temperature, T_o is the ambient temperature, T_m is the melting temperature of the material, and H_f is the latent heat of fusion of the material.

Fig. 2.3 shows the heat transfer efficiency as a function of the total welding power for Nd:YAG laser/GTA hybrid and arc and laser welding of mild steel.[37] The laser power[37] was a constant 453 W and the arc power was varied between 570 W to 3690 W. Laser spot size and welding speed were 300 μm and 8 mm s^{-1}, respectively.[37]

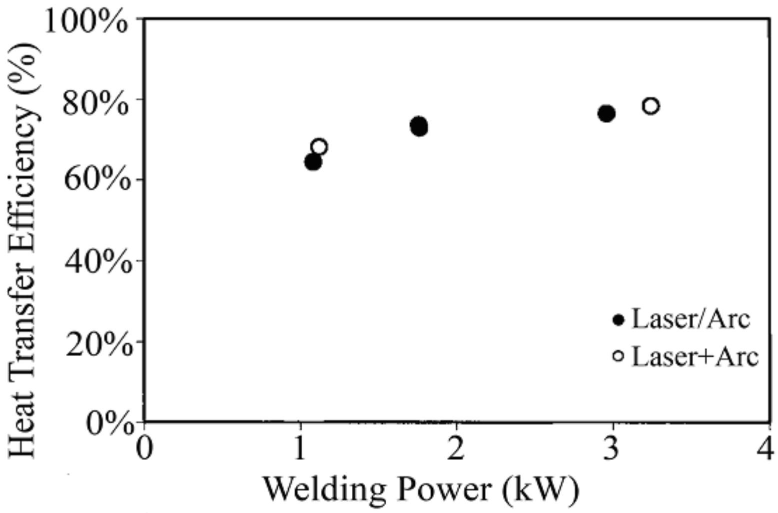

Fig. 2.3: Heat transfer efficiency as a function of welding power when the (laser + arc) arc and laser welding are performing separately or during (laser/arc) Nd:YAG laser/GTA hybrid welding of mild steel.[37]

Over the range of welding powers considered, the hybrid welding process does not result in a greater heat transfer efficiency compared to arc and laser welding.[37] It is known that the heat transfer efficiency of the laser welding process is closely related to keyhole formation. Therefore, changing from conduction to keyhole mode laser welding increases the heat transfer efficiency due to multiple reflections of the incident radiation inside the keyhole.[20, 37, 47] However, there is no change from conduction to keyhole mode laser welding depicted in Fig. 2.3 because all of the welds were keyhole mode welds.[37]

Melting efficiency for arc and laser welding and keyhole mode Nd:YAG laser/GTA hybrid welding is show in Fig 2.4. The laser power was held constant at 453 W and the arc power was varied[37] between 570 W to 3690 W. Laser spot size and welding speed were 300 μm and 8 mm s^{-1}, respectively.[37] Hybrid welding has a greater melting efficiency than arc and laser welding performed separately.[38, 48] However, the degree of interaction between the two heat sources is unclear.[37] Improved melting efficiency is the result of increased arc stability and arc constriction.[28, 36-38] The effect of the improved melting efficiency on heat transfer and fluid flow is unknown.

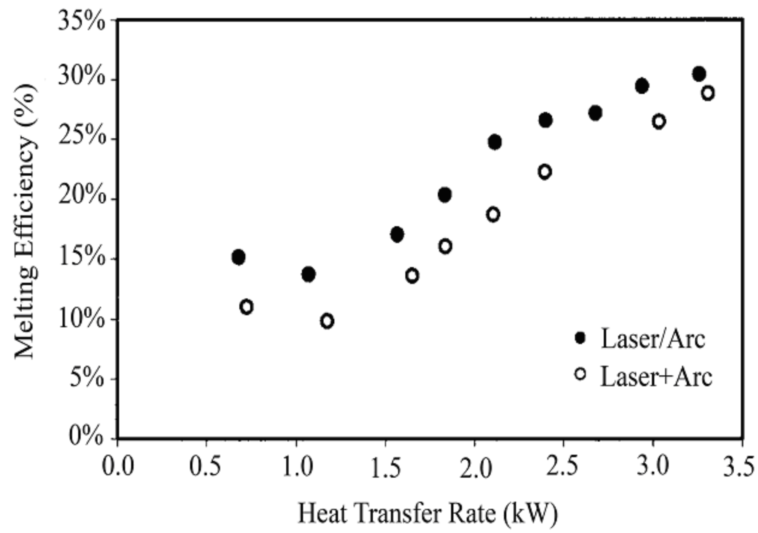

Fig. 2.4: Melting efficiency as a function of the heat transfer rate. The two data sets show the arc and laser welding (laser + arc) performed separately and (laser/arc) hybrid welding of mild steel.[37]

A clear distinction must be made as to when the arc and laser are acting in combination and when they are acting separately. This conclusion will aid in defining the hybrid welding process and help to develop a comprehensive understanding of the heat source interactions which occur during hybrid welding.

2.2 Keyhole formation

Laser welding can operate in either conduction or keyhole mode.[11] The welding mode is dependent upon the power density of the heat source, physical properties of the material, and welding speed.[1, 4, 20, 29] Fig. 2.5 shows micrographs of (a) keyhole (4500 W) and (b) conduction (800 W) mode laser weld cross sections. The welded material is A131 structural steel and travel speed is 8.5 mm s^{-1}. Keyhole mode laser weld bead geometries have a nail head shape close to the top surface and a relatively long narrow section deeper in the weld cross section (Fig. 2.5 (a)). A hemispherical transverse weld cross section is obtained during conduction mode laser welding (Fig. 2.5 (b)), which is similar to that obtained during arc welding.[11, 20] During conduction mode laser welding, the power density of the laser beam[34] is typically less than 10^5 W cm^{-2}, leading to a shallower weld pool than obtained during keyhole mode laser welding.[11, 20, 34]

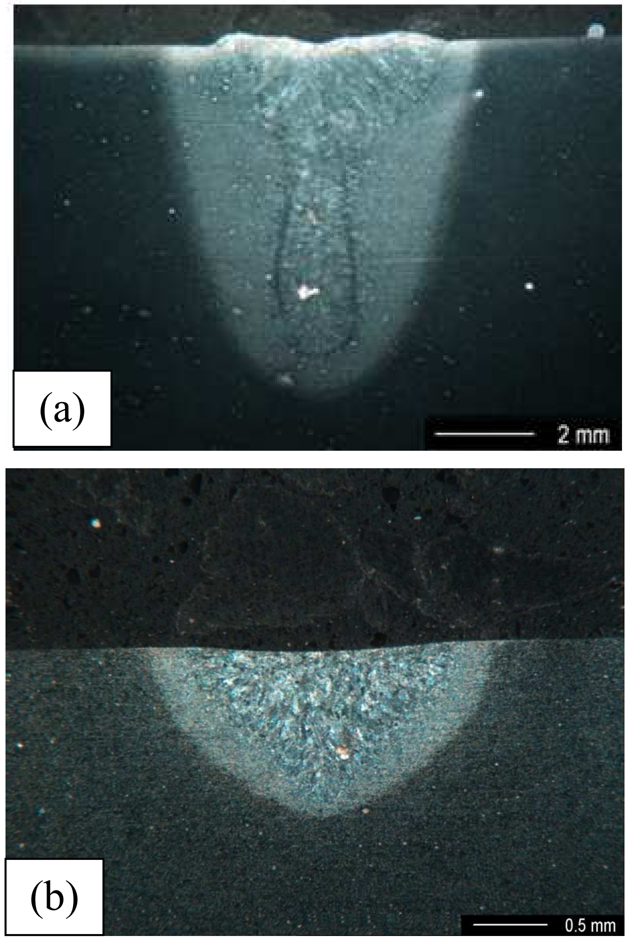

Fig. 2.5: Micrographs of (a) keyhole (4500 W) and (b) conduction (800 W) mode laser welds performed on A131 structural steel. The welding speed was 8.5 mm s^{-1}.

During keyhole mode laser welding, significant vaporization of the workpiece surface causes a keyhole to form.[1, 4, 11, 20] The depth of the keyhole strongly depends on the power density distribution of the laser beam, focal point of the laser, composition and flow rate of the shielding gas, laser beam radiation characteristic wavelength, welding speed, and workpiece material.[16, 18, 38, 49]

Keyhole profiles are often calculated by an energy balance at the keyhole wall, where temperatures are commonly assumed to be equal to the boiling point of the alloy.[50] At the boiling point, the sum of the vapor pressures of all alloying elements equals ambient pressure. Surface tension, hydrostatic, ambient pressure, vapor pressure, the pressure gradient driving metal vapor flow, and recoil pressures also affect the shape of the keyhole cavity.[4, 50-52] Hydrostatic and surface tension pressures tend to close the keyhole, while the vapor pressure, pressure gradient, and recoil pressure tend to maintain the keyhole. The balance of the keyhole pressures is given by:[4, 50, 52]

$$P_r + P_v + \Delta P = P_\gamma + P_o + \rho_l g h \tag{2.8}$$

where P_r is the recoil pressure, P_v is the vapor pressure, ΔP is the difference between the local pressure and the ambient pressure that drives the vapor flow out of the keyhole, P_γ is the pressure due to surface tension effects, P_o is the ambient pressure, ρ_l is the density of the liquid metal, g is the gravitational acceleration, and h is the depth of the keyhole. The recoil pressure is defined by:

$$P_r = J^2 / \rho_v \tag{2.9}$$

where J is the vaporization flux calculated from the modified Langmuir equation [7, 53] at local temperatures along the keyhole surface, and ρ_v is the density of the evaporating gas. The pressure difference due to vapor flow in the keyhole can be approximated by considering a cylindrical pipe flow pressure difference based upon the Hagen-Poiseulle equation: [54]

$$\Delta P = 8 \mu_v v_v h / r_k^2 \tag{2.10}$$

where μ_v is the viscosity of the metal vapor in the keyhole, v_v is the velocity of the metal vapor exiting the keyhole, h is the depth of the keyhole, and r_k is approximated as the radius of the keyhole at half the depth. The metal vapor velocity is approximated by:

$$v_v = J / c \tag{2.11}$$

where J is the vapor flux calculated from the modified Langmuir equation and c is the molar concentration of metal vapor in the keyhole. The surface tension pressure is given by: [4]

$$P_\gamma = \gamma / r \tag{2.12}$$

where γ is the surface tension and r is the keyhole radius.

The keyhole is constantly fluctuating, which makes keyhole stability an important consideration.[55] Several studies have evaluated keyhole formation and proposed various mechanisms for describing keyhole instability.[50, 55-57] Keyhole stability is dependent in part on the power density of the heat source, the competing pressures in the keyhole, welding speed, and workpiece material properties.[50] Fluctuations in the laser energy absorbed on the keyhole surface can cause the keyhole walls to oscillate and collapse or coalesce along the keyhole depth, which can lead to porosity formation.

2.3 Driving forces affecting weld pool fluid flow

Heat transfer and fluid flow affect weld pool size and shape and weldment cooling and solidification rates.[20, 33, 58] Since heat transfer affects the thermal cycles to which the material is subjected, the structure and properties of the weldment are also affected. Driving forces for liquid metal circulation in the weld pool include the surface tension, electromagnetic (in the case of arc or hybrid welding), buoyancy, and gas impingement or friction forces.

One of the primary driving forces affecting fluid flow in the weld pool during laser and hybrid welding is the Marangoni stress, which arises from the spatial gradient of surface tension driven by the temperature and compositional gradients existing in the weld pool.[7-8, 59] The Marangoni stress (τ) is defined by:[60]

$$\tau = \frac{d\gamma}{dT}\frac{dT}{dy} + \frac{d\gamma}{dC}\frac{dC}{dy} \tag{2.13}$$

where $d\gamma/dT$ is the temperature coefficient of surface tension, dT/dy is the spatial temperature gradient on the weld pool surface, and C is the concentration of surface active elements.

The presence of surface active elements such as sulfur and oxygen in the steel weld pool have an impact on the direction of convection.[60-61] If surface active elements are not present in the weld pool, the $d\gamma/dT$ term is negative, and liquid metal flows outwards from the heat source along the surface of the weld pool.[61] During arc[62-67] and low power density[42, 68] laser welding, outward flow from the heat source causes the weld pool to become shallower and wider.[68] If surface active elements are present in the weld pool, the $d\gamma/dT$ term is often positive.[60-61] The liquid metal flow is reversed, leading to a deeper and narrower weld pool during arc[62-67] and low power density[42, 68] laser welding.

During arc welding, the interaction between the divergent current path in the weld pool and current flow magnetic field produces the electromagnetic or Lorentz force.[20, 33] The Lorentz force causes liquid metal to flow down along the centerline of the weld away from the heat source, making the weld pool deeper.[69] The Lorentz force is defined by the following relationship:[70]

$$\mathbf{F_{emf}} = \mathbf{J_c} \times \mathbf{B} \tag{2.14}$$

where $\mathbf{J_c}$ is the current density and $\mathbf{B}$ is the magnetic flux in the weld pool.

The buoyancy or gravitational force arises from the spatial variation of the liquid metal density due to temperature variations in the weld pool.[71]

$$F_b = \rho_l g \beta (T - T_s) \tag{2.15}$$

where ρ_l is the density of the liquid metal, g is the acceleration due to gravity, β is the thermal expansion coefficient, T is the temperature of the liquid metal, and T_s is the alloy solidus temperature. The resulting fluid flow due to the buoyancy force is radially outward from the heat source location, causing the weld pool to become shallower and wider. The magnitude of the buoyancy force is commonly very small and can be neglected.

During high current arc welding, the arc plasma can exert a frictional shear stress along the weld pool surface.[72] The frictional force causes liquid metal to flow from the middle of the weld pool towards the weld pool solid/liquid boundary, resulting in a shallow and wide weld pool.[69] For most welding conditions,[72] this force is small and can be ignored, particularly at low and moderate currents (< 200 A).

The relative magnitudes of these driving forces dictate the resulting weld pool geometry. There are several dimensionless numbers that are used to gauge the relative importance and order of magnitude of the individual driving forces affecting fluid flow and the significance of convective heat transfer in the weld pool. These dimensionless numbers include the surface tension Reynolds number (Re_s), magnetic Reynolds number (Re_m), and Peclet number which are defined in the equations below:[7, 73-74]

$$Re_s = \frac{\text{Marangoni force}}{\text{viscous force}} = \frac{\rho_l L_R \Delta T |d\gamma / dT|}{\mu^2} \tag{2.16}$$

$$Re_m = \frac{\text{electromagnetic force}}{\text{viscous force}} = \frac{\rho_l \mu_m I^2}{4\pi^2 \mu^2} \tag{2.17}$$

$$Pe = \frac{\textit{convective heat transfer rate}}{\textit{heat transfer due to conduction}} = \frac{UL_R}{\alpha} \tag{2.18}$$

where ρ_l is the density of the liquid, L_R is the characteristic length of the weld pool and is taken as half of the weld pool width, ΔT is the difference between the weld pool peak temperature and the solidus temperature of the material, $d\gamma / dT$ is the temperature coefficient of surface tension, μ is the liquid viscosity, μ_m is the magnetic permeability, I is the arc current, U is the characteristic velocity of the liquid metal, and α (= $k/\rho C_p$) is the thermal diffusivity of the material.

The significance of convection in arc and laser welding has been extensively analyzed for steels.[8, 63, 67-68] Convection becomes less significant compared to heat transfer by conduction in the case of welding high thermal conductivity metals, for example aluminum and copper alloys. Compared to the electromagnetic force and Marangoni stress, the magnitude of the buoyancy force is small for arc and laser welding. The relative importance of the electromagnetic force to Marangoni stress can be obtained from the ratio Re_m/Re_s. Table 2.1 shows calculated values for the relative importance of electromagnetic force to Marangoni stress during 191 A, 11V arc welding and 1900 W laser welding of A131 structural steel at 8.5 mm s^{-1}.

Table 2.1: Calculated values of magnetic Reynolds number and surface tension Reynolds number for Nd:YAG laser and GTA welding of A131 structural steel. The laser power was 1900 W, and the arc current and voltage were 191 A and 11 V, respectively.

Process	**Arc**	**Laser**
Re_m	3.2×10^5	-
Re_s	5.9×10^4	3.5×10^5
Re_m/Re_s	5.4	-

Under most arc welding conditions, the order of magnitude for the electromagnetic force can be equal to or even greater than the Marangoni stress, depending on the current used. In laser welding, no electromagnetic force is present, and the Marangoni stress is the primary cause of convection in the weld pool. The relative magnitudes of the driving forces for hybrid welding are not known.

During arc welding, the Marangoni stress drives liquid metal from the middle of the top surface toward the edge of the weld pool and this stress tends to widen the weld pool when the surface active element concentrations are negligible.[69] The electromagnetic force, on the other hand, tends to drive the liquid metal downward. As a result, the shape of the weld pool during arc welding is often hemispherical.[62] Similar fluid flow behavior is seen in the case of conduction mode laser welding, where the weld pool shape is dictated by the Marangoni stress and is hemispherical.[68] Marangoni convection during keyhole mode laser welding moves the liquid metal at the surface of the weld pool toward the edge of the weld pool causing the upper part of the weld pool to be wider[69] than that of the lower portion.[7-8]

During welding, the rates of transport of heat, mass, and momentum are often enhanced because of the presence of fluctuating velocities in the weld pool.[7, 59] The contribution of the fluctuating velocities is quantitatively expressed by an appropriate turbulence model[7, 75-76] that provides a frame work for calculating effective viscosity and thermal conductivity values. Effective viscosity can be defined as the sum of the turbulent and molecular viscosities ($\mu_{eff} = \mu_T + \mu_m$). The turbulent viscosity is calculated using the Prandtl mixing length hypothesis given by:[7,8,24]

$$\mu_T = \rho l_m v_t \tag{2.19}$$

where ρ is the liquid metal viscosity, l_m is the mixing length, and v_t is the turbulence velocity. Effective thermal conductivity is then calculated from the definition of the Prandtl number equation given by: [7,8,24]

$$\Pr = \frac{\mu_T c_p}{k_T} \tag{2.20}$$

where C_p is the specific heat of the liquid metal, and k_T is the turbulent thermal conductivity. The Prandtl number is assumed to be 0.9. The values of effective thermal conductivity and viscosity vary with location in the weld pool and depend upon the local characteristics of fluid flow.[77-78]

2.3.1 Role of surface active elements during hybrid welding

Depending upon the significance of convective heat transfer, surface active elements can play a large role in dictating weld bead geometry by influencing the Marangoni stress,.[49, 79-80] Weld bead width and depth as a function of shielding gas oxygen content and alloy sulfur content are shown in Fig. 2.6 (a) and (b), respectively, for 7 kW fiber laser welding of mild[80] steel at a welding speed of 16.7 mm s^{-1}. Aside from the added oxygen, the shielding gas contained helium and argon.[80]

In both cases, the addition of oxygen to the shielding gas and the increase in sulfur content of the base metal during laser and laser-arc hybrid welding increases weld pool depth.[49, 79-80] Weld pool depth is measured as the distance from the weld fusion zone top surface to the bottom of the weld fusion zone at the centerline of the weld. However, the increase in weld depth is more significant when adding oxygen than sulfur.[80] Increasing the oxygen content of shielding gas[80] from 0% to 10% increases weld depth from 9.2 mm to 10.3 mm. Other research has shown that in the case of 3.3 kW Nd:YAG laser welding of 304 stainless steel, the addition of 10% oxygen to initially pure argon shielding gas resulted in an increase in weld pool depth of approximately 0.9 mm.[49] The welding speed in this case was 10 mm s^{-1}.

Increasing the amount of sulfur in the alloy or oxygen in the shielding gas causes the weld pool width to decrease.[49, 80-81] Weld bead width is measured as the distance between the left and right hand edges of the weld fusion zone at the weld bead top surface. The decrease in weld width can be explained by the effect of surface active elements on the Marangoni stress. As the surface active element content increases, $d\gamma/dT$ becomes more positive, depending upon the local weld pool temperature. If $d\gamma/dT$ becomes positive, the fluid flow direction can change, and may affect weld bead shape depending upon the significance of convective heat transport.

Fig. 2.7 shows micrographs of 7 kW fiber laser welded mild steel for various concentrations of oxygen in the shielding gas and sulfur in the base metal.[80] When oxygen was added to the shielding gas, the weld metal contained 60 ppm of sulfur. The shielding gas also contained argon and 60% helium. The deep and narrow portion of the weld bead, which is dictated by the keyhole, is increasing in depth with increasing oxygen and sulfur content in the shielding gas and base metal. However, the reason for this increase in the keyhole depth with increasing active element concentrations in the shielding gas or welded material is not known. The mechanism which causes the weld depth to be more sensitive to the amount of dissolved oxygen in the weld versus sulfur is unknown. In addition, a comparison of the fluctuations in weld depth due to spiking and the increase in weld depth with increasing the surface active element concentration needs to be analyzed. Further research is needed to understand this important phenomenon, especially since the keyhole shape and stability play such an important role in laser and hybrid welding fusion zone geometry and weld integrity.

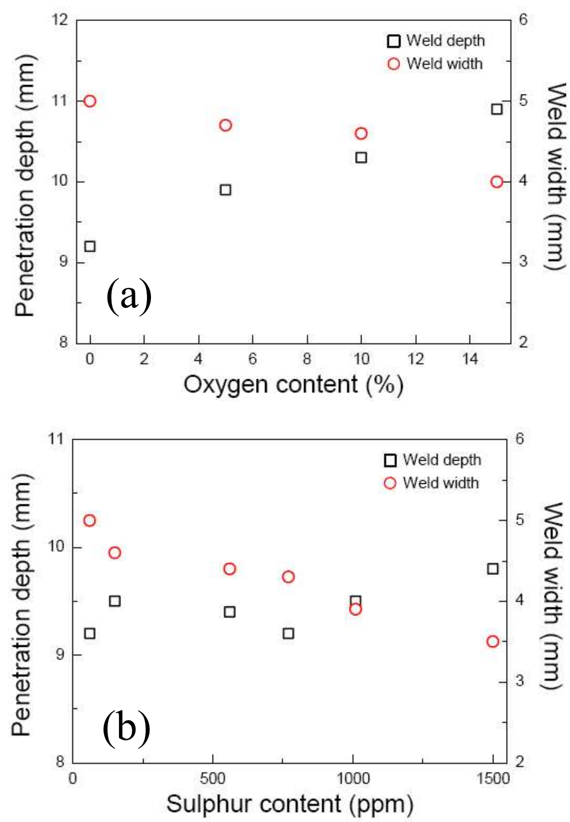

Fig. 2.6: Change in weld pool width and depth for increasing (a) shielding gas oxygen content and (b) alloy sulfur content for 7 kW laser welding of mild carbon steel at a welding speed of 16.7 mm s^{-1}. The material in Fig. 2.6 (a) contained 0.006 wt% sulfur.[80]

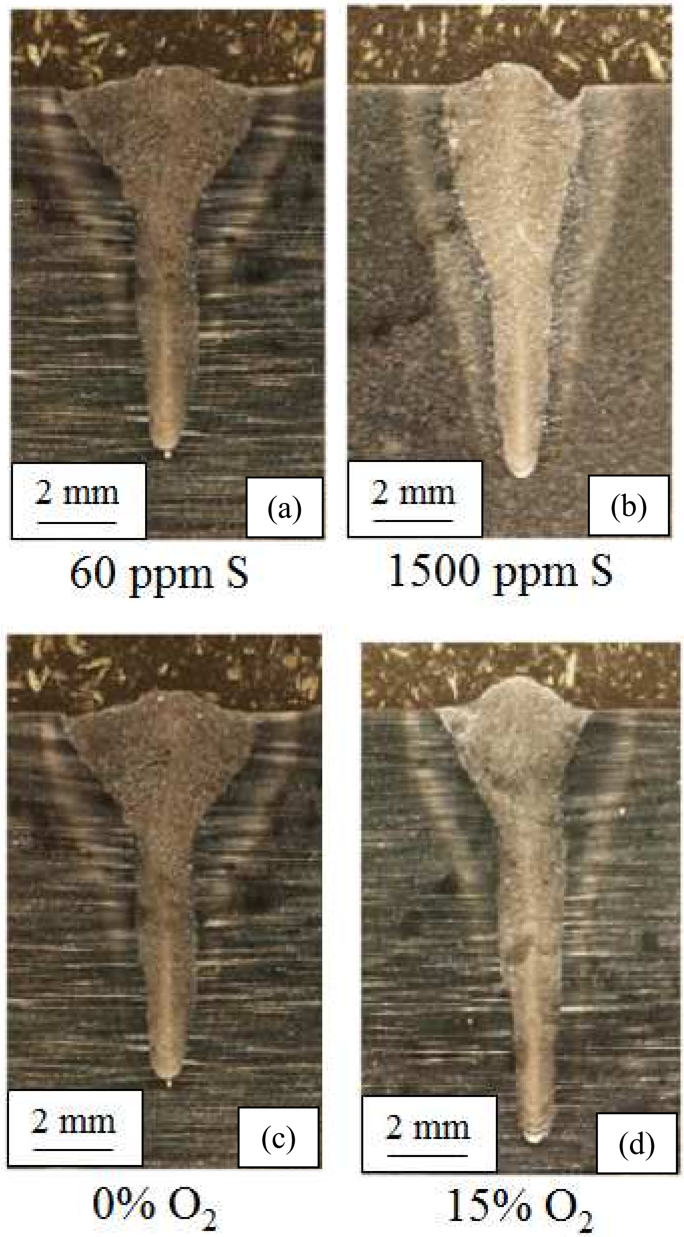

Fig. 2.7: Micrographs of laser welded mild steel for various concentrations of oxygen in the shielding gas and sulfur in the base metal.[80] The laser power and welding speed were 7 kW and 16.7 mm s^{-1}.

2.3.2 Fluid flow and hybrid weld pool geometry

One of the most beneficial aspects of combining laser and arc sources in hybrid welding is a wider weld bead than that achieved from lone laser welding and a deeper weld than that compared to lone GTAW for the same welding parameters.[82-85] A quantitative understanding on the effects of the driving forces for fluid flow on weld pool temperature profiles, fluid flow, bead geometry, and reducing the propensity for cracking, porosity, and brittle phase formation are essential and can be further understood.

Little work, though, has been done to quantitatively understand the fluid flow within the molten weld pool during hybrid welding.[59, 86-87] It is important to have a strong understanding on the liquid fluid flow in welding due to its importance to weld geometry, temperature gradients in the weld pool, and the resulting weld microstructure and properties. The use of x-ray transmission imaging of platinum and tungsten markers during hybrid welding shows that there is a strong liquid flow towards the rear of the weld pool.[49, 88] The fluid flow in the molten weld pool causes heat to flow away from the keyhole, thus elongating the weld pool parallel to the welding direction.[88-89] The flow is believed to be driven primarily by electromagnetic and surface tension forces.[59, 88]

According to the current process understanding, the primary process parameters which affect bead geometry in hybrid welding are laser power, arc power, welding speed, laser beam radius, defocusing, and the distance between the heat sources.[36, 59, 83, 90] Weld pool depth is primarily affected by the laser power density and welding speed.[59, 83] Currently, it is believed that the arc power density distribution is the primary processing factor in establishing the width of the weld pool[83, 88] because the arc is a more dispersed heat source. Increasing arc current increases the arc radius and the width of the weld pool. In addition, the interaction of the hybrid welding plasma with metal vapors from the laser generated keyhole impact the arc power density distribution and weld width.

Welding speed has a direct effect on the heat input per unit length per unit time of the welding process. At faster welding velocities, heat input decreases for a constant arc and laser power. Less molten metal is thus generated by the heat sources, causing both the width and penetration depth of the weld pool to decrease.

The power level ratio between the laser and the arc also can play a significant role in the hybrid welding process. This ratio can be used to determine whether the laser or the arc is dominant and which one has the greater influence on the change in penetration depth and the width of the weld pool.[37, 83] El Rayes et al[83] showed that increasing the ratio of arc to laser power, for constant CO_2 laser power levels of 8 kW and 4 kW, has a minimal effect on the total depth of the weld pool. Gao et al[91] evaluated the power level ratio and found that it plays an important role in determining steel weld microstructure.

The effect of the power ratio on laser vaporization and laser attenuation by the arc plasma has been experimentally observed during CO_2 laser/GTA hybrid welding.[36] It was observed that the arc plasma can affect keyhole stability and cause a weld cross section similar to a conduction mode laser weld to form.[36] The attenuation of the laser beam by the arc plasma keeps the laser from generating a significant amount of metal vapor necessary to continue the plasma interaction between the arc and laser.

Understanding the effects of power level ratio, heat source separation, and laser defocusing on fluid flow and weld pool geometry are essential for a more complete understanding of hybrid welding. The combinations of these important process parameters during the synergistic interaction between the arc and laser induced plasmas has not been thoroughly discussed in the literature. A fundamental understanding of the roles which these processing parameters play during hybrid welding is needed.

2.4 Plasma formation

During arc and laser welding, a plasma phase can form above the weld pool through the interaction between the arc or laser, the shielding gas, and possibly metal vapors. The plasma phase contains electrons, ions, excited atoms, and molecules. Knowledge of the number densities of these excited species and electrons can also provide insight into the important properties of the plasma. The electron temperature, which is a measure of the kinetic energy of the electrons within the plasma phase, is an important parameter used to characterize the plasma phase.

The existence of thermodynamic equilibrium in a plasma requires that temperature governs the excitation, ionization, and dissociation of molecules in the plasma.[92] The electron and heavy particle temperatures are nearly equal due to the high collision rates inside the plasma. In the case of a welding plasma, the radial gradient of plasma temperature interferes with the state of equilibrium.[92] If the change in temperature is small along the mean free path compared to the average plasma temperature of a region, the influence of the temperature gradient on the equilibrium condition can be considered negligible.[92] For the case of welding plasmas at atmospheric pressure, the mean free path of collisions is small. Welding plasmas are often considered in terms of separate volumes for a non-isothermal plasma and is referred to as local thermodynamic (thermal) equilibrium.[92] When the plasma is in local thermodynamic equilibrium the population of energy levels satisfies Boltzmann's distribution law, the ionization of species in the plasma is governed by Saha's relationship, and dissociation equilibria are described by the equation for chemical equilibria.[92] The Boltzmann's distribution law is given by:[92]

$$\frac{n_q}{n_o} = \frac{g_q}{g_o} \exp(-\varepsilon_q / kT) \tag{2.21}$$

where n_q is the density of particles in the excited state q, n_o is the density of ground state atoms, g_q and g_o are statistical weights for the corresponding levels, ε_q is the excitation energy of the state q, k is the Boltzmann constant, and T is the absolute temperature. Saha's equation is given by:[44, 92]

$$\frac{n_e n_i}{n_a} = \frac{Z_e Z_i (2\pi m_e kT)^{3/2} e^{(-V/kT)}}{Z_a h^3} \tag{2.22}$$

where n_e is the electron density, n_i is the ion density, n_a is the atom density, Z_e is the electron partition function (which is given a value of 2 for the two available spin orientations of the electron),[92] Z_i is the ion partition function, m_e is the resting mass of an electron (9.11 x 10^{-31} kg), V is the ionization potential of the species, Z_a is the atom partition function, and h is Planck's constant. The dissociation of molecules (XY = X + Y) can be defined using the general equation for chemical equilibria given by:[92]

$$K_n = \frac{n_X n_Y}{n_{XY}} \tag{2.23}$$

where n_X, n_Y, and n_{XY} are the particular species concentrations in number per unit volume.

When the plasma is in local thermodynamic equilibrium, electron temperatures are given by:[92]

$$T = \frac{5040(E_{qa} - E_{qb})}{\log\left[\frac{(g_q A_{qp})_a}{(g_q A_{qp})_b}\right] - \log\left[\frac{\lambda_a}{\lambda_b}\right] - \log\left[\frac{I_a}{I_b}\right]} \tag{2.24}$$

where E_{qa} and E_{qb} are the upper energy level potentials of measured spectral line peaks 'a' and 'b', g_q and A_{qp} are the upper energy level statistical weight and transition probability of the corresponding peaks, λ_a and λ_b are the wavelengths of peaks 'a' and 'b' respectively, and I_a and I_b are the measured intensities or calculated emissivities of the peaks.

In the case of high power density laser welding or hybrid welding, the plasma can contain a relatively high concentration of metal vapors compared to arc plasmas.[40, 93] In order to provide an accurate approximation of the species densities for these plasmas, the species densities are modified based upon the mole fraction of species in the plasma given by:

$$N_m^j = n_j^k x_k \tag{2.25}$$

where N_m^j is the atom, ion, or electron density for the multi-component plasma, n_j^k is the atom, ion, or electron density for pure element k calculated by Saha's equation, and x_k is the mole fraction of element k in a multicomponent system.

Complex characterization techniques, such as high temperature Langmuir probes or emission spectroscopy are often utilized to determine electron temperature and species densities at discrete locations within the plasma phase.[92, 94-95] A Langmuir probe is a device which consists of one or more electrodes which are placed in a plasma phase with a constant or time-varying electric potential between the electrodes. The current and potential drops across the probes are then measured and correlated with the electron temperature and density of the plasma.

An example of temperature measurements made using Langmuir probes[96] in a GTA welding arc is shown in Fig. 2.8. Temperatures at locations directly adjacent to the electrode are about 10,750 K. At these temperatures, ionization of gaseous species is prevalent. Throughout the remainder of the plasma phase in the arc column, the temperatures are high enough for significant dissociation of diatomic gases to occur and decrease as the workpiece is approached. Therefore, ionized species tend to dominate at locations closer to the electrode, and neutral species are dominant as the workpiece is approached. Fig. 2.8 also shows that the size of the arc plasma can have diameters of the order of 8 mm, which is considerably larger than the typical laser induced plasma.

Emission spectroscopy is a non-contact means for characterizing the species present in the plasma phase. With this technique, species within the plasma phase are identified by their characteristic wavelengths. One issue with optical emission spectroscopy is that it suffers from line of sight effects,[92, 94] in which the measured spectra are influenced by radiation emitted from other locations inside the plasma that also lie along the line of sight of the detector. To overcome this difficulty, measured spectral intensities need to be deconvoluted using an Abel transform. The transform requires that the plasma has a symmetrical cross section at the plane of interest.[97]

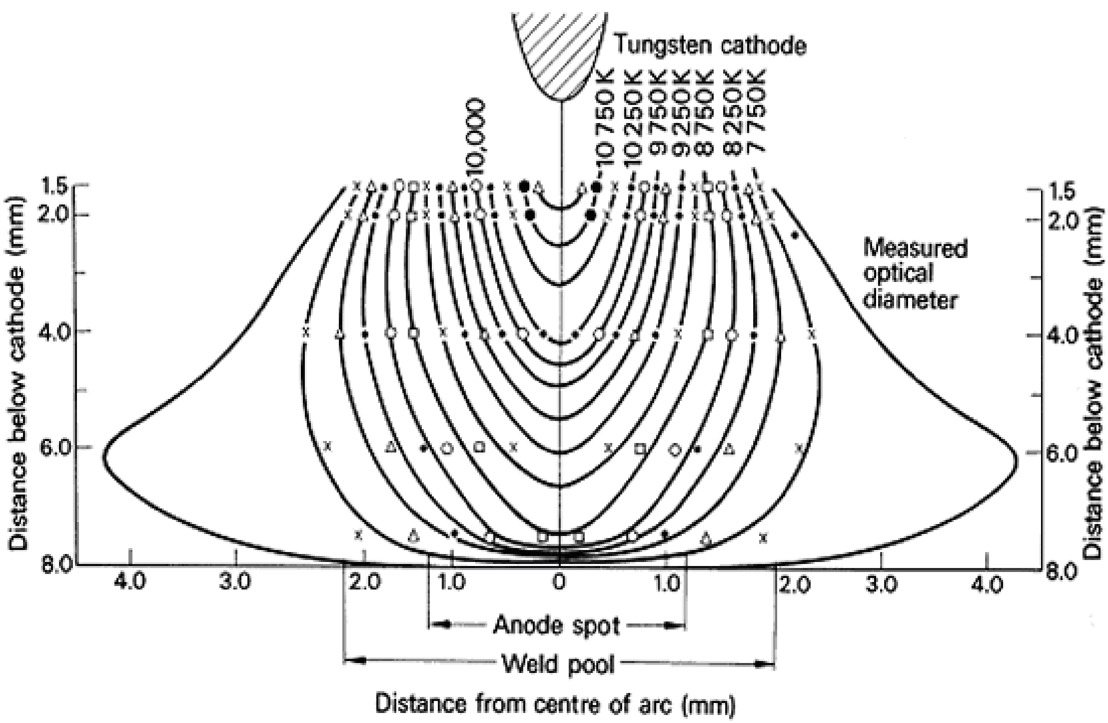

Fig. 2.8: Temperature distribution in the arc column under GTA welding conditions for an arc current of 100 A. The welded material was mild steel. The temperatures in the arc column were calculated using electrostatic probes.[96]

A number of researchers have theoretically and experimentally investigated the characteristics of the plasma phase formed in the arc column during GTA welding using emission spectroscopy.[96, 98-101] For example, Dunn and Eagar[102] calculated the electron densities and the resulting transport properties of argon and helium plasmas with small additions of metal vapors. Drellishak et al[103-104] investigated the species densities of both inert gaseous and pure nitrogen and oxygen plasmas at atmospheric pressures. Fig. 2.9 shows a measured spectra[99] of the plasma formed with helium shielding gas during the GTA welding of SUS304 stainless[99] steel at an arc current of 150 A and a travel speed of 0.5 mm s^{-1}. The arc plasma shows the presence of atomic metallic species and shielding gas.

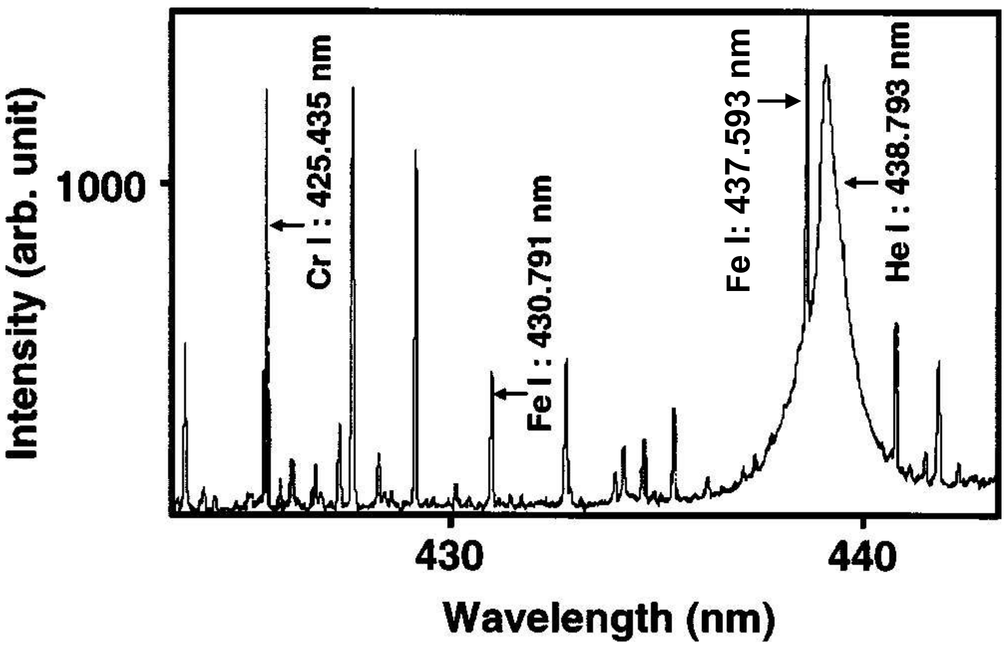

Fig. 2.9: Gas tungsten arc welding plasma. The shielding gas was helium and welded material was SUS304 stainless steel.[99] The arc current and welding speed were 150 A and 0.5 mm s^{-1}, respectively.

During laser welding, the interaction between the laser beam and the alloy produces significant vaporization of alloying elements, which vary depending on the composition of the alloy.[53, 105-106] For example, during laser welding of stainless steels, metal vapors may contain iron, chromium, and manganese.[40] Fig. 2.10 shows[40] a typical optical emission spectrum of the plasma produced during pulsed CO_2 laser welding of AISI 201 stainless steel using argon shielding gas. The iron and chromium peak intensities are relatively greater than those during GTAW (Fig. 2.9) due to increased vaporization rates.[44] In Fig. 2.10, peaks of atomic Fe, Cr, and Mn are observed because of their presence in the plasma.

Since the metal vapors are easily ionized compared to the argon shielding gas, their presence significantly affects the electron density and electron temperature of the laser induced plasma. Between 422 nm and 432 nm, there are five well characterized argon spectral lines,[107] yet these lines do not appear in the measured spectra due to the relatively greater intensity of the metal vapor lines.[107] The lack of shielding gas spectral lines in Fig. 2.10 and greater metallic species spectral line intensities are indicators that the laser plasma is dominated by the presence of metal vapors, unlike the GTA plasma (Fig 2.9). The greater concentration of metal vapors in the laser plasma contributes to increasing the plasma electron density. Depending upon the local plasma temperature, increasing the plasma metal vapor concentration can significantly increase electrical conductivity.

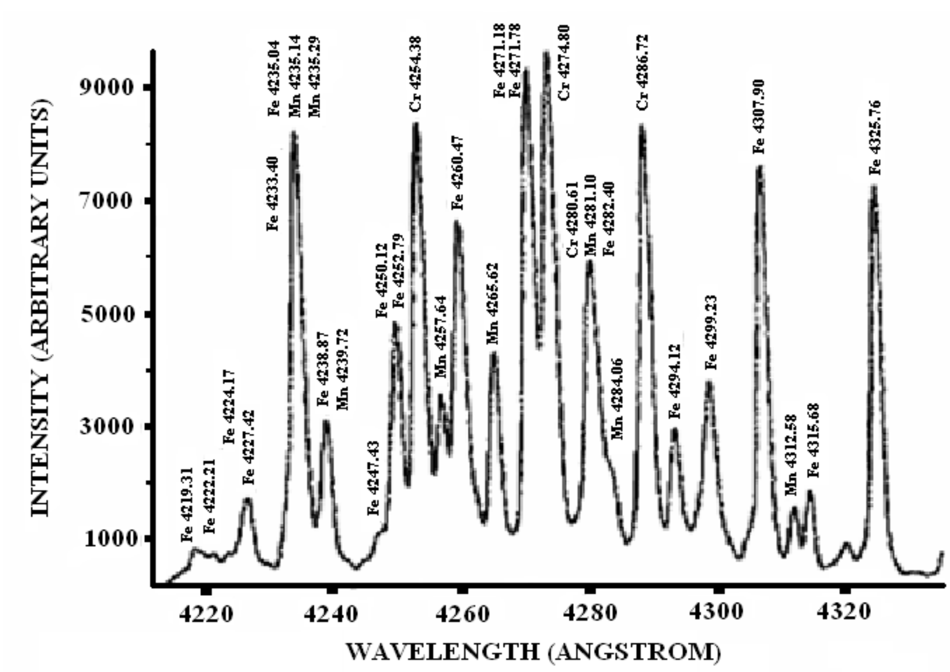

Fig. 2.10: Laser welding plasma spectrum during welding of AISI 201 stainless steel using argon shielding gas.[40] The laser power, beam radius, pulse duration, pulse frequency, and welding speed were 2462 W, 140 μm, 3 ms, 100 Hz, and 5 mm s^{-1}, respectively.

At any given electron temperature, the equilibrium number density for each pure species can be calculated considering the equilibrium condition for the ionization of that particular species via Saha's equation. In Fig. 2.11, the computed number density of singly ionized pure metal vapors, including Fe, Mn, and Cr, are significantly higher than that for argon over a range of electron temperatures in a laser plasma.[40, 102] The total electron density (Total Ne) is the summation of the mole fraction of each species in the plasma multiplied by the corresponding singly ionized species number density for a plasma composed of solely that element for a given temperature. The metallic ion densities are relatively higher due to their lower ionization potentials compared to that of the shielding gas. The gradient in species densities tends to decrease at higher electron temperatures due to volume expansion of the plasma with increasing temperature.

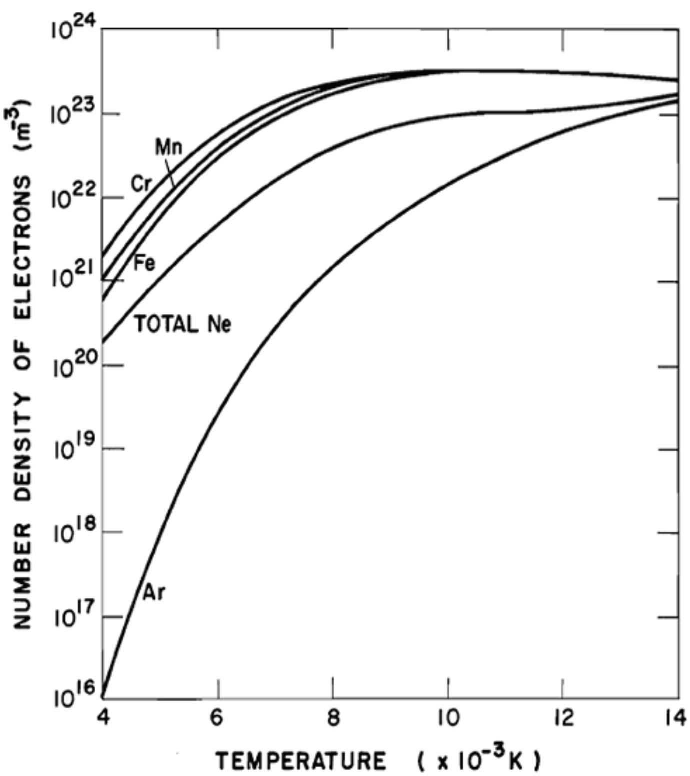

Fig. 2.11: Ion and total electron density as a function of electron temperature for various pure species for pulsed laser welded AISI 201 stainless steel.[40, 102] The laser power and welding speed were 2462 W and 5 mm s^{-1}, respectively.

During hybrid welding, metal vapors present in the plasma can significantly increase plasma electrical conductivity, depending upon the local plasma temperature.[102] Electrical conductivity is an important property for electrical arc plasmas, which can significantly influence arc stability. Analysis of combining laser and arc plasmas during hybrid welding and the resulting spectral characteristics are only beginning.[108-109] Since the plasma properties are so important to arc stability and weld integrity, a better understanding of hybrid welding plasma characteristics is needed.

2.4.1 Plasma formation during hybrid welding

During hybrid welding, a plasma phase forms due to the interaction of the high power density laser heat source, shielding gas, and metal vapors formed by the laser-material interaction. By using a high ionization potential shielding gas, such as helium, the formation of a laser induced plasma can be mitigated, particularly for high wavelength CO_2 lasers.[18-19, 38] Helium has been traditionally used only in the case of CO_2 lasers, not necessarily for YAG systems.

A plasma phase also forms by the interaction of the arc and the surrounding atmosphere during hybrid welding. Hybrid welding plasma size often depends on the distance between the heat sources, arc current density, arc length, and arc voltage. It has also been observed that the laser and arc interact, and the transmission of the laser through the plasma results in some additional laser attenuation.[28, 35, 37, 110]

During hybrid welding, the arc undergoes a contraction in which its width decreases to nearly the same size as the laser beam.[28, 35-36, 59] The arc contraction is attributed to the presence of the laser induced plasma which causes the arc electrical resistance and radius to decrease. Lower arc electrical resistance and enhanced arc stabilization[35] in the presence of a laser is shown via arc current and voltage data in Fig. 2.12 for GTA and CO_2 laser/GTA hybrid welding of mild steel.

The influence of laser radiation on arc electrical resistivity and stability can be explained by two phenomena. First, a small part of the laser energy is absorbed by the arc plasma, further ionizing the arc plasma and reducing its electrical resistance.[28, 36-37, 59] Second, significant vaporization of the workpiece material occurs at the location where the laser impinges on the surface of the workpiece,[20, 40, 42, 44] and metal vapor is then transported into the arc plasma. Since the metal atoms have a much lower ionization potential than the shielding gas, the effective ionization potential of the plasma is reduced, forming a more conductive, stable plasma channel for the arc root and column.[28, 35-37] Since the arc follows the path of least electrical resistance, the arc tends to bend and root within close proximity of the keyhole.[28, 36-37]

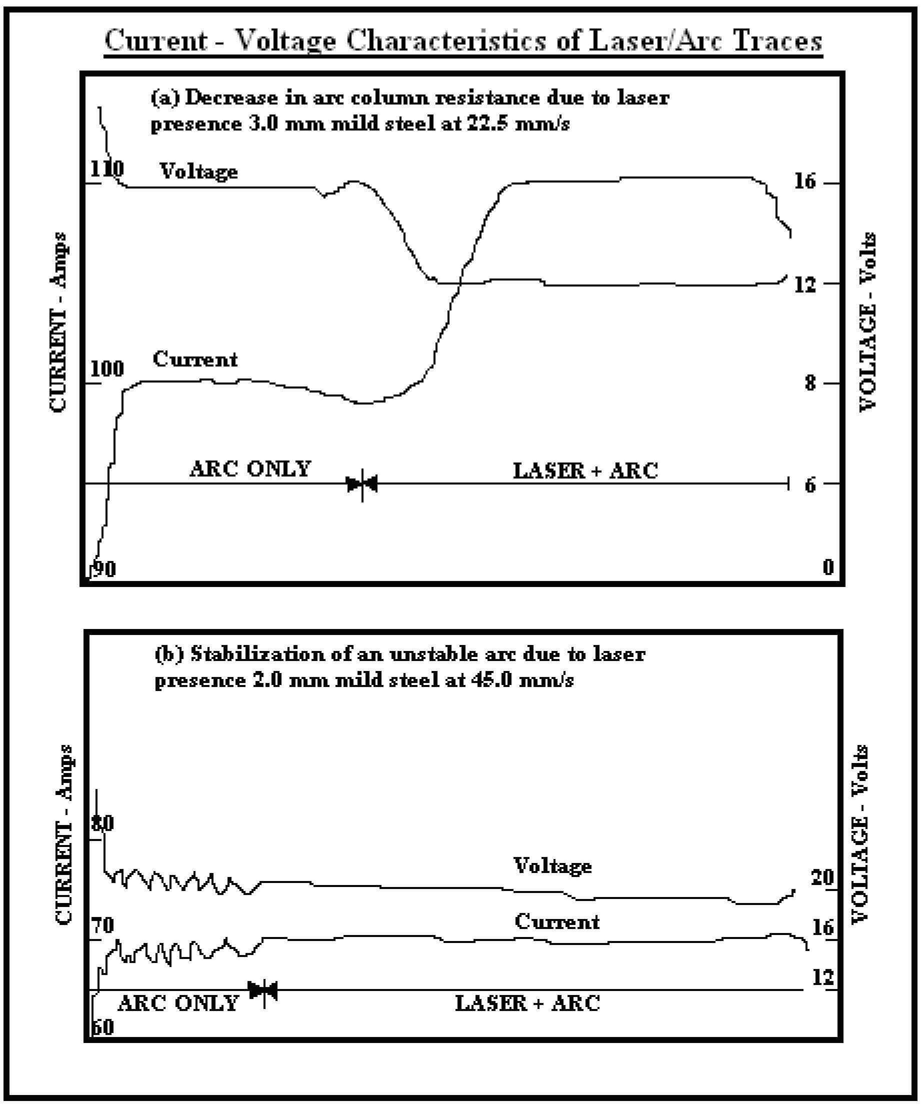

Fig. 2.12: Characteristics of current and voltage during GTA and CO_2 laser/GTA hybrid welding of mild steel.[1] (a) Arc electrical resistance decreasing due to the presence of the laser, and (b) laser stabilization of fluctuations in arc voltage and current.[35] The laser power was 1870 W.

2.5 Role of laser-arc separation on hybrid welding plasma and weld attributes

Often, hybrid welding is described as simply welding with an arc and a laser. However, changes in the distance between the arc and laser can cause two distinct welding processes, hybrid and tandem welding, to emerge. During hybrid welding, an interaction occurs between the laser and arc as a result of the close proximity of the two heat sources. Tandem welding occurs when the distance between the heat sources is significantly greater than the arc plasma radius, usually 5 to 8 mm. In tandem welding, the arc and laser act separately on the workpiece.

The distance between the heat sources plays a large role in the arc and laser induced plasma interactions.[13, 28, 35, 37] Experimental research has shown that, during the plasma interaction, the contracted arc rooting in close proximity of the keyhole can increase weld pool penetration depth.[13, 28, 36-37] The increase in depth is small relative to the penetration depth achieved by high power density laser welding.[36, 59] In addition, the laser-arc interaction results in a significant increase in weld pool width over laser welding.[59] Little scientific explanation has been presented to explain the fundamental physical processes which occur to enhance these weld pool dimensions. The influence of heat source separation distance on hybrid welding plasma properties is also not known. Since the plasma properties influence the arc stability, it is important to analyze the effects of heat source separation distance on hybrid welding plasma properties.

The effects of arc power, welding speed, defocusing distance, and heat source separation distance on weld bead shape, spatter, arc stability, and plasma formation were investigated during the CO_2 laser/GMA hybrid welding of low carbon steel.[13] Fig. 2.13 shows that as the distance between the heat sources decreases, the weld pool depth increases,[13] which is in agreement with the findings of Naito et al.[88] The laser power, arc current, and welding speed were 2 kW, 200 A, and 10 mm s^{-1}, respectively. An increase in negative beam defocusing may increase the penetration depth of the weld pool depending upon the operating mode of the laser beam and the depth of focus of the laser.

It has often been observed that the maximum hybrid weld penetration depth occurs at some intermediate heat source separation distance, rather than when the separation distance is zero.[13, 36, 82, 88] Fig. 2.14 is a schematic of how the weld penetration depth and weld pool geometry change for various separation distances between the heat sources during CO_2 laser/GMA hybrid welding of low carbon steel.[13, 88] The maximum hybrid weld penetration depth was achieved when the laser passed through the edge of the arc plasma, versus through the center or for a smaller separation distance. Very little is known as to why the penetration depth is not maximized when the separation between the heat sources is at its minimum, and a better understanding as to why this occurs would greatly benefit maximizing weld depth.

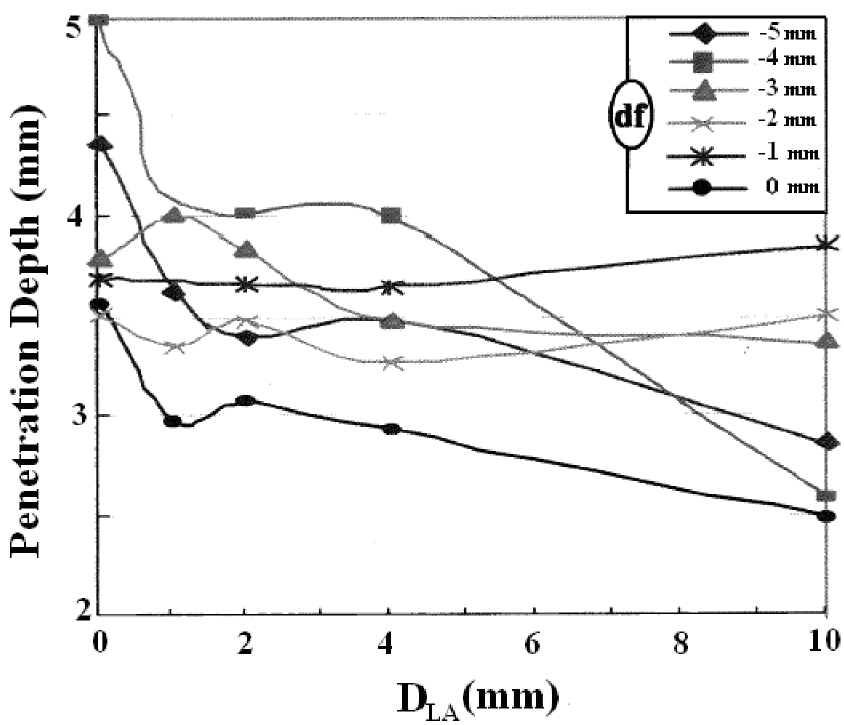

Fig. 2.13: Effect of the distance between the gas metal arc root and CO_2 laser focal point (D_{LA}) on hybrid weld pool penetration depth. In addition, the effect of defocusing (df) on penetration depth is shown for hybrid welding.[13] The base metal was low carbon steel. The laser power, arc current, and welding speed were 2 kW, 200 A, and 10 mm s^{-1}, respectively.

The exact role of heat source separation distance on the interaction of the heat sources and its effects on the weld properties and physical processes is not well defined and requires further research. When the distance between the laser and arc is significantly greater than the arc plasma radius, the laser and arc plasmas are separate. In contrast, when the distance between the two heat sources is less than or approximately the same as the arc plasma radius, the two plasmas interact.[13, 88] Therefore, the interaction of the laser beam and the arc plasma mainly depends on the distance between the heat sources, arc radius, and arc plasma radius.[28, 35, 110] A quantitative understanding of the hybrid welding plasma properties and their relationship with welding parameters will lead to a significant improvement in process control. Further research is needed on the role of heat source separation and its effect on hybrid welding plasma characteristics.

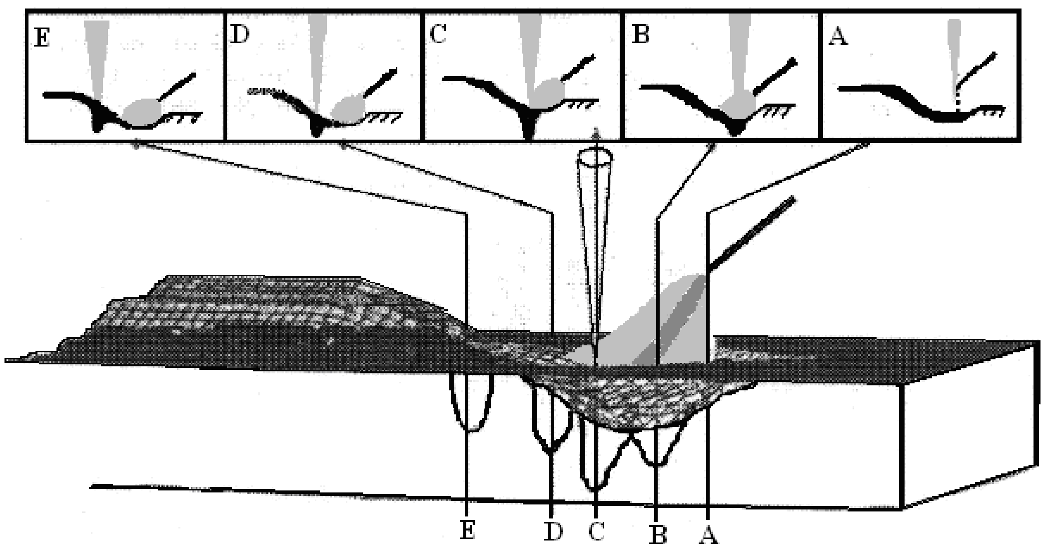

Fig. 2.14: Schematic of the effect of heat source separation distance on weld geometry and penetration depth during CO_2 laser/GMA hybrid welding. A, B, C, D, and E indicate the change in relative position of the arc and laser in the weld pool (images above workpiece) and their corresponding weld bead geometry.[13, 111] The base metal was low carbon steel. The laser power, arc current, and welding speed were 2 kW, 200 A, and 10 mm s^{-1}, respectively.

2.6 Defect Formation

Hybrid welds contain much lower levels of porosity in both size and number than laser welds.[88, 112-114] The reduced presence of porosity in hybrid welds is largely attributed to lower cooling rates compared to laser welding.[115] The addition of the arc increases solidification times and allows for gas porosity to escape the molten metal. However, much further research is required in order to understand porosity formation, particularly in the case of porosity due to unstable keyhole collapse and its material dependence.

The formation of microporosity (< 1 μm diameter) has been attributed to the entrapment of gas bubbles from dissolved hydrogen during high power density laser and laser/GMA hybrid welding of magnesium alloys.[115-116] In the case of laser welding of magnesium alloy AM60B, the porosity was attributed to the evolution of hydrogen gas pores due to the difference in hydrogen solubility between the liquid and solid phases.[116] Subsequent welding passes lead to the coalescence of these pores and resulted in much larger macropores.[116]

Larger macroporosity can arise from the unstable collapse of the laser induced keyhole during laser or hybrid welding due to fluctuations of welding process parameters. For example, variations in the focal point of the laser, laser power, or welding speed can influence keyhole stability.[50, 52]

Studies on the formation of macroporosity in magnesium AZ31B hybrid butt welded plates showed that the composition of the surface of the pores was 24.8 wt% oxygen and 9.4 wt% nitrogen.[113-114] Air from the atmosphere can enter the weld and generate nitrides and oxides. The addition of laser shielding gas was identified as the remedy for this problem.[113-114]

Macroporosity is also observed during the laser lap welding of zinc coated steels.[117-119] The boiling point of zinc is approximately 900ºC, which is significantly lower than the melting point of iron (1538ºC). When zinc coated sheets are lap welded, zinc vapor filled bubbles form and large amounts of macroporosity are in the final weldment.[117-119] With laser/GMAW hybrid welding, porosity is significantly diminished as compared to laser welding because a much longer time elapses before the molten metal solidifies, allowing for the bubbles to escape.[117, 120]

Additional defects can be caused, particularly in laser welding, by gaps which may form due to improper joint fit-up. The ability to bridge larger gaps during hybrid welding means less edge preparation. Because of the restricted width of the laser beam, perpendicular workpiece edges are required in laser welding.[110] Compared to laser welding, the wide power density distribution produced by the addition of the arc heat source allows for less stringent gap tolerances during hybrid welding.[110, 112, 121-122]

2.7 Microstructure and properties

Understanding how cooling rate changes with hybrid welding parameters can explain why the microstructure and mechanical properties of hybrid welds differ from those attained during arc or laser welding. In the following sections, the role of heat input and power density on microstructural formation and the effects of hybrid welding, relative to laser or arc welding, on weldment microstructure and mechanical properties for steels, magnesium, and aluminum alloys is evaluated.

2.7.1 Role of heat input and power density

Weldment cooling rate is dependent upon the thermophysical properties of the material, power density (W mm^{-2}) of the heat source,[2, 4, 91, 123] and heat input per unit length of the welding process (J mm^{-1}).[124-127] The heat input per unit length is dictated by the welding speed and power of the heat source and given by:[126]

$$H = \frac{P_n}{v} \tag{2.26}$$

where H is the heat input per unit length in J mm^{-1}, P_n is the nominal power of the heat source in W, and v is the welding speed in mm s^{-1}. As heat source power density increases, the heat input per unit length necessary for welding decreases.[2] Low heat input per unit length welding processes result in a relatively small amount of grain coarsening.[2, 91, 126, 128] For example, GTAW of Ti-6Al-4V[129] showed that the average prior β-grain size decreased from approximately 360 μm to 60 μm upon decreasing the heat input from 4330 J mm^{-1} to 2130 J mm^{-1}. In the case of GMAW of HSLA-100 steel,[130] decreasing the heat input from 4000 J mm^{-1} to 1000 J mm^{-1} resulted in a decrease in the HAZ prior austenite average grain size from 130 μm to 80 μm.

Decreasing the heat input per unit length of the welding process results in more rapid heating and cooling rates.[4, 126, 131] The cooling rate affects weld microstructure and mechanical properties. Studies which have analyzed the difference between Nd:YAG laser and laser/GMA hybrid weld cooling rates for steel samples have left important unanswered questions, such as the location of reported cooling rates relative to the weld centerline.[90, 131] Hybrid welding cooling rates for other important structural materials remain unknown and are needed.

It has been determined both experimentally and theoretically that hybrid welding can result in lower cooling rates than those during laser welding due to increased heat input per unit length.[90, 131] However, hybrid welding cooling rates are not known as a function of heat source separation distance. Since the distance between the heat sources affects the amount of metal vapors entering the plasma local to the arc, arc stability, energy absorption and plasma electrical conductivity can be influence by the heat source separation. Because arc energy absorption can affect the heat input per unit length of the welding process, an understanding of the influence of heat source separation distance on hybrid weldment cooling rates is needed. Modeling offers an effective means of analyzing weldment cooling rates. Previously, modeling has been successful at analyzing weldment cooling rates during arc[74, 132-133] and laser[6, 8, 134] welding.

Weld microstructures vary as a function of the distance relative to the weld pool centerline. Differences in the peak temperature experienced by the material, the cooling rate, and composition at different locations relative to the weld centerline lead to the formation of three regions of varying microstructures. The regions in order of increasing distance from the weld centerline are the fusion zone, heat affected zone (HAZ), and base metal.[2, 20, 126] Heat source power density, heat input per unit length, and filler metal additions can influence weld microconstituents, mean grain size, and width and shape of the HAZ and fusion zone. Changes in weld microstructure are very important to mechanical properties and weld integrity.[2, 126, 131, 135]

2.7.2 Steel hybrid welds

The application of hybrid laser/GMA welding has been limited primarily to the welding of low carbon steels.[90-91, 126] Research has focused on the microstructures formed during laser/GMA hybrid welding due to the metallurgical benefit which filler metal additions can offer.[90-91, 126] During laser/GMAW hybrid welding of pipeline steels, filler metal can promote the nucleation of microstructural constituents which improve toughness compared to autogenous welding.[90]

Recent research has also focused on the role of heat input on changes in the weldment microstructure for CO_2 laser, GMA, and laser/GMA hybrid welding.[90-91, 126] Fig. 2.15 shows micrographs of the (a) mild steel base metal and (b) CO_2 laser, (c) GMA, and (d) hybrid weld microstructures.[91]

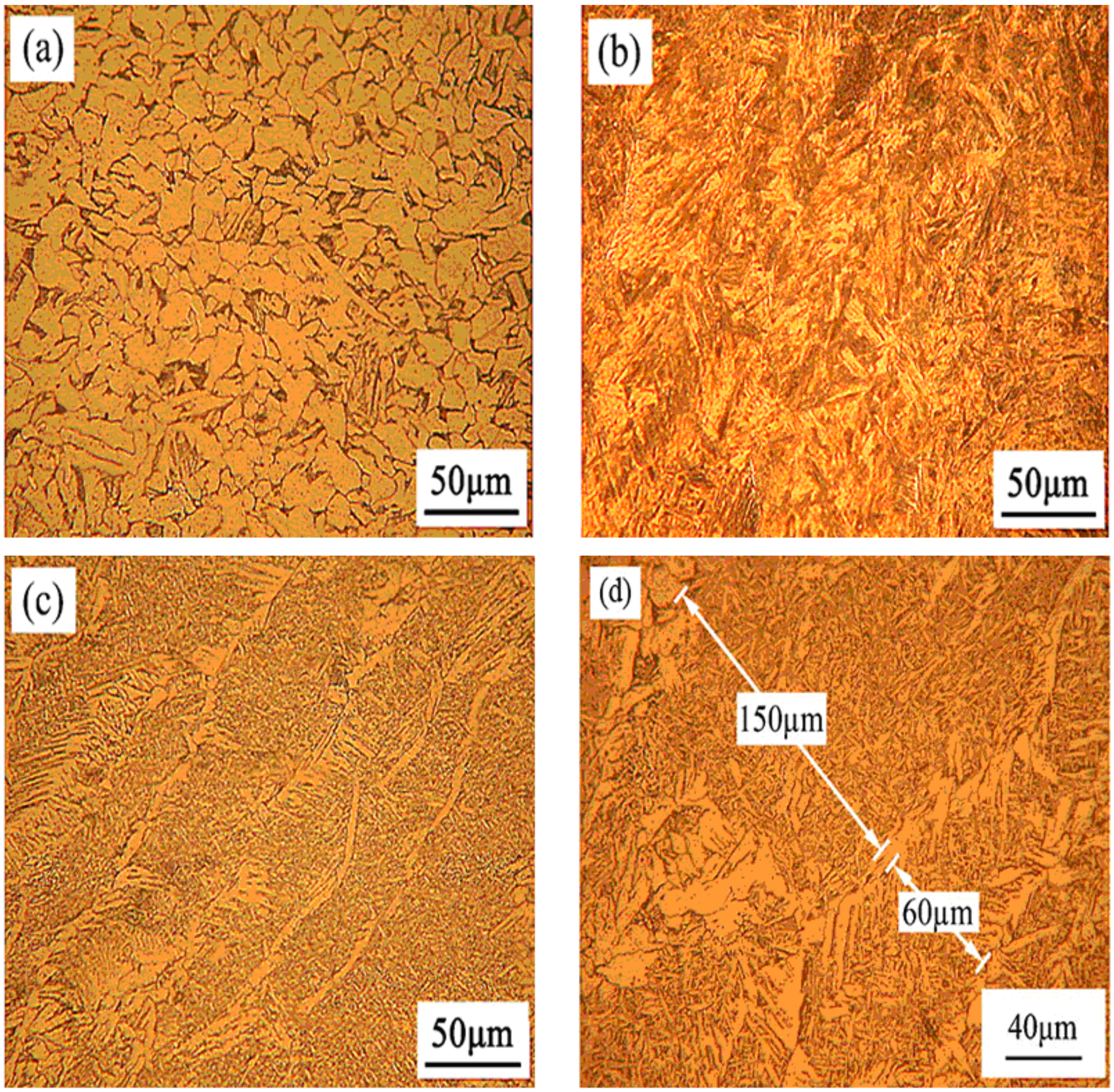

Fig 2.15: Micrographs of mild steel (a) base metal, (b) laser, (c) GMA, and (d) hybrid weld microstructures.[91] The laser and hybrid weld laser power was 4.5 kW. The GMA and hybrid welds' arc current was 180 A. The welding speed for all welds was 13.3 mm s^{-1}.

The mild steel (0.15 %C) base metal had a mean grain size of 25 μm and equiaxed ferrite with pearlite.[91] After laser welding (heat input of 338 J mm^{-1}), the microstructure consisted primarily of lath martensite in the weld fusion zone with a small fraction of proeutectoid ferrite at the prior austenite grain boundaries.[91] The width of the laser weld HAZ was relatively small compared to hybrid or arc welding due to the lower heat input per unit length.[91, 126] Arc welding (432 J mm^{-1}), resulted in a coarser fusion zone microstructure and wider HAZ than that of the laser or hybrid welds due to the low power density and high heat input of the arc welding process.[91] The arc weld fusion zone[91] microstructure was composed of columnar proeutectoid ferrite with intergranular acicular ferrite and pearlite. The hybrid weld (770 J mm^{-1}) displayed a higher heat input than the arc weld, resulting in a fusion zone microstructure that contained a greater amount of pearlite than the arc weld.[91]

Microhardness profiles are shown in Fig. 2.16 for GMA, CO_2 laser, and laser/GMA hybrid welded mild steel.[91] The fusion zone of the laser weld has the highest microhardness of the three welding processes and is significantly higher than that of the base metal, due to its small grain size and large fraction of martensite. The hardness and strength values of the arc fusion zone are lower than those for laser and hybrid welds due to a coarser grain size and the presence of ferrite and pearlite. Compared to laser welding, the additional heat input from the arc during hybrid welding reduces the cooling rate of the weld and prevents the formation of martensite. The relatively higher amount of pearlite present in the hybrid weld fusion zone contributes to its higher strength and hardness compared to arc welding.

The current literature indicates that the hybrid welding process consistently improves weldment microstructure.[15, 110, 136-137] However, modifying the heat input per unit length can cause the hybrid welding process to produce microstructures similar to either laser or arc welding.[126] Relatively high heat input (796 J mm^{-1}) CO_2 laser/GMAW hybrid welding of medium carbon steel results in the formation of coarse columnar grains in the weld fusion zone.[126] The columnar grains are composed of proeutectoid and acicular ferrite, and the microstructure contains intergranular pearlite.[126] The HAZ is composed of a large fraction of coarse pearlite with intergranular proeutectoid ferrite.

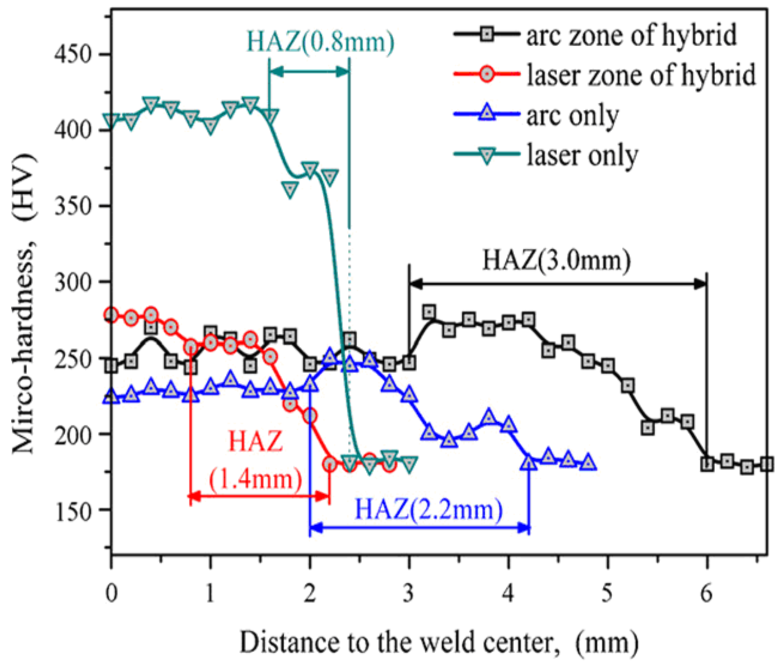

Fig. 2.16: Microhardness as a function of distance from the weld centerline for GMA, CO_2 laser, and laser/GMA hybrid welds made on mild steel samples. The hybrid weld is represented by two microhardness profiles. The arc zone is located closer to the surface of the weld pool, while the laser zone of the hybrid weld is located closer to the weld root. The arc and laser weld microhardness samples were taken relatively close to the weld pool surface.[91]

Decreasing the heat input per unit length to 547 J mm^{-1} results in the formation of a much finer microstructure composed of martensite and very little proeutectoid ferrite.[126] The HAZ is primarily composed of martensite with intergranular proeutectoid ferrite.[126] The drastic change in the microconstituents of the medium carbon steel is due to large differences in heat input and cooling rate. The temperature gradients and cooling rates in the low heat input hybrid weld are greater than the higher heat input case.

2.7.3 Magnesium and aluminum hybrid welds

Magnesium alloys can be easily recycled and have a relatively high strength to weight ratio, making them an attractive alternative for the replacement of denser structural materials. Since magnesium alloys are precipitation hardened, the heat input per unit length of the welding process becomes very important. Heat input is particularly important for these alloys in determining precipitate size, shape, distribution, and mean grain size and orientation of the α phase.[128] Research on the hybrid welding of magnesium alloys (primarily AZ31B) has focused on the laser/GTAW process.[124, 128, 136, 138]

The microstructure of AZ31B magnesium alloys is composed of equiaxed α-Mg (HCP) with interspersed ellipsoidal β-$Mg_{17}(Al,Zn)_{12}$ precipitates.[128, 139] Fusion zone (FZ), heat affected zone (HZ), and base metal (BZ) microstructures for (a) Nd:YAG laser, (b) GTA, and (c) hybrid welded AZ31B magnesium alloy are shown in Fig 2.17.[124]

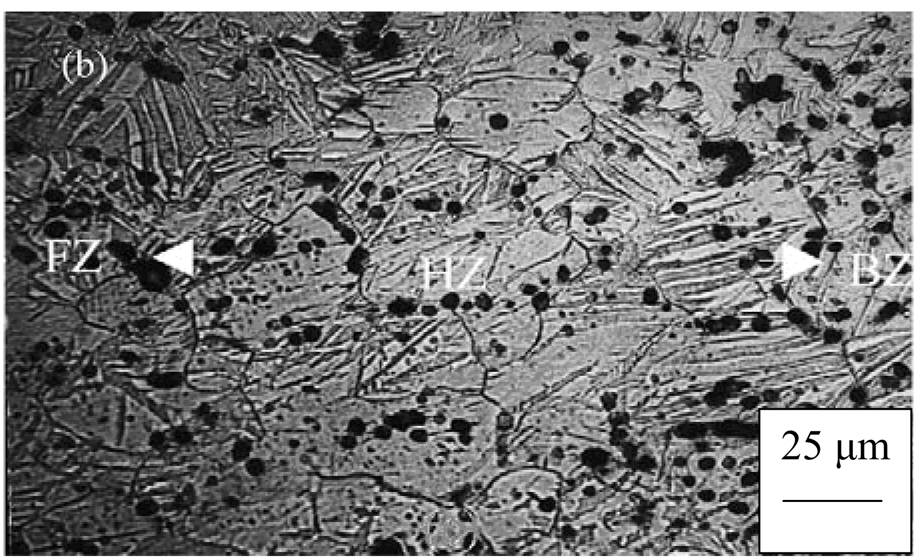

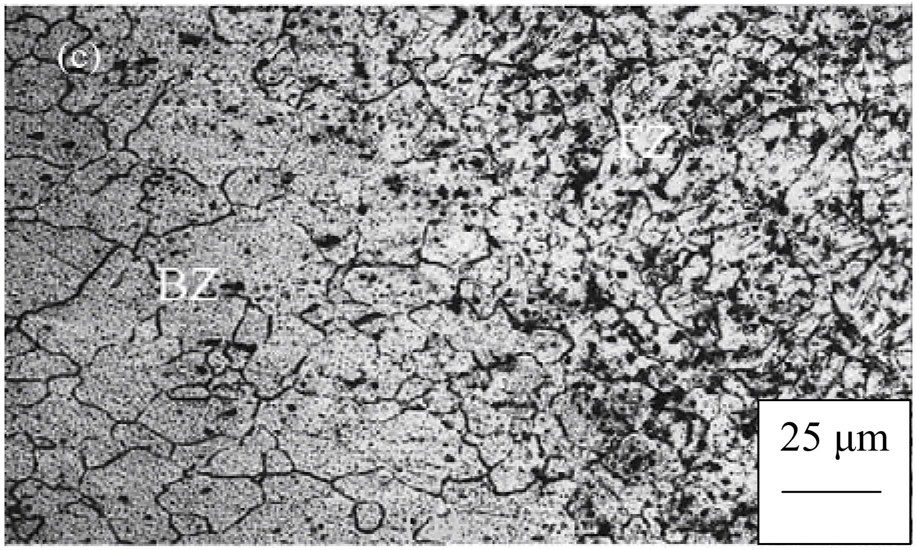

Fig. 2.17: Fusion zone (FZ), heat affected zone (HZ), and base metal (BZ) microstructures for (a) Nd:YAG laser, (b) GTA, and (c) hybrid welded AZ31B magnesium alloy.[124] The laser power was 400 W for the laser and hybrid welds. The arc current for the arc and hybrid welds[6] is approximately 70 A.

Compared to the base metal, Nd:YAG laser welding of 1.7 mm thick AZ31B magnesium alloy at a 400 W laser power (Fig. 2.17 (a)) results in finer equiaxed grains and precipitate coarsening in the weld fusion zone.[124] The mean grain size for the base metal α phase is approximately 25 μm, and base metal β precipitates are on the order of 200 nm in length.[115, 124, 128] The mean grain size of the laser weld fusion zone α phase is approximately 6 μm, but the length of the β precipitates is not apparent.[124] Coelho et al[128] evaluated 2.2 k W Nd:YAG laser welding of AZ31B magnesium alloy and determined that the lengths of β phase precipitates in the fusion zone after laser welding are between 300 and 500 nm for a welding speed of 91.7 mm s^{-1}.[128] Precipitate coarsening results from segregation of aluminum within the fusion zone.[115, 128]

GTA welding of 1.7 mm thick AZ31B magnesium alloy at 70 A results in a mean fusion zone grain size of 30 μm, as shown in Fig. 2.17 (b).[124] The fusion zone microstructure is composed of an α-Mg matrix with α-Mg + β-$Mg_{17}Al_{12}$ eutectic phase, which is coarser in the fusion zone than HAZ.[124, 140] The HAZ microstructure is predominantly α-Mg with small β precipitates.[124, 140] In the case of GTA welding of AZ31B magnesium alloy, the HAZ width is much larger than that obtained during laser welding, and the high heat input of the arc process results in significantly larger grains.[140]

Hybrid welding tends to result in a fusion zone weld microstructure composed of equiaxed α-Mg grains which are similar to that obtained during arc welding.[115, 124] Fig. 2.17 (c) shows the fusion zone and base metal microstructures of 400 W laser power, 70 A arc current hybrid welded AZ31B magnesium alloy.[124] The β precipitates in the fusion zone are much coarser than those in the base metal.[124] The quantitative effects of heat input on β precipitate sizes for GTA and hybrid welding are unknown and would be a beneficial area of research in order to further the application of hybrid welding magnesium alloys.

Changes in weld microstructure influence the mechanical behavior of the weld material relative to the base metal. Table 2.2 compares the microstructural features and mechanical properties of AZ31B arc, laser, and hybrid welds.[3] In the longitudinal direction, the laser fusion zone and base metal yield and ultimate tensile strengths are similar,[128] but the ductility of the fusion zone is lower. The reduced fusion zone ductility compared to that of the base metal is due to precipitate coarsening.[115] In the transverse direction, the relatively lower tensile strength for laser welded AZ31B magnesium alloy compared to that of the base metal can be attributed to undercut and porosity.[115] Arc welded AZ31B magnesium alloy tensile strength is approximately 94% that of the base metal.[140] The HAZ and fusion zone have similar microhardness values, which are slightly less than that of the base metal due to α grain coarsening.[140] In the case of hybrid welding, the mean grain size is similar to that of the base metal, resulting in similar microhardness and ultimate tensile strength.[115, 138] The increase in hybrid weld ultimate tensile strength compared to that during laser welding is due to lower porosity content.[115] However, the ductility decreases due to precipitate coarsening, which can provide a pathway for crack propagation. [115]

While the relatively high thermal conductivity and reflectivity to laser radiation[58, 123, 125, 127] can be overcome in the laser welding of Al alloys, the ability to easily add filler metals during hybrid welding makes it very attractive to join large sections of aluminum sheet quickly. Most of the current research on the hybrid welding of 7xxx series aluminum alloys uses the laser/GMAW hybrid welding process.[58, 123, 125, 127] These aluminum alloys gain their strength via precipitation hardening.[127] The size and distribution of these precipitates are dictated primarily by the temperature cycles and alloying element additions in the weld fusion zone.[127]

Nd:YAG laser/GMA hybrid[127] and fiber laser[125] welding of 7XXX series aluminum alloys with the addition of filler metal result in very similar microconstituents,[58, 125, 127] as shown in Fig. 2.18. However, the fusion zone mean grain size for hybrid welding is larger than that for laser welding. The microstructures consist of columnar dendrites at the fusion zone boundary and fine equiaxed grains along the weld centerline. During solidification, segregation of the alloying elements causes precipitates or eutectic films to form along the dendrite boundaries in the fusion zone,[127] resulting in decreased ductility.[127] The hybrid weld HAZ width is significantly larger than of the laser weld due to a relatively higher heat input. It is important to have a low heat input per unit length in order to retain more of the base metal mechanical properties.

Table 2.2: The microstructural features and mechanical properties of AZ31B magnesium alloy arc, laser, and hybrid welds.[3]

	Base Metal	Arc Welding	Laser Welding	Hybrid Welding
Fusion Zone Microstructure and grain size or Base metal microstructure	Equiaxed α grains with mean[115, 124] grain size of 25 µm β precipitates[128] with max length of 200 nm	30 µm mean grain size[124] Coarse α-Mg matrix with eutectic α-Mg + β-$Mg_{17}Al_{12}$ eutectic phase[128]	Columnar α grains with mean[124] grain size of 6 µm Coarse β precipitates[128] with max length of 300 to 500 nm	Equiaxed α-Mg grains of varying size[124] Mean α grain[115, 124] size of approximately 20 to 30 µm No quantitative data for precipitate sizes
HAZ Microstructure, grain size, and width		Predominantly α-Mg with small precipitates[140] Grain size[140] ranges from 10 to 60 µm HAZ width[140] is approximately 0.3 mm	HAZ microstructure is similar to that of base metal with little β precipitate coarsening[128] HAZ width[128] is 10 µm	HAZ width[138] is approximately 0.2 mm
Ultimate Tensile Strength	249 MPa ± 5 MPa in longitudinal direction[128] 251 MPa ± 5 MPa in transverse direction[128] 268 MPa ± 2 MPa in transverse direction[115]	Approximately[160] 230 MPa	247 MPa ± 5 MPa in longitudinal direction [128] 247 MPa ± 5 MPa in transverse direction[128] 251 MPa ± 4 MPa in transverse direction[115]	262 MPa ± 5 MPa in transverse direction[115]
Yield Strength	146 MPa ± 5 MPa in longitudinal direction[128] 148 MPa ± 5 MPa in transverse direction[128]		134 MPa ± 5 MPa in longitudinal direction[128] 92 MPa ± 5 MPa in transverse direction[128]	
Percent Elongation	20% ± 1.5 % in longitudinal direction[128] 24% ± 1.5 % in transverse direction[128] 16 % ± 1 % in transverse direction[115]		15 % ± 1.5 % in longitudinal direction[128] 19 % ± 1.5 % in transverse direction[128] 12 % ± 1.7 % in transverse direction[115]	14 % ± 1 % in transverse direction[115]

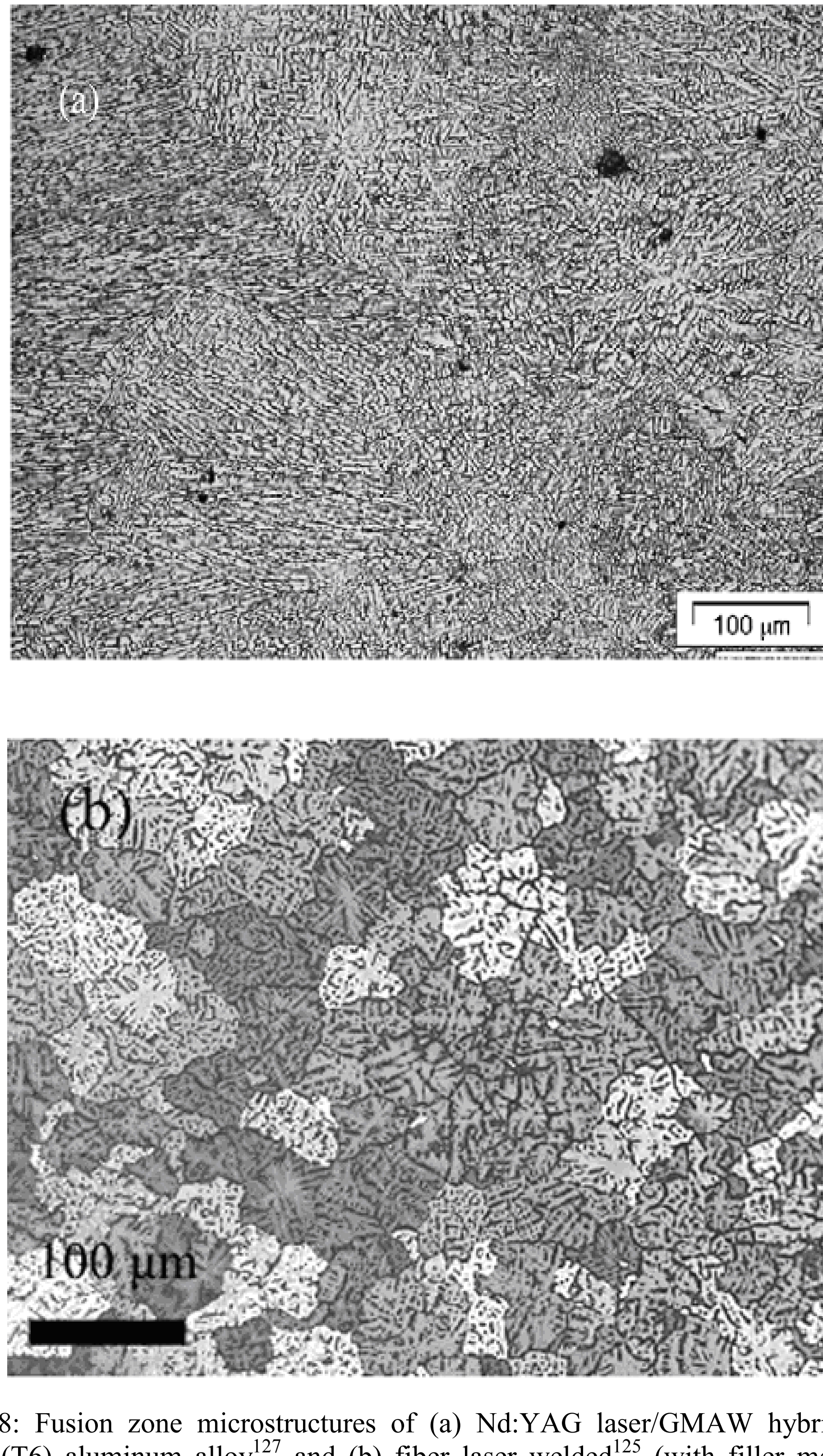

Fig. 2.18: Fusion zone microstructures of (a) Nd:YAG laser/GMAW hybrid welded AA7075(T6) aluminum alloy[127] and (b) fiber laser welded[125] (with filler metal) 7xxx series aluminum alloy.

Autogenous laser (Yb fiber laser and Nd:YAG) and laser/GMAW hybrid welding processes cannot achieve the same mechanical properties and microstructural characteristics of the base metal in 7xxx series aluminum alloys without additional heat treatment.[125] In Fig. 2.19, the microhardness profiles for a 7xxx series aluminum alloy are shown for autogenous (a) Yb fiber laser,[125] (b) autogenous Nd:YAG laser,[127] (a) Yb laser/GMAW hybrid,[125] and (c) Nd:YAG laser/GMAW[127] hybrid welds.

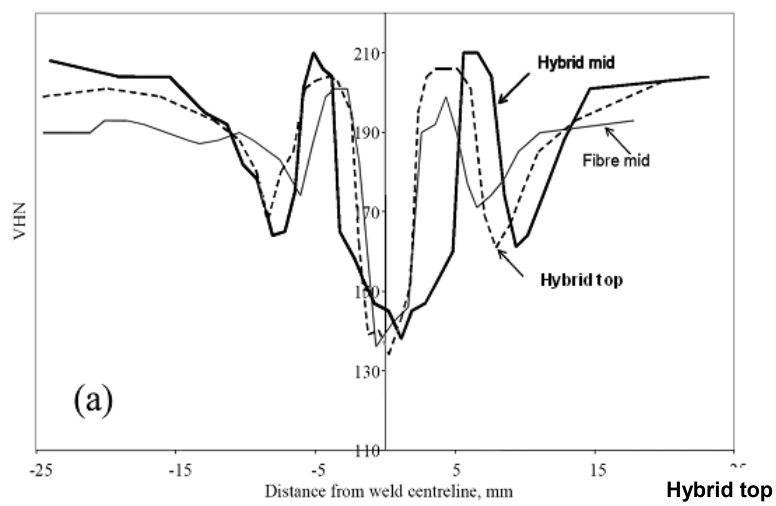

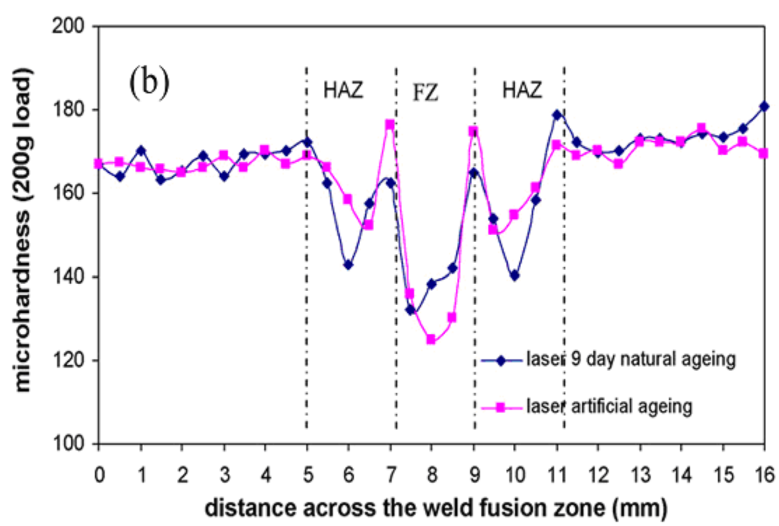

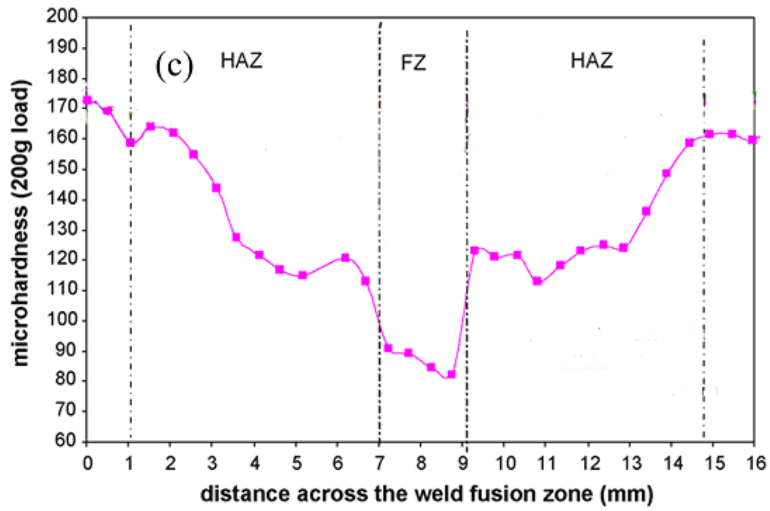

Fig. 2.19: Microhardness profiles of (a) post welding heat treated Yb fiber laser and Yb laser/GMAW hybrid,[125] (b) aged Nd:YAG laser,[127] and (c) as-welded Nd:YAG laser/GMAW hybrid welds based upon the work of Hu and Richardson.[125] The welds were made on (a) 7xxx series and (b and c) AA7075(T6) aluminum alloys. The hybrid weld was evaluated close to the top surface of the weld (hybrid top) and at the mid depth of the weld (hybrid mid) in Fig. 2.19 (a). The hardness profiles are functions of the distance across the weld fusion zone and distance from the weld centerline.

The results in Fig. 2.19 (a) and (b) are measured after a post weld heat treatment or aging (actual procedure unknown for (a) and 120 ^{o}C for 24 hours (b)), and the results shown in Fig. 2.19 (c) are in the as-welded condition.[125, 127] The low hardness of the fusion zone arises from the formation of precipitates and eutectic films along the boundaries of the columnar dendrites in the weld fusion zone, for both laser and hybrid welding.[125, 127] The HAZ hardness is greater than that of the fusion zone but tends to taper off due to coarsening or phase transformations at high temperatures.[127] Tensile testing of the 7xxx series aluminum alloy laser and hybrid welds shows that the fusion zones for the two welding processes can have similar mean tensile strength compared to the base metal depending upon the post weld heat treatment (~550 MPa).[125, 127] Depending upon the post welding heat treatment, the welded material percent elongation was 6% or less compared to 14% for the base metal. The HAZ shows higher strength and ductility than the fusion zone.[125]

The benefit of the hybrid welding process for the joining of aluminum and magnesium alloys mainly originates from the ability of this process to adjust filler metal additions, heat input, and post heat treatment processes. However, further characterization and analysis of filler metal and base metal combinations and processing parameters and their effect on weldment structure and mechanical properties is necessary.

2.8 Summary

Hybrid welding involves simultaneous interactions between energy absorption, alloying element vaporization, plasma formation, keyhole formation, heat transfer, and fluid flow processes. These physical processes influence weld width and depth, cooling rates, and weld composition. In turn, heating and cooling rates and weldment composition affect the resulting weld microstructure and mechanical properties. Hence, understanding the physical processes which occur during hybrid welding is very important and necessary to utilize the benefits of hybrid welding reliably.

The simultaneously occurring physical processes of hybrid welding are very complicated and interconnected. The plasma properties influence the liquid weld pool physical processes and vice-versa. Plasma characteristics affect arc stability and can influence the laser beam energy absorption. The absorption of the high power density laser during hybrid welding results in rapid vaporization and significantly affects arc stability and plasma characteristics.

Several important unanswered questions remain regarding the physical processes during hybrid welding. The heat transfer and fluid flow during hybrid welding are not well understood. The driving forces for fluid flow and significance of convection need to be addressed due to their importance in determining the resulting weldment shape, temperature profiles, and cooling rates. Energy absorption and heat transfer influence the vaporization rates of metal vapors entering the hybrid welding plasma. The introduction of metal vapors into the plasma affects arc stability, plasma electrical conductivity, and arc energy absorption, which influences heat transfer in the weld pool. A better understanding of the heat transfer and fluid flow is necessary to analyze the influence of the laser-arc interaction on weld bead shape during hybrid welding.

Modeling has been a useful technique for successfully analyzing heat transfer and fluid flow for arc and laser welding. Numerical methods offer a means of understanding the influence which heat transfer and fluid flow have on important weld attributes, such as cooling rate. These analytical techniques can help to better understand the source of increased weld width during hybrid welding, which is important for weld integrity.

Evaluating the role which surface active elements play in low power density laser and arc welding has been successful in the past with the use of phenomenological based models. Increasing the surface active element content in the base metal or shielding gas increases weld depth during high power density laser and laser/GTA hybrid welding. Weld depth is very important to structural integrity. However, the processes which result in increased weld depth are not known. Modeling can be useful for analyzing the role of surface active elements during high power density laser and hybrid welding.

Process parameters have an impact on the physical processes occurring during hybrid welding. Many questions remain regarding the effects of important process parameters on hybrid welding physical processes. These important process parameters include: arc current, heat source separation distance, and laser power. For example, the influence of heat source separation distance on hybrid weldment temperature profiles and cooling rates remains unknown. By understanding the effects of these important process parameters on heat transfer, fluid flow, cooling rates, weld temperature profiles, and weld bead shape, the benefits of hybrid welding can be better utilized to expand applicability of the process and repeatability. A systematic approach must be undertaken to realize the effects of the important process parameters on weld dimensions, weld pool cooling rates, and plasma characteristics.

Understanding the effects of arc current and heat source separation individually, while keeping all other parameters the same, on fluid flow and weld pool geometry are essential for more complete understanding of hybrid welding. The combinations of these individual process parameters during the synergistic interaction between the arc and laser induced plasmas has not been thoroughly discussed in the literature. Plasma properties are very important to the laser-arc interaction and arc stability. Hybrid welding plasma characterization is only beginning. Further analysis of the hybrid welding plasma characteristics is necessary to explain the role of important process parameters on arc stability. A fundamental understanding of the roles which these process parameters play during hybrid welding, particularly when an arc-laser plasma interaction is occurring, would greatly benefit the welding industry to improve process control.

Optical emission spectroscopy has been useful for analyzing arc and laser welding plasma characteristics in the past. This experimental technique allows for a non contact method of determining plasma temperatures, species densities, and electrical conductivity. Plasma electrical conductivity can provide a means of analyzing the influence of important process parameters on arc stability during hybrid welding.

The subsequent sections of the thesis aim to analyze the important aforementioned issues through theoretical and experimental analysis of the hybrid welding process. The focus of all of the studies is an improved understanding of heat transfer, fluid flow, and plasma properties during hybrid welding. Since hybrid welding can perform linear welds on thick material quickly with good gap tolerance, automotive, ship construction, and pipeline welding industries are expected to benefit most from this research

2.9 References

1. W. W. Duley, *Laser Processing and Analysis of Materials*. (Plenum Press, New York and London, 1983).
2. S. Kou, *Welding Metallurgy*, 2nd ed. (John Wiley & Sons, Inc., 2003).
3. B. Ribic, T. Palmer, T. DebRoy, International Materials Reviews **54** (4), 223-244 (2009).
4. J. F. Lancaster, *The Physics of Welding*. (Pergamon Press, New York, NY, 1986).
5. S. Herbert, Welding Journal **83** (6), 39-43 (2004).
6. R. Rai, G. G. Roy, T. DebRoy, Journal of Applied Physics **101** (5), 054909 (2007).
7. R. Rai, J. W. Elmer, T. A. Palmer, T. DebRoy, Journal of Physics D- Applied Physics **40** (18), 5753-5766 (2007).
8. R. Rai, S. M. Kelly, R. P. Martukanitz, T. DebRoy, Metallurgical and Materials Transactions A-Physical Metallurgy and Materials Science **39A** (1), 98-112 (2008).
9. A. De, T. DebRoy, Welding Journal **84** (7), 101s-112s (2005).
10. H. Zhao, T. Debroy, Metallurgical and Materials Transactions B- Process Metallurgy and Materials Processing Science **32** (1), 163-172 (2001).
11. H. Zhao, T. Debroy, Journal of Applied Physics **93** (12), 10089-10096 (2003).
12. H. Zhao, D. R. White, T. Debroy, International Materials Reviews **44** (6), 238-266 (1999).

13. M. Kutsuna, L. Chen, presented at the First International Symposium on High-Power Laser Macroprocessing, Osaka, Japan, 2002 (unpublished).
14. G. Casalino, Journal of Materials Processing Technology **191** (1-3), 106-110 (2007).
15. T. Kim, Y. Suga, T. Koike, JSME International Journal Series A-Solid Mechanics and Material Engineering **46** (3), 202-207 (2003).
16. G. L. Qin, Z. Lei, S. Y. Lin, Science and Technology of Welding and Joining **12** (1), 79-86 (2007).
17. J. F. Lancaster, Physics in Technology **15** (2), 73-79 (1984).
18. A. Fellman, V. Kujanpaa, Journal of Laser Applications **18** (1), 12-20 (2006).
19. G. Tani, G. Campana, A. Fortunato, A. Ascari, Applied Surface Science **253** (19), 8050-8053 (2007).
20. T. DebRoy, S. A. David, Reviews of Modern Physics **67**, 85-112 (1995).
21. G. S. Arnold, Applied Optics **23** (9), 1434-1436 (1984).
22. S. B. Boyden, Y. W. Zhang, Journal of Thermophysics and Heat Transfer **20** (1), 9-15 (2006).
23. J. Greses, P. A. Hilton, C. Y. Barlow, W. M. Steen, Journal of Laser Applications **16** (1), 9-15 (2004).
24. M. Von Allmen, *Laser-Beam Interactions with Materials*. (Springer-Verlag, New York, NY, 1987).
25. X. Z. Jin, L. J. Li, Y. Zhang, Journal of Physics D- Applied Physics **35** (18), 2304-2310 (2002).
26. T. P. Hughes, *Plasmas and Laser Light*. (John Wiley and Sons, New York, NY, 1975).
27. R. G. Lerner, G. L. Trigg, *Encyclopedia of Physics*. (VCH Publishers, Inc., 1991).
28. B. Hu, and G. Den Ouden, Science and Technology of Welding and Joining **10** (1), 76-81 (2005).
29. G. Xu, Z. Cheng, J. Xia, X. Li, J. Jiang, presented at the Proceedings of the SPIE: High-Power Lasers in Manufacturing Osaka, Japan, 2000 (unpublished).
30. C. J. Nonhof, *Material Processing with Nd-Lasers*. (Electrochemical Publications Limited, 1988).
31. S. Pfalzner, P. Gibbon, Physical Review E **57** (4), 4698-4705 (1998).
32. J. Mazumder, in *ASM Handbook: Welding, Brazing, and Soldering*, edited by F. Reidenbach (ASM International, 1993), Vol. 6, pp. 262-269.
33. S. A. David, T. Debroy, Science **257** (5069), 497-502 (1992).
34. W. W. Duley, *CO_2 Lasers Effects and Applications*. (Academic Press, Inc., San Diego, CA, 1976).
35. W. M. Steen, Journal of Applied Physics **51** (11), 5636-5641 (1980).
36. Y. B. Chen, Z. L. Lei, L. Q. Li, L. Wu, Science and Technology of Welding and Joining **11** (4), 403-411 (2006).
37. B. Hu, and G. Den Ouden, Science and Technology of Welding and Joining **10** (4), 427-431 (2005).
38. M. Gao, X. Zeng, Q. W. Hu, Journal of Materials Processing Technology **184** (1-3), 177-183 (2007).
39. K. C. Hsu, K. Etemadi, E. Pfender, Journal of Applied Physics **54** (3), 1293-1301 (1982).

40. R. Miller, T. DebRoy, Journal of Applied Physics **68** (5), 2045-2050 (1990).
41. G. Y. Zhao, M. Dassanavake, K. Etemadi, Plasma Chemistry and Plasma Processing **10** (1), 87-98 (1990).
42. P. Sahoo, M. M. Collur, T. DebRoy, Metallurgical Transactions B-Process Metallurgy **19** (6), 967-972 (1988).
43. X. Zhou, J. Herberlein, Journal of Physics D- Applied Physics **31** (19), 2577-2590 (1998).
44. M. M. Collur, T. DebRoy Metallurgical Transactions B-Process Metallurgy **20** (2), 277-286 (1989).
45. J. Wang, K. Kusumoto, K. Nezu, Science and Technology of Welding and Joining **9** (4), 369-373 (2004).
46. S. Akbar, K. Etemadi, Plasma Chemistry and Plasma Processing **17** (2), 251-262 (1997).
47. J. H. Cho, S. J. Na, Journal of Physics D-Applied Physics **39** (24), 5372-5378 (2006).
48. M. Gao, X. Y. Zeng, Q. W. Hu, Science and Technology of Welding and Joining **11** (5), 517-522 (2006).
49. Y. Naito, M. Mizutani, S. Katayama, Journal of Laser Applications **18** (1), 21-27 (2006).
50. J. Kroos, U. Gratzke, G. Simon, Journal of Physics D- Applied Physics **26** (3), 474-480 (1993).
51. V. Semak, A. Matsunawa, Journal of Physics D- Applied Physics **30** (18), 2541-2552 (1997).
52. T. Klein, M. Vicanek, J. Kroos, I. Decker, G. Simon, Journal of Physics D-Applied Physics **27** (10), 2023-2030 (1994).
53. P. A. A. Khan, T. DebRoy, Metallurgical Transactions B-Process Metallurgy **15** (4), 641-644 (1984).
54. D. R. Poirier, G. H. Geiger, *Transport Phenomena in Materials Processing*. (The Minerals, Metals, and Materials Society, Warrendale, PA, 1994).
55. J. Kroos, U. Gratzke, M. Vicanek, G. Simon, Journal of Physics D- Applied Physics **26** (3), 481-486 (1993).
56. Tsukamoto et al., presented at the Proc. Of SPIE, First International Symposium on High-Power Laser Macroprocessing, Osaka, Japan, 2002 (unpublished).
57. P. Solana, J. L. Ocana, Journal of Physics D- Applied Physics **30** (9), 1300-1313 (1997).
58. H. Pinto, A. Pyzalla, H. Hackl, J. Bruckner, Residual Stresses VII **524-525**, 627-632 (2006).
59. B. Ribic, R. Rai, T. DebRoy, Science and Technology of Welding and Joining **13** (8), 683-693 (2008).
60. W. Zhang, PhD Thesis, Pennsylvania State University, 2004.
61. P. Sahoo, T. DebRoy, M. J. McNallan, Metallurgical Transactions B-Process Metallurgy **19** (3), 483-491 (1988).
62. S. Mishra, T. J. Lienert, M. Q. Johnson, T. DebRoy, Acta Materialia **56** (9), 2133-2146 (2008).
63. Y. Wang, H. L. Tsai, Metallurgical and Materials Transactions B- Process Metallurgy and Materials Processing Science **32** (3), 501-515 (2001).

64. Y. Wang, Q. Shi, H. L. Tsai, Metallurgical and Materials Transactions B- Process Metallurgy and Materials Processing Science **32** (1), 145-161 (2001).
65. Y. Z. Zhao, Y. P. Lei, Y. W. Shi, Acta Metallurgica Sinica **40** (10), 1085-1092 (2004).
66. Y. Z. Zhao, Y. P. Lei, Y. W. Shi, Journal of Materials Science & Technology **21** (3), 408-414 (2005).
67. Y. Z. Zhao, H. P., Zhou, Y. W. Shi, Modeling and Simulation in Materials Science and Engineering **14** (3), 331-349 (2006).
68. W. Pitscheneder, T. DebRoy, K. Mundra, R. Ebner, Welding Journal **75** (3), S71-S80 (1996).
69. D. A. Schauer, W. H. Giedt, S. M. Shintaku, Welding Journal **57** (5), S127-S133 (1978).
70. J. D. Jackson, *Classical Electrodynamics*, 3rd ed. (Wiley, New York, 1998).
71. K. Mundra, T. DebRoy, K. M. Kelkar, Numerical Heat Transfer Part A-Applications **29** (2), 115-129 (1996).
72. R. T. C. Choo, J. Szekely, Welding Journal **70** (9), S223-S233 (1991).
73. G. M. Oreper, J. Szekely, Metallurgical Transactions A-Physical Metallurgy and Materials Science **18** (7), 1325-1332 (1987).
74. W. Zhang, G. G. Roy, J. W. Elmer, T. DebRoy, Journal of Applied Physics **93** (5), 3022-3033 (2003).
75. B. E. Launder, D. B. Spalding, *Lectures in Mathematical Model of Turbulence*. (Academic Press, London, 1972).
76. D. C. Wilcox, *Turbulence Modeling for CFD*. (DCW industries, CA, 1993).
77. A. De, T. Debroy, Journal of Applied Physics **95** (9), 5230-5240 (2004).
78. A. De, T. DebRoy, Journal of Physics D- Applied Physics **37** (1), 140-150 (2004).
79. T. Fuhrich, P. Berger, H> Hugel, Journal of Laser Applications **13** (5), 178-186 (2001).
80. S. Tsukamoto, (Personal Communication, University Park, PA, 2009), pp. 1-20.
81. L. Zhao, S. Tsukamoto, G. Arakane, T. Sugino, T. DebRoy, (Personal Communication, 2009), pp. 26.
82. G. Campana, A. Fortunato, A. Ascari, G. Tani, L. Tomesani, Journal of Materials Processing Technology **191** (1-3 Sp. Iss. SI), 111-113 (2007).
83. M. El Rayes, C. Walz, G. Sepold, Welding Journal **83** (5), 147s-153s (2004).
84. U. Jasnau, J. Hoffmann, P. Seyffarth, Robotic Welding, Intelligence and Automation **299**, 14-24 (2004).
85. A. Mahrle, E. Beyer, Journal of Laser Applications **18** (3), 169-180 (2006).
86. J. Zhou, W. H. Zhang, H. L. Tsai, S. P. Martin, P. C. Wang, R. Menassa, presented at the ASME International Mechanical Engineering Congress and Exposition, Washington, D.C., 2003 (unpublished).
87. J. Zhou, H. L. Tsai, International Journal of Heat and Mass Transfer **51** (17-18), 4353-4366 (2008).
88. Y. Naito, S. Katayama, A. Matsunawa, presented at the First International Symposium on High-Power Laser Macroprocessing, Osaka, Japan, 2003 (unpublished).
89. J. Dowden, P. Kapadia, Journal of Physics D- Applied Physics **28** (11), 2252-2261 (1995).

90. P. L. Moore, D. S. Howse, E. R. Wallach, Science and Technology of Welding and Joining **9** (4), 314-322 (2004).
91. M. Gao, X. Y. Zeng, J. Yan, Q. W. Hu, Applied Surface Science **254** (18), 5715-5721 (2008).
92. P. W. J. M. Boumans, *Theory of Spectrochemical Excitation*. (Plenum Press, New York, 1966).
93. M. M. Collur, A. Paul, T. DebRoy, Metallurgical Transactions B-Process Metallurgy **18** (4), 733-740 (1987).
94. H. R. Griem, *Plasma Spectroscopy*. (McGraw-Hill, New York, 1964).
95. F. Cabannes, J. Chapelle, *Spectroscopic Plasma Diagnostics*. (Wiley Interscience, New York, 1971).
96. A. E. F. Gick, M. B. C. Quigley, P. H. Richards, Journal of Physics D- Applied Physics **6** (16), 1941-1949 (1973).
97. W. L. Barr, Journal of the Optical Society of America **52** (8), 885-888 (1962).
98. G. N. Haddad, A. J. D. Farmer, Welding Journal **64** (12), S399-S342 (1985).
99. H. Terasaki, M. Tanaka, M. Ushio, Metallurgical and Materials Transactions A-Physical Metallurgy and Materials Science **33** (4), 1183-1188 (2002).
100. T. A. Palmer, T. DebRoy, Metallurgical and Materials Transactions B- Process Metallurgy and Materials Processing Science **31** (6), 1371-1385 (2000).
101. C. Fanara, I. M. Richardson, Journal of Physics D- Applied Physics **34** (18), 2715-2725 (2001).
102. G. J. Dunn, T. W. Eager, Metallurgical Transactions A-Physical Metallurgy and Materials Science **17** (10), 1865-1871 (1986).
103. K. S. Drellishak, D. P. Aeschlim, A. B. Cambel, Physics of Fluids **8** (9), 1590-1600 (1965).
104. K. S. Drellishak, C. F. Knopp, A. B. Cambel, Physics of Fluids **6** (9), 1280-1288 (1963).
105. M. Pastor, H. Zhao, R. P. Martukanitz, T. DebRoy, Welding Journal **78** (6), 207S-216S (1999).
106. X. He, T. DebRoy, P. W. Fuerschbach, Journal of Applied Physics **94** (10), 6949-6958 (2003).
107. Y. Ralchenko, A.E. Kramida, J. Reader, and NIST ASD Team (2008), (National Institute of Standards and Technology, Gaithersburg, MD, 2008).
108. X. Hao, and G. Song, IEEE Transactions of Plasma Science **37** (1), 76-82 (2009).
109. L. M. Liu, R. Huang, G. Song, X. Hao, IEEE Transactions on Plasma Science **36** (4), 1937-1943 (2008).
110. C. Bagger, F. O. Olsen, Journal of Laser Applications **17** (1), 2-14 (2004).
111. Y. Naito, S. Katayama, A. Matsunawa, presented at the First International Symposium on High-Power Laser Macroprocessing, Osaka, Japan, 2002 (unpublished).
112. E. W. Reutzel, M. J. Sullivan, D. A. Mikesic, Welding Journal **85** (6), 66-71 (2006).
113. L. Liu, G. Song, J. F. Wang, Magnesium-Science, Technology and Applications **488-489**, 361-364 (2005).

114. L. M. Liu, G. Song, G. Liang, and J. F. Wang, Materials Science and Engineering A-Structural Materials Properties Microstructure and Processing **390**, 76-80 (2005).
115. M. Gao, X. Y. Zeng, B. Tan, J. C. Feng, Science and Technology of Welding and Joining **14** (4), 274-281 (2009).
116. H. Zhao, T. DebRoy, Welding Journal **80** (8), 204S-210S (2001).
117. M. Ono, Y. Shinbo, A. Yoshitake, M. Ohmura, NKK Technical Review **86**, 8-12 (2002).
118. M. Ono, Y. Shinbo, A. Yoshitake, M. Ohmura, presented at the First International Symposium on High-Power Laser Macroprocessing, Osaka, Japan, 2003 (unpublished).
119. S. M. Joo, Y. P. Kim, C. S. Ro, H. S. Bang, J. U. Park, Advances in Nondestructive Evaluation, PT 1-3 **270-273**, 2383-2388 (2004).
120. W. H. Zhang, J. Zhou, H. L. Tsai, presented at the First International Symposium on High-Power Laser Macroprocessing, Osaka, Japan, 2003 (unpublished).
121. C. Walz, T. Seefeld, G. Sepold.
122. J. Defalco, Welding Journal **86**, 47-51 (2007).
123. B. Hu, I. M. Richardson, Materials Science and Engineering A-Structural Materials Properties Microstructure and Processing **429** (1-2), 287-294 (2006).
124. L. M. Liu, J. F. Wang, G. Song, Materials Science and Engineering A-Structural Materials Properties Microstructure and Processing **381** (1-2), 129-133 (2004).
125. C. M. Allen, G. Verhaeghe, P. A. Hilton, C. P. Heason, P. B. Prangnell, Aluminum Alloys 2006, PTS 1 and 2 **519-521**, 1139-1144 (2006).
126. M. Gao, X. Zeng, Q. W. Hu, J. Yan, Science and Technology of Welding and Joining **13** (2), 106-113 (2008).
127. B. Hu, I. M. Richardson, Materials Science and Engineering A-Structural Materials Properties Microstructure and Processing **459** (1-2), 94-100 (2007).
128. R. S. Coelho, A. Kostka, H. Pinto, S. Riekehr, M. Kocak, A. R. Pyzalla, Materials Science and Engineering A-Structural Materials Properties Microstructure and Processing **485** (1-2), 20-30 (2008).
129. S. Mishra, T. DebRoy, Acta Materialia **52** (5), 1183-1192 (2004).
130. M. Shome, Materials Science and Engineering A-Structural Materials Properties Microstructure and Processing **445**, 454-460 (2007).
131. E. A. Metzbower, P. E. Denney, D. W. Moon, C. R. Feng, S. G. Lambrakos, THERMEC'2003, PTS 1-5 **426-4**, 4147-4152 (2003).
132. C. H. Kim, W. Zhang, T. DebRoy, Journal of Applied Physics **94** (4), 2667-2679 (2003).
133. S. Mishra, T. DebRoy, Materials Science and Engineering A **454-455**, 477-486 (2007).
134. X. He, J. W. Elmer, T. DebRoy, Journal of Applied Physics **97** (8), 084909 (2005).
135. L. M. Liu, G. Song, J. F. Wang, G. L. Liang, Transactions of Nonferrous Metals Society of China **14** (3), 550-555 (2004).
136. T. W. Kim, J. C. Kim, Y. Hasegawa, Y. Suga, Designing, Processing and Properties of Advanced Engineering Materials, PTS 1 and 2 **449-4**, 417-420 (2004).

137. L. M. Liu, X. J. Liu, S. H. Liu, Scripta Materialia **55** (4), 383-386 (2006).
138. G. Song, L. M. Liu, M. S. Chi, J. F. Wang, Magnesium-Science, Technology and Applications **488-489**, 371-375 (2005).
139. L. M. Liu, G. Song, M. S. Chi, Materials Science and Technology **21** (9), 1078-1082 (2005).
140. Z. D. Zhang, L. M. Liu, Y. Shen, L. Wang, Materials Characterization **59** (1), 40-46 (2008).

Chapter 3

HEAT TRANSFER AND FLUID FLOW IN LASER/GTA HYBRID WELDING

3.1 Introduction

During high power density laser and laser-arc hybrid welding, the keyhole depth, liquid metal flow, weld geometry, and weld integrity are affected in part by base-metal sulfur content and oxygen (O_2) present in the atmosphere or shielding gas. Laser power, arc current, and heat source separation distance also influence weld bead geometry,[1-8] microstructure,[9-12] arc stability,[12-17] and plasma light emission.[13-15, 18] While the role of surface active elements during arc welding[19-24] and low power density (less than 10^5 W cm^{-2}) laser welding[7, 25-28] has been extensively studied, their influence during high power density keyhole mode laser and laser-arc hybrid welding is not as well understood. Previous studies[29-36] have focused on experimentally demonstrating the empirical relationships between weld attributes and process parameters during laser-arc hybrid welding. However, these studies have left unanswered questions about how the benefits of hybrid welding are achieved in a narrow window of process parameters.

Sulfur is commonly present in steels, whereas oxygen is often introduced into the workpiece from the atmosphere or shielding gas.[6] The presence of surface active elements in the workpiece can influence weld pool fluid flow by changing the surface tension gradient, which impacts convective heat transport and weld bead geometry.[3, 7, 37-42] In the case of high power density laser welding and laser-arc hybrid welding, it has been reported that increasing the O_2 concentration in the environment reduces weld width and increases weld penetration depth.[6] The effects of O_2 present in the environment on weld geometry have been attributed to its effect on surface-tension driven flow,[6] enhanced absorption of laser energy,[6] and the pressure exerted by formation of gaseous[43] carbon monoxide (CO). No definite mechanism for the behavior of oxygen in keyhole mode welding has been established.

Naito et al.[6] observed that increasing O_2 content in the environment of the workpiece resulted in deeper penetration and narrower weld width for keyhole mode laser and laser-arc hybrid welds. The post-weld oxygen concentration in the weld metal was greater for welds made under environments where oxygen was introduced to the shielding gas.[6] X-ray measurements showed that the direction of fluid flow at the top surface was reversed when O_2 was present in the atmosphere compared to when welding was done under pure argon atmosphere. [6] This effect of dissolved oxygen on Marangoni convection near the top surface was related to a lack of "nail head" shape in welds which were made in O_2 containing environments.[6] The presence of dissolved oxygen only altered the direction of fluid flow near the weld pool top surface and an influence on penetration depth was not directly evident due to a lack of change in fluid flow along the keyhole walls.

Welds made under the same welding parameters can have somewhat different penetration depths and weld widths, often in different transverse sections of the same weld. This is particularly true of keyhole-mode welds which can encounter spiking or fluctuations in weld penetration depth due to variation in the laser power density absorbed at the bottom of the keyhole. Therefore, variation in weld dimensions with change in any process variable (for example, sulfur or oxygen content) should be compared to the amount of spiking for a given welding condition. Such statistical studies of the effect of oxygen and sulfur on keyhole mode welds have not been reported in open peer-reviewed literature.

Heat transfer and fluid flow are important to weld bead geometry, cooling rates, microstructure, mechanical properties, and weld integrity.[42, 44-47] The weldment temperature profile establishes the weld bead geometry and cooling rates which influence weldment microstructure, mechanical properties, and weld integrity. The base metal composition and process parameters influence the heat transfer and fluid flow during welding and consequently the resulting weld integrity. Hence, understanding the influence of surface active elements and process parameters on heat transfer and fluid flow is important and necessary.

Zhao et al.[43] showed that the penetration depth in keyhole mode laser welding coincides with the keyhole depth. They argued that the changes in fluid flow induced by the presence of dissolved O_2 in the surrounding weld metal do not affect the keyhole depth. They proposed, instead, that formation of gaseous CO in the keyhole could influence the keyhole shape by exerting a pressure on the keyhole walls.[43] However, a quantitative understanding of the influence of CO formation on keyhole geometry remains to be developed.

Experimentally, it is difficult to determine the influence of CO pressure on the laser generated keyhole. High temperatures, the presence of metal vapors and plasma, and the small size of the keyhole, all make experimental measurements very difficult. Numerical modeling has previously offered a means of successfully evaluating the roles of heat transfer and fluid flow during high power density laser welding and laser-arc hybrid welding .[41-42, 48] Several models based on the influence of pressures acting inside the keyhole have been proposed,[27, 49-52] but these models did not consider the influence of surface active elements.[27, 49-52]

Fuhrich et al.[2] considered the fluid flow in keyhole mode laser welding of steel using a fixed keyhole geometry and a constant $d\gamma/dT$ for two cases: (1) a positive value of $d\gamma/dT$, and (2) a negative value of $d\gamma/dT$. They suggested that presence of surface active elements causes downward fluid flow at keyhole walls by making $d\gamma/dT$ positive and leads to deeper penetration welds.[2] However, it is known that the effect of surface-active elements on $d\gamma/dT$ of liquid steel is limited to temperatures much below the boiling point.[53] Furthermore, temperature variation along the keyhole walls is very small in laser beam welding and the temperature is often assumed to be constant.[40-42] Therefore, the magnitude of the surface tension gradient along the keyhole walls is small in keyhole mode laser beam welding.[40-42]

The physical processes during hybrid welding include energy absorption, vaporization, keyhole formation, plasma formation, heat transfer, and fluid flow. The process parameters and material properties influence these simultaneously occurring processes. For example, keyhole geometry depends upon the laser power density,[12, 41-42, 48] laser power, the concentration of surface active elements in the weld metal,[2, 6, 43] heat source separation distance,[13-15, 17, 42] the defocusing of the laser beam,[12] and the laser beam characteristic wavelength.[12] Experimentally analyzing physical processes during welding is difficult because they are complex, interconnected, and simultaneously occurring.

Modeling has allowed researchers to analyze the heat transfer and fluid flow during numerous weld processes.[7, 42, 44-46, 48, 54-55] Phenomenological modeling has offered a successful means of analyzing the influence of surface active elements[2, 4-5, 7] and process parameters[3, 41, 44-46] on arc and laser welding. These studies have successfully analyzed the role of surface active elements on fluid flow, and the significance of convective heat transfer in arc welding and low power density laser welding. The results have lead to better process control and repeatability for several alloy systems and welding processes. Hence, it is likely modeling can offer a means of successfully analyzing the influence of important process parameters and surface active elements on hybrid welding physical processes.

Beyond a critical separation distance, the arc is unable to bend and root on the keyhole due to the lack of metal vapor introduced to the arc plasma, explaining why the effect decreases as the distance between the two heat sources increases.[13-15, 17] Chen et al.[13] experimentally studied the hybrid welding of AISI 321 Stainless Steel and observed the laser-arc interaction. They did not attribute the observed effects to any particular phenomena, but described that a particular value of separation between the two heat sources resulted in a relatively small increase in the penetration of the weld pool. Chen et al.[13] also observed, with the aid of camera, that for relatively small separation distance, the arc appeared to focus down inside the keyhole of the weld pool throughout the welding process.[13]

All of the benefits of hybrid welding are achieved at high welding speeds (~ 1 m min^{-1}) while maintaining deep weld penetration depth similar to high power density laser welding. It is the interaction of the heat sources which give rise to the benefits of hybrid welding. Hence, a model which considers the laser-arc interaction is therefore necessary to accurately model the hybrid welding process.

Modeling of the heat transfer and fluid flow of the hybrid welding process is in its early stages. A limited number of studies have been completed for idealized cases. The current transport phenomena based modeling of hybrid welding lacks validation, applicability, and consideration of the important laser-arc interaction.[56-57] For example, Zhao et al. modeled laser/GMAW spot welding. They analyzed the influence of metal droplets falling in the laser induced keyhole on liquid metal droplet momentum transfer and weld composition, yet their work did not consider the important laser-arc interaction or include any experimental validation.

In order to analyze the role of important process parameters and surface active elements on heat transfer and fluid flow during hybrid welding, a three-dimensional heat transfer and fluid flow model is presented. Previous models have yet to analyze the influence of sulfur and oxygen on keyhole and weld pool geometry. This model considers the influence of convection during hybrid and high power density laser welding for the determination of temperature and fluid flow profiles, which has yet to be analyzed using a model for hybrid welding in three dimensions. The model utilizes a pressure balance at the keyhole walls to account for the influence of oxygen introduced to the shielding gas. In order to incorporate the effect of the laser-arc interaction, the model allows for the modification of the arc power density distribution shape and arc root location. Previous models have typically used a constant temperature condition at the keyhole boundary for the solution of the temperature and fluid flow profiles. In the model presented here, a novel heat flux balance condition is utilized in order to overcome previous issues encounter with the constant temperature condition.

The model results are experimentally validated using data provided in the literature, on experimental work performed at the Applied Research Laboratory (ARL) at The Pennsylvania State University. The modeling results show the role of heat source separation distance and arc current on weld bead cooling rates. In addition, the importance of convection and the significance of various driving forces for fluid flow during hybrid welding are determined. Effects of heat source separation distance and laser power on weld bead dimensions are presented. An analysis of the influence of surface active elements on weld bead geometry and fluid flow during high power density laser welding is presented so as to better understand the role of surface active elements during hybrid welding.

3.2 Mathematical Model

3.2.1 Model capabilities

The computer code can calculate the following parameters for steady state keyhole mode laser, arc, and hybrid welding:

- Three dimensional keyhole geometry
- Three dimensional temperature fields in the workpiece
- Two dimensional superimposed weld cross section
- Fluid velocities in the weld pool in three dimensions
- Cooling rates at user specified locations in the workpiece
- Effects of welding variables on temperature fields, fluid flow, and cooling rates in the workpiece.

3.2.2 Special features of the program

- Laser beam characteristics, shielding gas oxygen percentage, welding process parameters, material properties, and grid information is specified by the user through a text file.
- Properties of some common materials are stored in the program and need not be user specified.
- Output in the form of a text file shows the peak temperature, the maximum fluid velocities in three directions, heat loss at different workpiece surfaces, and weld pool depth and half-width every 100 iterations.
- The output also contains various data files for visualization of results.
- A user friendly formatted output (heatbal.txt) of pertinent energy balance data concerning error in integration due to coarse grid, absorbed energy inside the keyhole, energy loss due to vaporization, and energy absorbed outside the keyhole.
- Uses a turbulence model to estimate the enhanced heat and mass transfer due to fluctuating components of velocity.

- Uses a dynamic adjustment factor to insure what energy is provided by the laser beam inside the keyhole is actually what is transferred to the workpiece material.
- A pressure balance in used along the keyhole surface in order to determine local keyhole wall temperatures and account for the formation of gaseous species which influence keyhole shape.

3.2.3 Input file

The input file contains user specified variables. The input file consists of five categories: process parameters, material properties, numerical scheme parameters, boundary conditions, and geometrical grid parameters.

1. The process parameters include the input power for the heat sources, material absorption coefficient, welding speed, the location of the heat sources on the workpiece surface, a switch to indicate whether laser or electron beam welding is occurring, laser beam characteristics (distribution factor, profile shape, beam divergence, and beam radius at focal point), the percentage of oxygen in the shielding gas, a switch to indicate the necessity of an electromagnetic force calculation, arc power density distribution factor, and arc efficiency.

2. A material index identifies the workpiece material as indicated in the input file below. If the user specifies zero as the value for any material property (thermal conductivity, specific heat, concentration of surface active elements, etc.), the program implements an appropriate default value stored in the database (matselect.for). Alternatively, if a better estimate is available, the user can specify a non-zero value for any material property. The database values will be selected only if the user provides zero as the input for any material property (surface active element concentrations and emissivity are zero by default).

3. The numerical scheme parameters include the maximum number of iterations, the time step and maximum time for a transient calculation, the under-relaxation for pressure,

velocity, and enthalpy, and also the indices for saving and loading file. If the index for saving a file is 1, the u, v, w velocities, pressure, and temperature at each grid location are stored in a file tmp.sv. If the index for loading is 1, the u, v, w velocities, pressure and temperature at each grid location is read from the file tmp.sv and taken as the starting value of calculations. However, the total number of grid locations in x, y and z directions must be kept the same as that in the tmp.sv file.

4. The boundary conditions contain the heat transfer coefficient at the 5 faces of the workpiece (all except the symmetry face), the temperature at these faces, the initial temperature (or pre-heat temperature) of the work-piece, and ambient temperature. We allow three types of boundary conditions at east, west, bottom, top, and north surfaces. (I) surface temperature is given; (II) convective heat flux with h_c calculated using equation:

$$h_c = (1.3571 \times 10^{-5}) C' (1.8 \times \Delta T)^{0.25}$$

and (III) convective heat flux with hc supplied by the user. This is done by determining the value of heat transfer co-efficient hc in the input file as follows.

$$If \begin{cases} h_c > 100 \\ 0 < h_c < 20 \\ h_c < 0 \end{cases} then \begin{cases} (I) \\ (II) \\ (III) \end{cases}$$

5. Fixed non-uniform rectangular grids are used for x, y, and z directions. The geometrical parameters specifies by the user generate the mesh – the number of zones in each direction, length of each zone, number of control volumes in each zone, and the exponents to control the location of control volume interfaces. Finer grids are used near the heat source compared to regions further away.

```
!-----process parameters--------------
7000.0    !laser power (watt)
0.27      !material absorption coefficient
1.0       !plasma attenuation coefficient,(1/cm)
0         !laser or e-beam weld? (0 = laser, 1 = e-beam)
1         !laser beam profile type (1= hyperbolic, 2= Kaplan model, 3= uses
          divergence)
0.0       !divergence, mm/mm
0.0048   !c1, beam profile parameter, coeff of x^2
0.02     !c2, beam profile parameter, coeff of x
0.025     !laser beam radius at focal point(cm)
0.0       !defocus (cm)
1.5       !laser power distribution factor
```

```
0.0       !arc current, A
13.0      !arc voltage, V
0.4       !arc efficiency
0.055     !arc radius, cm
0.5       !arc distribution factor
1         !emf calculation necessary? (1=yes, 0=no for load file)
0.0       !percentage of oxygen in shielding gas
1.3       !starting location of beam, cm
1.3       !staring location of the arc, cm
1.67      !welding speed, cm/s
!-----material properties----------------------
5      !1 -> 304L SS, 2 -> V, 3 -> Ta, 4 -> Ti-6Al-4V, 5 -> 21-6-9 stainless
98.54  !wt % of a, Fe/V/Ta/Ti
0.0    !wt % of b, Cr/ / /Al
0.0    !wt % of c, Ni/ / /V
1.46   !wt % of d
7.0            !density of liquid (gm/cm3)
5.8          !density at boiling point (gm/cm3)
0.07           !molecular viscosity of liquid (gm/cm-sec)
1745.          !solidus temperature  (K)
1785.          !liquidus temperature (K)
286.8          !enthalpy of solid at melting point  (cal/gm)
301.14         !enthalpy of liquid at melting point (cal/gm)
0.17           !specific heat of solid  (cal/gm-K)
0.19           !specific heat of liquid (cal/gm-K)
0.191        !specific heat of liquid at boiling point (cal/gm-K)
0.05           !thermal conductivity of solid,(cal/cm-sec-K)
0.07           !thermal conductivity of liquid, (cal/cm-sec-K)
0.0717       !thermal conductivity at boiling point,(cal/cm-sec-K)
1.3e-5         !coefficient of thermal expansion (1/K)
0.0            !emissivity of the material
-0.49            !d(gamma)/dT of pure material (dynes/cm-K)
0.006            !concentration of surface active species (wt%)
0.13e-8          !surface excess at saturation (mole/cm2)
-0.397e5         !enthalpy of segregation (cal/mole)
0.318e-2         !entropy factor
!-----numerical scheme parameters---------------
100            !maximum number of iterations
0.6              !underrelaxation for u-velocity
0.6              !underrelaxation for v-velocity
0.6              !underrelaxation for w-velocity
0.8              !underrelaxation for pressure
1.0              !underrelaxation for enthalpy
0                !index for saving file  (1 = save)
0               !index for loading file (1 = load)
!-----boundary conditions------------------------------------------
100.0          !heat transfer coefficient at west face   (cal/cm2-s-K)
100.0            !heat transfer coefficient at east face   (cal/cm2-s-K)
100.0             !heat transfer coefficient at north face  (cal/cm2-s-k)
0.005              !heat transfer coefficient at bottom face (cal/cm2-s-K)
-100.0               !heat transfer coefficient at top face    (cal/cm2-s-K)
298.0             !temperature at west face   (K)
298.0             !temperature at east face   (K)
298.0             !temperature at north face  (K)
298.0             !temperature at bottom face (K)
298.0             !preheat temperature (K)
298.0             !ambient temperature (K)
!-----geometrical parameters---------
8             !number of x-zones
1.0   0.15 0.15 0.15  0.8 0.3 9.0  0.15       !length of each x-zone (cm)
8     10   25   25    80  20  15   10   !number of control volumes in each x-
zone
```

```
-1.8 -1.4  1.0  1.0   1.0 1.0 1.0  1.0  !exponents to locate control volume
interfaces
4               !number of y-zones
0.05 0.3  0.8  0.15 !length of each y-zone (cm)
10   45   20   10   !number of control volumes in each y-zone
1.0  1.0  1.0  1.0   !exponents to locate control volume interfaces
5               !number of z-zones
0.1  0.8  0.5 0.4 0.2       !length of each z-zone (cm)
10   15   40  25   25      !number of control volumes in each z-zone
1.0 -1.2  1.0 1.0 1.0      !exponents to locate control volume interfaces
```

3.2.4 Output file

The output.txt file contains all of the input parameters specified in the input file. It also contains the x, y, and z-grid locations in the domain e.g. positions of x(i) and xu(i) as shown below. A section of the output file generated by these is given below.

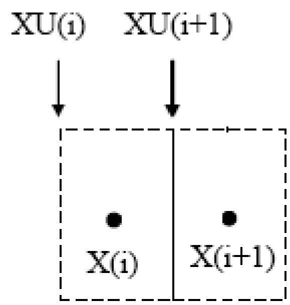

A section of output file:

```
  i=    50        51        52        53        54        55        56
  x=  3.911E-01 4.021E-01 4.135E-01 4.253E-01 4.373E-01 4.496E-01 4.623E-01
 xu=  3.856E-01 3.965E-01 4.077E-01 4.193E-01 4.312E-01 4.434E-01 4.559E-01
```

Every 100 iterations, the code gives the peak temperature, maximum fluid velocities in three directions, heat loss from the workpiece surface, weld depth and half-width, and the residuals for the enthalpy, mass conservation, and momentum calculations, the average values of viscosity and thermal conductivity, the diameter of the keyhole along the welding direction in centimeters, the radius of the keyhole in transverse to the welding direction in centimeters, the effective absorption coefficient in the keyhole due to multiple reflections, and the ratio of the initial calculated keyhole surface area relative to the adjusted area to match the energy absorbed by the laser beam in the keyhole with the energy supplied from the keyhole surface to the workpiece material. As a rule of thumb, the residuals should be on the order of 1 x 10^{-3} at a maximum in order to ensure convergence to a correct solution. An example of the code output is provided below.

```
iter    time/iter    res_enth    res_mass     res_u      res_v      res_w
3000      0.347      1.10E-06    2.83E-07    5.89E-06    5.71E-06    7.41E-06
Tmax       umax         vmax        wmax       length      depth    half-width
3102.      17.9         18.6        13.6        0.881       0.929      0.270
north   south    top   toploss  bottom   west     east  hout    hin     ratio
-94.0     0.0    23.4    -3.0     0.0  1240.4 -1768.0  -618.6  613.4    1.01
muAv     muM     kAv      kM      xk        yk        AbsMR    Aratio
 0.76    7.37    0.21    1.61    0.186     0.053     0.938     2.163
```

After the completion of calculations, the following summary of results is given which includes the time to cool, and the cooing rate, between two temperatures (1073 K and 773 K):

```
Length of the pool      (cm)                 1.0947E+00
Depth of the pool       (cm)                 1.8236E-01
Half-width of the pool  (cm)                 3.2329E-01
Peak temperature        (K)                  3.1859E+03
x1073(cm), x773(cm), t8-5(s)    1.869   3.581   1.025
Maximum u-velocity      (cm/s)               2.0402E+01
Maximum v-velocity      (cm/s)               3.6398E+01
Maximum w-velocity      (cm/s)               9.7249E+00
Rate of heat input      (cal/s)              2.0746E+02
Rate of heat output     (cal/s)             -2.0821E+02
Ratio of heat input to heat output           1.0036E+00

Date: 2008- 7- 2  time: 11:15:15

Total time used:     0  hr    18  m     1  s
```

b) Tecout.dat contains following variables in ordered form, obtained after the final iteration:

"X", "Y", "Z", "U", "V", "W","T","P","VIS"

X, Y and Z are the co-ordinates (in mm) of grid points. U, V and W are the velocities (in mm/s) at the grid point in x, y and z-direction. T is the temperature in K, P is the pressure in dyne/cm^2, and VIS is the viscosity in kg/m-s. This file can be directly opened using Tecplot® graphing program. It is very important for visualization of results obtained.

c) For all values of z, geometry.dat stores the y boundary of the keyhole wall (or vapor-liquid interface), the weld pool, and 100K temperature isotherms, which can be used to plot weld cross-sections in visualization software like Tecplot®.

d) EMF_out.dat is an output data file which contains the electromagnetic force field data, which is calculated during an arc or hybrid welding simulation. Emf_out.dat contains the calculated values of the current density vector (J) and magnetic flux (B) vectors for a specified arc condition, i.e. radius and current. This file is either repeatedly used assuming the same grids and arc conditions are implemented, or is written by the code for each individual simulation.

e) Heatbal.txt is a formatted output of the laser power, arc power, Fresnel absorption coefficient, arc efficiency, laser beam radius at the focal point, arc radius, laser power density distribution factor, arc power density distribution factor, computed keyhole depth, computed keyhole surface area, calculated laser energy falling inside the keyhole, outside the keyhole, and on half the workpiece, the actual laser energy falling on half the workpiece, the error in the energy integration, the calculated arc energy falling on half the workpiece, the actual amount of arc energy falling on half the workpiece, the error in arc energy integration, the computed laser energy absorbed inside the keyhole and outside the keyhole, the calculated laser beam energy lost to vaporization of alloying elements, the effective absorption coefficient due to multiple reflections of the laser beam inside the keyhole, the net heat input rate, and the net heat output rate.

f) Keyholecalc.txt provides the calculated pressure terms, local keyhole wall temperature, and local keyhole radius along the keyhole depth. In addition, the file provides the calculated keyhole depth from the keyhole calculation.

3.2.5 Calculation procedure

The program calculates the three dimensional temperature and fluid velocity profiles for steady state keyhole mode laser, GTA, and laser/GTAW hybrid welding where the heat sources are acting on the workpiece at either the same or different locations. Below is a flow chart demonstrating the calculation procedure for the code. Initially the input file is read and the grids are generated for the workpiece. An initial keyhole profile is calculated based on a point by point energy balance and pressure balance at the keyhole surface. Once the initial keyhole profile is calculated, the Rosenthal equation is solved to determine the three-dimensional temperature keyhole geometry based upon the calculated temperature profile for the entire workpiece. The code then initializes all variables and calculates spatial variation of any heat source intensities. In the case when an arc heat source is present, the EMF field is also calculated. The iteration loop commences and proceeds until the maximum number of iterations is achieved, or the convergence criterion is met. Once the iterative looping process of the code commences, enthalpy values are determined for the entire workpiece, accounting for the respective boundary conditions, and enthalpy is converted into temperature values. Then, the temperature of the workpiece is updated and the pool geometry is calculated based upon the thermophysical properties. As the temperature of the workpiece changes throughout the iterative process, the physical properties of the material are updated. The velocity of the fluid in the liquid weld pool is calculated considering the effects of surface tension, buoyancy, and emf forces. Residuals of the velocities, mass, and enthalpy are calculated to ensure the convergence to a precise solution. The keyhole heat input is adjusted after 500 iterations to ensure that the total heat input from the keyhole surface is equal to the energy absorbed inside the keyhole from the laser beam. Finally, the aforementioned output and data files are generated. An outline of the calculation procedure is given in the flow chart in Fig.3.1.

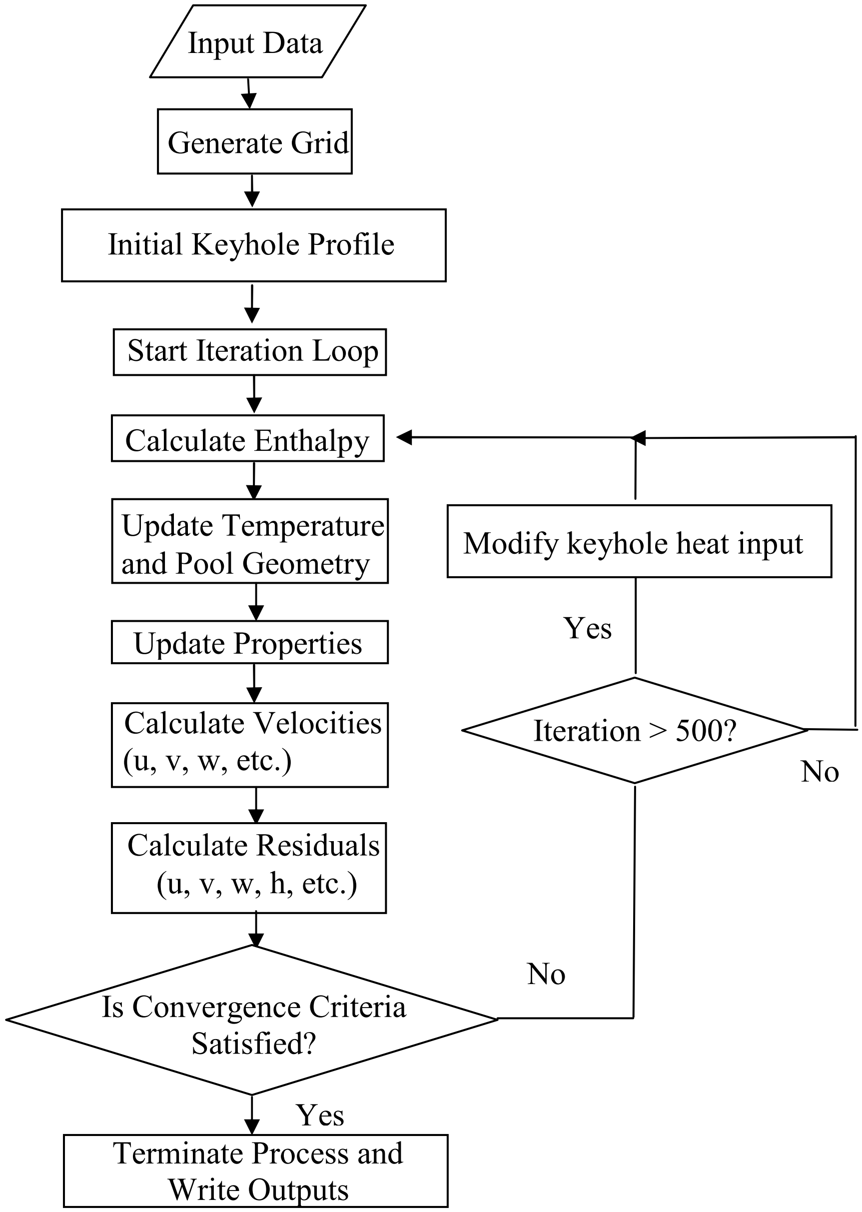

Fig. 3.1: Outline of calculation procedure.

3.2.6 Major components of the code

3.2.6.1 Calculation of keyhole geometry

The following assumptions are made in the model: 1) Since the keyhole walls are nearly vertically, heat is transported mainly along the horizontal planes. 2) Plasma in the keyhole is assumed to have a constant absorption coefficient independent of location. Although this assumption cannot be rigorously defended, it greatly simplifies calculations.

Three groups of input data are necessary to run the model: the material properties, welding parameters, and the computational and geometrical parameters. The output of the model includes geometry of the keyhole and three-dimensional temperature field of the weldment based on heat conduction in the workpiece. The keyhole geometry is calculated based on point-by-point energy and pressure balance on the keyhole wall. The model then calculates the three-dimensional temperature field in the weldment. The energy absorption by multiple reflections within the keyhole is also considered.

3.2.6.1.1 Initial keyhole shape from energy and pressure balance

Laser energy is absorbed and transferred into the molten metal on the keyhole wall. The initial calculation of the local angle of the keyhole wall is considered to be determined by the balance between heat flux transferred into the keyhole wall, I_c, the locally absorbed beam energy flux, I_a, and the heat loss due to heat of evaporation, I_v. The heat balance equation is given as:[55]

$$\tan(\theta) = \frac{I_c}{I_a - I_v / \sin\theta} \tag{3.1}$$

The calculation of local keyhole angle θ requires the determination of I_c, I_a, and I_v. The calculation is done in two steps. In the first step, the effects of plasma absorption and multiple reflections are not considered. In the second step, these effects are taken into account based on the keyhole geometry obtained in the first set of calculations. Cartesian (x, y, z) and cylindrical (r, φ, z) coordinate systems are used alternatively in this document. In the Cartesian system, x is the coordinate in the welding direction, z the beam axis direction and y perpendicular to both x and z. In the cylindrical system, r and φ are to equivalent polar coordinates corresponding to x and y, z is also the coordinate in the beam axis direction. The co-ordinate system is shown by a schematic in Fig. 3.2.

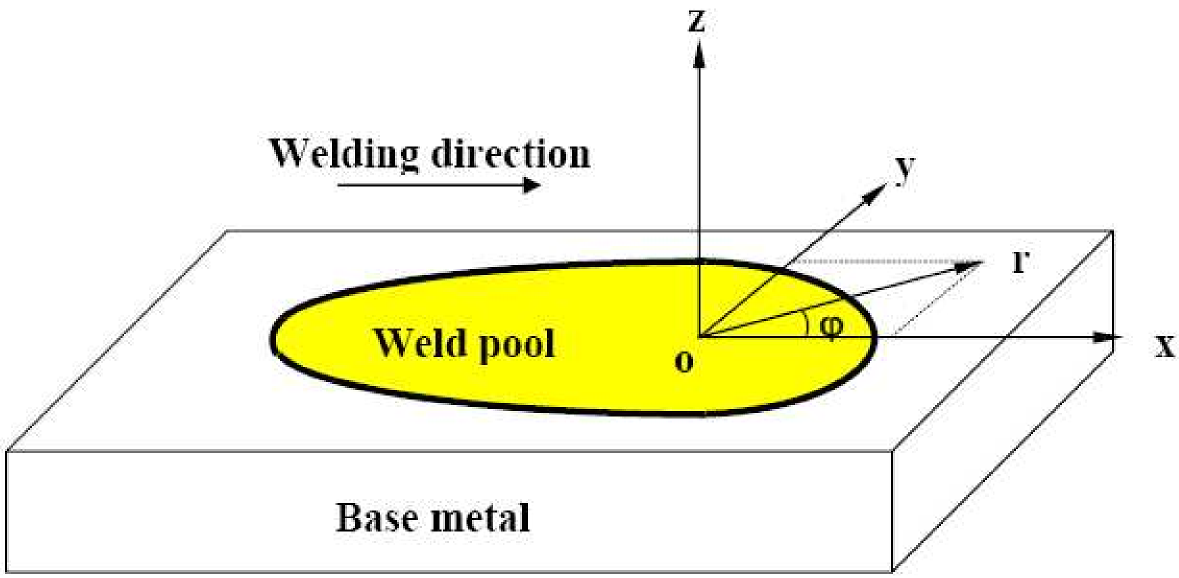

Fig. 3.2: Co-ordinate system for keyhole profile calculation.

The heat flux conducted into the keyhole wall is deduced from a moving line source model developed by Rosenthal, which gives a solution for the temperature field in an infinite plate of certain thickness by:[41-42, 55]

$$T(r,\varphi) = T_a + \frac{P'}{2\pi\lambda_{th}} K_o(Pe'r)e^{-Pe'r\cos\theta} \tag{3.2}$$

where r and φ are defined schematically in the coordinate system shown in Fig. 3.2, T_a is the ambient temperature, P' is the strength of the line source, i.e., power per unit depth, λ_{th} is the thermal conductivity, the function of Pe'r, $K_o(\ )$, is the second kind and zeroth order solution of the modified Bessel function, and Pe' is defined as $Pe' = v/(2\kappa)$, where v is the welding speed and κ is the thermal diffusivity.

Assuming the heat flow in the z direction to be negligible, Fourier's law of heat conduction determines the heat flux in the radial direction to be:[41-42, 55]

$$I_c(r,\varphi) = -\lambda_{th}\frac{\partial T}{\partial r} \tag{3.3}$$

The spatial gradient of temperature with respect to r is obtained from equation. (3.3) as:[41-42, 55]

$$\frac{\partial T}{\partial r} = \frac{P'}{2\pi\lambda_{th}} Pe'\left[-K_o(Pe'r)\cos\varphi + K_o'(Pe'r)\right]e^{-Pe'r\cos\varphi} \tag{3.4}$$

where K_o'( ) is the derivation of K_o( ) and[55]

$$K_o'(x) = -K_1(x) \tag{3.5}$$

where $K_1(x)$ is the second kind and first order solution to the modified Bessel function. For the first set of calculations, only Fresnel absorption on the keyhole wall is considered. Therefore, the absorbed laser beam energy flux at any point (r, φ, z) on the keyhole wall is given by:[41-42, 55]

$$I_a(r,\varphi,z) = e^{-\beta l}(1-(1-\alpha)^{1+\pi/4\theta})I_o(r,\varphi,z) + I_{a,o}\eta\exp\left(-f_a\left(\frac{D_{LA}\pm r}{r_a}\right)^2\right) \tag{3.6}$$

where the first term accounts for multiple reflections of the laser beam along the keyhole walls, and the second term accounts for the heat flux from the arc. β is the inverse Bremsstrahlung absorption coefficient of the plasma generated by the laser, α is the absorption coefficient of the workpiece material, θ is the average angle between the keyhole wall and the incident beam axis, I_o is the local incident laser beam intensity that varies as a function of depth and radial distance, $I_{a,o}$ is the peak intensity of the arc, η is the arc efficiency (~ 0.25 - 0.7), r_a is the arc radius, f_a is the arc power density distribution factor, and D_{LA} is the distance between the heat sources. The local incident beam intensity is defined by:[41-42, 55]

$$I_o(r,\varphi,z) = I_{fol}\alpha\left(\frac{r_{fo}}{r_f}\right)^2\exp\left(-f_l\frac{r^2}{r_f^2}\right) \tag{3.7}$$

where I_{fol} and is the peak intensity of the laser at the focal points, r_{fo} is the beam radius at the focal point, f_l is the laser energy distribution factor, and r_f is the local beam radius,. The peak laser and arc intensities are defined by:[41-42, 55]

$$I_{fol} = \frac{f_l P}{\pi r_{fo}^2} \tag{3.8}$$

$$I_{a,o} = \frac{f_a P}{\pi r_a^2} \tag{3.9}$$

where P is the power of the heat source. The laser beam profile is chosen by the user in the input file. The laser beam radius along the depth can be calculated using three methods, which is determined by the user. First, the local beam radius (r_f) as a function of the depth (z) can defined by the user (option number 2, Kaplan model) as:[41-42, 55]

$$r_f = r_{fo}\left[1+\left(\frac{z+z_o}{2r_{fo}f/d_b}\right)^2\right]^{1/2} \tag{3.10}$$

where z_o is the beam defocusing, f is the laser beam focal length, and d_b is the diameter of the laser beam on the laser focusing lens. Second, the laser beam radius may be determined using the divergence (option number 3) of the laser beam by:

$$r_f = r_{fo} + D(z+z_o) \tag{3.11}$$

where D is the divergence of the laser beam per unit depth in units of cm/cm. Finally, the laser beam radius can be approximated by a polynomial fit (option 1) of a measured laser beam profile and is defined by:

$$r_f = A(z+z_o)^2 + B(z+z_o) + r_{fo} \tag{3.12}$$

where A and B are constants determined by the polynomial fit to the data. At each horizontal xy plane, the keyhole boundary is identified by a minimum and a maximum x value for any y value. If the user chooses to perform electron beam welding, the laser beam has a constant radius equal to the laser beam radius at the focal point.

The evaporative heat flux, I_v, on the keyhole wall is calculated from the following relation:[55]

$$I_v = \sum_{i=1}^{n} J_v \Delta H_{v,i} \tag{3.13}$$

where n indicates the total number of alloying elements in the alloy, J_v is the evaporation flux of element i and $\Delta H_{v,i}$ is the heat of evaporation. The evaporation flux at very low pressures can be accurately calculated from the Langmuir equation. However, at one atmosphere pressure the Langmuir equation significantly over predicts the vaporization rate. Based on previous studies at Penn State, the calculated evaporation flux using the Langmuir equation is usually 5 to 10 times higher than the experimental results. In this model, a factor of 7.5 is used to calculate the evaporation flux in g cm^{-2} s^{-1} from the modified Langmuir equation:[55]

$$J_v = \frac{44.34}{7.5} a_i P_i^o (T_v) \sqrt{\frac{M_i}{T_v}} \tag{3.14}$$

where a_i is the activity of the element i in the liquid alloy, $P_i^o(T_v)$ is the equilibrium vapor pressure of element i over pure liquid at temperature T_v, M_i is the molecular weight of element i. The activity of each alloying element is taken as its atomic fraction in the alloy.

Rather than assuming a constant keyhole temperature along the depth of the keyhole, the keyhole temperature varies along the depth depending upon the local pressure balance. The temperature at which the sum of partial pressures of the alloying elements weighted by their respective mole fractions equals the vapor pressure calculated from the pressure balance is taken as the keyhole wall temperature. Partial pressures are determined from equilibrium temperature-pressure relationships. Calculated keyhole temperatures provide a means of determining the keyhole geometry. The pressure balance at the keyhole walls is given by:

$$P_r + P_v + P_{CO} = P_\gamma + P_o + \rho_l gh \tag{3.15}$$

where P_r is the recoil pressure, P_v is the vapor pressure, P_{CO} is the equilibrium pressure due to carbon monoxide (CO) formation in the keyhole, P_γ is the pressure due to surface tension, P_o is the ambient pressure (1 atm), and the final term on the right hand side represents the hydrostatic pressure.

Several reactions were considered for the pressure balance at the keyhole wall for equation 3.15. Table 3.1 shows several reactions considered at the keyhole wall temperature (3000 K) and the resulting order of magnitude of the gaseous species. The most likely reaction to influence the pressure balance is the formation of carbon monoxide from dissolved carbon and oxygen in the weld pool.

Table 3.1: Partial pressure of various gaseous species reactions considered at the keyhole wall calculated at 3000 K.

Reaction	**Partial pressure (atm) at 3000 K**
1/2 S_2= [S]	$P_{S2} \sim 1 \times 10^{-4}$
1/2 O_2 = [O]	$P_{O2} \sim 1 \times 10^{-8}$
$S_2 + 2\ O_2 = 2\ SO_2$	$P_{SO2} \sim 1 \times 10^{-9}$
2 CO (g) + S_2 (g) = 2 COS (g)	$P_{COS} \sim 1 \times 10^{-6}$
C + O = CO (g)	$P_{CO} \sim 0.15$
C + 1/2 S_2 = CS (g)	$P_{CS} \sim 1 \times 10^{-4}$
C + S_2 (g) = CS_2 (g)	$P_{CS2} \sim 1 \times 10^{-5}$

CO may form at the keyhole walls through the combination of dissolved carbon and oxygen: $[\underline{C}]+[\underline{O}]=CO(g)$. The standard energy change for this reaction (ΔG^o) is equal to (–22390.0 –39.7∗T) in J/mol.[58-60] The standard free energy change was used to determine the reaction equilibrium constant, K_{eq} from the relation ΔG^o = -RTlnK_{eq} in order to estimate the equilibrium partial pressure of CO. The equilibrium constant for the formation of CO is defined by:[58]

$$K_{eq} = \frac{P_{CO}}{a_C a_O} \tag{3.16}$$

where a_C and a_O are the activities of dissolved carbon and oxygen in the steel. The activity of the dissolved species is defined by:[58]

$$a_i = \gamma_i^o (\%i) \tag{3.17}$$

where %i is the weight percent of element i in the alloy and γ_i^o is the activity coefficient of element i, which is defined by:[58]

$$\log \gamma_i^o = e_i^i (\%i) + \sum e_i^j (\%j) \tag{3.18}$$

where e_i^i is the first order interaction coefficient for the solute, and e_i^j is the first order interaction coefficient which accounts for the effect of the alloying element j on the activity coefficient of the solute i. The oxygen concentration in the weld metal was measured after welding at two depths along the center of weld cross-section. The carbon and sulfur concentrations were taken from the nominal material composition before welding.

The activity coefficients were determined using the first order interaction coefficients from Sigworth and Elliott.[60] The following are the first order interaction coefficients for carbon:[60]

$e_C^{C} = 158/T + 0.0581$ $e_C^{Mn} = -0.012$ $e_C^{Si} = 162/T - 0.008$

$e_C^{P} = 0.051$ $e_C^{N} = 0.11$ $e_C^{S} = 0.046$

$e_C^{O} = -0.34$ $e_C^{Cr} = -0.024$ $e_C^{Ni} = 0.012$

The following are the first order interaction coefficients for oxygen:

$e_O^{C} = -0.45$ $e_O^{Mn} = -0.021$ $e_O^{Si} =- 0.131$

$e_O^{P} = 0.07$ $e_O^{N} = 0.057$ $e_O^{O} = -1750/T+0.734$

$e_O^{S} = -0.133$ $e_O^{Cr} = 0.04$ $e_O^{Ni} = 0.006$

where T is the local keyhole wall temperature. The partial pressure of carbon monoxide (P_{CO}) is given by.

$$P_{CO} = K_{eq\,CO} a_{[O]} a_{[C]} \tag{3.19}$$

where $a_{[C]}$ is the activity of dissolved carbon in the weld metal. The equilibrium constant for gaseous carbon monoxide is given by:[59]

$$K_{eq[CO]} = \exp\left(\frac{22390 + 39.7(T)}{RT}\right) \tag{3.20}$$

The partial pressure of CO near the keyhole walls depends not only on the reaction thermodynamics but also the kinetic factors such as diffusion of solute atoms through the interfacial boundary layers. The equilibrium partial pressure of a gas calculated based on the reaction constants and bulk solute concentrations can be considered the maximum possible value of the actual gas pressure at the keyhole walls. The pressure of CO at the keyhole walls was taken as a constant factor times the equilibrium pressure calculated using bulk concentrations of dissolved oxygen and carbon. The choice of this factor was 0.8.

The pressure gradient along the keyhole is given by:[61]

$$\Delta P = \frac{8\mu v l}{r^{2}} \tag{3.21}$$

where μ is the viscosity of the metal vapor in the keyhole, v is the average velocity of the metal vapors inside the keyhole, l is the depth of the keyhole, and r is the average keyhole radius. The average velocity is approximated by J/c, where c is the molar concentration of metal. The average keyhole radius is approximated by dividing the sum total of keyhole radii at various xy-planes along the keyhole depth by the total number of xy-planes.

The surface tension pressure term is given by:[47]

$$P_{\gamma} = \frac{\gamma}{r} \tag{3.22}$$

where γ is the coefficient of surface tension, and r is the radius of the keyhole. The surface tension is given by:[53]

$$\gamma = \gamma_{p} - A(T - T_{l}) - RT\Gamma_{s}\ln[1 + k_{l}a_{i}\exp(-\Delta H^{o}/RT)] \tag{3.23}$$

where γ_p is the surface tension of the pure material, A is the negative of dγ/dT for the pure material (-0.43 dynes cm^{-1} K^{-1} for pure iron), T is the local temperature, T_l is the liquidus of the alloy, R is the gas constant, Γ_s is the surface access at saturation (2.03 x 10^{-12} kmol cm^{-2} for Fe-O), k_l is a constant related to entropy of segregation (1.38 x 10^{-2} for Fe-O), a_i is the activity of oxygen (wt% of oxygen in metal), and ΔH^o is the enthalpy of segregation (-1.463 x 10^5 cal mol^{-1}).

3.2.6.1.2 Adjustment of keyhole heat input

The keyhole heat input is adjusted as a means to ensure that the total heat input from the keyhole surface to the workpiece is equal to the energy supplied and absorbed inside the keyhole from the laser beam. The condition is satisfied by:

$$\sum F_{i}A_{i} = H_{a} - H_{v} \tag{3.24}$$

where F_i is a flux at location i from the keyhole wall, A_i is the local area transverse to the flux direction at location i, H_a is the heat input absorbed in calories per second for the entire keyhole, and H_v is the evaporative heat loss inside the keyhole in calories per second. The heat input from the keyhole walls is equated to the absorbed energy inside the keyhole minus that loss to vaporization of alloying elements by modifying the heat source power per unit depth based upon the value of the dynamic adjustment factor defined by:

$$f = \frac{H_a - H_v}{\sum F_i A_i} \tag{3.25}$$

The adjustment factor is calculated after 500 iterations to allow the temperature isotherms to stabilize in the heat transfer and fluid flow domain before modifying the keyhole total heat input. The factor is then used as a metric for modifying the heat source power per unit depth until the calculated adjustment factor results in a value close to one. It is important to realize that the adjustment of the keyhole heat input can result in an effective keyhole diameter that is larger than previously reported in the literature for instantaneous measurements. The keyhole adjustment in this model is used as a means to obtain weld bead geometry and maintain the energy balance in the heat transfer and fluid flow calculations.

3.2.6.2 Turbulence model

During keyhole mode laser welding, the rates of transport of heat, mass and momentum are often enhanced because of the presence of fluctuating velocities in the weld pool. The contribution of the fluctuating velocities is considered by an appropriate turbulence model that provides a systematic framework for calculating effective viscosity and thermal conductivity. The values of these properties vary with the location in the weld pool and depend on the local characteristics of the fluid flow. In this work, a turbulence model based on Prandtl's mixing length hypothesis is used to estimate the turbulent viscosity:[41, 48]

$$\mu_t = \rho l_m v_t \tag{3.26}$$

where μ_t is the turbulent viscosity, l_m is the mixing length, and v_t is the turbulence velocity. Turbulence velocity can be estimated from the turbulent kinetic energy. Assuming turbulent kinetic energy to be about 12% of the mean kinetic energy, the turbulent velocity is approximately 35% of the mean velocity. Thus, the turbulent viscosity becomes,

$$\mu_t = 0.35\rho l_m v \tag{3.27}$$

The corresponding local turbulent thermal conductivities are calculated by using turbulent Prandtl number, defined as $Pr = \frac{\mu_T c_p}{k_T}$, to be 0.9. Effective viscosity at a particular point is given as the sum of the turbulent (μ_t) and laminar (μ_l) viscosities, i.e., $\mu = \mu_t + \mu_l$.

3.2.6.3 EMF field calculation

The electromagnetic force is generated by the interaction of the diverging current and the self induced magnetic field. This electromagnetic force is also called the Lorentz force, which in the weld pool is a radially acting force inward and downward. The Lorentz force pulls the liquid metal along the surface towards the center and pushes it down to the bottom of the weld pool, as shown by Fig. 3.3.

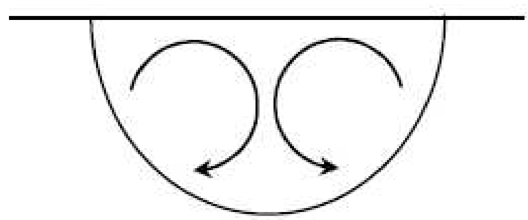

Fig. 3.3: The effect of the Lorentz force on fluid motion in the weld pool.

The electromagnetic force, F_{em}, can be expressed as:[62]

$$F_{em} = J \times B \tag{3.28}$$

where J is the current density vector and B is the magnetic flux vector. The EMF field is axisymmetric about the arc. Therefore, the current density, J, and magnetic flux, B, were first calculated in the axisymmetric coordinates, J_r is the radial component of J, J_z is the axial component of J, B_θ is the θ component of B. For semi-infinite thickness of the workpiece J_r, J_z, and B_θ can be given as:[62]

$$J_z = \frac{I}{2\pi}\int_0^\infty \lambda J_o(\lambda r)\exp(-\lambda^2\sigma_j^2/12)\frac{\sinh[\lambda(c-z)]}{\sinh(\lambda c)}d\lambda \tag{3.29}$$

$$J_r = \frac{I}{2\pi}\int_0^\infty \lambda J_1(\lambda r)\exp(-\lambda^2\sigma_j^2/12)\frac{\cosh[\lambda(c-z)]}{\sinh(\lambda c)}d\lambda \quad (3.30)$$

$$B_\theta = \frac{\mu_m I}{2\pi}\int_0^\infty J_1(\lambda r)\exp(-\lambda^2\sigma_j^2/12)\frac{\sinh[\lambda(c-z)]}{\sinh(\lambda c)}d\lambda \quad (3.31)$$

where μ_m is the magnetic permeability (1.26 x 10^{-6} H m^{-1}), I the welding current (A), J_o is the Bessel function of zero order and first kind, c is the thickness of the workpiece, z is the vertical distance from the origin, J_r is the radial component of current density, J_1 is the first kind of Bessel function of first order and B_θ is the angular component of the magnetic field. The above expressions are valid only for the current density distribution equal to 3.0 and when the radial and axial components of the magnetic field (i.e. B_r and B_z) are both zero. A more general expression for the calculation of J_r, J_z, and B_θ that can take into account various current distribution factors is as follows:[62]

$$J_z = \frac{I}{2\pi}\int_0^\infty \lambda J_o(\lambda r)\exp(-\lambda^2\sigma_j^2/4d)\frac{\sinh[\lambda(c-z)]}{\sinh(\lambda c)}d\lambda \quad (3.32)$$

$$J_r = \frac{I}{2\pi}\int_0^\infty \lambda J_1(\lambda r)\exp(-\lambda^2\sigma_j^2/4d)\frac{\cosh[\lambda(c-z)]}{\sinh(\lambda c)}d\lambda \quad (3.33)$$

$$B_\theta = \frac{\mu_m I}{2\pi}\int_0^\infty J_1(\lambda r)\exp(-\lambda^2\sigma_j^2/4d)\frac{\sinh[\lambda(c-z)]}{\sinh(\lambda c)}d\lambda \quad (3.34)$$

where, d is the current density distribution factor. The current density, J, and magnetic flux, B, calculated above in cylindrical coordinates can be transformed to the Cartesian coordinates using the following expressions:[62]

$$J_x = J_r \frac{x}{\sqrt{x^2+y^2}} \quad (3.35)$$

$$J_y = J_r \frac{y}{\sqrt{x^2+y^2}} \quad (3.36)$$

$$B_x = B_\theta \frac{y}{\sqrt{x^2+y^2}} \quad (3.37)$$

$$B_y = -B_\theta \frac{x}{\sqrt{x^2+y^2}} \quad (3.38)$$

$$B_z = 0.0 \quad (3.39)$$

The finale expressions for the three components of the electromagnetic force are given by:[62]

$$F_x = J_y \cdot B_z - J_z \cdot B_y \tag{3.40}$$

$$F_y = J_z \cdot B_x - J_x \cdot B_z \tag{3.41}$$

$$F_z = J_x \cdot B_y - J_y \cdot B_x \tag{3.42}$$

Fig. 3.4 is a flow chart of the EMF calculation as performed by the code.

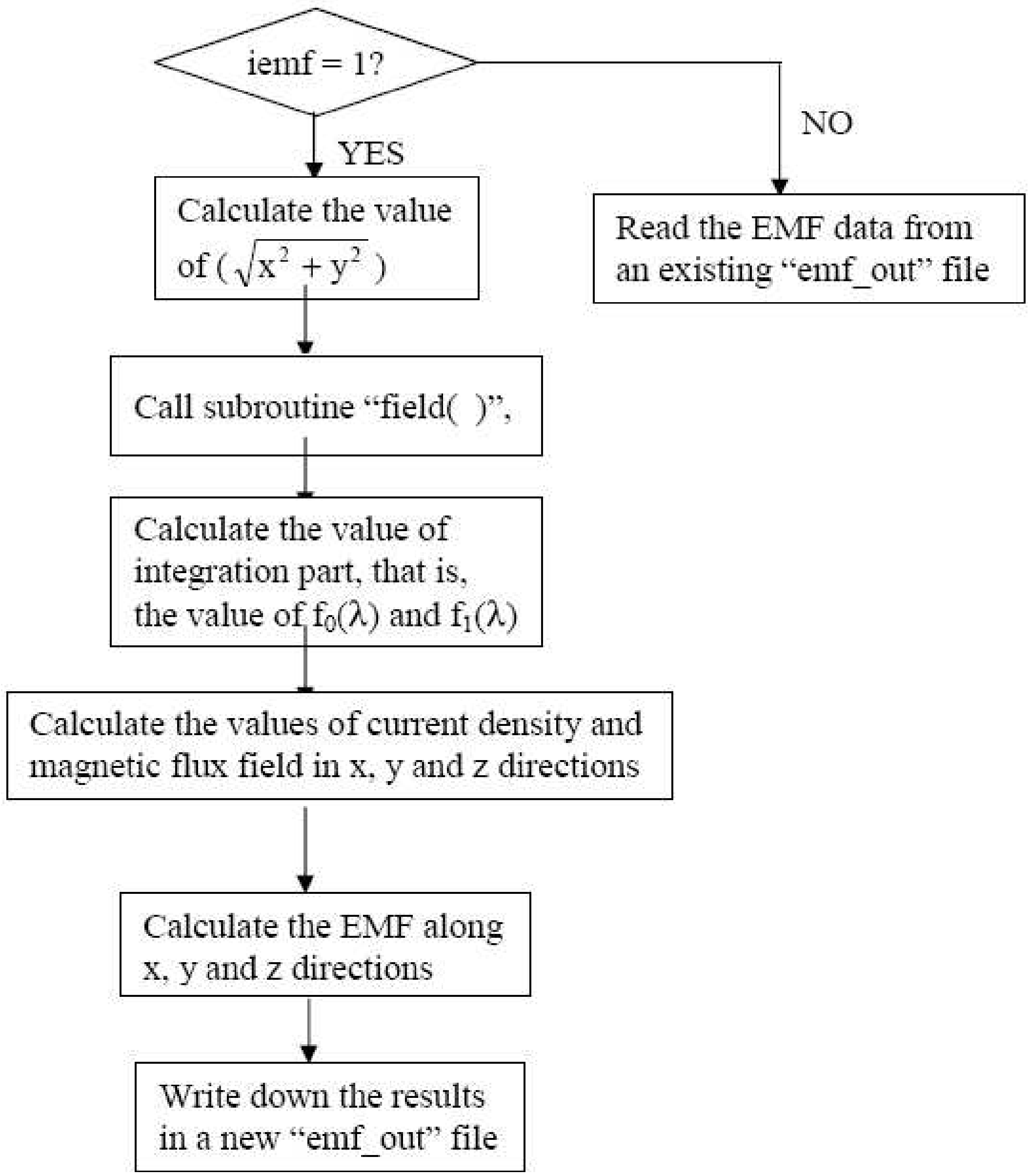

Fig. 3.4: Flow chart of the EMF calculation subroutine.

3.2.6.4 Enthalpy Calculation

The discretized form of the enthalpy equation can be written as:[63]

$$A_P H_P = A_E H_E + A_W H_W + A_N H_N + A_S H_S + A_T H_T + A_B H_B + A_P^o H_P^o + S_U \Delta V \qquad (3.43)$$

where ΔV is the volume of a cell, S_U is the constant part of the source term S ($S=S_U + S_P h_P$), A_E, A_W, A_N, A_S, A_T, A_B represent the coefficients at the east, west, north, south, top and bottom neighbors respectively. The variables A_P^o and H_P^o represent the coefficient and temperature of the previous time neighbor. Fig. 3.5 shows the control volume in three dimensions.

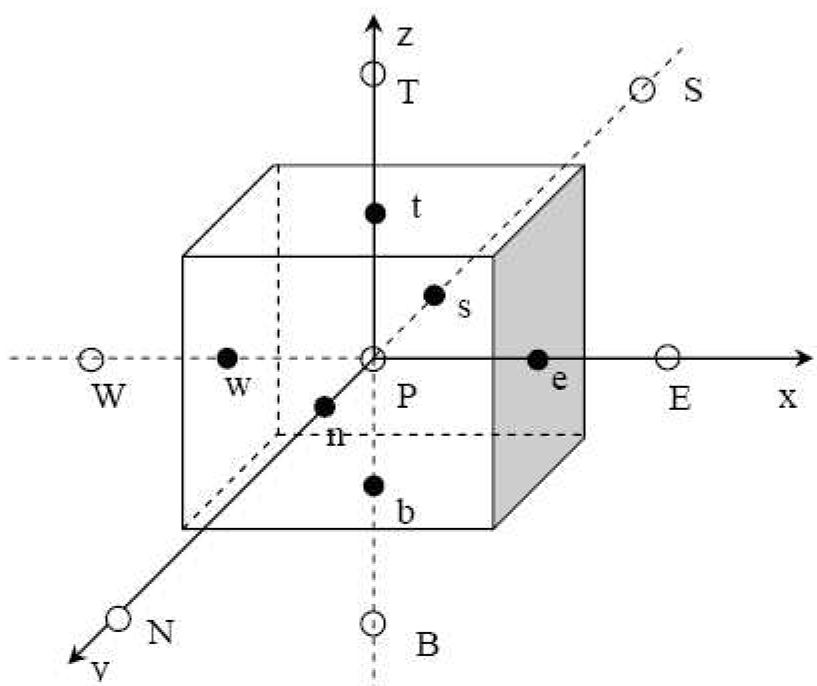

Fig. 3.5: Control volume in three dimensions

According to the power law scheme, the coefficient A_P is given by:[63]

$$A_P = A_E + A_W + A_N + A_S + A_T + A_B + A_P^o - S_P \Delta V \tag{3.44}$$

where $$A_E = D_e \left\| 0, \left(1 - 0.1\left|\frac{F_e}{D_e}\right|\right)^5 \right\| + \left\| -F_e, 0 \right\| \tag{3.45}$$

$$A_W = D_w \left\| 0, \left(1 - 0.1\left|\frac{F_w}{D_w}\right|\right)^5 \right\| + \left\| F_w, 0 \right\| \tag{3.46}$$

$$A_N = D_n \left\| 0, \left(1 - 0.1\left|\frac{F_n}{D_n}\right|\right)^5 \right\| + \left\| -F_n, 0 \right\| \tag{3.47}$$

$$A_S = D_s \left\| 0, \left(1 - 0.1\left|\frac{F_s}{D_s}\right|\right)^5 \right\| + \left\| F_s, 0 \right\| \tag{3.48}$$

$$A_T = D_t \left\| 0, \left(1 - 0.1\left|\frac{F_t}{D_t}\right|\right)^5 \right\| + \left\| -F_t, 0 \right\| \tag{3.49}$$

$$A_B = D_b \left\| 0, \left(1 - 0.1\left|\frac{F_b}{D_b}\right|\right)^5 \right\| + \left\| F_b, 0 \right\| \tag{3.50}$$

$$A_P^o = \frac{\rho \Delta x \Delta y \Delta z}{\Delta t} \tag{3.51}$$

The convective strength and diffusive strength can be defined as:[63]

$$F_e = (\rho u)_e \Delta y \Delta z \qquad D_e = \frac{\Gamma_e \Delta y \Delta z}{(\delta x)_e} = \left(\frac{k}{C_p}\right)_e \frac{\Delta y \Delta z}{(\delta x)_e} \tag{3.52}$$

$$F_w = (\rho u)_w \Delta y \Delta z \qquad D_w = \frac{\Gamma_w \Delta y \Delta z}{(\delta x)_w} = \left(\frac{k}{C_p}\right)_w \frac{\Delta y \Delta z}{(\delta x)_w} \tag{3.53}$$

$$F_n = (\rho v)_n \Delta x \Delta z \qquad D_n = \frac{\Gamma_n \Delta x \Delta z}{(\delta y)_e} = \left(\frac{k}{C_p}\right)_n \frac{\Delta x \Delta z}{(\delta y)_n} \tag{3.54}$$

$$F_s = (\rho v)_s \Delta x \Delta z \qquad D_s = \frac{\Gamma_s \Delta x \Delta z}{(\delta y)_s} = \left(\frac{k}{C_p}\right)_s \frac{\Delta x \Delta z}{(\delta y)_s} \tag{3.55}$$

$$F_t = (\rho w)_t \Delta x \Delta y \qquad D_t = \frac{\Gamma_t \Delta x \Delta y}{(\delta z)_t} = \left(\frac{k}{C_p}\right)_t \frac{\Delta x \Delta y}{(\delta z)_t} \tag{3.56}$$

$$F_b = (\rho w)_b \Delta x \Delta y \qquad D_b = \frac{\Gamma_b \Delta x \Delta y}{(\delta z)_b} = \left(\frac{k}{C_p}\right)_b \frac{\Delta x \Delta y}{(\delta z)_b} \tag{3.57}$$

where Γ represents the general diffusion coefficient. For the enthalpy equation, it can be expressed as k/C_p. k is the thermal conductivity (cal/cm-sec-K), C_p is the specific heat (cal/gm-K).

In order to calculate the value of diffusion strength D, we need to know the value of diffusion coefficient Γ (k/C_p). In the weld pool, because of non-homogeneity of temperature field, the temperature-dependent diffusion coefficients will be non-homogeneous. So it is necessary to calculate the value of diffusion coefficients of every grid point first. Therefore, interpolations are required to obtain the value of diffusion coefficients. Fig. 3.6 is of a scalar control volume in order to aid in understanding the derivation of the heat flux term.

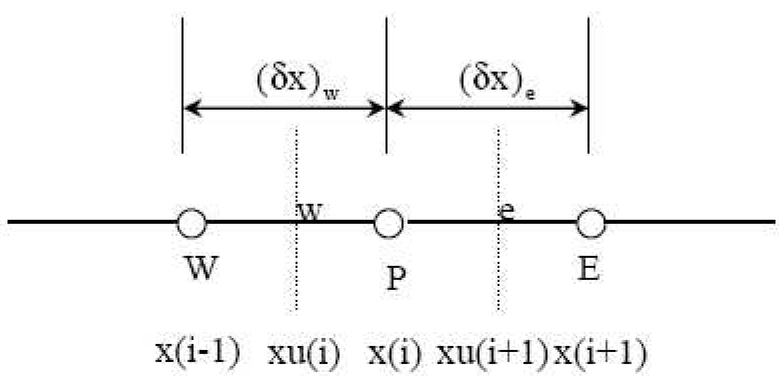

Fig. 3.6: Scalar control volume

According to Fig. 3.6, the heat flux at the interface 'e' can be expressed as:[63]

$$q_e = \frac{k_e(T_P - T_E)}{(\delta x)_e} = \frac{\Gamma_e(h_P - h_E)}{(\delta x)_e} = \frac{\Gamma_e(h(i) - h(i+1))}{x(i+1) - x(i)} \tag{3.58}$$

A stepwise profile assumption is used (shown in Fig. 3.7) to describe the value of the diffusion coefficient in a control volume. In order to maintain the heat flux continuity at the interface, we have:[63]

$$q_e = \frac{\Gamma_P(h_P - h_e)}{(\delta x)_{Pe}} = \frac{\Gamma_E(h_e - h_E)}{(\delta x)_{eE}} \tag{3.59}$$

$$h_e = \frac{(\delta x)_{eE}\Gamma_P h_P + (\delta x)_{Pe}\Gamma_E h_E}{(\delta x)_{Pe}\Gamma_E + (\delta x)_{eE}\Gamma_P} \tag{3.60}$$

Then substituting equation (3.60) into equation (3.59), we have:

$$q_e = \frac{h_P - h_E}{\frac{(\delta x)_{Pe}}{\Gamma_P} + \frac{(\delta x)_{eE}}{\Gamma_E}} = \frac{h(i) - h(i+1)}{\frac{xu(i+1) - x(i)}{\Gamma(i)} + \frac{x(i+1) - xu(i+1)}{\Gamma(i+1)}} \tag{3.61}$$

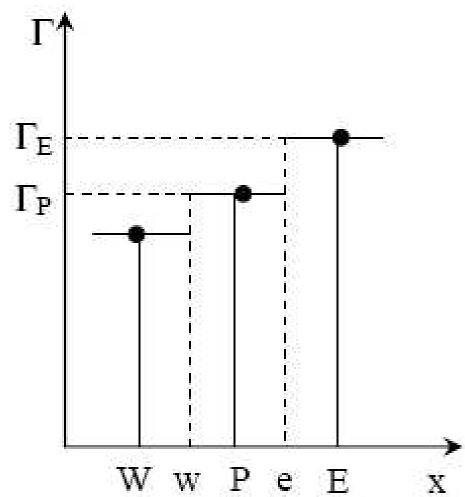

Fig. 3.7: Stepwise profile assumption for Γ

According to equation (3.58) and equation (3.61), we can have:

$$\Gamma_e = \frac{\Gamma(i)\Gamma(i+1)}{h_E(xu(i+1)-x(i)) + h_P(x(i+1)-xu(i+1))}(x(i+1)-x(i))$$

$$= \frac{\Gamma(i)\Gamma(i+1)}{fracx(i)\Gamma(i) + (1-fracx(i))\Gamma(i+1)} \tag{3.62}$$

$$\text{where } fracx(i) = \frac{x(i+1)-xu(i+1)}{x(i+1)-x(i)} \tag{3.63}$$

3.2.6.5 Calculation of boundary conditions for enthalpy

The enthalpy-temperature relationship to calculate the latent heat content (liquid fraction) is shown by Fig. 3.8.

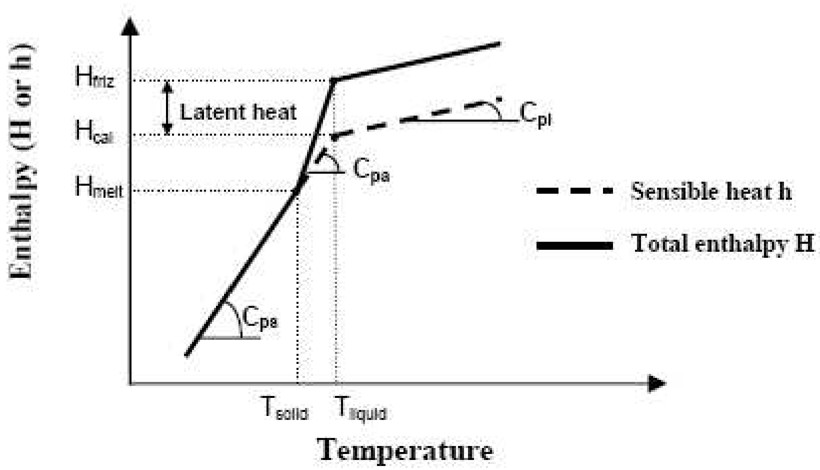

Fig. 3.8: Plot of enthalpy as a function of temperature

The specific heat in the mushy zone is calculated by $C_{pa} = (C_{ps} + C_{pl}) / 2$. H_{cal} is given as: $H_{cal} = H_{melt} + C_{pa} (T_{liquid} - T_{solid})$ and the latent heat is defined as: $L = H_{friz} - H_{cal}$. The heat exchange between the heat source and the surface of the sample is given by a Gaussian distribution:[42]

$$H_{input} = \frac{f_l Q \eta_l}{\pi r_l^2} \exp\left(-\frac{f_l (x_l^2 + y^2)}{r_l^2} \right) + \frac{f_a IV \eta_a}{\pi r_a^2} \left(\frac{f_a (x_a^2 + y^2)}{r_a^2} \right) \tag{3.64}$$

where f_l and f_a are the power distribution factors for the laser and arc, respectively, (0.5 for arc and 3 for laser welding), x_l and x_a are the distances along the x axis from the heat sources, y is the distance along the y axis from the heat sources, r_l and r_a are the radii for the laser beam and arc, respectively, Q the laser power in watts, I is the arc current in ampere, V is the arc voltage in volts, and η_l and η_a are the laser absorption coefficient and arc efficiency, respectively.

Total heat flux on top surface is $(q_{in} - q_{out}) = F_1 + F_2 + F_3$ where F_1 is the input heat flux, F_2 is the radiation heat loss, and F_3 is the convective heat loss. In the present application, the heat flux is taken as a source term:

$$F_1 + F_2 + F_3 = su + sp*T \tag{3.65}$$

where su = su1 + su2 + su3 and sp = sp1 + sp2 + sp3. F_1 is initialized to be zero, and is determined further by successive iterations using equation (3.64). F_2 is given by:

$$F_2 = -\sigma\varepsilon\left(T_w^4 - T_a^4\right) \tag{3.66}$$

where σ is the Stefan-Boltzmann constant (5.670×10^{-12} J K^{-4} cm^{-2} s^{-1}), ε is the emissivity (0.5~0.9 for steels), T_w is the wall temperature in K, and T_a is the ambient temperature.

The relationship between temperature and enthalpy is given by:

$$T_w = \begin{cases} T_{solid} + \dfrac{h - H_{melt}}{C_{ps}} & \text{for } h \le H_{melt} \\ T_{solid} + \dfrac{h - H_{melt}}{C_{pa}} & \text{for } H_{melt} \le h \le H_{cal} \\ T_{liquid} + \dfrac{h - H_{cal}}{C_{pl}} & \text{for } h \ge H_{cal} \end{cases} \tag{3.67}$$

Upon substituting equation (3.67) into (3.66):

$$F_2 = \varepsilon\sigma t_a^4 - \frac{\varepsilon\sigma}{C_p^4}(A+h)^4 \tag{3.68}$$

Here,

$$\begin{cases} A = C_p T_{solid} + H_{melt} & C_p = C_{ps} \quad \text{for } h \le H_{melt} \\ A = C_p T_{solid} + H_{melt} & C_p = C_{pa} \quad \text{for } H_{melt} \le h \le H_{cal} \\ A = C_p T_{liquid} + H_{melt} & C_p = C_{pl} \quad \text{for } h \ge H_{cal} \end{cases}$$

The flux is dependent on the variable h. It can be linearized as:

$$S = S^* + \left(\frac{dS}{dh}\right)^* \left(h - h^*\right) = S^* - \left(\frac{dS}{dh}\right)^* h^* + \left(\frac{dS}{dh}\right)^* h = su + (sp)h$$

The variable h^* is the guess value or the previous iteration value of h. Using this methodology we have:

$$su2 = \sigma\varepsilon(T_a)^4 - \frac{\varepsilon\sigma}{C_p^4}(A+h^*)^4 + \frac{4\sigma\varepsilon}{C_p^4}(A+h^*)^3 h^* \tag{3.69}$$

$$sp2 = -\frac{4\sigma\varepsilon}{C_p^4}(A+h^*)^3 \tag{3.70}$$

Here, the variables A and C_p have the same values as in equation (3.68). Convective heat loss (F_3) is given by:

$$F_3 = -h_c(T_w - T_a) = h_c(T_a - T_w) \tag{3.71}$$

where h_c is the heat transfer coefficient. Substituting (3.67) into (3.71):

$$F_3 = \begin{cases} h_c\left(\frac{H_{melt}}{C_{ps}} - T_{solid}\right) - \frac{h_c}{C_{ps}h} & \text{for } h \le H_{melt} \\ T_{solid} + \frac{h - H_{melt}}{C_{pa}} & \text{for } H_{melt} \le h \le H_{cal} \\ T_{liquid} + \frac{h - H_{cal}}{C_{pl}} & \text{for } h \ge H_{cal} \end{cases} \tag{3.72}$$

From equation (3.72) we get su3 and sp3:

$$\begin{cases} A = C_p T_{solid} + H_{melt} & C_p = C_{ps} \quad \text{for } h \le H_{melt} \\ A = C_p T_{solid} + H_{melt} & C_p = C_{pa} \quad \text{for } H_{melt} \le h \le H_{cal} \\ A = C_p T_{liquid} + H_{melt} & C_p = C_{pl} \quad \text{for } h \ge H_{cal} \end{cases}$$

3.2.6.6 Three dimensional fluid flow and heat transfer

3.2.6.6.1 Governing equations

In order to determine how the velocity and temperature change with respect to position in the weld pool due to the effects of the Marangoni force, Lorentz force, Buoyancy, arc pressure and plasma flow, the following equations of change are evaluated by the code:

1. Mass conservation or continuity equation
2. Momentum conservation or Navier-Stokes equation
3. Energy conservation equation

Fig. 3.9 shows a schematic diagram of the weld pool with the liquid metal circulating. The vectors represent the velocity fields inside the weld pool. We take a small volume element ($\Delta x \Delta y \Delta z$) inside the weld pool and use it to derive the above equations of change.

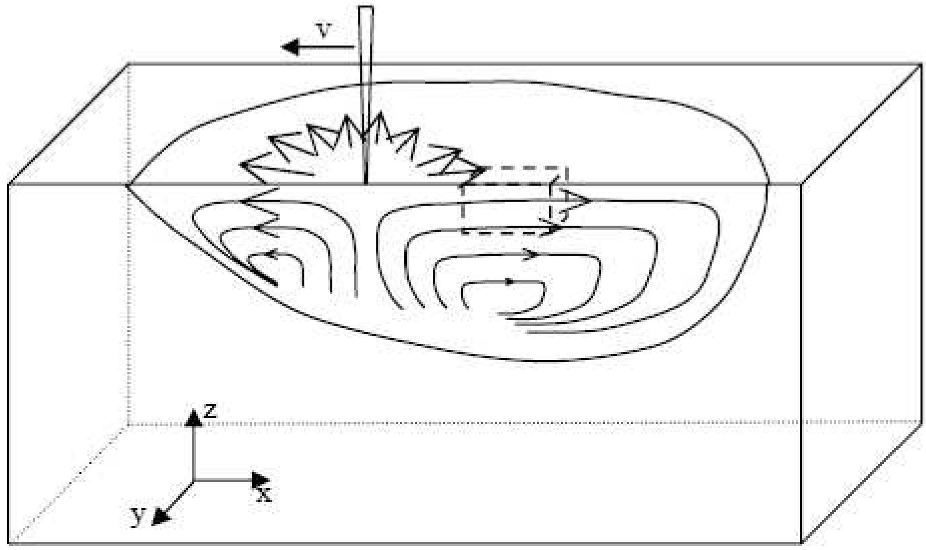

Fig. 3.9: Schematic of control volume in liquid weld pool used for calculating equations of change

The mass conservation equation is developed by writing a mass balance over the stationary volume element ($\Delta x \Delta y \Delta z$) shown above through which the fluid is flowing. Basically:

$$\begin{Bmatrix} \text{rate of mass} \\ \text{accumulation} \end{Bmatrix} = \{\text{rate of mass in}\} - \{\text{rate of mass out}\} \tag{3.73}$$

Fig. 3.10 lists the mass fluxes entering and leaving the system in the x-direction. The fluxes in the other two directions are analogous.

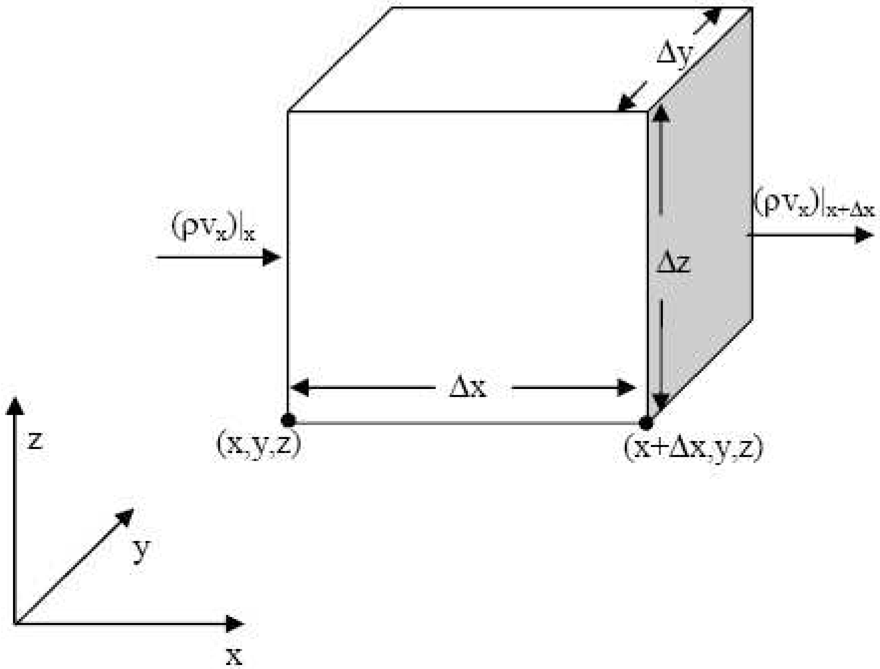

Fig. 3.10: Mass fluxes entering and leaving control volume in the x-direction.

Considering first the pair of faces perpendicular to the x-axis as shown in Fig. 3.10. The rate of mass in through the face at x is $(\rho v_x)\big|_x \Delta y \Delta z$. The rate of mass out through the face at x +Δx is $(\rho v_x)\big|_{x+\Delta x} \Delta y \Delta z$. Similar expressions can be written for the y and z directions. The rate of mass accumulation within the volume element is $\Delta x \Delta y \Delta z (\partial \rho / \partial t)$. Using equation (54) the mass balance can be written as:

$$\begin{aligned}\Delta x \Delta y \Delta z \frac{\partial \rho}{\partial t} = \Delta y \Delta z \left[(\rho v_x)\big|_x - (\rho v_x)\big|_{x+\Delta x} \right] + \Delta x \Delta z \left[(\rho v_y)\big|_y - (\rho v_y)\big|_{y+\Delta y} \right] \\ + \Delta x \Delta y \left[(\rho v_z)\big|_z - (\rho v_z)\big|_{z+\Delta z} \right]\end{aligned} \tag{3.74}$$

Dividing equation (3.74) by (ΔxΔyΔz) and taking the limit as these dimensions approach zero, we get the differential form of the continuity equation as:[64]

$$\frac{\partial \rho}{\partial t} = -\left(\frac{\partial}{\partial x} \rho v_x + \frac{\partial}{\partial y} \rho v_y + \frac{\partial}{\partial z} \rho v_z \right) \tag{3.75}$$

where, ρ is density of the liquid at a point (x,y,z) (g/cm^3), v_x is the instantaneous velocity in the x-direction at (x,y,z) (cm/s), v_y is the instantaneous velocity in the y-direction at (x,y,z) (cm/s), v_z is the instantaneous velocity in the z-direction at (x,y,z) (cm/s), and t is time (s). This equation states that the rate of increase of the density within a small volume element fixed in space is equal to the net rate of mass influx to the element divided by its volume.

For an incompressible fluid i.e. a fluid of constant density (ρ) the time derivative of density i.e. $\partial\rho/\partial t$ becomes zero and the continuity equation reduces to:[64]

$$\nabla \cdot \mathrm{v} = 0 \tag{3.76}$$

This is the continuity equation used in the heat transfer and fluid flow code. There is one discrepancy through, i.e. when calculating buoyancy force we do not consider density as a constant. However, for this discrepancy, Boussinesq has stated that a physical quantity can be taken as constant in one equation and variable in another so long as it does not cause any significant variation in the observed results.

Considering the same volume element as above, the momentum balance can be written as:

$$\begin{Bmatrix}\text{rate of}\\ \text{momentum}\\ \text{accumulation}\end{Bmatrix} = \begin{Bmatrix}\text{rate of}\\ \text{momentum}\\ \text{in}\end{Bmatrix} - \begin{Bmatrix}\text{rate of}\\ \text{momentum}\\ \text{out}\end{Bmatrix} + \begin{Bmatrix}\text{sum of forces}\\ \text{acting on}\\ \text{the system}\end{Bmatrix} \tag{3.77}$$

Momentum flows in and out of the volume by two mechanisms: (i) by convection (i.e. by virtue of the bulk fluid flow) and (ii) by molecular transfer or diffusion (i.e. by virtue of the velocity gradient). The forces acting on the volume element include: (i) pressure forces acting on the surface and (ii) gravity forces acting on the volume as a whole.

When using the Navier-Stokes equation for the calculation of fluid flow in the weld pool we assume an incompressible fluid and Newtonian flow. Incompressible fluid implies the density is assumed constant. Newtonian flow implies that the momentum flux is proportional to the negative of the local velocity gradient. The x-component of the momentum conservation equation can be written as:[41-42]

$$\rho\frac{\partial \mathrm{v}_x}{\partial t} = -\rho\frac{\partial}{\partial x_i}(\mathrm{v}_i \mathrm{v}_x) + \frac{\partial}{\partial x_i}\left(\mu\frac{\partial \mathrm{v}_x}{\partial x_i}\right) - \frac{\partial p}{\partial x} + S_x \tag{3.78}$$

where ρ is the density of the fluid (g cm^{-3}), μ is viscosity of the fluid (g cm^{-1} s^{-1}), p is the fluid pressure on the surface of the volume element (g cm^{-1} s^{-2}), S_x is the source term which includes all effects that are not included in the other terms, such as buoyancy force, electromagnetic force, the gravitational force, and Marangoni stress, v_i and x_i represent velocity and distance along the "i" direction where i = x, y, z. Hence the terms having these actually represent a sum of three terms; for example:

$$\frac{\partial v_x}{\partial x_i} = \frac{\partial v_x}{\partial x} + \frac{\partial v_x}{\partial y} + \frac{\partial v_x}{\partial z} \tag{3.79}$$

In the case of Gas Tungsten Arc (GTA) welding if we fix our reference frame to the heat source then the problem becomes one of pseudo-steady state. Hence the time derivative terms vanishes i.e.:

$$\rho \frac{\partial v_x}{\partial t} = 0 \tag{3.80}$$

Considering the same volume element as above, the energy balance can be written as:

$$\begin{Bmatrix} \text{rate of} \\ \text{accumulation} \\ \text{of energy} \end{Bmatrix} = \begin{Bmatrix} \text{rate of} \\ \text{energy in by} \\ \text{convection} \end{Bmatrix} - \begin{Bmatrix} \text{rate of} \\ \text{energy out by} \\ \text{convection} \end{Bmatrix} + \begin{Bmatrix} \text{net rate of} \\ \text{heat addition} \\ \text{by conduction} \end{Bmatrix} - \begin{Bmatrix} \text{net rate of work} \\ \text{done by system} \\ \text{on surroundings} \end{Bmatrix} \tag{3.81}$$

The equation for the calculation of heat transfer in the weld pool for incompressible fluid flow can be written as:[41-42]

$$\rho \hat{C}_p \frac{\partial T}{\partial t} = -\rho \hat{C}_p \frac{\partial}{\partial x_i}(v_i T) + \frac{\partial}{\partial x_i}\left(k \frac{\partial T}{\partial x_i} \right) + S \tag{3.82}$$

where S is the source term which includes all effects that are not included in the other terms, such as the work done on the fluid per unit volume by the gravitational forces, pressure forces, viscous forces and electromagnetic forces, $\hat{C}_p$ is the specific heat of fluid at constant pressure (cal g^{-1} K^{-1}), T is the local temperature (K), k is the thermal conductivity of the fluid (cal s^{-1} cm^{-1} K^{-1}).

3.2.6.7 Boundary conditions

For a steady state problem initial conditions are not needed. The calculation domain is shown by Fig. 3.11.

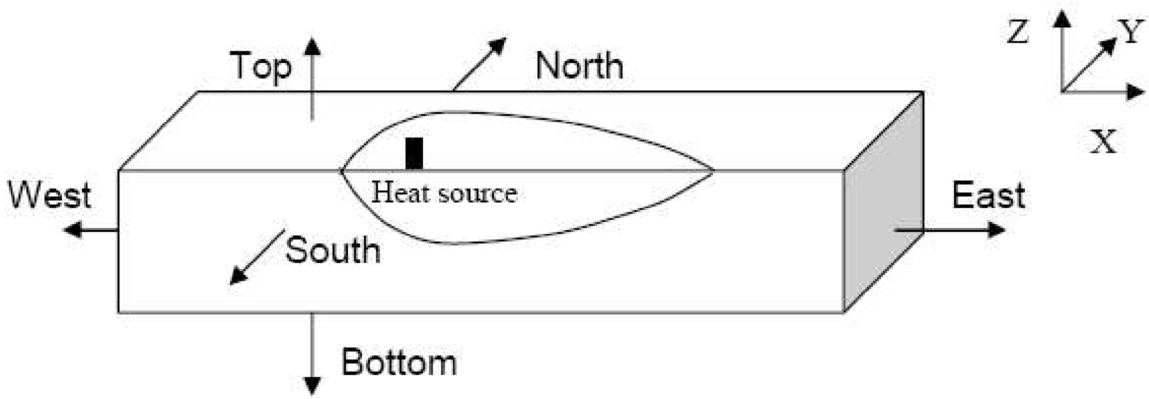

Fig. 3.11: Boundary conditions and calculation domain

3.2.6.7.1 Top surface

Net heat flux, F, is given by the following equation:

$$F = F_i + F_r + F_c + F_o \tag{3.83}$$

where F_i is the input heat flux, F_r is the radiation heat loss, F_c is the convective heat loss, and F_o is the other heat loss such as evaporative heat loss.

3.2.6.7.1.1 Input heat flux

The heat transfer from the heat source, such as arc and laser, to the workpiece is a very complicated physical phenomenon. Although some experimental and theoretical works have been carried out, this process has not been well understood to date. In the literature, a Gaussian distribution function has been widely used to approximate the heat flux from the heat source:[41-42]

$$F_i = \frac{f_l Q \eta_l}{\pi r_l^2} \exp\left(-\frac{f_l (x_l^2 + y^2)}{r_l^2} \right) + \frac{f_a I V \eta_a}{\pi r_a^2} \left(\frac{f_a (x_a^2 + y^2)}{r_a^2} \right) \qquad (3.84)$$

where f_l and f_a are the power distribution factors for the laser and arc, respectively, x_l and x_a are the distances along the x axis from the heat sources, y is the distance along the y axis from the heat sources, r_l and r_a are the radii for the laser beam and arc, respectively, Q the laser power in watts, I is the arc current in ampere, V is the arc voltage in volts, and η_l and η_a are the laser absorption coefficient and arc efficiency, respectively, where f_h is the distribution factor, Q is the total energy of the heat source, η is the energy efficiency, r_b is the heat source distribution parameter, and x and y are distances from the center of the heat source. Some typical values of arc efficiency, laser and arc power distribution factors, and arc radius (r_b in table) are summarized in Table 3.2.

Table 3.2: Typical values of arc efficiency, laser and arc power distribution factors, and arc radius

f_h	0.5 for arc [1]; 3.0 for laser conduction mode [2]
η	0.25 ~ 0.75 for GTA welding of Steel (Ar as shielding gas) [3]
r_b	Arc welding: 1.5 ~ 3.6 mm depending on the arc length, arc current and electrode tip angle.

It should be recognized that equation (3.84) is only valid under certain conditions for arc welding. For example, the electrode angle should be perpendicular to the workpiece, the arc length should be neither too small nor too large, and the electrode tip angle should be in a certain range (Tsai and Eager, 1985). When the electrode is inclined to the workpiece, equation (3.84) requires modification to reasonably approximate the heat flux distribution. The Gaussian distribution can approximate the heat flux from the heat source very well under most conditions. However, careful consideration of the nature of the heat source is still required.

3.2.6.7.1.2 Radiation heat loss

The radiation heat flux is given as:

$$F_r = -\sigma\varepsilon(T^4 - T_o^4) \tag{3.85}$$

where σ is the Stefan-Boltzmann constant (5.670×10^{-12} J K ^{4} cm^{-2} s^{-1}), ε is the emissivity (0.5~0.9 for steels), T is the wall temperature in K, and T_o is the ambient temperature. The following is a calculation of the radiation heat loss during welding in order to provide an example as to the order of magnitude of the radiation heat loss as compared to the heat input from an electrical arc. Arc current = 100A, arc voltage = 18V, η = 0.7, surface area = 0.5 cm x 0.5 cm, σ = 5.670×10^{-12} J K ^{4} cm^{-2} s^{-1}, ε = 0.9, T = 2000 K, T_o = 300 K. After substituting these values into equation (3.85), the total energy loss due to surface radiation is about 17.2 J s^{-1} (the heat input from the arc is about 1.26×10^3 J s^{-1}).

3.2.6.7.1.3 Convective heat loss

The convective heat flux is given by the following empirical equation:

$$F_c = -h_c(T - T_o) \tag{3.86}$$

where h_c is the heat transfer coefficient. On the weld top surface, the heat transfer coefficient can be estimated using the approximation of a gas jet impinging on a surface by Schlunder and Gniclinski. Schuhmann also formulated the methods of evaluating h_c for some most common types of natural and forced convection. For example, the heat transfer coefficient is approximated by the following equation for large plane surfaces:

$$h_c = C'(\Delta T)^{0.25} \tag{3.87}$$

where ΔT is the difference between the surface temperature and the bulk fluid temperature, C' = 0.38 for horizontal plates facing upward, C' = 0.2 for horizontal plates facing downward, C' = 0.27 fro vertical plates. The following is a calculation of the convective heat loss during welding in order to provide an example as to the order of magnitude of the convective heat loss as compared to the heat input from an electrical arc. Arc current = 100A, arc voltage = 18V, η = 0.7, surface area = 0.5cm x 0.5cm, h_c = 3.0 x 10^{-3} J K^{-1} cm^{-2} s^{-1}, T = 2000 K, T_o = 300 K. After substituting these values into equation (3.87), the convective energy loss is about 1.3 J s^{-1} (the heat input from the arc is about 1.26 x 10^3 J s^{-1}).

3.2.6.7.1.4 Evaporative heat loss

The evaporative heat loss is given by:

$$F_v = -\sum_i J_i \Delta H_i \tag{3.88}$$

where J_i and ΔH_i are the vaporization flux and the enthalpy of vaporization of the element I, respectively. Both the pressure and concentration gradient contribute to the vaporization flux. The details of the calculation are available in Mundra and Debroy, 1993. It was found that the evaporative heat loss could significantly reduce the temperatures on the pool surface under high energy input conditions. However, when the peak temperature on the pool surface is much lower than the boiling temperature, the evaporative heat loss can be ignored. The heat loss by radiation, convection, and evaporation is negligible when the surface temperature is not very high.

The heat flux and velocity boundary conditions for all surfaces are shown in the following schematic.

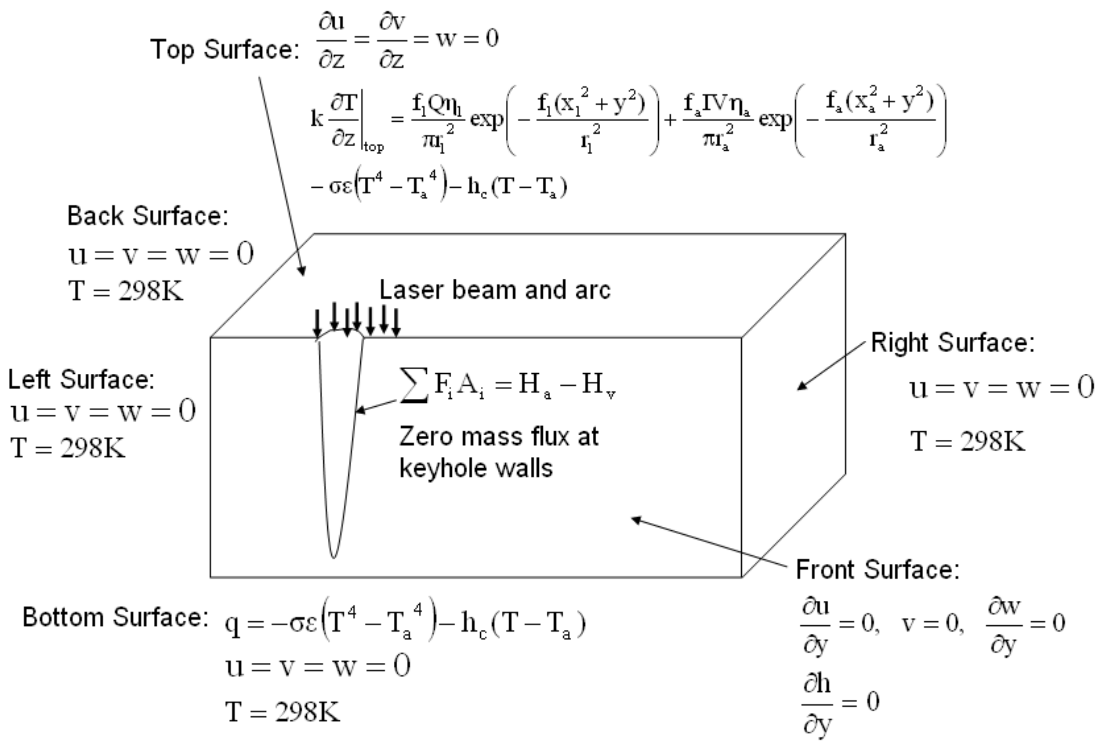

Fig. 3.12: Schematic of the boundary conditions of the weld pool

3.2.6.8 Solution methodology

The governing equations are discretized using the control volume technique where the workpiece is divided into small rectangular volumes. The scalar variable is stored on the grid point which is located inside the control volume. The grid points for storing the vectors like the velocities in the x, y and z direction are staggered with respect to the scalar grid points to ensure stability. The discretized equations are formulated using the fully implicit power law technique. The final discretized equation at a grid point "P" takes the following form:[63]

$$a_P \phi_P = \sum_{nb} (a_{nb}\phi_{nb}) + a_P^o \phi_P^0 + S_U \Delta V \tag{3.89}$$

where, ϕ represents a general variable such as velocity or enthalpy, "a" represents the coefficient of the variables calculated based on the power law scheme, subscript nb represents the neighbors of the grid point P, ΔV is the volume of the control volume, a_P^o

and ϕ_P^o are the coefficient and value of the general variable at the concerned grid point P at the previous time step, respectively. The coefficient of ϕ at the point P is defined in terms of neighboring grid points as follows:[63]

$$a_P = \sum_{nb} a_{nb} + a_P^o - S_P \Delta V \tag{3.90}$$

The terms SU and SP are the coefficients of the linearized source term, defined as:[63]

$$S = S_U + S_P \phi \tag{3.91}$$

3.2.7 Convergence criteria

The convergence is achieved when the residuals of enthalpy, mass, and u, v, and w velocities are less than 5 x 10^{-4} and the ratio between the heat input and out going from the workpiece is between 0.99 and 1.02.

3.2.8 Remarks about the Code

The various files which compose the code are:

1. Input.for - Provides the data required for the program.
2. Keyhole.f – Calculates the keyhole geometry using the various material process parameter and numerical scheme inputs
3. Emf.for - Calculates emf field
4. Coeff.for - Calculates the coefficients of the discretized equations
5. Modify.for - Incorporates special source terms and modifies the coefficients of the discretized equations
6. Correct.for - Performs pressure and velocity corrections
7. Solve.for - Solves the set of linear algebraic equations arising out of discretization
8. Residual.for - Calculates the residual
9. Convert.for - Converts enthalpy to temperature
10. Poolsize.for - Calculates the dimensions of the weld pool
11. Fluxes.for - Calculates the surface fluxes

12. Block_corr.for - Corrects near-boundary enthalpy values to maintain the overall heat balance for steady state calculations

13. Pressure.for-Calculates the partial pressures of the keyhole pressure balance and local keyhole wall temperatures

14. Keyhole.f- Calculates the keyhole geometry laser power per unit depth.

15. Header.for - Contains all global variables for the code

16. Matselect.for- The database of material thermophysical properties and default values.

17. User.for – contains iterative loop of code and majority of subroutines. The following are a list of those subroutines:

1.geom- Generates the grid, calculates area, volume and interpolation distances

2. tbarray – Stores keyhole wall temperatures in an array for the determination of keyhole wall enthalpies

3. keyTcalc- Calculation of temperature for entire workpiece based on line source strength in heat transfer and fluid flow domain

4. initialize_new - Initializes the variables.

5. heatbal- Write the output heatbal.txt

6. heatin_kw_zw – Calculates fluxes along keyhole wall

7. keyadj – Adjusts laser power per unit depth according to the adjustment of keyhole surface area

8. props - Updates the physical properties

9. enhance - enhances liquid metal thermal conductivity and viscosity using Prandtl mixing length hypothesis (turbulence model)

10. cleanuvw - makes liquid metal velocities zero in the solid

11. geometry- calculates two-dimensional superimposed weld cross section for output file geometry.dat.

3.3 Experimental procedure

3.3.1 Role of laser-arc spacing on weld geometry and cooling rate

CO_2 laser/GTA hybrid welding with the laser leading was performed by Chen et al[13] on 4 mm thick AISI 321 stainless steel. The chemistry of the material was taken from standard commercial values given in Table 3.3. During the hybrid welding experiments, the distance between the arc electrode and laser beam was varied. The experiment was repeated for three arc current levels with the laser at sharp focus. The laser beam radius, welding velocity, and laser power were 100 μm, 16.7 mm s^{-1} (1 m min^{-1}), and 900 W, respectively. The arc voltage was 14 V and various arc currents were used including: 60, 120, and 180 A. The arc length and angle relative to the workpiece surface were 5.0 mm and 70^o, respectively. The arc was tilted backwards relative to the laser head, i.e. 30^o relative to the normal. The separation distance between the heat sources was varied from 3.5 mm to approximately 9.2 mm. The photographic results of Chen et al. showed that for a 60 A arc, the arc and laser formed two separate plasma plumes at different locations on the welded surface when the distance of separation between the two sources was greater than a critical value of 6.5 mm. However, the published observations did not include the critical distance for the 120 and 180 A cases. It was assumed that the heat sources acted at the same location for the 120 and 180 A cases for all of the separation distances studied.

Table 3.3: Chemical composition of the AISI 321 stainless steel

Element	C	Cr	Mn	Mo	Ni	Fe	P	S	Ti	Si
Amount (wt%)	0.08	18.0	2.0	1.0	11.0	66.0	-	-	0.5	1.0

3.3.2 Role of laser power on weld pool geometry and fluid flow

Bead-on-plate Nd:YAG laser/GTAW hybrid, laser, and arc welding were performed on 10 mm thick A131 structural steel at 8.5 mm s^{-1}. Table 3.4 shows the chemical composition of the A131 structural steel samples determined using atomic emission spectroscopy. The separation distance between the heat sources was 3.0 mm.

The heat source separation distance was as small as possible to ensure an interaction between the heat sources. The laser and hybrid welding laser power levels were 800, 1900, 3800, and 4500 W with a 12% loss in power assumed due to the laser optics and delivery.[41, 65] The laser was at sharp focus and had a beam radius of 250 μm. The GTAW voltage and current were 11 V and 191 A, respectively. The arc electrode symmetry axis was at a 45^{o} angle relative to the workpiece surface and the distance between the electrode tip and workpiece surface was 1.5 mm. Table 3.5 shows the measured arc current and voltages for the various hybrid welding cases. The laser power was varied in order to systematically understand the influence of the laser power on hybrid welding temperature and fluid flow profiles for a relatively constant arc power and heat source separation distance. Three weld cross sections were analyzed for each laser power and compared to the calculated weld results. The material properties used in order to complete the welding calculations for AISI 321 stainless and A131 structural steels are given in Table 3.6.

Table 3.4: Chemical composition of the A131 structural steel

Element	**C**	**Cr**	**Cu**	**Mn**	**Mo**	**Ni**	**P**	**S**	**Ti**	**V**
Amount (wt%)	0.06	0.02	0.02	1.38	0.01	0.02	0.01	0.004	0.02	0.05

Table 3.5: Measured hybrid welding arc current and voltage values and their corresponding laser power levels for hybrid welding of A131 structural steel. The arc current and voltage were not constant for the various hybrid welding cases.

Weld Type	**Welding Velocity (mm s^{-1})**	**Arc Voltage (V)**	**Arc Current (A)**	**Laser Power (W)**
Hybrid	8.47	12.3	190	4500
		10.3	191	3800
		20	185	1900
		11	191	800

Table 3.6: Material properties used in welding calculations for AISI 321 stainless and A131 structural steels.

Property	A131 Structural Steel	AISI 321 Stainless Steel
Density (kg m^{-3})	7000	7000
Solidus[48] Temperature (K)	1745	1673
Liquidus[48] Temperature (K)	1785	1723
Enthalpy[48] of Solid at Melting Point (J kg^{-1})	1.20×10^6	1.20×10^6
Enthalpy[48] of Liquid at Melting Point (J kg^{-1})	1.26×10^6	1.26×10^6
Specific[48] Heat of Solid (J kg^{-1} K^{-1})	711.62	711.62
Specific Heat of Liquid (J kg^{-1} K^{-1})	795.34	795.34
Thermal[48, 66] Conductivity of Solid (J m^{-1} K^{-1} s^{-1})	29.3	20.9
Thermal[48, 66] Conductivity of Liquid (J m^{-1} K^{-1} s^{-1})	29.3	29.3
Coefficient[48, 66] of Thermal Expansion (K^{-1})	1.96×10^{-5}	1.96×10^{-5}
Emissivity	0	0
$d\gamma/dT$ of Pure[48, 66] Material (N m^{-1} K^{-1})	-0.00049	-0.00049
Concentration of Surface Active Species (wt%)	0.004	0.0
Surface Excess[53] at Saturation (mole m^{-2})	1.30×10^{-5}	1.30×10^{-5}
Enthalpy[53] of Segregation (J mol^{-1})	-1.66×10^5	-1.66×10^5
Entropy Factor[53]	0.00318	0.00318

3.3.3 Role of surface active elements on fluid flow and weld geometry

Yb doped fiber laser welding was performed on 20 mm thick mild steel at sharp focus. The laser power was 7 kW and the beam radius at the focal point was 200 μm. The laser beam characteristic wavelength was between 1070 and 1080 nm. The welding speed for all cases was 16.7 mm s^{-1}. The alloy sulfur content was specifically varied for the fiber laser welds to analyze the influence of sulfur on the heat transfer and fluid flow in the weld pool. The various base metal sulfur concentrations were 0.006 wt%, 0.015 wt%, 0.056 wt%, 0.077 wt%, 0.101 wt%, and 0.150 wt%. The chemical composition of the mild steel samples[42, 48, 67] is provided in Table 3.7. Various shielding gas compositions were also used for a constant concentration of sulfur in the base metal of 0.006 wt%. Three gases were mixed in a gas mixer where the flow rate of each gas was measured to 0.1 L min^{-1} accuracy. The gas composition was controlled by adjusting the flow rate of each gas. The shielding gas compositions were 61% He + Ar, 58% He + Ar + 5% O_2, 55% He + Ar + 10% O_2, and 52% He + Ar + 15% O_2 and the corresponding concentrations of oxygen in the weld metal were measured after welding. In addition, oxygen concentrations in the upper and lower halves of the weld bead were measured along the weld centerline. The measured oxygen concentrations in the lower half were[68] 0.0033 wt% (0% O_2), 0.0056 wt% (5% O_2), 0.0088 wt% (10% O_2), and 0.0157 wt% (15% O_2). The measured oxygen concentrations in the upper half were 0.0044 wt% (0% O_2), 0.0101 wt% (5% O_2), 0.0182 wt% (10% O_2), and 0.0358 wt% (15% O_2). The shielding gas flow rate was 0.42 L s^{-1}. The material properties[42, 48, 67] used for the welding calculations are presented in Table 3.8.

Table 3.7: Chemical composition of mild steel samples

Element	**C**	**Mn**	**Si**	**P**	**S**	**O**	**N**
wt%	0.16	1.46	0.35	0.016	0.006, 0.015, 0.056 0.077, 0.101, 0.15	0.001	0.0025

Table 3.8: Material properties for the mild steel used in the fiber laser welding calculations

Material	**Mild steel**
Density[37] of the liquid (kg m^{-3})	7000
Density[37] at the boiling point (kg m^{-3})	5800
Solidus[37] Temperature (K)	1745
Liquidus[37] Temperature (K)	1785
Enthalpy[37] of Solid at Melting Point (J kg^{-1})	1.20×10^6
Enthalpy[37] of Liquid at melting Point (J kg^{-1})	1.20×10^6
Specific Heat[37] of Solid (J kg^{-1} K^{-1})	711
Specific Heat[37] of Liquid (J kg^{-1} K^{-1})	795
Thermal[48] Conductivity (W m^{-1} K^{-1})	21
Coefficient[67] of Thermal Expansion (K^{-1})	1.30×10^{-5}
$d\gamma/dT$ of Pure Material[37] (N m^{-1} K^{-1})	-0.00049
Surface excess[37] at Saturation (mole m^{-2})	1.30×10^{-5}
Enthalpy[28] of Segregation (J mol^{-1})	-1.66×10^5
Entropy Factor[28]	0.00318

3.3.4 Data analysis

A single factor analysis of variance (ANOVA) was used to statistically evaluate if weld bead depth and width differed significantly with increasing concentrations of O_2 in the shielding gas and of sulfur in the base metal with 95% confidence for the fiber laser welding of the mild steel. Twenty weld pool depths and twenty widths were measured to examine the effect of oxygen. Weld pool depth is the distance from the weld fusion zone top surface to the bottom of the weld fusion zone at the centerline of the weld. Weld bead width is the distance between the left and right hand edges of the weld fusion zone at the weld bead top surface. Four cross sections were evaluated for each of the two highest levels of oxygen, and six cross sections each were examined for the other two levels. Thirty weld pool depths and thirty widths were examined to evaluate the effect of sulfur. Six cross sections each were evaluated for the lowest and two highest sulfur concentrations and four cross sections each for the other three levels.

The ANOVA assesses whether the expected values of a variable within several groups of observations differ from each other. For example, if the expected values of the weld depth differ statistically for various groups of oxygen concentrations, the weld depth is thought to vary with oxygen concentration and the calculated F statistic is greater than a critical value. The critical value is dependent upon the number of observations and concentration levels considered. The F statistic is a ratio of the between group variability and within group variability. When the F statistic is large and the within group variability is small, there is a correlation between the increasing surface active element concentration and the measured weld dimension. Correspondingly, the P value will be less than 5%. The P value asses the likelihood that a given surface active element concentration has no influence on the considered weld dimension. The details of the ANOVA calculation procedure are provided Appendix A.

3.4 Results and discussion

3.4.1 Role of laser-arc spacing on weld geometry and cooling rate

According to Chen et al.[13], when the separation distance between the heat sources was greater than 6.5 mm, two separate plasma plumes were observable for hybrid welding done with a 60 A arc. In this case, the welding performed was a tandem process. During tandem welding, the arc primarily acts as a post heat treatment, which significantly decreases the cooling rate of the weld pool material.

When the separation distance between the arc electrode tip and laser beam symmetry axis was less than 6.5 mm for the 60 A arc hybrid welding case, arc bending caused the heat sources to act at the same location. For an arc applied at 45^o relative to the welding surface and with a 1.5 mm arc length, data presented by Tsai and Eager[80] suggests the typical GTA arc radius should be 4.2 mm. In the case of the 120 A and 180 A arcs, the arc radii are 5.5 mm and 6.1 mm, respectively.

It was observed that for the range of laser-arc separation distances considered in these experiments, the calculated penetration depth did not change significantly when using the arc radius determined from the work of Tsai and Eager.[80] Hence, the arc radius was reduced in order to determine the effective radius necessary to achieve the reported experimental weld penetration. Table 3.9 shows the arc radii values necessary in order to calculate the experimental weld dimensions of Chen et al.[13] Calculations were done assuming that the arc radius decreases because of the laser-arc interaction. In order to achieve the experimentally observed weld pool depths, the arc radius was reduced to account for arc contraction. Table 3.9 shows that the arc radius decreases to a minimum value at an optimal separation distance. Further investigation is needed to understand how the separation distance affects the plasma interaction in hybrid welding.

For the case of 120 A and 180A arc current hybrid welding, the model calculated penetration depth obtained using the arc radii predicted from the results of Tsai and Eager[80] did not result in the penetration depth observed by Chen et. al., even when the laser and arc power density distribution symmetry axes were location at the same point on the workpiece surface. Therefore, it was assumed that the heat source plasmas interacted for all of the separation distances during the 120 and 180 A arc hybrid welds despite the increase in separation distance between the electrode and laser beam.

Table 3.9: Arc radii used in heat transfer and fluid flow simulations to achieve the measured results of Chen et al. when hybrid welding AISI 321 stainless steel.

Measured heat source separation (mm)	**Arc radius (mm) 60A arc**	**Arc radius (mm) 120A arc**	**Arc radius (mm) 180A arc**
3.5	0.39	0.55	0.6
4.6	0.32	0.5	0.49
5.4	0.39	0.38	0.47
6.5	0.39	0.47	0.44
7.6	4.16	0.43	0.38
8.2	4.16	0.52	0.44
9.2	4.16	0.52	0.45

Fig. 3.13 (a) shows the calculated hybrid weld pool depth as a function of the distance between the arc electrode and laser beam. Weld pool depth is measured as the distance from the weld fusion zone top surface to the bottom of the weld fusion zone at the centerline of the weld. The figure shows that the penetration increases slightly at an optimal separation distance. In addition, increasing the arc current causes a small increase in penetration depth of the weld pool. The experimental observations of Chen et al.[13] are shown in Fig. 3.13 (b). The average error between the experimental and calculated results was less than 5%.

Fig. 3.14 shows calculated weld pool velocity vectors (mm/s) and temperature (K) profiles for 900 W laser 60 A arc hybrid welds with two different separation distances, 3.5 mm and 7.6 mm. The welding direction is along the negative x-axis. Marangoni convection primarily dictates the fluid flow[41] and causes the weld pool to bulge towards the rear. The high energy density of the laser heat source results in the deep penetration of the weld pool. The maximum temperature experienced in the weld pools is 3100 K at the keyhole wall. When the separation distance is 3.5 mm, the arc and laser are acting at the same location. The arc in this case, although originally located 3.5 mm from the laser, is bending and rooting at the same location of the laser beam. This is accounted for in the model by moving the heat source location to the same location as the laser beam symmetry axis and reducing the effective radius of the arc power density distribution. The arc bending and contraction increases the penetration depth of the weld pool.

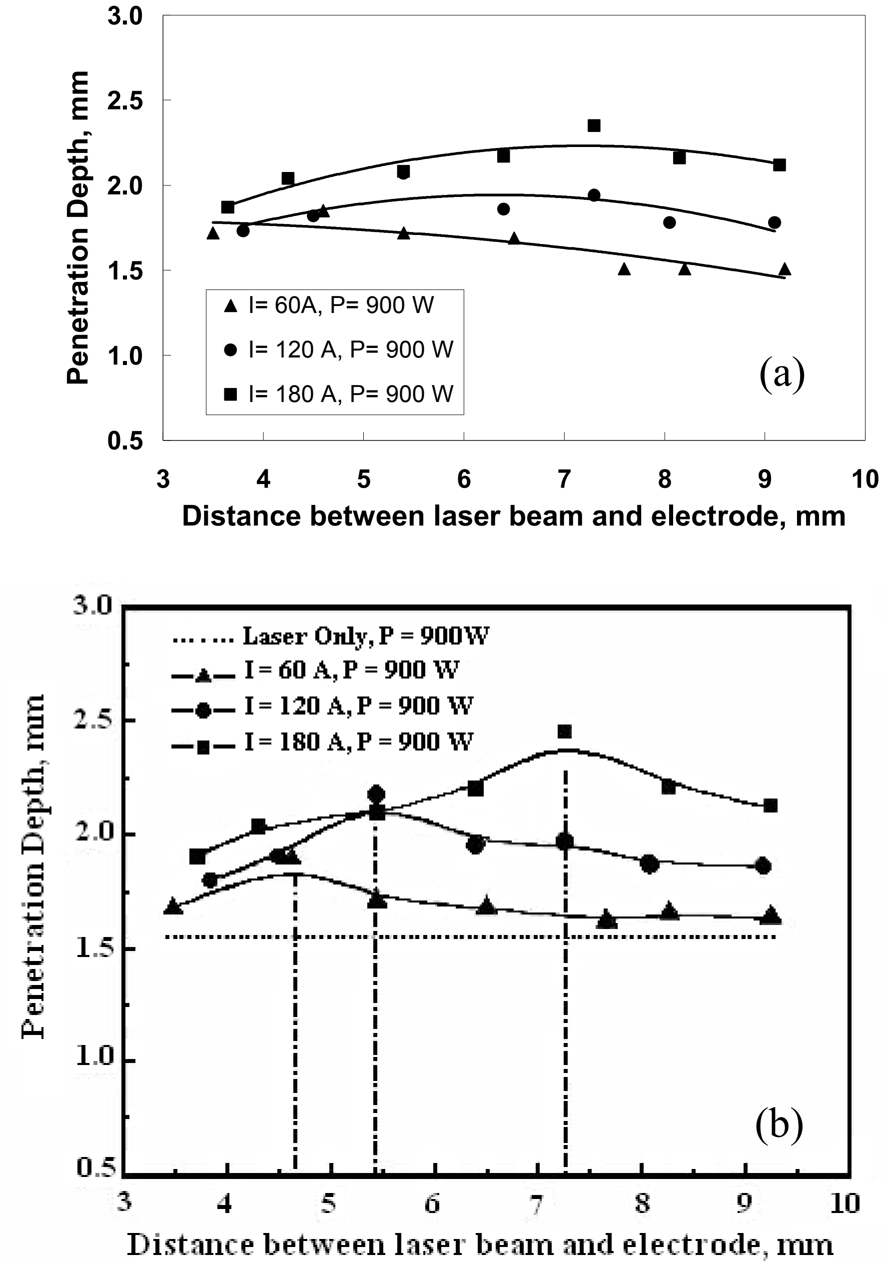

Fig. 3.13: Penetration depth of the hybrid welding of AISI 321 stainless steel samples as a function of the distance between the laser beam and arc electrode and the current of the arc heat source. The laser power level was 900 W for all welding cases. The welding velocity was 16.7 mm s^{-1} for all welds. The arc current levels were 60, 120, and 180 A. The dashed horizontal line is the penetration depth achieved by lone laser welding. The calculated result (a) and experimental measured result[13] (b) are both depicted.

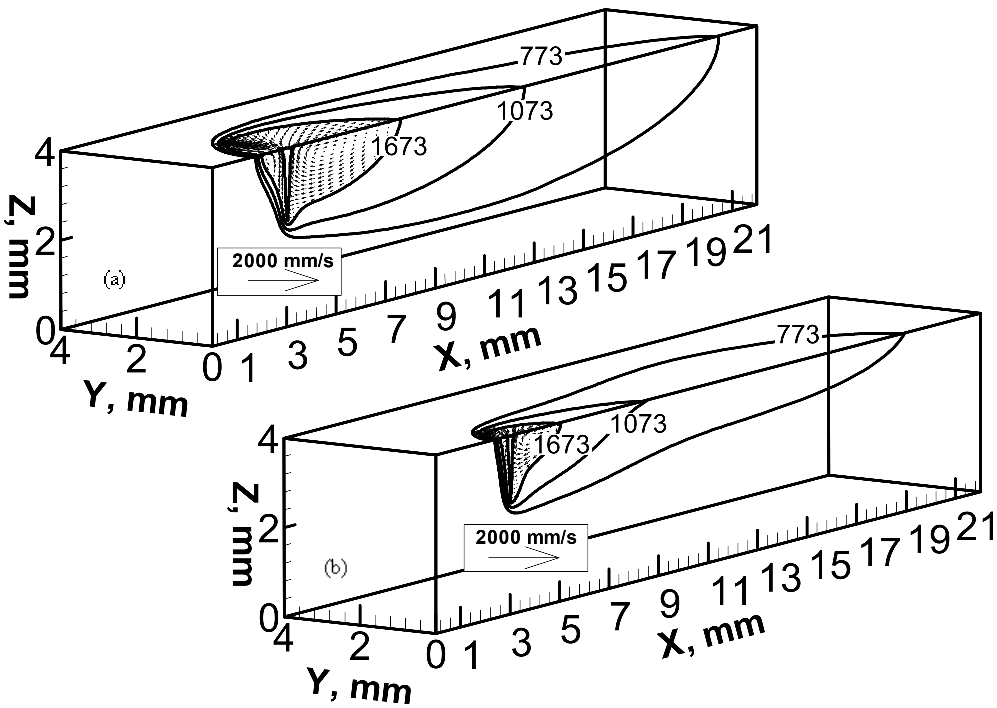

Fig. 3.14: Temperature and velocity profiles for hybrid welded AISI 321 stainless steel when the separation between the heat sources is (a) 3.5 mm and (b) 7.6 mm. All of the temperature values are in units of Kelvin. In figure 3.14 (a), the arc and laser are located at approximately x = 3 mm and in figure 3.2 (b) the laser is location at x = 3 mm and the arc is located at x = 10.6 mm.

Increasing the distance between the arc electrode and laser beam beyond a critical distance results in tandem welding. Fig. 3.14 (b) depicts a tandem weld with a laser-arc separation distance of 7.6 mm. The arc and laser are not interacting and are at two separate physical locations on the workpiece surface. Increasing the laser-arc separation distance distorts the 1073 K and 773 K isotherms. In addition, the interaction of the heat sources increases the melting efficiency of the hybrid welding process, which is made evident by the larger volume of molten metal generated in Fig. 3.14 (a). This result agrees with the work of Hu and Den Ouden,[15] which shows that hybrid welding results in increased melting efficiency over tandem welding.

The time to cool from 1073 K to 773 K (800 ^{0}C to 500 ^{0}C) and the cooling rate along the weld centerline can be calculated by dividing the distance between the two contours where they intersect the x-axis by the welding speed. The separation distance between the heat sources affects the shape and relative distance between isotherms.

When the separation distance increases from 3.5 mm to 7.6 mm, the cooling rate between 1073 K and 773 K along the weld centerline at the top surface decreases from approximately 617 K s^{-1} to 481 K s^{-1}. The cooling rate of the material was calculated by:

$$R = \frac{\Delta T}{\Delta x} v \tag{3.92}$$

where R is the cooling rate in K/s, ΔT is the temperature difference (300 K), Δx is the distance between the 1073 K and 773 K isotherms in millimeters, and v is the welding velocity in mm/s.

The time to cool from 1073 K to 773 K along the weld centerline as a function of the heat source separation distance for 60 A, 120 A, and 180 A arc current hybrid welds is shown in Fig. 3.15.

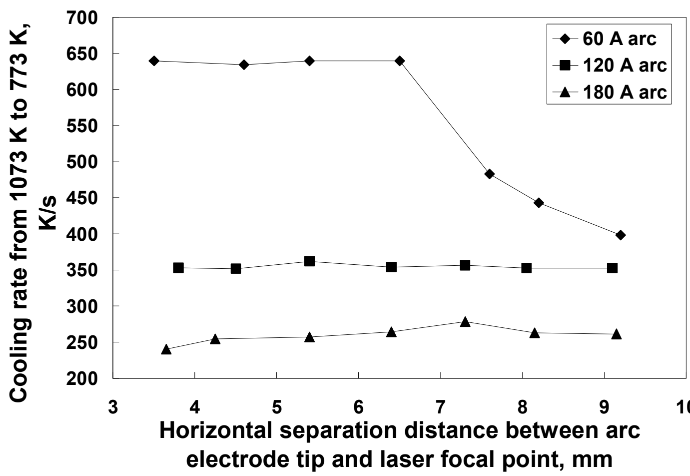

Fig. 3.15: Cooling rate from 1073 K to 773 K along the weld centerline as a function of the horizontal distance between the arc electrode tip and laser beam focal point for hybrid welded AISI 321 stainless steel using a 60, 120, and 180 A arc and 900 W laser beam.

Beyond the critical separation distance, the welding process becomes tandem, rather than hybrid when the arc current is 60 A. In this case, the arc acts as a post heat treatment process and deforms the 1073 K and 773 K isotherms. The arc radius increases significantly beyond the critical separation distance due to the lack of metal vapors entering the arc plasma, and the energy density of the arc decreases. Hence, the cooing rate decreases with increasing separation distance.

Since the heat sources interact throughout the range studied for the 120 A and 180 A arc currents, the welding process never changes from hybrid to tandem welding.

During the interaction of the heat sources, the arc and laser are assumed to act at the same location, and therefore there is no significant decrease in cooling rate. When the heat sources are interacting, the change in arc radius is not significant enough to drastically affect the heat input per unit length of the welding process or the cooling rate of the material for a constant arc current. However, increasing arc current significantly affects the cooing rate of the material. The decrease in cooling rate, when changing from 60 to 120 or 180 A, is due to an increase in heat input per unit length of the welding process.

3.4.2 Role of laser power on weld pool geometry and fluid flow

Laser, GTA, and hybrid bead-on-plate welds were performed on A131 structural steel with various laser power levels, while maintaining a constant heat source separation distance. The results of the experiments were modeled using the three-dimensional heat transfer and fluid flow model. Fig. 3.16 shows the experimentally observed weld cross-sections for laser (a), GTA (b), and hybrid (c) welds. The laser and hybrid welds were made using a 4.5 kW laser. A 191 A, 11 V arc was used in the case of the GTAW and 190 A, 12.3 V arc in the case of the hybrid weld. The welding velocity was 8.5 mm s^{-1}. The hybrid welding process results in a wider weld pool than laser or arc welding. However, there is minimal or no increase in weld pool depth in hybrid laser-arc welding over laser welding. The GTAW process results in much lower depth compared to laser or hybrid welds.

A comparison of GTA, laser, and hybrid weld depths (a) and widths (b) is presented in Fig. 3.17. The weld dimensions for GTAW are depicted as dashed horizontal lines on the graphs. The error bars in the figures represent the standard deviation of the measure weld depths and widths for the three cross sections of the welds analyzed. Laser weld depth and width standard deviation were 0.12 mm and 0.07 mm, respectively. Hybrid weld depth and width standard deviation were 0.13 mm and 0.17 mm, respectively. Fig. 3.17 (a) shows that the weld penetration depth is primarily a function of the laser power. The laser and hybrid welding processes offer deeper weld pool penetration than the GTAW process. However, the hybrid welding process does not result in a significant increase in weld pool penetration depth over lone laser welding. On the other hand, the hybrid welding process results in wider weld pools than lone laser or arc welding, as shown in fig. 3.17 (b). Weld bead width is measured as the distance between the left and right hand edges of the weld fusion zone at the weld bead top surface. Increased weld pool width is beneficial when attempting to bridge gaps present between welded sections and increases productivity.

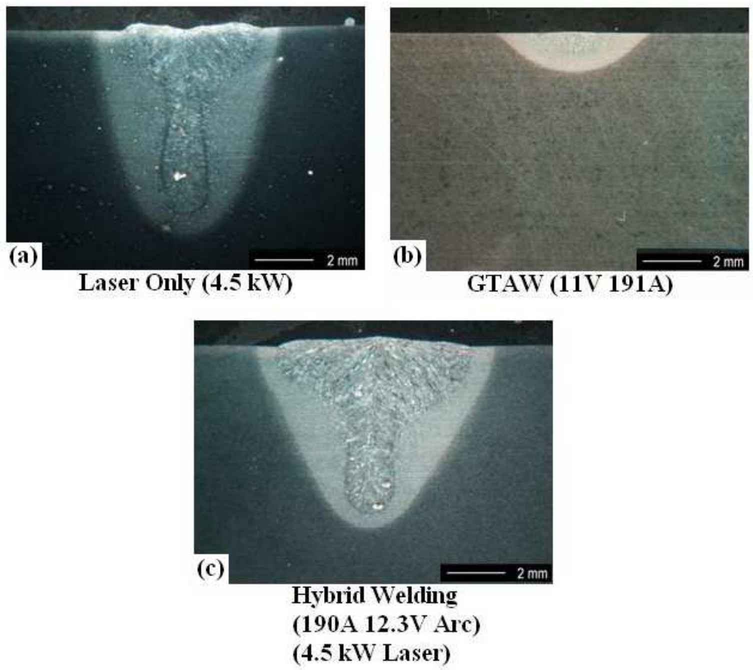

Fig. 3.16: Weld cross sections of (a) laser, (b) arc, and (c) hybrid welded A131 structural steel. For the laser and hybrid welds, the laser power is 4.5 kW. The arc current and voltage are 191 A and 11 V for the arc weld, and 190 A and 12.3 V for the hybrid weld, respectively. The welding velocity was 8.5 mm s^{-1} for all welds.

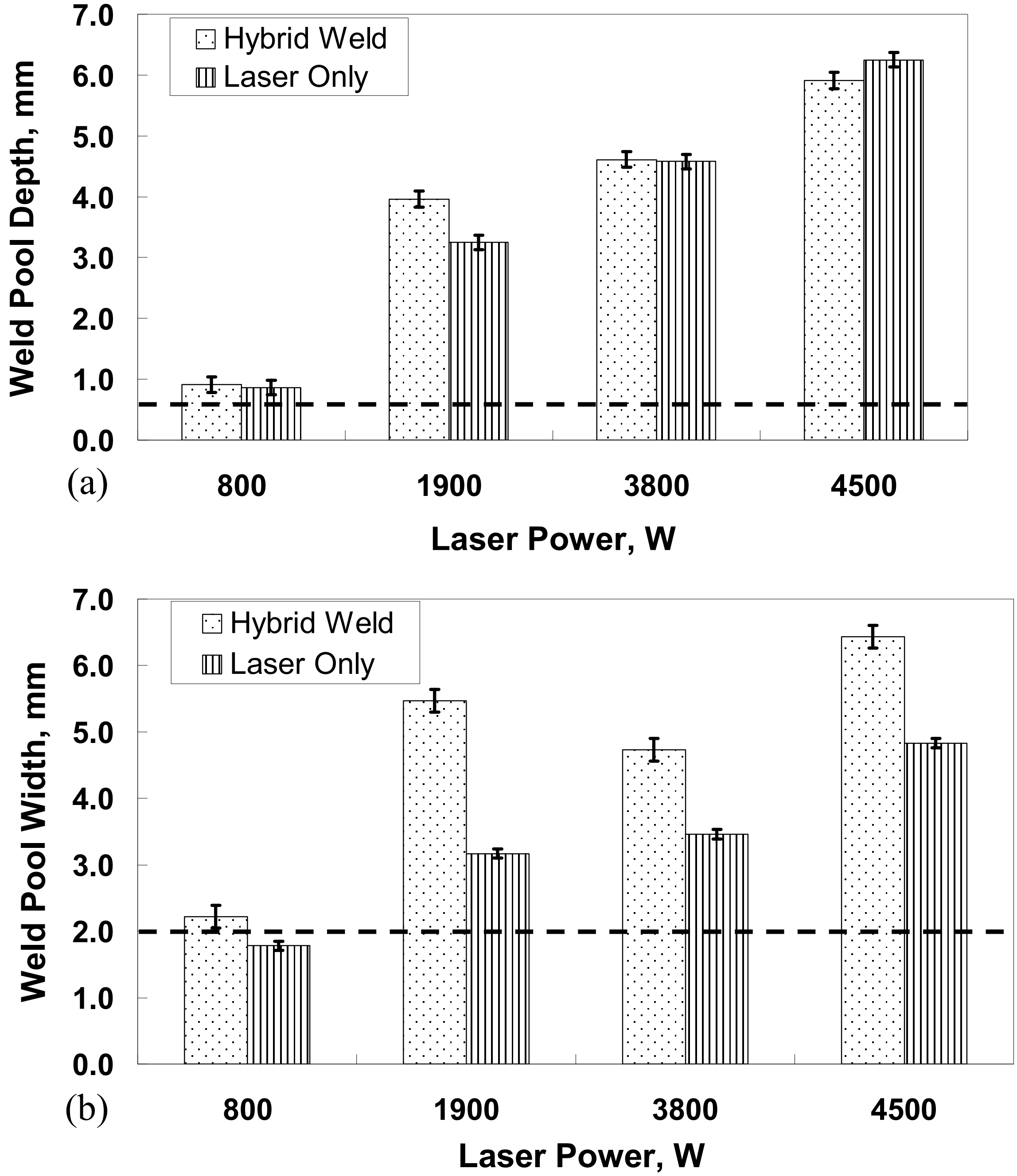

Fig. 3.17: Measured weld pool depth (a) and width (b) as a function of laser power for hybrid and lone laser welding of A131 structural steel. The travel speed was 8.5 mm s^{-1}. The dashed line is the weld pool depth and width achievable by lone GTAW.

The reason for these weld pool shapes is explained by the nature of the welding processes. The laser beam is a high energy density heat source which is very focused at the surface of the workpiece and results in deep penetration. The Marangoni force causes the weld pool to widen near the work-piece surface.[39, 64, 69-70] The GTAW process results in strong electromagnetic and Marangoni (surface tension driven) forces.[39, 69, 71] It will be shown later that the Marangoni force and the electromagnetic forces were of the same order for the conditions of the experiments.[72] When both arc and laser are used, the amount of liquid metal generated by the two heat sources increases relative to lone arc or laser welding. Both the increase in the volume of liquid metal generated by the heat sources and strong Marangoni convection increase the width of the hybrid weld pool.

Fig. 3.18 shows the calculated three-dimensional fluid flow for arc (a), laser (b), and hybrid (c) welded A131 structural steel. The laser power in this case is 4500 W. The arc current and voltage were 190 A and 12.3 V for the hybrid welding, and 11 V and 191 A for the arc welding. The welding velocity was 8.5 mm s^{-1}.

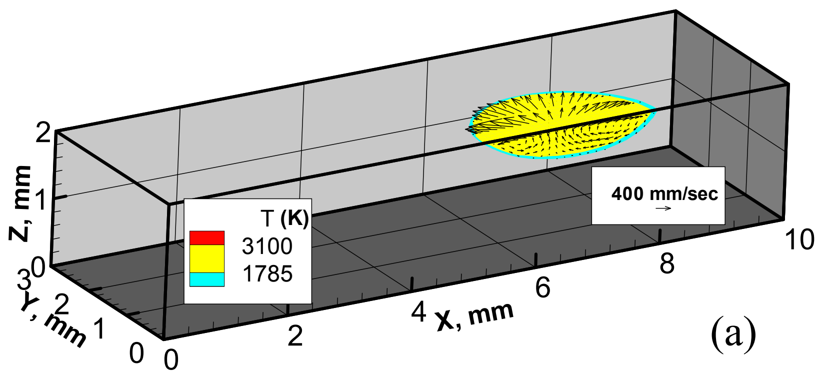

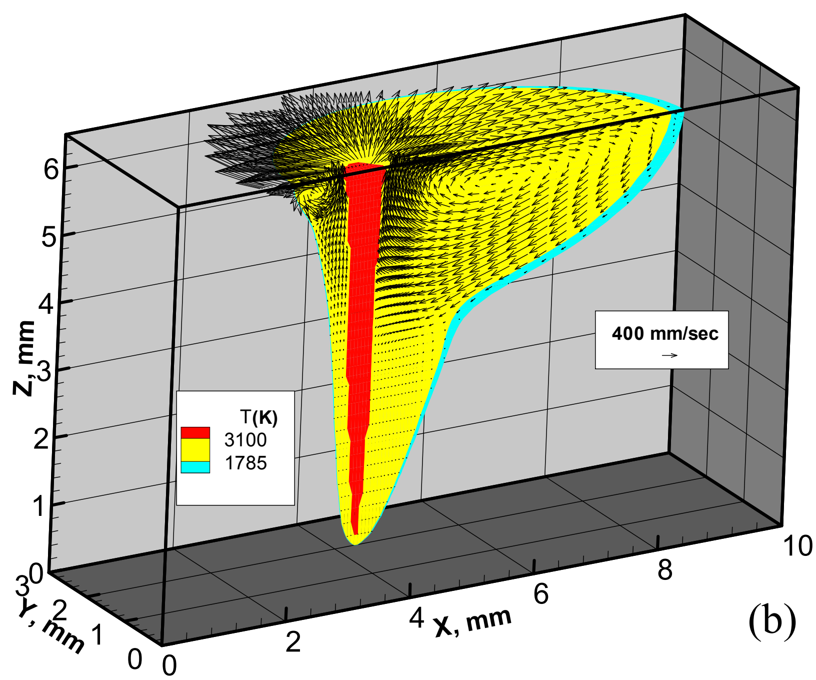

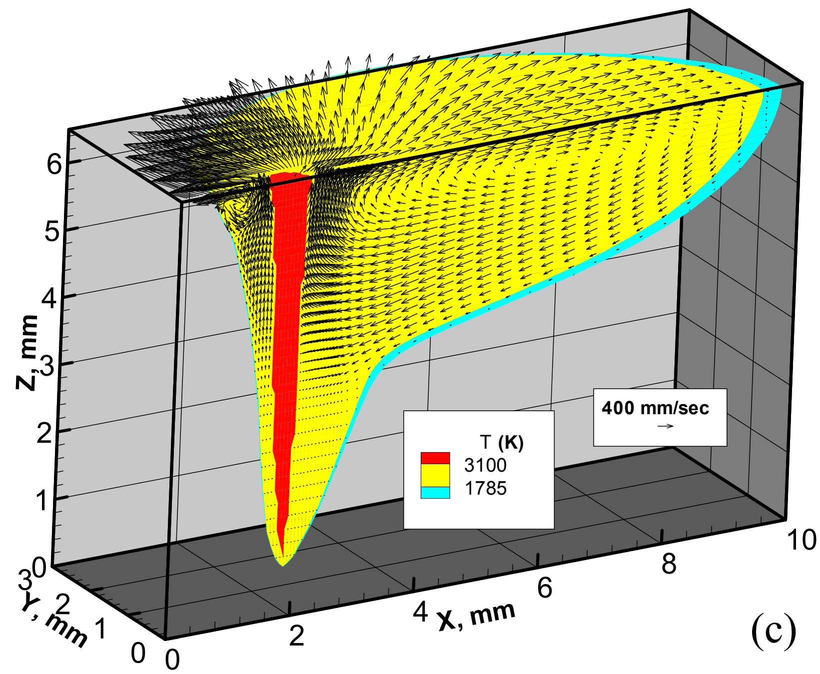

Fig. 3.18: (a) Arc, (b) laser, and (c) hybrid weld geometry and fluid flow calculated using the three-dimensional heat transfer and fluid flow model. The welded material was A131 structural steel. The welding direction is towards the origin of the coordinate axes.

The shape of the arc, laser, and hybrid weld cross sections can be explained by the nature of the welding processes. The laser beam is a high energy density heat source which is very focused at the surface of the workpiece and results in deep penetration. Marangoni stress causes the weld pool to widen near the work-piece surface.[39, 64, 70] GTA welding results in strong electromagnetic and Marangoni (surface tension driven) forces.[39, 69, 71] During hybrid welding, the additional heat input from combining the two heat sources causes more liquid to form and results in a larger weld pool than during laser welding. The depth of the hybrid weld pool is almost the same as the laser weld since the laser beam power level is the same. The increase in the hybrid weld pool width can be attributed to increased heat input. Since the weld pool depth is relatively unchanged, additional heat input and convection causes the liquid metal to flow outward from the weld centerline toward the solid/liquid boundary and increases the weld pool width relative to laser welding [39, 64, 70].

The dimensionless Peclet number is used to understand the significance of the role of heat transfer by convection relative to heat transfer by conduction:[64]

$$Pe = \frac{convection}{conduction} = \frac{UL}{\alpha} \quad (3.93)$$

where U is the characteristic velocity of the molten metal, L is a characteristic length (half of the weld pool width), and α (= $k_l / \rho C_p$) is the thermal diffusivity of A131 steel (5.26×10^{-6} $m^2 s^{-1}$). Table 3.10 shows the calculated Peclet numbers for the GTA, laser, and hybrid A131 structural steel weldments.

Table 3.10: Dimensionless Peclet number for GTA, laser, and hybrid welding of A131 steel. The laser power was 1900 W, and arc current and voltage were approximately 191 A and 12 V.

	GTAW	**Laser**	**Hybrid**
L (mm)	1.3	2.0	3.0
u (mm s^{-1})	100	300	300
Pe	25	114	171

Since the Peclet number is much greater than 1, convection plays a significant role in the heat transfer process during GTA, laser, and hybrid welding of steels. Convection becomes less significant compared to heat transfer by conduction in the case of welding high thermal conductivity metals, for example aluminum and copper alloys. When switching from laser to hybrid welding the characteristic velocity of the molten metal is similar, which suggests increased weld width during hybrid welding is primarily the result of increased arc power density and melting efficiency due to arc contraction.

The relative importance of the Marangoni and electromagnetic forces are given by the dimensionless magnetic and surface tension Reynolds numbers. The magnetic Reynolds number defines the ratio of the electromagnetic force to the viscous forces and is given by:[72-73]

$$\mathrm{Re}_m = \frac{electromagnetic}{viscous} = \frac{\rho \mu_o \mu_r I^2}{4\pi^2 \mu^2} \quad (3.94)$$

where ρ is the density of the material (7000 kg m^{-3}), μ_o is the magnetic permeability of free space ($4\pi \times 10^{-7}$ N A^{-2}), μ_r is the relative permeability (1.0), I is the arc current (~190 A), and μ is the viscosity of the material (5×10^{-3} kg m^{-1} s^{-1}). The magnetic Reynolds number in the case of hybrid or GTA welding of A131 structural steel for the conditions of the experiment is 3.2 x 10^5, which indicates that the electromagnetic force plays an important role in convective heat transfer during hybrid welding. The surface tension Reynolds number defines the ratio of the surface tension (Marangoni) forces to the viscous forces and is given by:[72-73]

$$\mathrm{Re}_s = \frac{surface\ tension}{viscous} = \frac{\rho L \Delta T \left| \dfrac{d\gamma}{dT} \right|}{\mu^2} \qquad (3.95)$$

where L is a characteristic length (2x 10^{-3} m), ΔT is the temperature difference between the peak temperature (3100 K) and the liquidus temperature (1745 K), and dγ/dT is the temperature coefficient of surface tension (-4.7 x 10^{-4} N m^{-1} K^{-1}). The surface tension Reynolds number in the case of hybrid welding for the conditions of experiment is 3.5 x 10^5, which means that the Marangoni stress plays an important role in convective heat transfer during hybrid welding. The ratio of the magnetic and surface tension Reynolds numbers gives the relative importance of the electromagnetic to surface tension forces (Re_m/Re_s). The ratio of electromagnetic forces to surface tension forces is 0.9, which means that the two forces are of the same order.

In order to achieve the experimentally measured weld pool depth and width, arc bending and contraction had to be included in the numerical model calculations. This was accounted for by moving the location of the arc in the model solution domain to a location near the laser beam heat source. In addition, the arc power density distribution effective radius was reduced. The arc radius for a 191 A arc with an arc length of 1.5 mm, in the absence of metal vapors from another source like a keyhole, was observed to be approximately 1.0 mm. The values used for the heat source separation distance and arc radius in the hybrid welding calculations are shown in Table 3.11. Data are ordered according to the laser power level of the particular hybrid weld.

Table 3.11: Separation distance and arc radius values used in the numerical model in order to achieve the experimentally observed hybrid weld pool width and depth. The results are arranged by laser power level.

Laser Power (W)	Separation Distance (mm)	Arc Radius (mm)
4500	2	1
3800	0	0.9
1900	0.2	0.65
800	0.3	0.5

A comparison of the A131 structural steel GTA, laser and hybrid welding experimental and calculated results is shown in Fig. 3.19 and 3.20. Fig. 3.19 shows GTA, laser, and hybrid weld cross sections. The calculated cross section is overlaid on top of the micrograph. The dashed line shown in the calculated result is the 3100 K isotherm, which represents the keyhole wall. In addition to the weld pool solid/liquid boundary (1745 K isotherm), the HAZ-base metal boundary is also shown (1000 K isotherm). The laser power in the case of the hybrid and laser welds was 1.9 kW. The GTA weld was performed using a 191 A, 11 V arc. The arc current and voltage for the hybrid weld were 185 A and 20 V, respectively. The calculated and measured results showed that the laser power level is the primary factor affecting weld pool penetration depth.

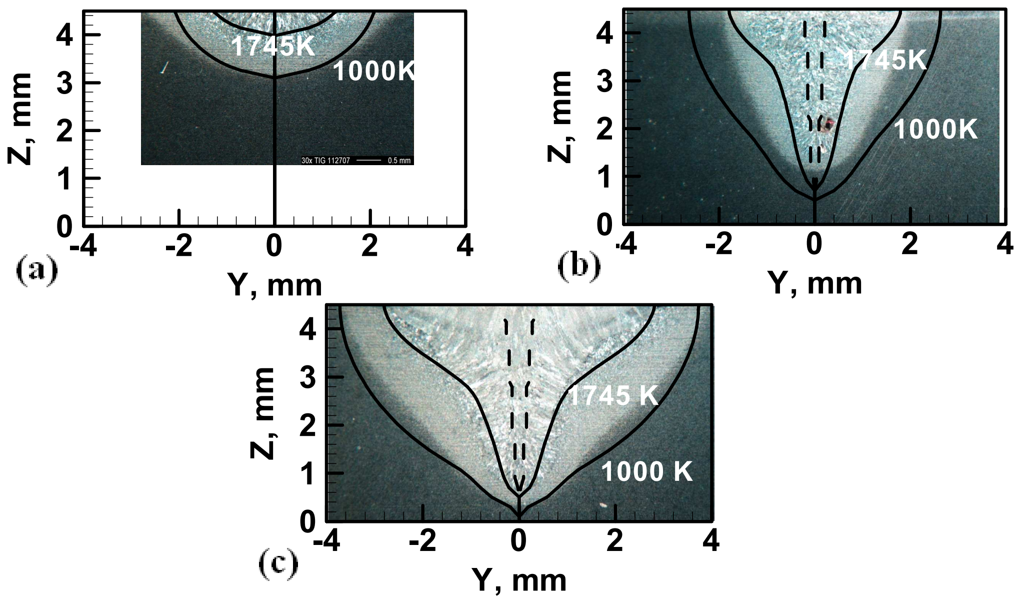

Fig. 3.19: GTA (a), laser (b), and hybrid welded (c) A131 structural steel cross sections with the calculated cross section overlaid on top of the experimental result. The dashed isotherm is the 3100K isotherm, i.e. the location of the keyhole.

Fig. 3.20 (a) is a comparison of the calculated and measured laser and hybrid weld pool depths. The error bars on the experimental results in the figure represent the standard deviation of the measured weld dimensions calculated for three experimental weld cross sections analyzed. Laser weld depth and width standard deviation were 0.12 mm and 0.07 mm, respectively. Hybrid weld depth and width standard deviation were 0.13 mm and 0.17 mm, respectively. The error bars on the calculated weld depth and width represent the error in calculated weld depth and width compared to the experimentally measured dimension. Percent error between the hybrid welding experimental and calculated depth and width were 6.5% and 7.7%, respectively. The error between the experimental and calculated laser weld depth and width were 18.5% and 19%, respectively. Hybrid welding results in similar weld pool depth compared lone laser welding. Weld pool width increases significantly when comparing hybrid to laser welding, which is shown in Fig. 3.20 (b). Increased weld pool width improves the ability to bridge gaps between components being welded, which is particularly important for welding large sections of material.

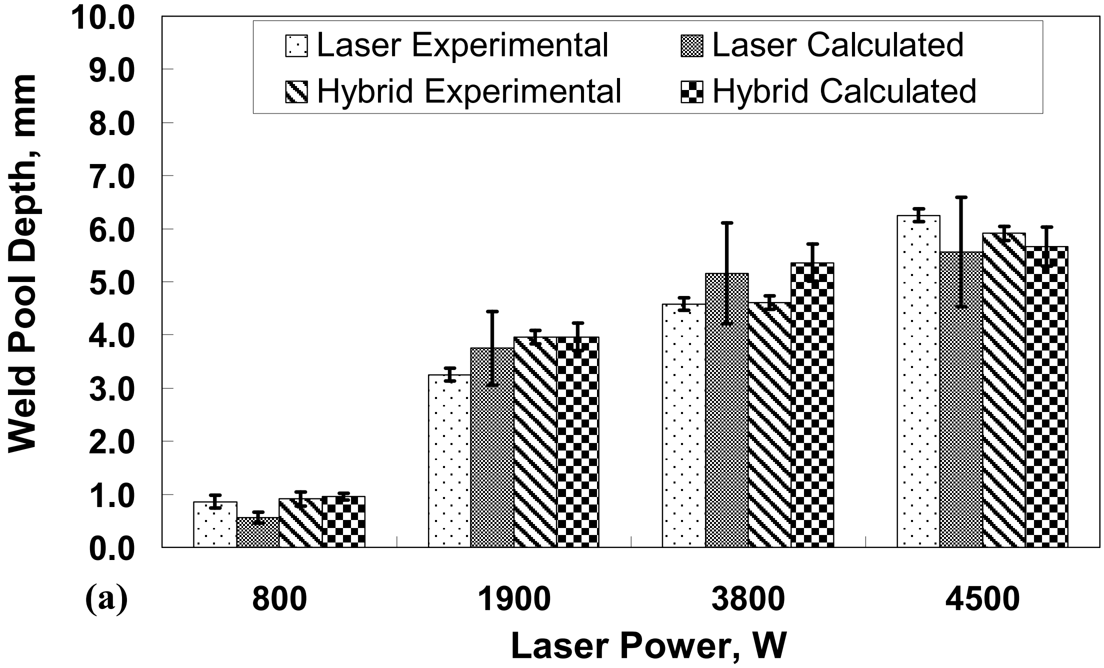

(a)

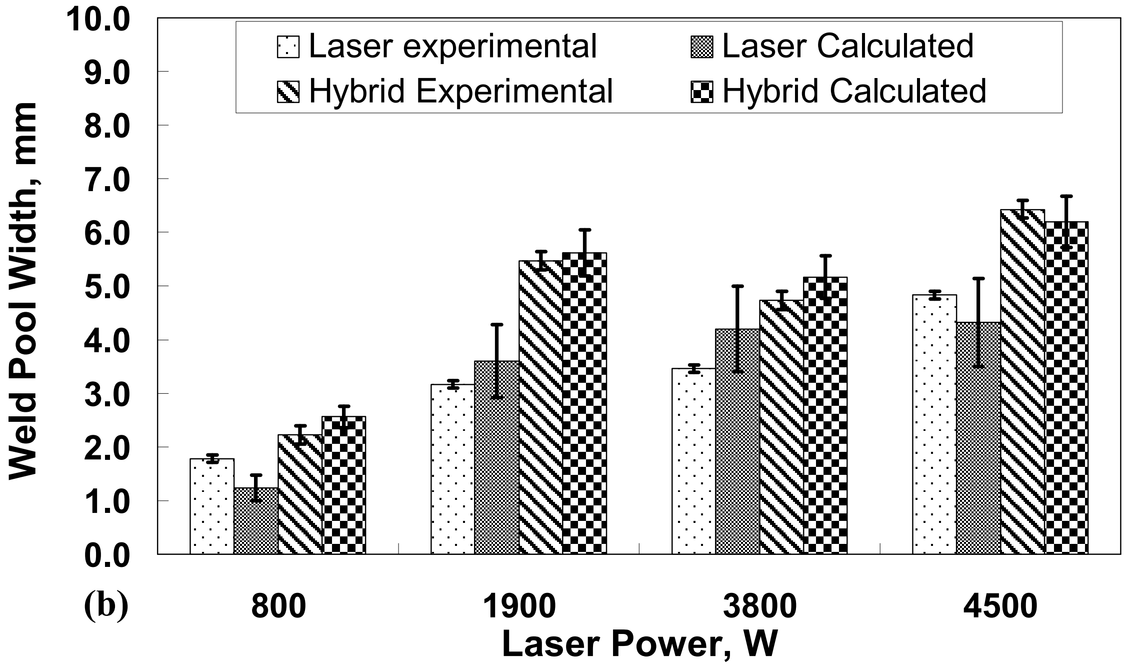

(b)

Fig. 3.20: Comparison of calculated and measured laser and hybrid A131 structural steel welds depth (a) and width (b) as a function of laser power.

3.4.3 Influence of sulfur

3.4.3.1 Statistical analysis of effect of base metal sulfur concentration

Table 3.12 shows the ANOVA results for the influence of weld metal sulfur concentration on measured laser weld bead width and depth. The p-value is the probability of obtaining an F value equal to that calculated from experimental data, assuming that the null hypothesis is true. Conversely, for a given F-value, a high p-value implies greater probability that the null hypothesis is true. The null hypothesis may be rejected if the p-value is lower than 0.05 (for a 95% confidence interval). Table 3.12 shows that the null hypothesis – i.e. the sulfur content does not influence the weld dimension – can be rejected for width, but not for depth. In other words, the effect of base metal sulfur content is statistically significant for weld width but not for weld depth.

Table 3.12: ANOVA results for the influence of sulfur concentration on fiber laser weld bead depth and width. The welded material was mild steel (0.16 %C, 1.46 %Mn).

	Source of Variation	Degrees of Freedom	F value	P-value	F critical
Depth	Between Groups	5	0.63	0.68	2.62
	Within Groups	24			
Width	Source of Variation	Degrees of Freedom	F value	P-value	F critical
	Between Groups	5	40.45	6.30×10^{-11}	2.62
	Within Groups	24			

3.4.3.2 Effect of sulfur: experimental and computational study

Fig. 3.21 shows variation of the experimental and calculated 7 kW laser weld (a) depths and (b) widths as a function of the sulfur concentration in the base metal (0.16 %C, 1.46 %Mn). Error bars representing the standard deviation for a given sulfur content are shown for the mean measured depths and widths. Fig. 3.21 shows that increasing the concentration of sulfur in the base metal, over the range considered here, significantly influenced the measured weld bead width but did not appreciably affect the measured weld pool depth. The error in the calculated penetration depth compared to the experimental measured depth was less than 2% in Fig. 3.21 (a). The variation of calculated weld width with increasing sulfur content is qualitatively similar to the experiments, although there is some difference in the calculated and measured values at high sulfur concentrations. The higher experimental weld widths may be due to lower effective sulfur concentration on the surface as a result of evaporation.

The decrease in laser weld width with increasing sulfur concentration, as shown in Fig. 3.21 (b), is due to changes in heat and fluid transport in the molten weld pool. The average errors between the experimental and calculated weld dimensions were 1.3% for weld depth and 17.7% for weld width. At low sulfur concentrations (< 0.002 wt%), the surface tension gradient ($d\gamma/dT$) at the top surface is negative. This drives the fluid near the top surface outward forming convection currents that result in enhanced heat transport near the top surface and widening of weld pool near the top surface. The effect on increasing sulfur content on the fluid flow and weld width is discussed below with the help of Fig. 3.22.

Fig. 3.22 shows calculated three-dimensional temperature and fluid flow profiles for the laser welded mild steel containing (a) 0.015 wt%, (b) 0.056 wt%, and (c) 0.101 wt% sulfur. When the sulfur concentration is above 0.002 wt%, $d\gamma/dT$ depends on the local temperature. At temperatures close to the solidus, $d\gamma/dT$ is positive and fluid flow is inwards. At higher temperatures close to the keyhole, $d\gamma/dT$ is negative and fluid flow is outwards. The two flows meet somewhere between the solid-liquid boundary and the keyhole walls resulting in two circulating currents. The location where the two flows meet depends on the sulfur concentrations and the local temperatures; as sulfur concentration increases, this location moves closer to the keyhole.

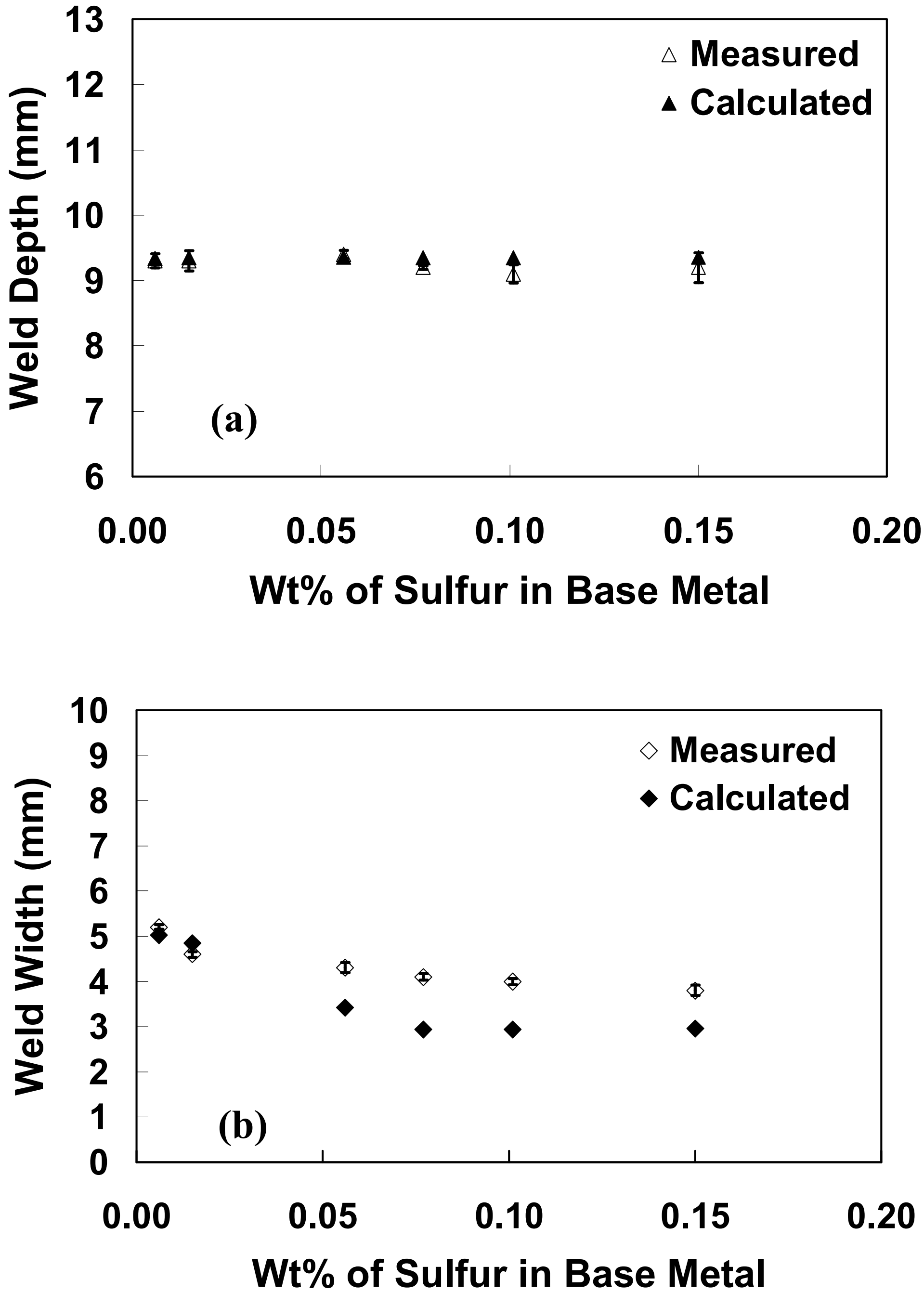

Fig. 3.21: Plots comparing the experimental and calculated laser weld (a) depths and (b) widths as a function of the sulfur concentration in the base metal for 7 kW laser welds on mild steel (0.16 %C, 1.46 %Mn) at 16.7 mm s^{-1}. Standard error bars are shown for the measured weld dimensions.

A laser weld with medium sulfur concentration (0.015 wt%) is shown in Fig. 3.22 (a). The fluid moving away from the keyhole (and carrying heat) is limited to a small distance from the keyhole walls due to the opposing flow from the weld pool boundary. At sulfur concentrations greater than 0.03 wt% (Fig. 3.22 (b)), when the fluid flow is predominantly inward, the circulation current due to outward flow on the top surface is much smaller and limited to a very small region near the top surface. As the sulfur content approaches concentrations of 0.101 wt% (Fig. 3.22 (c)) and 0.150 wt%, the size of the region where fluid flow is towards the solid/liquid boundary reduces in size. However, weak radially outward flow is present near the keyhole walls even at these very high sulfur concentrations. In other words, fluid flow at top surface becomes increasing inwards with greater sulfur content leading to less heat transport in radially outward direction and narrower welds.

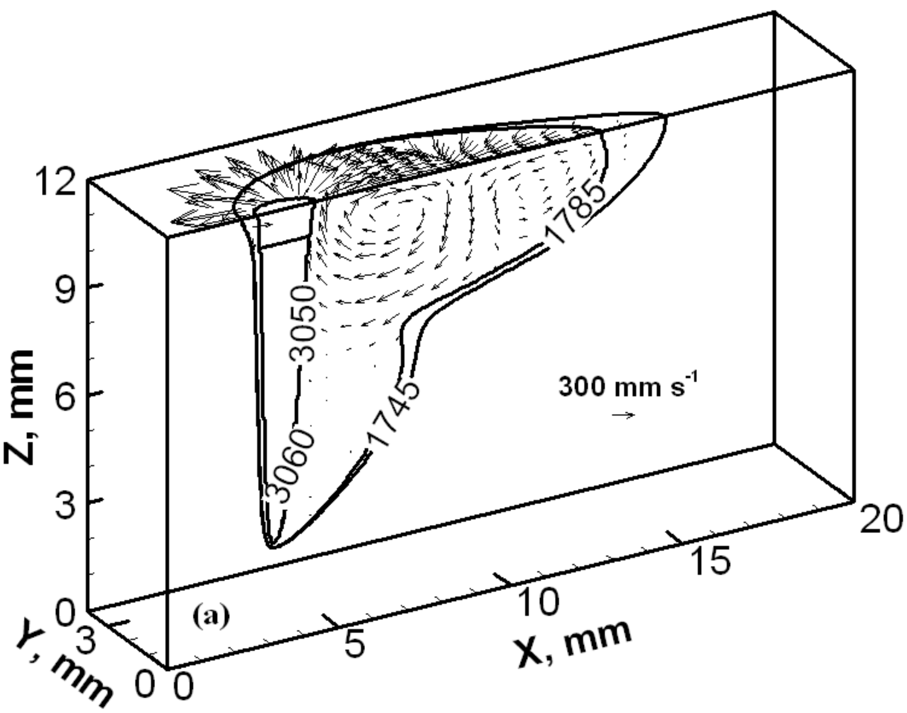

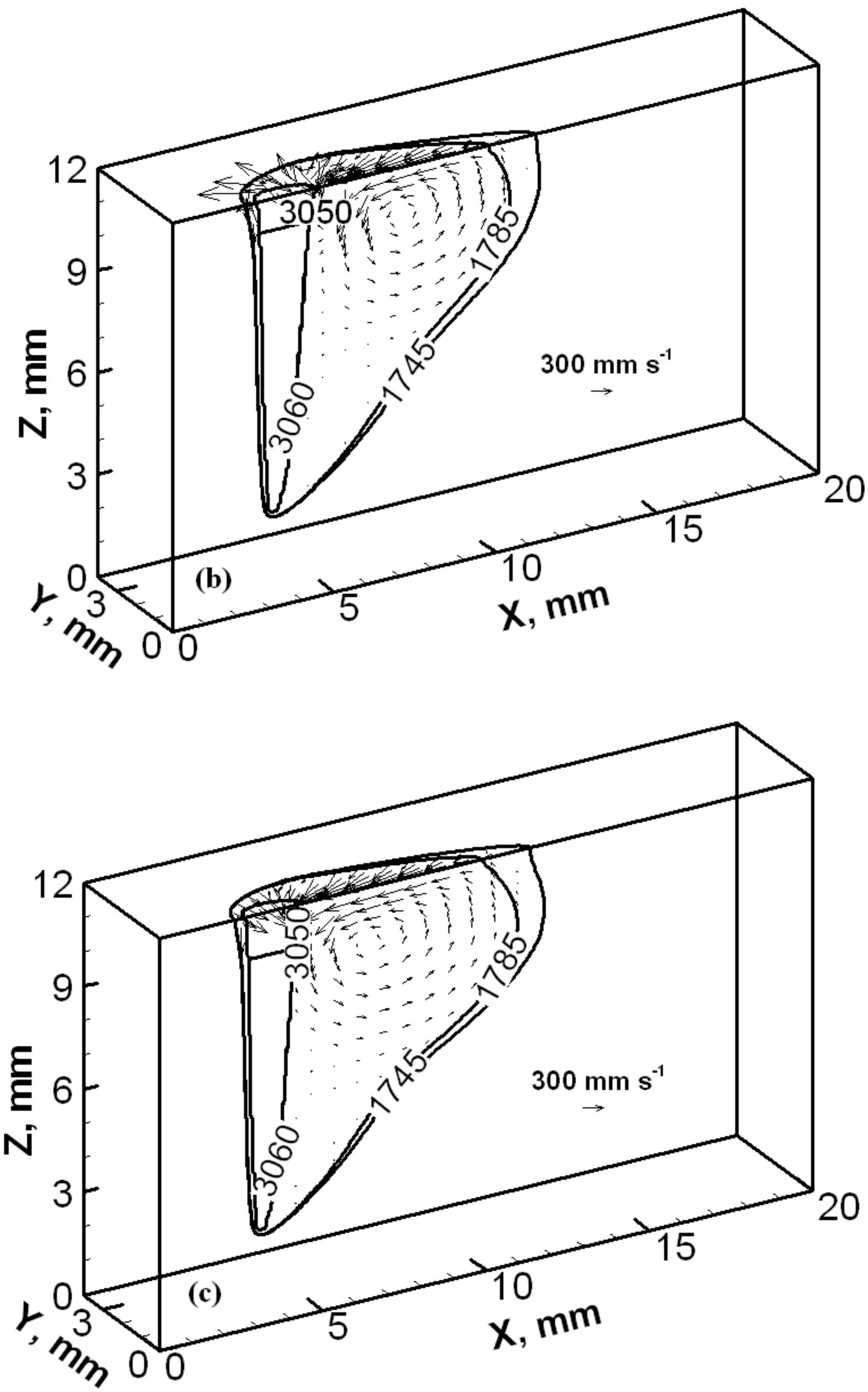

Fig. 3.22: Calculated three-dimensional temperature and fluid flow profiles during 7 kW laser welding of mild steel (0.16 %C, 1.46 %Mn) containing (a) 0.015 wt%, (b) 0.056 wt%, and (c) 0.101 wt% sulfur at a welding speed of 16.7 mm s^{-1}.

Fig. 3.23 shows comparison of the calculated and experimental weld cross sections for the laser welded sample for 0% O_2 in shielding gas (i.e. approximately 0.0038 wt% oxygen in base metal) and (a) 0.006 wt%, (b) 0.015 wt%, (c) 0.056 wt%, (d) 0.077 wt%, (e) 0.101 wt%, and (f) 0.150 wt% sulfur. The calculated weld geometries agree reasonably well with the experimental results. With increasing sulfur concentration in the weld pool, the weld width decreases due to the top surface fluid flow direction becoming more radially inward from the solid/liquid boundary.

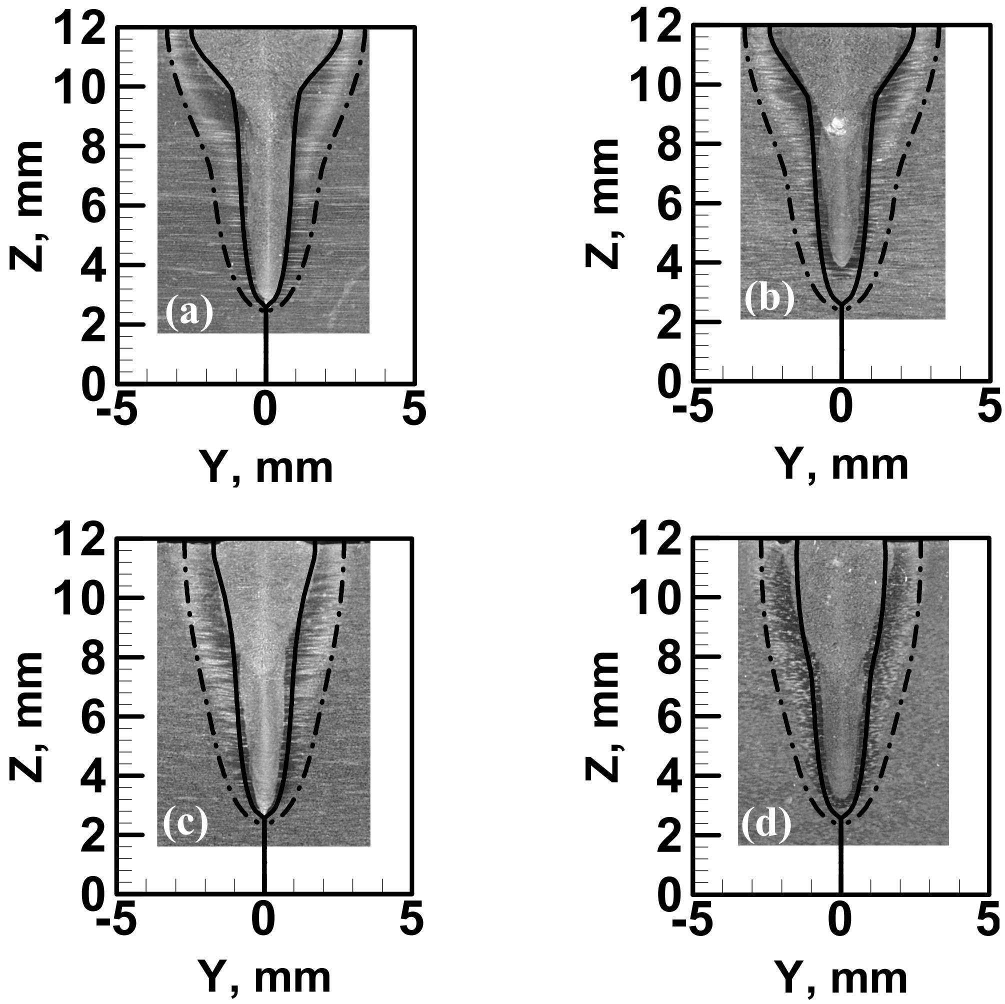

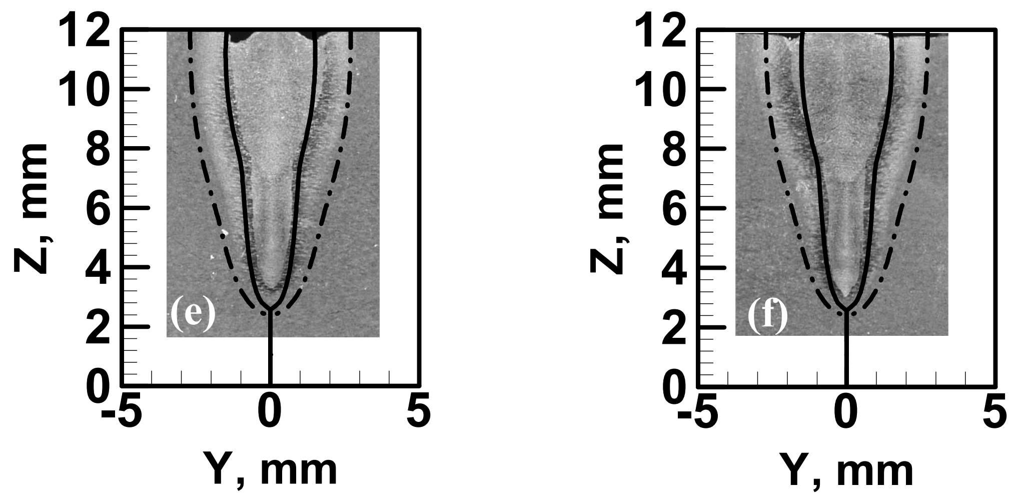

Fig. 3.23: Comparison of calculated and measured 7 kW laser weld cross sections when the base metal (0.16 %C, 1.46 %Mn) contained (a) 0.006 wt%, (b) 0.015 wt%, (c) 0.056 wt%, (d) 0.077 wt%, (e) 0.101 wt%, and (f) 0.150 wt% sulfur. The dotted line in the cross sections is the 1000 K isotherm and the solid line outlining the fusion zones is the 1745 K solidus isotherm. The welding speed was 16.7 mm s^{-1}.

Of the various pressure terms considered in the keyhole pressure balance (equation 3.15), the most significant pressures in the keyhole are the vapor pressure, surface tension pressure, and pressure of CO. Table 3.13 shows the calculated pressures used to determine the keyhole wall temperatures for different sulfur concentrations. $d\gamma/dT$ at keyhole walls is not affected by the sulfur content of the base metal due to the high wall temperatures. The effect of sulfur concentration on the activities of dissolved oxygen and carbon, and consequently, on the CO pressure is negligible. Due to the very small variation in the various pressure terms as shown in Table 3.13, the keyhole wall temperatures varied negligibly, and a constant penetration of 9.3 mm was obtained throughout the range of sulfur concentrations considered. It has been shown that the keyhole and weld penetration depth during laser and laser-arc hybrid welding are similar.[12, 41] Since increasing the concentration of sulfur in the base metal results in a negligible change in keyhole depth, the penetration depth does not change significantly. It should be noted that the conclusion regarding the effect of sulfur on penetration depth applies only to the range of process conditions and workpiece material considered in this work.

Table 3.13: Calculated keyhole dimensions, keyhole wall temperature, and magnitudes of partial pressures acting at keyhole surface 4.5 mm below the top surface of the weld pool for various concentrations of sulfur in the base metal during 7 kW laser welding of mild steel (0.16 %C, 1.46 %Mn).

Concentration of sulfur in base metal (wt%)	0.015	0.056	0.077	0.101	0.15
Total Keyhole Depth (mm)	9.30	9.30	9.30	9.30	9.30
Keyhole Radius* (mm)	0.54	0.57	0.57	0.54	0.54
Keyhole Wall Temperature (K)	3052	3052	3052	3053	3053
Metal Vapor Pressure (atm)	9.24×10^{-1}	9.23×10^{-1}	9.24×10^{-1}	9.26×10^{-1}	9.27×10^{-1}
Surface Tension ($N\ m^{-1}$)	1.41	1.41	1.41	1.41	1.41
Surface Tension Pressure (atm)	2.57×10^{-2}	2.44×10^{-2}	2.44×10^{-2}	2.57×10^{-2}	2.57×10^{-2}
Hydrostatic pressure (atm)	3.03×10^{-3}	3.03×10^{-3}	3.03×10^{-3}	3.03×10^{-3}	3.03×10^{-3}
Recoil pressure (atm)	2.08×10^{-3}	2.08×10^{-3}	2.08×10^{-3}	2.10×10^{-3}	2.10×10^{-3}
P_{CO} (atm)	0.103	0.102	0.101	0.101	0.100

*Keyhole radius reported here is half of the distance between the front and rear keyhole walls along the weld symmetry line 4.5 mm below the top surface.

3.4.4 Influence of oxygen

3.4.4.1 Statistical analysis of the effect of ambient oxygen

Table 3.14 shows the ANOVA results for the influence of weld metal oxygen concentration on laser weld bead depth and width. The low p-values mean that the changing the O_2 content of the shielding gas has a significant influence on weld depth and width.

Table 3.14: ANOVA results for the influence of weld metal oxygen concentration on laser weld bead depth and width. The weld material was 0.16 %C, 1.46 %Mn mild steel.

	Source of Variation	Degrees of Freedom	F value	P-value	F critical
Depth	Between Groups	3	42.56	7.50×10^{-8}	3.24
	Within Groups	16			
	Source of Variation	Degrees of Freedom	F value	P-value	F critical
Width	Between Groups	3	99.32	1.48×10^{-10}	3.24
	Within Groups	16			

3.4.4.2 Effect of oxygen: experimental and computational study

Table 3.15 shows the various computed pressures at the keyhole walls from equation 3.15 when 0%, 5%, 10%, and 15% O_2 is added to the shielding gas during 7 kW laser welding of 0.16%C, 1.46 %Mn mild steel. The significant terms in pressure balance are due to metal vapors and CO. As the oxygen concentration increases, the CO pressure increases significantly. As a result, the pressure balance at keyhole walls can be attained with lower keyhole wall temperatures. The lower wall temperatures permit increased keyhole penetration and somewhat narrower weld widths.[47, 74] In this work, CO pressure at keyhole walls for each case was taken as a fixed fraction of the equilibrium value calculated using bulk concentrations of dissolved oxygen and carbon. The assumption is based upon that during laser welding the equilibrium carbon monoxide pressure is not likely to occur during laser welding. A factor of 0.8 was chosen for good agreement between experimental and calculated weld widths as oxygen concentration was varied (Fig. 3.24 (b)).

The plots of the experimental and calculated laser weld depths and widths as functions of shielding gas O_2 percentage are shown in Fig. 3.24. Standard error bars have been added for the experimental results. Fig. 3.24 clearly shows that with increasing O_2 percentage in the shielding gas, the experimental weld widths decrease whereas the experimental weld depths increase. The decrease in weld width (Fig. 3.24 (b)) with increasing oxygen content can be attributed to the effect of oxygen on Marangoni convection. Measured penetration depth was about 16% higher for Ar-15% O_2 shielding gas compared to the penetration depth with Ar-0 % O_2 shielding gas. The error of the calculated weld depths and widths compared to the measured experimental dimensions were less than 12% and 20%, respectively. However, present calculations somewhat under-predict the effects of increase in O_2 content of the shielding gas on the penetration depth, especially for 10% and 15% O_2 cases.

As discussed before, experimental weld penetration was not influenced by base-metal sulfur content. It should be noted that the sulfur concentrations were higher, and had larger variation, than oxygen concentrations in this study. Therefore the increase in the weld penetration due to O_2 content in shielding gas is not primarily due to the influence of surface-active oxygen on the fluid flow. It also seems that the effect of CO generation, as modeled in this study, can qualitatively explain the increase in penetration depth. The reasons for the lack of excellent agreement between the computed and the experimentally determined depth values (Fig. 3.24 (a)) are not known.

Table 3.15: Calculated keyhole dimensions, local keyhole wall temperature, and magnitudes of partial pressures acting at keyhole surface 4.5 mm below the top surface of the weld pool when O_2 content of shielding gas is varied during 7 kW laser welding of 0.16 %C, 1.46 %Mn mild steel.

% O_2 in shielding gas	0	5	10	15
Concentration of Oxygen in Weld Metal (wt%)	0.0038	0.0078	0.0135	0.0257
Keyhole Depth (mm)	9.30	9.39	9.59	10.1
Keyhole Radius* (mm)	0.51	0.54	0.60	0.75
Keyhole Wall Temperature (K)	3052	3023	2972	2782
Metal Vapor Pressure (atm)	9.25×10^{-1}	8.15×10^{-1}	6.52×10^{-1}	2.69×10^{-1}
Surface Tension ($N\ m^{-1}$)	1.41	1.42	1.44	1.52
Surface Tension Pressure (atm)	2.73×10^{-2}	2.60×10^{-2}	2.37×10^{-2}	2.01×10^{-2}
Hydrostatic Pressure (atm)	3.03×10^{-3}	3.03×10^{-3}	3.03×10^{-3}	3.03×10^{-3}
Recoil Pressure (atm)	2.08×10^{-3}	1.64×10^{-3}	1.07×10^{-3}	1.94×10^{-4}
P_{CO} (atm)	0.10	0.21	0.37	0.75

*Keyhole radius reported here is half of the distance between the front and rear keyhole walls along the weld symmetry line 4.5 mm below the top surface.

Calculated and experimentally obtained weld cross sections when the shielding gas contained (a) 0%, (b) 5%, (c) 10%, (d) 15% O_2 are shown in Fig. 3.25. The computed weld geometries in Fig. 3.25 are in good agreement with the experimental results.

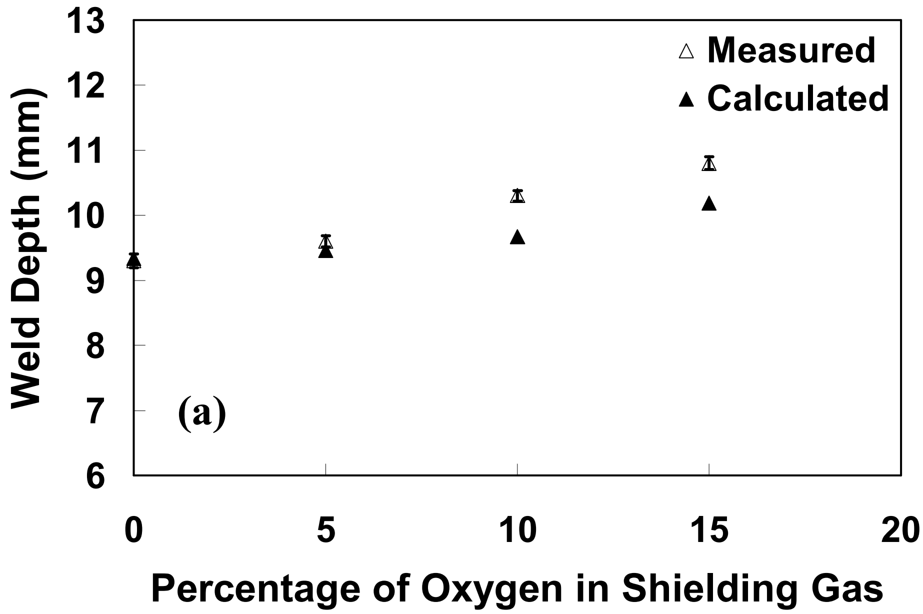

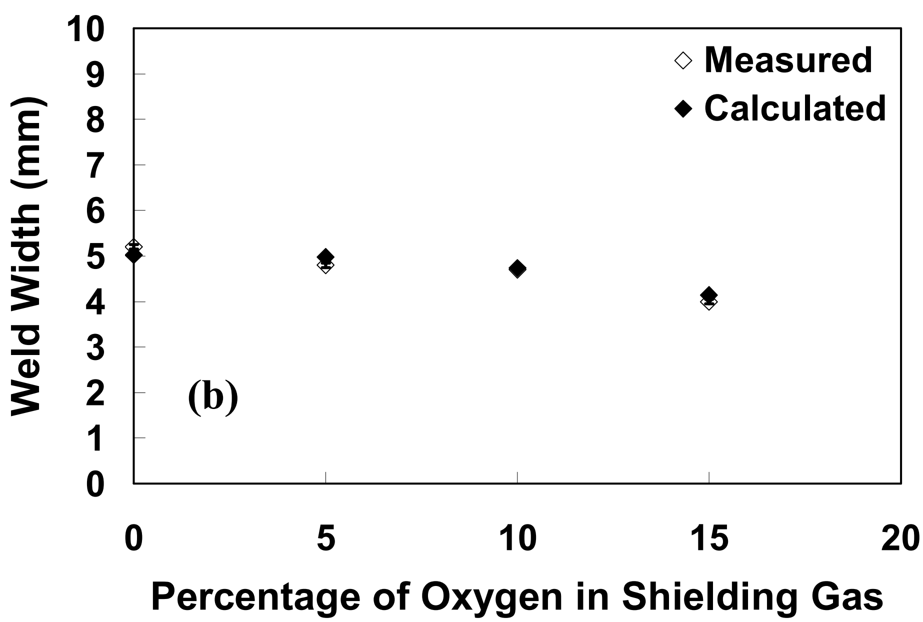

Fig. 3.24: Comparison of the experimental and calculated 7 kW laser welds (a) depths and (b) widths as a function of shielding gas O_2 percentage. Standard error bars are shown for measured weld dimensions. The base metal was 0.16 %C, 1.46 %Mn mild steel and welding speed was 16.7 mm s^{-1}.

Temperature and fluid velocity profiles calculated for 7 kW laser welding of mild steel for (a) 0% and (b) 10% O_2 in the shielding gas are shown in Fig. 3.26. The presence of oxygen and sulfur (0.006 wt% sulfur) causes radially inward flow towards the keyhole at the weld pool surface close to the weld pool solid/liquid boundary. Near the keyhole, the fluid flow is radially outward due to the relatively high liquid metal temperatures compared to the solid/liquid boundary. As the oxygen concentration increases in the liquid weld metal, the radially outward fluid flow decreases in magnitude and the radially inward flow increases. The increase in radially inward flow is due to a more positive $d\gamma/dT$ with increasing concentrations of oxygen in the weld metal. As the inward fluid flow becomes more dominant, the weld pool width decreases. No significant vertical flow of liquid metal resulted from surface tension gradients at the keyhole walls because the temperature gradients along the keyhole walls are small in keyhole mode laser welding. For both 0 % and 10% O_2 cases, shown in Fig. 3.26 (a) and 3.26 (b), fluid velocities near the keyhole walls at short distances from the top surface are upwards whereas the flow direction is downwards farther away from the top surface. The similarities in flow patterns near the keyhole walls suggest that keyhole depth is not significantly affected by the fluid flow.

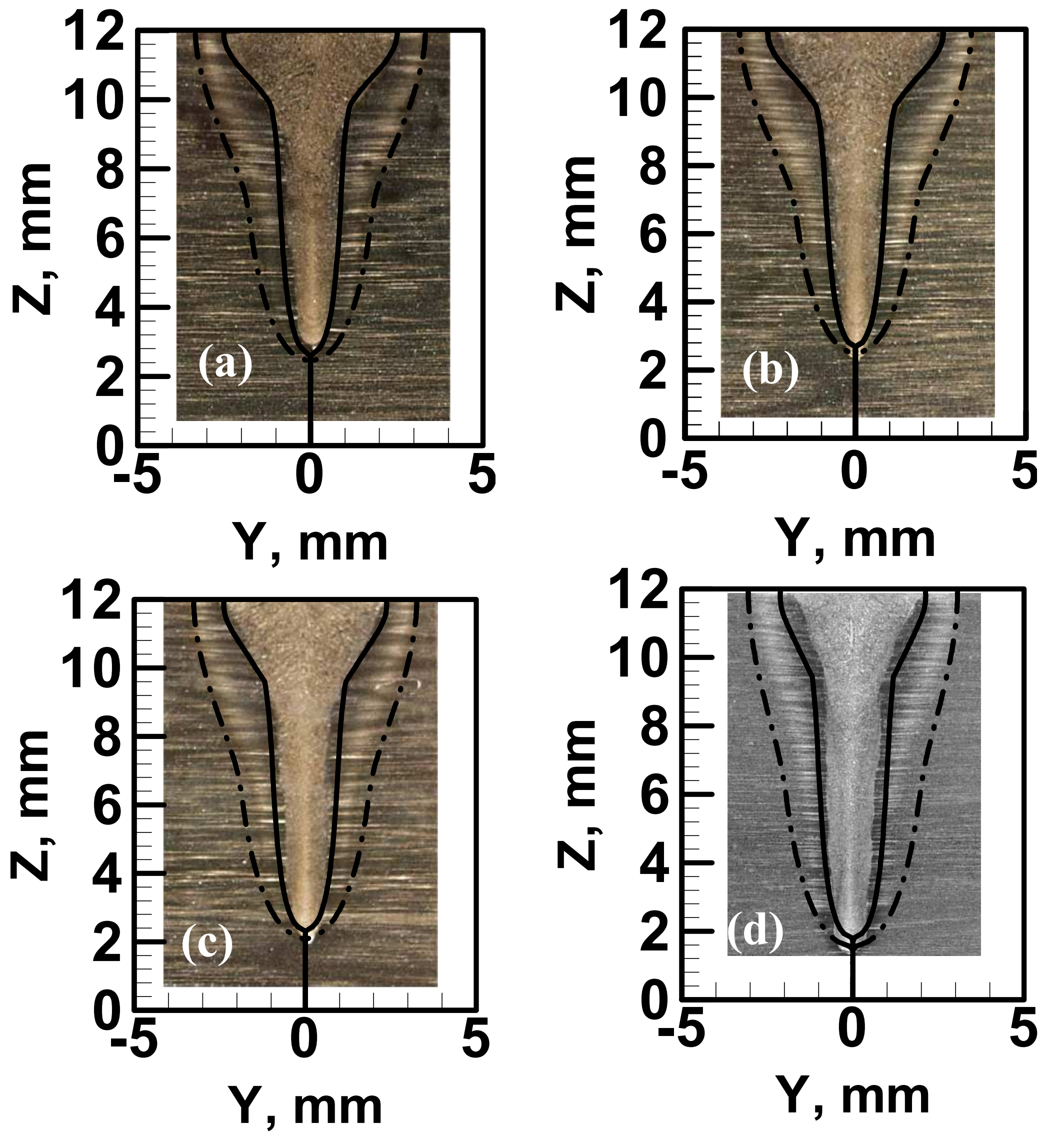

Fig. 3.25: Comparison of experimental and calculated 7 kW laser weld cross sections when welding with shielding gas containing (a) 0%, (b) 5%, (c) 10%, and (d) 15% O_2 on mild steel (0.16 %C, 1.46 %Mn) at 16.7 mm s^{-1} travel speed. The dotted lines in the cross sections are the 1000 K isotherm and the solid line outlining the fusion zones is the 1745 K solidus isotherm.

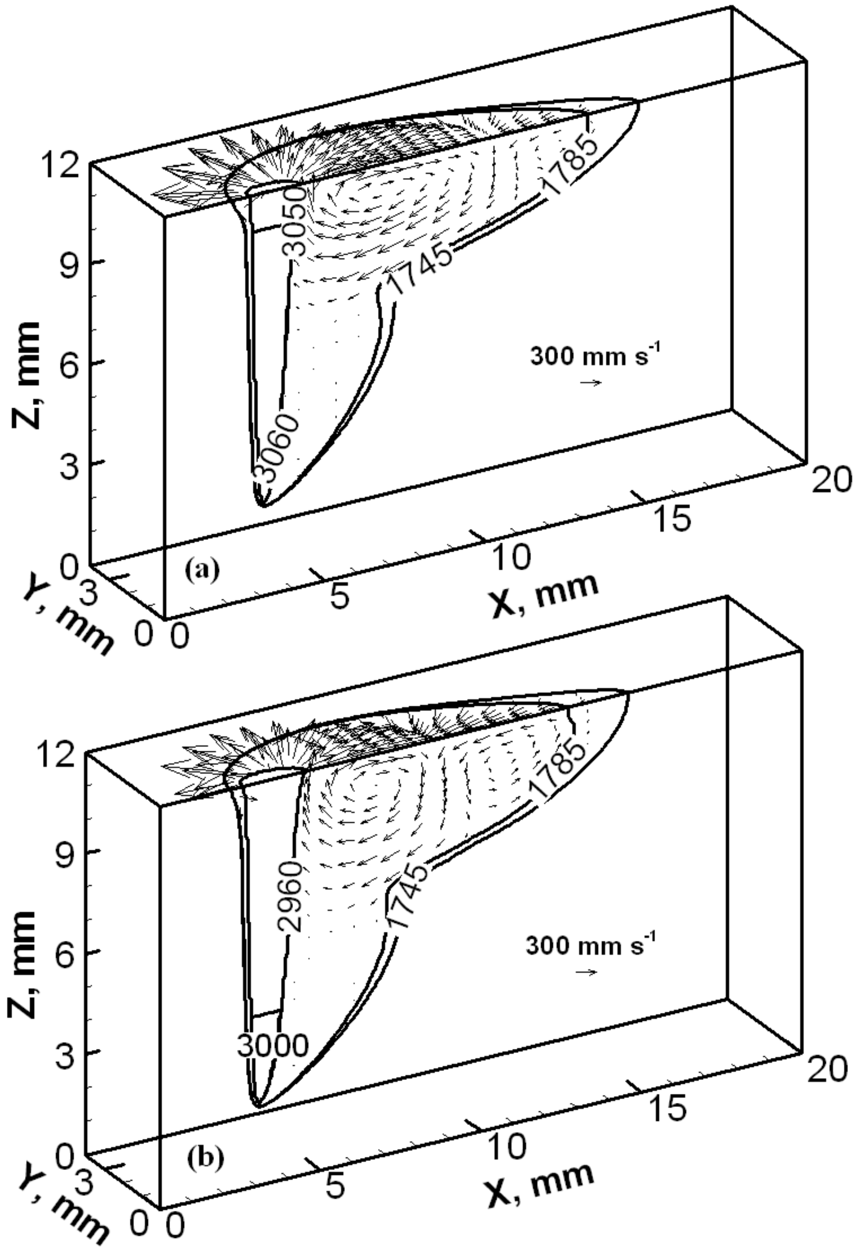

Fig. 3.26: Temperature and fluid velocity profiles during 7 kW laser welding of mild steel when (a) 0% and (b) 10% O_2 is introduced to the shielding gas.

3.5 Summary and conclusions

A three-dimensional heat transfer and fluid flow model for arc, laser, and laser/GTA hybrid welding has been proposed and successfully validated using experimental results. The model considers the enhanced absorption of the laser beam due to multiple reflections inside the keyhole, the influence of surface active elements via the fluid flow and keyhole pressure balance calculations, and the amount of arc energy absorbed about the keyhole. Temperature and fluid velocity profiles were calculated for GTA, CO_2 laser, and CO_2 laser/GTA hybrid welding of A131 structural steel and 321 stainless steel. The effects of oxygen and sulfur on the temperature profiles and fluid flow in keyhole mode Yb doped fiber laser welding of 0.16 %C mild steel were successfully evaluated both experimentally and theoretically. Since, the effects of surface active elements seen in hybrid and laser welding have not be attributed to an influence by the arc, as presented in the literature, this research is expected to be significant for Nd:YAG and fiber laser/GTA hybrid welding. In addition, the influence of heat source separation distance and arc current on temperature profiles, cooling rates, weld depth, and fluid flow were successfully analyzed for hybrid welding of 321 stainless steel. Laser power and its influence on heat transfer, weld depth and width, and temperature and fluid flow profiles were successfully evaluated for GTA, Nd:YAG laser, and Nd:YAG laser/GTA hybrid welded A131 structural steel.

A single factor analysis of variance (ANOVA) was used to statistically evaluate if keyhole mode Yb doped fiber laser weld bead depth and width differed significantly with increasing concentrations of dissolved oxygen or sulfur in 0.16 %C mild steel with 95% confidence. The ANOVA showed laser weld depth was not affected by increasing the mild steel sulfur concentration from 0.006 wt% to 0.15 wt%, but increasing the dissolved oxygen content of the weld pool from 0.0038 wt% to 0.0257 wt% did significantly impact laser weld depth. Weld metal oxygen concentration increased as a result of increasing O_2 content of the shielding gas. The experimentally measured weld width decreased from 5.2 mm to 3.8 mm as the base metal sulfur concentration was increased Increasing the dissolved oxygen content of the weld pool decreased laser weld width from 5.2 to 4 mm.

Computed results of the heat transfer and fluid flow model showed that the effects of sulfur and oxygen on laser weld width could be explained considering their influence on Marangoni convection. In weld pools containing either oxygen or sulfur, the flow of liquid metal on the weld pool surface very near the keyhole was always away from the keyhole while the direction of the flow was just the opposite close to the solid-liquid boundary. The laser molten metal flow speeds were on the order of 300 mm s^{-1}. This behavior is consistent with positive temperature coefficient of surface tension ($d\gamma/dT$) at temperatures close to the liquidus temperature of the steel and negative $d\gamma/dT$ at temperatures close to the boiling point of the alloy.

During the fiber laser welding of the mild steel, convective flow of heat and mass in the weld pool was driven by the Marangoni flow at the weld pool surface and the resulting recirculation in the weld pool. At the keyhole walls, temperature gradients were small (~1.K mm^{-1} to ~4 K mm^{-1}) and, as a result, no significant vertical flow of the liquid metal resulted from surface tension gradients at the keyhole wall. This behavior is consistent with the negligible changes (< 0.2 mm) in the weld depth with increasing the mild steel sulfur concentration. Since computations showed no major differences in the liquid metal flow near the keyhole with changes in the oxygen concentration, Marangoni convection is not the source of increase in weld penetration with the concentration of oxygen. The increased weld penetration observed with the increased O_2 concentration of the shielding gas is consistent with the formation of CO at the keyhole wall. Carbon monoxide formation was the result of reacting carbon and oxygen dissolved in the weld pool and results in increased pressure within the keyhole. Increasing the dissolved oxygen content of the weld pool from 0.0038 to 0.0257 wt% resulted in an increase in the calculated partial pressure of carbon monoxide at the keyhole wall from 0.1 atm to 0.75 atm. The measured laser weld depth increased from 9.3 to 10.8 mm with increasing the dissolved oxygen content of the weld pool.

In order to calculate the increase in keyhole depth with the addition of oxygen to the weld metal, a pressure balance was considered along the keyhole surface. The primary factors influencing the keyhole geometry and temperature profile of the keyhole were the vapor pressure of the alloy, the surface tension pressure, and the partial pressure of carbon monoxide. The vapor pressure, surface tension pressure, and carbon monoxide partial pressure were on the order of 0.9 atm, 1×10^{-2} atm, and 0.1 atm, respectively.

When the inner heat source spacing was greater than 6.5 mm for 60 A arc, 900 W CO_2 laser/GTA hybrid welding of 321 stainless steel, the cooling rate from 1073 K to 773 K at the centerline of the molten weld pool reduces from approximately 650 K s^{-1} to 400 K s^{-1}. The reduction in the cooling rate was the result of the welding process transitioning from hybrid to tandem welding. For all of the heat source separation distances analyzed during hybrid welding of 321 stainless steel, increasing arc current to 120 A and 180 A reduced the average cooling rate to approximately 350 K s^{-1} and 250 K s^{-1}, respectively.

Hybrid weld depth and heat source separation distance were not found to be directly proportional experimentally and theoretically for the CO_2 laser/GTA hybrid welded 321 stainless steel samples. The maximum hybrid weld depth was seen at some optimal heat source separation distance. The error between the calculated and experimental hybrid weld depths were less than 5%.

Nd:YAG laser/GTA hybrid welding resulted in similar weld depth compared to Nd:YAG laser welding (< 0.7 mm difference in this analysis) of A131 structural steel. However, hybrid welding lead to a significant increase in weld pool width over laser welding of A131 structural steel. The increase in weld width was on the order of 1 mm to 2.5 mm for the process parameters studied. The increase in weld pool width was the result of heat input from the arc, improved melting efficiency, and heat transfer aided by strong Marangoni convection. Wider weld pools improve the ability of the hybrid welding process to allow for gaps between large welded sections of material, without the necessity of additional bracing. Hybrid welding of plain carbon and stainless steels results in faster fluid flow (on the order of 400 mm s^{-1}), than laser (~300 mm s^{-1}) or arc welding (~100 mm s^{-1}). The faster fluid flow is the result of improved electromagnetic force and Marangoni stress driven convection by the addition of an arc heat source. However, the convection and fluid flow behavior can be expected to differ in the case of relatively high thermal conductivity materials compared to plain carbon and stainless steels, such as aluminum and copper alloys.

3.6 References

1. D. K. Aidun, S. A. Martin, Journal of Materials Engineering and Performance **6** (4), 496-502 (1997).
2. T. Fuhrich, P. Berger, H> Hugel, Journal of Laser Applications **13** (5), 178-186 (2001).
3. S. Kou, D. K. Sun, Metallurgical Transactions A-Physical Metallurgy and Materials Science **16** (2), 203-213 (1985).
4. C. Limmaneevichitr, S. Kou, Welding Journal **79** (5), 126S-135S (2000).

5. C. Limmaneevichitr, S. Kou, Welding Journal **79** (11), 324S-330S (2000).
6. Y. Naito, M. Mizutani, S. Katayama, Journal of Laser Applications **18** (1), 21-27 (2006).
7. W. Pitscheneder, T. DebRoy, K. Mundra, R. Ebner, Welding Journal **75** (3), S71-S80 (1996).
8. Y. Z. Zhao, Y. P. Lei, Y. W. Shi, Journal of Materials Science & Technology **21** (3), 408-414 (2005).
9. M. Gao, X. Zeng, Q. W. Hu, J. Yan, Science and Technology of Welding and Joining **13** (2), 106-113 (2008).
10. M. Gao, X. Y. Zeng, J. Yan, Q. W. Hu, Applied Surface Science **254** (18), 5715-5721 (2008).
11. M. Gao, X. Y. Zeng, B. Tan, J. C. Feng, Science and Technology of Welding and Joining **14** (4), 274-281 (2009).
12. B. Ribic, T. Palmer, T. DebRoy, International Materials Reviews **54** (4), 223-244 (2009).
13. Y. B. Chen, Z.L. Lei, L. Wu, Science and Technology of Welding and Joining **11** (4), 403-411 (2006).
14. B. Hu, and G. Den Ouden, Science and Technology of Welding and Joining **10** (1), 76-81 (2005).
15. B. Hu, and G. Den Ouden, Science and Technology of Welding and Joining **10** (4), 427-431 (2005).
16. B. D. Ribic, R. Rai, T. A. Palmer, T. DebRoy, presented at the Trends in Welding Research, Pine Mountain, GA, USA, 2008 (unpublished).
17. W. M. Steen, Journal of Applied Physics **51** (11), 5636-5641 (1980).
18. X. Hao, and G. Song, IEEE Transactions of Plasma Science **37** (1), 76-82 (2009).
19. Z. H. Rao, J. Zhou, S. M. Liao, H. L. Tsai, Journal of Applied Physics **107** (5), 054905 (2010).
20. J. Hu, H. L. Tsai, Journal of Physics D- Applied Physics **41** (6), 065202 (2008).
21. J. J. Lowke, M. Tanaka, M. Ushio, Journal of Physics D- Applied Physics **38** (18), 3438-3445 (2005).
22. S. Mishra, T. J. Lienert, M. Q. Johnson, T. DebRoy, Acta Materialia **56** (9), 2133-2146 (2008).
23. M. Tanaka, J. J. Lowke, Journal of Physics D- Applied Physics **40**, R1-R23 (2007).
24. M. Do-Quang, G. Amberg, C. O. Pettersson, Journal of Heat Transfer-Transactions of the ASME **130** (9), 092102 (2008).
25. J. Zhou, H. L. Tsai, T. F. Lehnhoff, Journal of Physics D- Applied Physics **39** (24), 5338-5355 (2006).
26. S. Safdar, L. Li, M. A. Sheikh, Journal of Physics D- Applied Physics **40** (2), 593-603 (2007).
27. B. J. Aalderink, D. F. de Lange, R. G. K. M. Aarts, J. Meijer, Journal of Physics D- Applied Physics **40** (17), 5388-5393 (2007).
28. C. Limmaneevichitr, S. Kou, Welding Journal **79** (8), 231S-237S (2000).
29. M. G. Deutsch, A. Punkari, D. C. Weckman, H. W. Kerr, Science and Technology of Welding and Joining **8** (4), 246-256 (2003).

30. U. Jasnau, J. Hoffmann, P. Seyffarth, Robotic Welding, Intelligence and Automation **299**, 14-24 (2004).
31. T. Jokinen, T. Viherva, H. Riikonen, V. Kujanpaa, Journal of Laser Applications **12** (5), 185-188 (2000).
32. T. Jokinen, P. Jernstrom, M. Karhu, I. Vanttaja, V. Kujanpaa, presented at the First International Symposium on High-Power Laser Macroprocessing, Osaka, Japan, 2002 (unpublished).
33. T. Kim, Y. Suga, T. Koike, JSME International Journal Series A-Solid Mechanics and Material Engineering **46** (3), 202-207 (2003).
34. M. Kutsuna, L. Chen, presented at the First International Symposium on High-Power Laser Macroprocessing, Osaka, Japan, 2002 (unpublished).
35. L. M. Liu, J. F. Wang, G. Song, Materials Science and Engineering A-Structural Materials Properties Microstructure and Processing **381** (1-2), 129-133 (2004).
36. G. Song, L. M. Liu, M. S. Chi, J. F. Wang, Magnesium-Science, Technology and Applications **488-489**, 371-375 (2005).
37. Y. Wang, H. L. Tsai, Metallurgical and Materials Transactions B- Process Metallurgy and Materials Processing Science **32** (3), 501-515 (2001).
38. Y. Z. Zhao, H. P., Zhou, Y. W. Shi, Modeling and Simulation in Materials Science and Engineering **14** (3), 331-349 (2006).
39. T. DebRoy, S. A. David, Reviews of Modern Physics **67**, 85-112 (1995).
40. R. Rai, G. G. Roy, T. DebRoy, Journal of Applied Physics **101** (5), 054909 (2007).
41. R. Rai, J. W. Elmer, T. A. Palmer, T. DebRoy, Journal of Physics D- Applied Physics **40** (18), 5753-5766 (2007).
42. B. Ribic, R. Rai, T. DebRoy, Science and Technology of Welding and Joining **13** (8), 683-693 (2008).
43. L. Zhao, S. Tsukamoto, G. Arakane, T. Sugino, presented at the International Congress on Applications of Laser and Electro-Optics, Orlando, FL, 2009 (unpublished).
44. X. He, J. W. Elmer, T. DebRoy, Journal of Applied Physics **97** (8), 084909 (2005).
45. S. Mishra, T. DebRoy, Materials Science and Engineering A **454-455**, 477-486 (2007).
46. K. Mundra, T. DebRoy, K. M. Kelkar, Numerical Heat Transfer Part A-Applications **29** (2), 115-129 (1996).
47. R. Rai, P. Burgardt, J.O. Milewski, T.J. Lienert, and T. DebRoy, Journal of Physics D- Applied Physics **42** (2), 025503 (2009).
48. R. Rai, S. M. Kelly, R. P. Martukanitz, T. DebRoy, Metallurgical and Materials Transactions A-Physical Metallurgy and Materials Science **39A** (1), 98-112 (2008).
49. A. F. H. Kaplan, M. Mizutani, S. Katayama, A. Matsunawa, Journal of Physics D-Applied Physics **25** (11), 1218-1228 (2002).
50. J. Y. Lee, S. H. Ko, D. F. Farson, C. D. Yoo, Journal of Physics D- Applied Physics **35** (13), 1570-1576 (2002).
51. H. Ki, P. S. Mohanty, J. Mazumder, Metallurgical and Materials Transactions A-Physical Metallurgy and Materials Science **33** (6), 1817-1830 (2002).

52. W. Sudnik, Radak, D., Erofeew, W., Journal of Physics D- Applied Physics **31** (24), 3475-3480 (1998).
53. P. Sahoo, T. DebRoy, M. J. McNallan, Metallurgical Transactions B-Process Metallurgy **19** (3), 483-491 (1988).
54. A. Kumar, T. DebRoy, Metallurgical and Materials Transactions A-Physical Metallurgy and Materials Science **38A**, 506-519 (2007).
55. H. Zhao, T. Debroy, Journal of Applied Physics **93** (12), 10089-10096 (2003).
56. J. Zhou, W. H. Zhang, H. L. Tsai, S. P. Martin, P. C. Wang, R. Menassa, presented at the ASME International Mechanical Engineering Congress and Exposition, Washington, D.C., 2003 (unpublished).
57. J. Zhou, H. L. Tsai, International Journal of Heat and Mass Transfer **51** (17-18), 4353-4366 (2008).
58. R. J. Fruehan, United States Steel Co., American Society for Metals, *The Making, Shaping and Treating of Steel*, 11th ed. (AISE Steel Foundation, Pittsburgh, PA, 1999).
59. T. Rosenqvist, *Principles of Extractive Metallurgy*. (Tapir Academic Press, Trondheim, Norway, 2004).
60. G. K. Sigworth, J. F. Elliott, Metal Science **8**, 298-310 (1974).
61. D. R. Poirier, G. H. Geiger, *Transport Phenomena in Materials Processing*. (The Minerals, Metals, and Materials Society, Warrendale, PA, 1994).
62. A. Kumar, T. DebRoy, Journal of Applied Physics **94** (2), 1267-1277 (2003).
63. S. V. Patankar, *Numerical Heat Transfer and Fluid Flow*. (Hemisphere Publishing Corp., New York, New York, 1980).
64. R. B. Bird, W. E. Stewart, E. N. Lightfoot, *Transport Phenomena*. (John Wiley & Sons, New York, 1960).
65. T. A. Palmer, J.W. Elmer, R. Pong, M.D. Gauthier, Internal Report Report No. UCRL-TR-206885, 2004.
66. X. He, J. T. Norris, P. W. Fuerschbach, T. DebRoy, Journal of Physics D-Applied Physics **39** (3), 525-534 (2006).
67. E. A. Brandes, G. B. Brook, *Smithells Metals Reference Book*, 7th ed. (Butterworth-Heinemann, Woburn, MA, 1992).
68. S. Tsukamoto, L. Zhao, G. Arakane, T. Sugino, K. Yasuda, presented at the International Congress on Applications of Laser and Electro-Optics, Orlando, FL, 2009 (unpublished).
69. S. Kou, *Welding Metallurgy*, 2nd ed. (John Wiley & Sons, Inc., 2003).
70. D. A. Schauer, W. H. Giedt, S. M. Shintaku, Welding Journal **57** (5), S127-S133 (1978).
71. J. F. Lancaster, *The Physics of Welding*. (Pergamon Press, New York, NY, 1986).
72. W. Zhang, G. G. Roy, J. W. Elmer, T. DebRoy, Journal of Applied Physics **93** (5), 3022-3033 (2003).
73. G. M. Oreper, J. Szekely, Metallurgical Transactions A-Physical Metallurgy and Materials Science **18** (7), 1325-1332 (1987).
74. R. Rai, T. A. Palmer, J. W. Elmer and T. Debroy, Welding Journal **88** (3), 54S-61S (2009).

Chapter 4

HYBRID WELDING PLASMA CHARACTERISTICS

4.1 Introduction

The interaction between an electric arc and a laser beam is important for the operation of laser-arc hybrid welding. Although both arc and laser plasmas have been studied before, the underlying mechanism of the synergistic interaction between the two heat sources during hybrid welding is not well understood. During laser-arc hybrid welding, plasma properties affect arc stability[1-4] and the absorption of laser energy by the plasma.[5-8] Pronounced vaporization of alloying elements due to the high power density of the laser beam can lead to increased arc stability resulting from enhanced plasma electrical conductivity,[1, 9-13] electron density,[11, 14] electron temperature,[15] and arc current density.[15] Electron density and plasma temperature have a significant impact on the electrical conductivity of arc and laser induced plasmas.[16-17] A recent spectroscopy study of hybrid welding plasmas[18] found that the average plasma temperature calculated using the Boltzmann plot method decreased with increase in metal vapor concentration in the plasma. However, a detailed study of the electron temperature, electron density, and the electrical conductivity of the hybrid welding plasma for various welding conditions remains to be undertaken.

Optical emission spectroscopy has been successfully used previously for determining temperatures, species densities, and electrical conductivities of laser,[19-22] electrical arc[16, 23-25] and hybrid welding plasmas. Previous research in hybrid welding[26-29] has indicated the two most important variables that significantly affect weld bead porosity, weld geometry and plasma light emission are heat source separation distance and arc current. Here, we examine hybrid welding plasmas using optical emission spectroscopy for various heat source separation distances and arc currents to better understand plasma electron temperatures, atomic and ionic species densities, total electron density, and plasma electrical conductivity during hybrid welding. The electrical conductivity of the hybrid welding plasma is compared with that of the arc plasma to understand the arc stability during hybrid welding.

4.2 Experimental procedures

Nd:YAG laser, arc, and laser/ gas tungsten arc (GTA) hybrid welding were performed on 304L stainless steel tubing with a 200 mm outer diameter and 6.4 mm wall thickness. The composition of the 304L stainless steel is shown in Table 4.1. Arc current and heat source separation distance were varied in order to determine their effects on hybrid welding plasma electron temperatures, composition, atom, ion, and electron densities, electrical conductivity, and arc stability. Important welding process parameters are provided in Table 4.2. The arc and trailing shielding gases were argon. The distance between the laser beam symmetry axis and arc electrode tip on a horizontal plane is referred in this paper as the heat source separation distance.[30] The laser beam was the leading heat source. High speed video was taken of the hybrid welding plasmas in order to observe the plasma cross section shape close to the laser focal point. The light intensity observed by the camera was attenuated by an appropriate combination of low pass and neutral density filters.

Table 4.1: 304L Stainless Steel composition

Element	C	P	Si	Ni	N	Mn	S	Cr	Mo
Weight %	0.019	0.036	0.410	8.150	0.070	1.420	0.015	18.280	0.460

A 0.5 m focal length spectrometer using a 1200 lines inch^{-1} grating was used for the optical emission spectroscopy. The entrance slit and median wavelength were 20 µm and 535 nm, respectively. Light was collected from the plasmas in a 0.2 mm radius spot for a sampling time of 0.2 seconds. The relatively long exposure time provided a time-average evaluation of the plasma properties. In order to avoid saturation, a 0.5 neutral density filter was placed in front of the spectrometer entrance slit. The intrinsic resolution of the spectrometer was determined to be approximately 0.75 nm. The spectroscopic data were obtained within a horizontal plane 0.75 mm above top dead center of the cylindrical workpiece. Fig. 4.1 is a schematic diagram of the optical emission spectroscopy and high speed camera setup. The aperture leading to the spectrograph was 200 mm from the laser focal point on the cylindrical workpiece. The incoming light from the aperture traveled along an optical fiber to the spectrograph and liquid nitrogen cooled CCD detector. The high speed camera lens was located approximately 1040 mm from the laser focal point.

Table 4.2: Nd:YAG laser, GTA, and laser/GTA hybrid welding process parameters

Process Parameters	
Laser power (W)	1700
Arc currents (A)	101, 121, 141
Arc voltage (V)	14
Laser beam radius (μm)	200
Heat source separation distance (mm)	4, 6
Arc angle relative to workpiece surface (degrees)	65
Arc electrode included tip angle (degrees)	40
Arc electrode material	Thoriated tungsten
Arc electrode diameter (mm)	2.4
Arc electrode length (mm)	32
Arc length (mm)	3
Welding speed (mm s^{-1})	8.5
Arc shielding gas flow rate (L min^{-1})	17
Trailing shielding gas flow rate (L min^{-1})	30

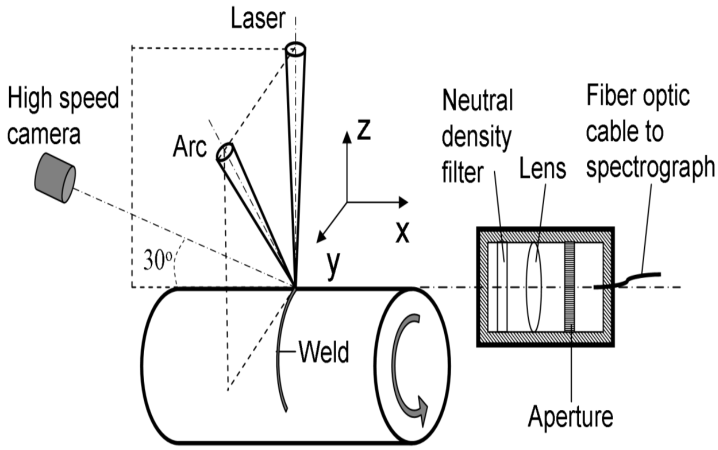

Fig. 4.1: A schematic diagram of the spectroscopy and high speed camera experimental setup. The rotation of the cylindrical workpiece is indicated in the figure.

4.3 Data analysis

4.3.1 Time-average plasma electron temperatures

Time-average plasma electron temperatures were calculated for arc, laser, and hybrid welding plasmas using deconvoluted measured spectral line intensities obtained via optical emission spectroscopy. The spectral lines were chosen to have upper energy level potentials which differed on the order of kT (approximately 1 eV), were of the same element and ionization state, and did not differ significantly in wavelength.[23, 31] Based upon these criteria, the two wavelengths chosen were the 522.49 nm and 534.83 nm Cr I peaks. The Cr I lines used were free of self-absorption, which was confirmed by the method described by Miller and DebRoy.[9] This spectroscopic method measures excitation temperature, which is not always equal to the electron temperature. However, for the chosen metal lines and the experimental conditions, it is reasonable to equate the excitation and electron temperatures. The time-average, T_e, electron temperature was calculated using:[23, 31]

$$T_e = \frac{c(E_{qa} - E_{qb})}{\log\left[\frac{(g_q A_{qp})_a}{(g_q A_{qp})_b}\right] - \log\left[\frac{\lambda_a}{\lambda_b}\right] - \log\left[\frac{I_a}{I_b}\right]} \tag{4.1}$$

where c is a constant whose value is 5040 K cm, E_{qa} and E_{qb} are the upper energy level potentials of peak 'a' and peak 'b' in units of cm^{-1}, g_q and A_{qp} are the upper energy level statistical weight (dimensionless) and transition probability in unit of s^{-1} for the corresponding peaks, λ_a and λ_b are the wavelengths of peaks 'a' and 'b', respectively in nm, and I_a and I_b are the deconvoluted intensities of the peaks (measured in counts). Fig. 4.2 shows that the data collected by the spectrometer includes the sum of the emissions from various radial locations along the line of sight of the spectroscope. However, in order to determine the local values of light intensity from various line of sight measurements within the plasma, an appropriate deconvolution scheme is needed.

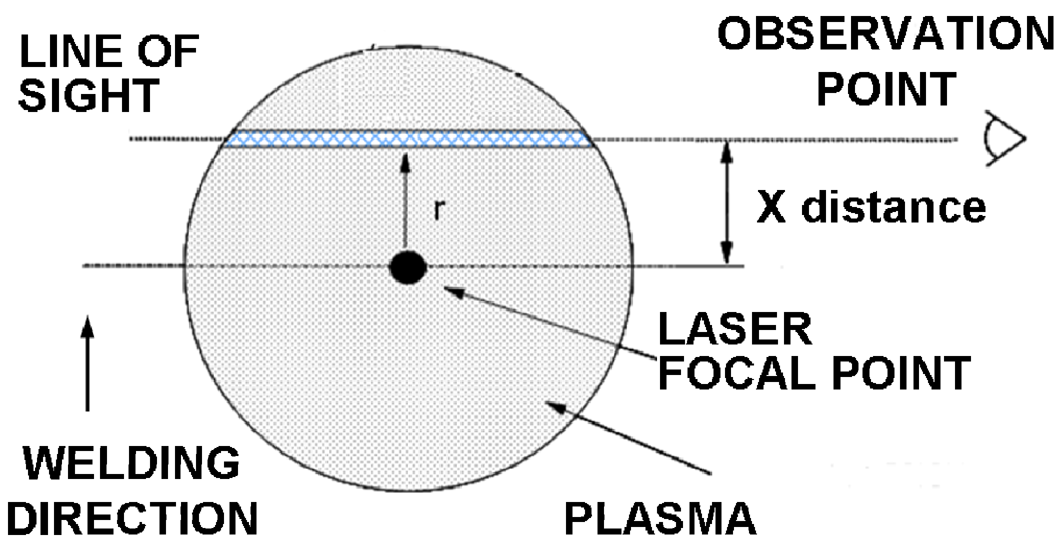

Fig. 4.2: A schematic diagram of the spectrometer line of sight data collection arrangement. The welding direction is perpendicular to the spectrometer line of sight.

An Abel transformation was performed on the measured spectral line intensities to deconvolute the measured line of sight data to intensity as a function of radius based on the method outlined by Barr.[32] The model used to perform the Abel transform and calculate the plasma average electron temperatures from measured spectral data is presented in Appendix B. A similar procedure has been applied for arc and laser plasmas.[31-32] High speed video imaging of the hybrid welding plasma close to the laser focal point, shown by Fig. 4.3, provided images of the circular plasma cross section necessary to justify the use of an Abel transform. Fig. 4.3 (a) shows the circular plasma cross section near the opening of the keyhole and weld pool top surface. In addition, the symmetry along the vertical axis of the cylindrical plasma above the weld pool top surface is shown in Fig. 4.3 (b).

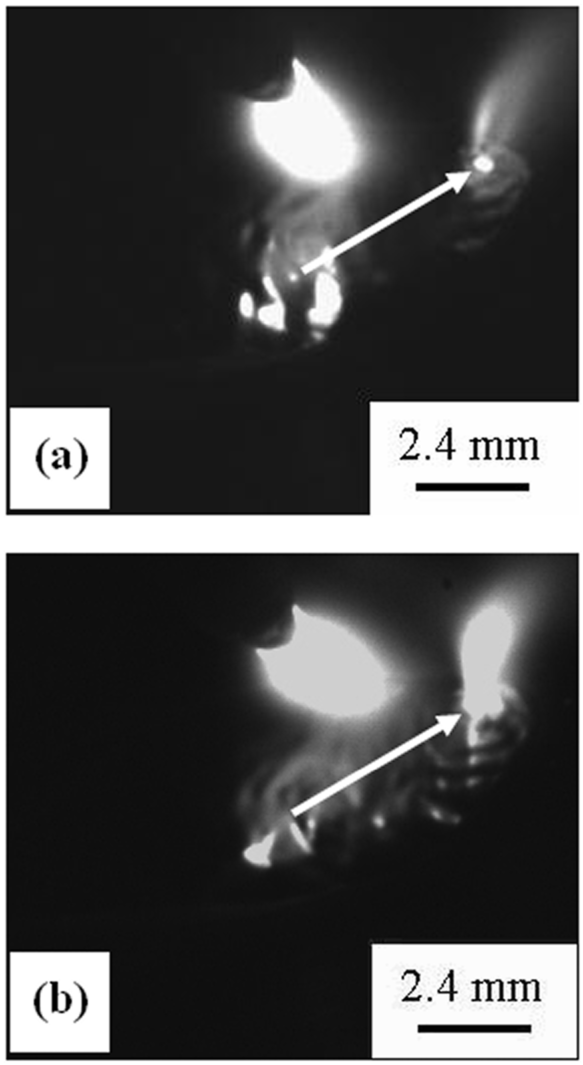

Fig. 4.3: Hybrid welding plasma circular cross section (a) close to keyhole opening and weld pool top surface and (b) circular symmetric plasma shape along the plasma vertical axis above weld pool top surface. The arc current and heat source separation distance are 101 A and 4mm, respectively. The arrows indicate the proximity of the laser focal point and the welding direction.

4.3.2 Atom, ion, and electron densities

The concentrations of the metal vapors and the shielding gas were needed for the calculation of plasma species densities and electrical conductivity.[23] The rates of vaporization of the alloying elements were calculated from numerically computed weld pool surface temperature fields obtained from a well tested, three dimensional, heat transfer and fluid flow model detailed in Chapter 3.[30, 33-34] The material properties[33] used to calculate the weld pool temperature and fluid velocity profiles for the welds on the 304L pipe are provided in Table 4.3.

The modified Langmuir equation has been used to calculate the vaporization flux during laser and laser-arc hybrid welding.[30, 33-34] Several experimental and theoretical studies[35-38] have determined vapor compositions,[36] weld material composition,[38] and welded specimen weight loss[35-36] using the modified Langmuir equation and is defined as:

$$J_i = \frac{a_i P_i}{b\sqrt{2\pi R M_i T}} \tag{4.2}$$

where J_i is the local molar vaporization flux of alloying element i in kg m^{-2} s^{-1}, a_i is the activity of alloying element i, P_i is the equilibrium partial pressure of alloying element i in atm at the local keyhole or weld pool surface temperature in Kelvin, T, b is a dimensionless constant with a value of 7.5 which accounts for the reduced vaporization rate at atmospheric pressure compared to that in perfect vacuum,[35-38] M_i is the atomic mass of alloying element i in kg $mole^{-1}$, and R is the ideal gas constant (8.314 J $mol^{-1}K^{-1}$). Using equation 4.2, the vaporization rate of an alloying element i inside the keyhole (in moles per second) is given by:

$$r_i^k = \int_k J_i \, dA_k \tag{4.3}$$

where k refers to an element of surface dA_k on the keyhole wall. The rate of vaporization of element i at any location along the weld pool top surface (r_i^s) was also calculated in a similar manner. The approximate chemical composition of the plasma was determined by assuming that the shielding gas and the metal vapors were well mixed:

$$x_i = \frac{r_i^k + r_i^s}{\sum r} \tag{4.4}$$

where $\sum r$ is the sum of the vaporization rates of all alloying elements inside the keyhole and along the top surface of the weld pool and the molar flow rate of the shielding gas given in Table 4.2. The mole fractions of the argon shielding gas in the plasma were calculated by replacing the numerator in equation 4.4 with the shielding gas molar flow rate. These mole fractions are needed to calculate the total electron density which is taken as the summation of the product of the mole fraction of each species and the electron density in a plasma comprised solely of each species:

$$N_e = \sum_{i=1}^{N} x_i n_e^i \tag{4.5}$$

where N is the total number of elements in the plasma and n_e^i is the electron density of a plasma composed of only pure element i.

For each pure species, the electron, ion and atom densities were obtained by solving the following three equations:

$$\frac{n_e^i n_i^i}{n_a^i} = \frac{Z_e^i Z_i^i (2\pi m_e k T_e)^{3/2} \exp(-V^i / kT_e)}{Z_a^i h^3} \tag{4.6}$$

$$n_e^i = n_i^i \tag{4.7}$$

$$n_e^i + n_i^i + n_a^i = 7.34\text{x}10^{27} / T_e \tag{4.8}$$

where n_e^i is the electron density, n_i^i is the ion density, n_a^i is the atom density, Z_e^i is the electron partition function (which is given a value of 2 based upon the degeneracy), Z_i^i is the ion partition function,[23, 39] m_e is the resting mass of an electron (9.11 x 10^{-31} kg), k is the Boltzmann constant, T_e is the time-average electron temperature in Kelvin, V^i is the ionization potential, Z_a^i is the atom partition function,[23, 39] and h is Planck's constant. Equation 4.6, often referred to as the Saha's equation, provides an equilibrium constant relating the number densities of electrons, ions and atoms of a pure species, at a given temperature T_e. Equation 4.7 represents quasi-neutrality of the plasma and equation 4.8 follows from an ideal gas behavior of the plasma where 7.34 x 10^{27} is a constant in units of K m^{-3} for a plasma at ambient pressure.[16, 23] For the calculation of the equilibrium number density of atoms, ions, and electrons, it was assumed that the temperatures of the plasma and atoms, ions, and electrons were equal. The model used to calculate the atom and ion species densities is presented in Appendix C.

Table 4.3: 304L stainless steel material properties used for numerical model calculations[30]

Property	
Density of solid (kg m^{-3})	7000
Density at boiling point (kg m^{-3})	5800
Solidus temperature (K)	1697
Liquidus temperature (K)	1727
Enthalpy of solid at melting point (J kg^{-1})	1.20×10^6
Enthalpy of liquid at melting point (J kg^{-1})	1.26×10^6
Specific heat of solid (J kg^{-1} K^{-1})	711
Specific heat of liquid (J kg^{-1} K^{-1})	795
Thermal conductivity of the solid (W m^{-1} K^{-1})	27
Thermal conductivity of the liquid (W m^{-1} K^{-1})	29
Coefficient of thermal expansion (1 K^{-1})	1.96×10^{-5}
Emissivity	0.2
$d\gamma/dT$ of the pure material (N m^{-1} K^{-1})	-4.3×10^{-4}
Concentration of surface active species (wt%)	0.015
Surface excess at saturation (mole m^{-2})	1.3×10^{-5}
Enthalpy of segregation (J mol^{-1})	-1.66×10^5
Entropy factor	0.00318

Apart from the calculation of total electron density using the calculated plasma composition and Saha's equation, which will be henceforth referred to as the model, Stark broadening[14, 40-41] was also used to estimate the total electron density in m^{-3} :

$$N_e \approx s\frac{\lambda_{1/2}^s}{\omega} \tag{4.9}$$

where s is a constant with a value of 0.5 x 10^{22} m^{-3}, $\lambda_{1/2}^s$ is the full-width-half-maximum (FWHM) of the 538.34 nm Fe I spectral line in Å and ω is the electron collision broadening parameter as a function of electron temperature available in the literature.[42] Since the Stark broadening total electron densities were calculated without considering the radial variation of the spectral line FWHM, the results were used only for an order-of-magnitude estimation of the total electron densities. The 538.34 nm Fe I spectral line was chosen for this study since previous studies have shown that this spectral line results in negligible self absorption.[43-44] The FWHM of spectral lines may increase due to natural, Doppler, and Stark broadening.[14] Therefore, in order to utilize Stark broadening for the calculation of total electron density, other forms of spectral line broadening should be negligible in comparison.[42] Natural broadening is often considered to be negligible.[14, 23, 45] Doppler broadening was also found to be negligible in this study and was calculated[14, 46] to be approximately 0.0056 nm at 12000 K .

4.3.3 Electrical conductivity

The electrical conductivities of the plasmas evaluated are given by:[23]

$$\sigma = \frac{e^2}{\sqrt{3kT_e m_e}}\frac{N_e}{N_e Q_i + \sum n_a^i Q_a^i} \tag{4.10}$$

where σ is the electrical conductivity in Siemens m^{-1}, e is the electron charge (1.6 x 10^{-19} C), T_e is the electron temperature of the plasma in Kelvin, N_e is the total electron density (m^{-3}), n_a^i is the atom density (m^{-3}), Q_i is the momentum transfer cross section for an electron-ion interaction (m^2), and Q_a^i is the momentum transfer cross section for an electron-atom interaction (m^2). The electron-atom interaction cross section values and calculation procedure for the momentum transfer cross section for an electron-ion interaction were taken from the literature.[23, 47-49]

4.4 Results and discussion

4.4.1 Temperature and velocity fields and alloying element vaporization

Alloying element vaporization rates are dependent on local temperature. Fig. 4.4 shows the computed three-dimensional heat transfer and fluid flow profiles for (a) arc, (b) laser, and (c) hybrid welding. At the weld pool surface, liquid metal is the result of surface tension driven Marangoni convection. Hybrid and laser welding result in the formation of a narrow vapor filled keyhole cavity due to the relatively high power density of the laser beam, which is the primary source of metal vapors in the plasma due to high temperatures at the keyhole walls. The keyhole is shown in Fig. 4.4 (b) and (c) by the 3034 K isotherm. The keyhole depth is very similar to the depth of the weld pool.[30, 33, 50] Higher temperature gradients during laser and laser-arc hybrid welding, compared to arc welding, result in faster fluid flow and better mixing. The radially outward fluid flow during laser welding is primarily the result of Marangoni convection while the fluid flow pattern during laser-arc hybrid welding is the result of both surface tension gradient and electromagnetic force.[30]

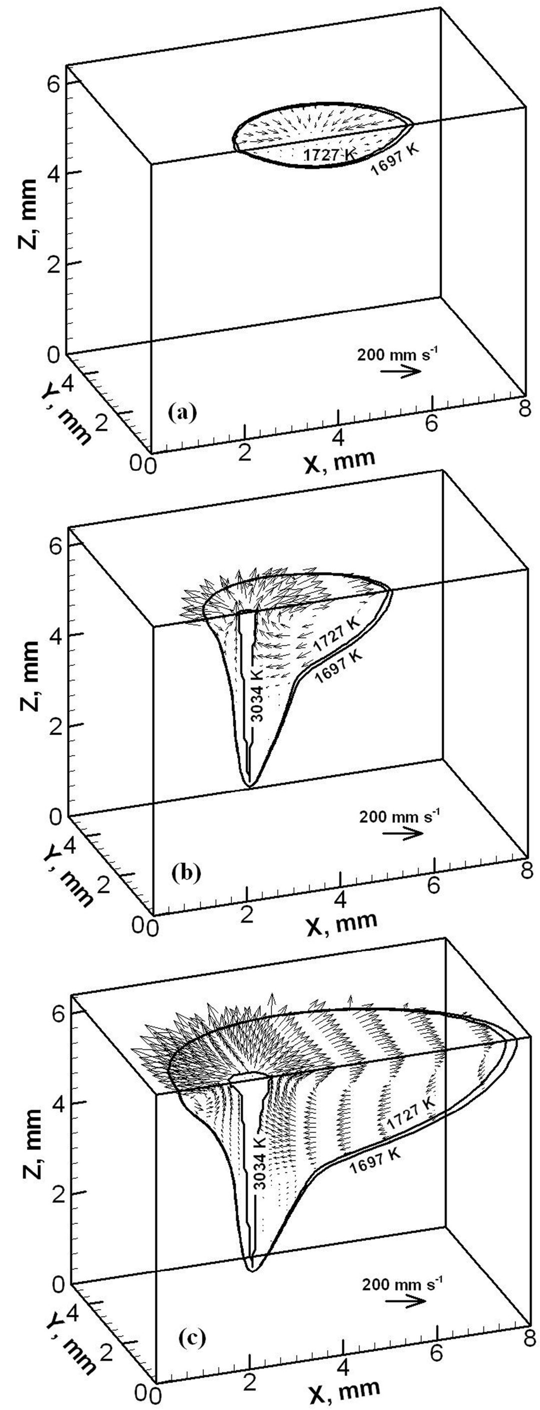

Fig. 4.4: Calculated (a) arc, (b) laser, and (c) hybrid welding three dimensional temperature and fluid flow profiles used for determining plasma composition. The arc current and laser power were 141 A and 1700 W. The hybrid welding heat source separation distance was 4 mm. All welds were performed at 8.5 mm s^{-1} on 304L stainless steel. The 1727 K and 1697 K isotherms are the alloy liquidus and solidus temperatures.

Fig. 4.5 shows calculated (a) laser, (b) arc, and (c) hybrid weld cross sections overlaid on top of experimentally obtained cross sections. Laser and laser-arc hybrid welding results in relatively deeper penetration due to the high power density of the laser beam and keyhole formation. The wide and shallow weld pool during arc welding results from the low power density of the arc and weld pool convection. The laser and laser-arc weld pools are relatively wider near the weld pool top surface due to the fast radially outward fluid flow in the weld pool. Hybrid welding results in a wider weld pool width than the arc or laser welds due to increasing arc power density with arc contraction and convection.[11, 27, 30, 51] The average error between the experimental and calculated weld bead depths and widths for all welding conditions considered were 6.4% and 8.2%, respectively.

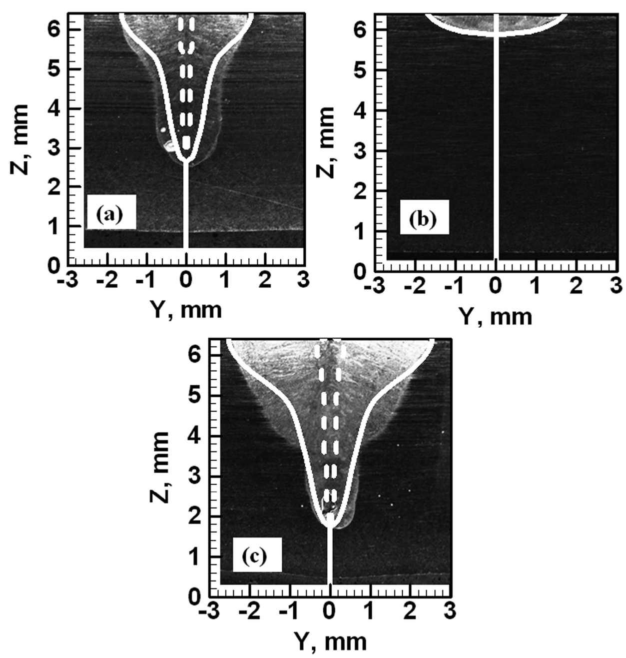

Fig. 4.5: (a) Laser, (b) arc, and (c) hybrid welding calculated weld bead cross sections overlaid on top of experimental weld bead cross sections. The laser power and arc current were 1700 W and 141 A. The heat source separation distance during hybrid welding was 6 mm. All welds were performed at 8.5 mm s^{-1} on 304L stainless steel. The solid isotherm indicates the 1697 K solidus. The dashed isotherm is the keyhole boundary, 3034 K.

The computed temperature fields are used to estimate the vaporization rates of alloying elements and the compositions of various species in the plasma. Table 4.4 shows calculated arc, laser, and hybrid welding plasma chemical compositions and weld depths. Arc welding plasma metal vapor concentrations are lower than those during laser and hybrid welding. Metal vaporization rates increase with keyhole formation and lead to higher amounts of metal vapors in the plasma during high power density laser and hybrid welding. Table 4.4 also shows that there may be an optimal heat source separation distance for a given arc current where hybrid weld penetration depth is greatest. This agrees with observations reported in the literature.[26, 51-52]

Table 4.4: Calculated arc, laser, and hybrid welding plasma compositions and weld depths for various arc current and heat source separation distances determined by the heat transfer and fluid flow model. The laser power was 1700 W.

Process	Arc Current (A)	Separation Distance (mm)	Calculated weld depth (mm)	Mole % Ar	Mole % Fe	Mole % Cr	Mole % Mn	Mole % Ni
Arc	101		0.56	99.98	1.08×10^{-3}	1.44×10^{-3}	1.34×10^{-2}	9.09×10^{-5}
	121		0.59	99.98	1.67×10^{-3}	2.39×10^{-3}	1.87×10^{-2}	1.44×10^{-4}
	141		0.68	99.98	9.99×10^{-4}	1.28×10^{-3}	1.56×10^{-2}	7.75×10^{-5}
Hybrid	101	4	4.26	92.43	3.66	2.34	1.26	0.3
	121	4	4.26	92.72	3.52	2.23	1.23	0.29
	141	4	4.26	92.42	3.66	2.33	1.29	0.3
	101	6	4.33	91.62	4.1	2.57	1.38	0.33
	121	6	3.87	94.89	2.47	1.55	0.89	0.2
	141	6	4.66	89.99	4.94	3.08	1.59	0.4
Laser			3.87	95.21	2.39	1.46	0.75	0.19

When the heat source separation distance is 4 mm, the calculated weld depths for all of the considered arc currents are very similar during hybrid welding. The arc current has a negligible affect on hybrid weld pool penetration when the heat source separation is 4 mm and the keyhole surface area does not change appreciably. As a result, the metal vaporization rates are similar. When the heat source separation distance is 6 mm, weld penetration depth is greatest when the arc current is 141 A. Chen et al.[26] showed optimal heat source separation distance for maximum weld penetration depth increases with increasing arc current. In addition, when the heat source separation distance is 6 mm, the keyhole depth varies significantly with arc current resulting in variation of the metal vapor content of the plasma.

4.4.2 Time-average plasma electron temperatures

Fig. 4.6 shows a typical measured intensity versus wavelength plot for plasma formed during hybrid welding with several spectral lines identified by wavelength and species type. Within the observed wavelength range, atomic iron and chromium were the most prominent species in the spectra for the welding of 304 L stainless steel. The plasma temperature affects the equilibrium number density of ionized species contained within the plasma and the plasma electrical conductivity. The time-average hybrid welding plasma electron temperatures calculated from deconvoluted spectral line intensities at the laser beam symmetry axis are shown as a function of arc current in Fig. 4.7. The error bars shown in Fig. 4.7 are for a 2% variation in the data based upon the maximum standard deviation for all of the arc current levels observed. Heat source separation distance affects electron temperatures close to the laser focal point during hybrid welding. Increasing heat source separation distance from 4 mm to 6 mm reduces electron temperatures during hybrid welding by approximately 500 K, 700 K, and 900 K when arc current is 101 A, 121 A, and 141 A, respectively. Electron temperatures decrease with increasing heat source separation distance because of the reduction in heat flux near the laser focal point. Increasing heat source separation distance more significantly affects electron temperatures during hybrid welding than increasing arc current within the range of currents studied.

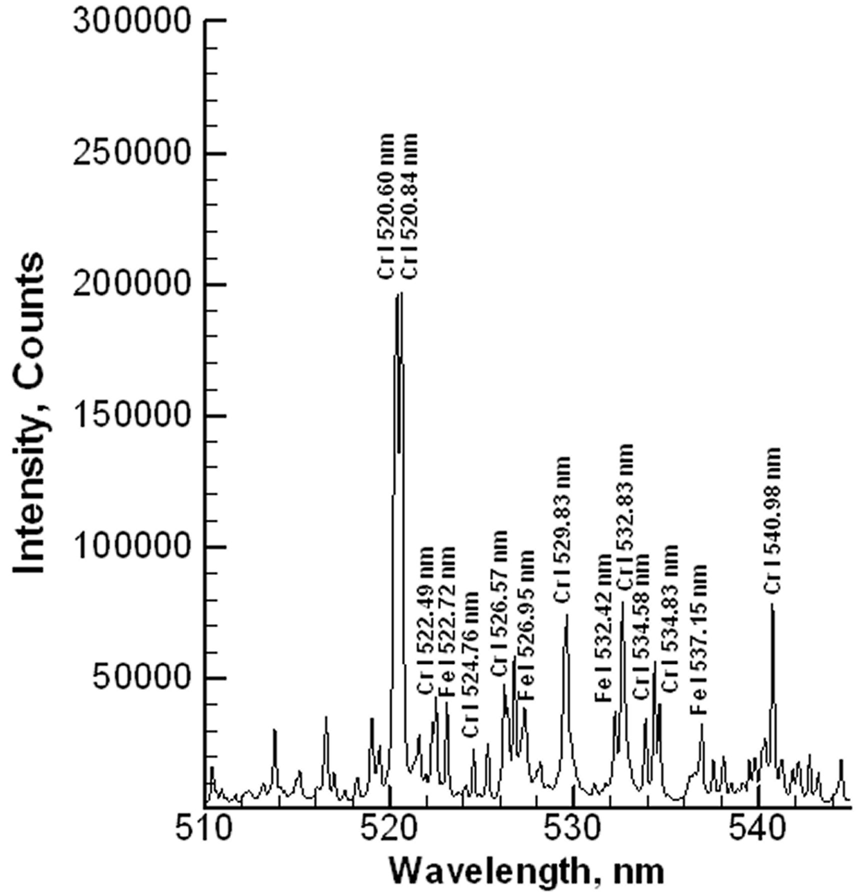

Fig. 4.6: Measured intensity versus wavelength plot for plasma formed during hybrid welding with several spectral lines identified by wavelength and species type. The laser power and arc current were 1700 W and 141 A, respectively. The heat source separation distance was 4 mm. The spectral data were taken from 0.75 mm above the laser focal point.

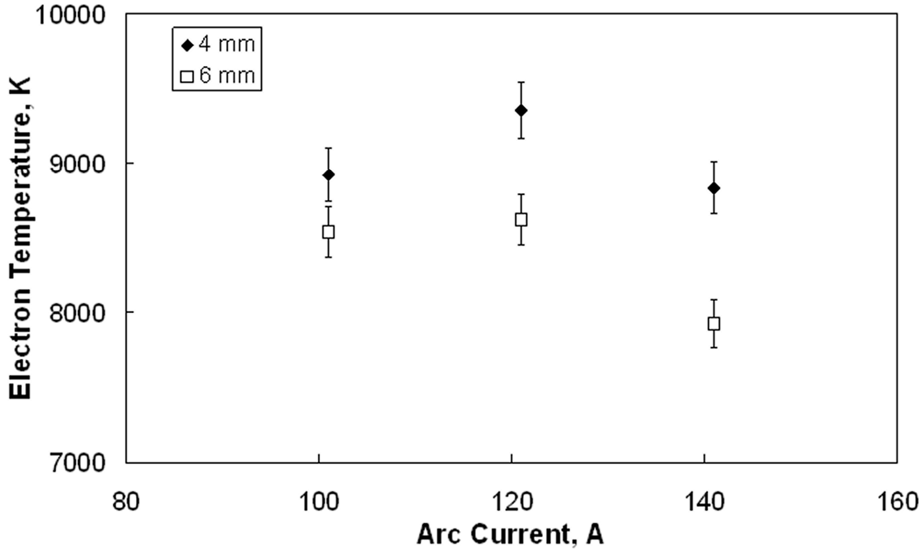

Fig. 4.7: Time-average electron temperatures calculated from spectral measurements as a function of arc current for hybrid welding plasmas when the heat source separation distance is 4 mm and 6 mm. The laser power was 1700 W. The data were obtained from 0.75 mm above the laser focal point. The laser was focused at the workpiece surface.

A comparison of laser-arc hybrid, arc, and laser welding plasma electron temperatures is shown in Fig. 4.8 as a function of arc current. The temperature values are from the arc symmetry axis during arc welding and laser beam symmetry axis during laser and hybrid welding. Laser welding plasma electron temperatures were slightly lower than those during arc welding and may be due to variations in the measured spectra or fluctuations in the plasma characteristics due to keyhole in stability. In addition, it could be due to the laser plasma geometry being very different to the arc and hybrid welding plasmas and the observation location was more on the plasma fringe (simply a cooler region) compared to the arc plasma. Due to high heat flux from the addition of a second heat source during hybrid welding, the time-average electron temperatures are greater than those during arc or laser welding. This may appear to be somewhat different from a previous work[14] which suggested that the electron temperatures in hybrid welding may be slightly lower than that during arc welding. It was argued that radiation energy losses in the plasma resulted in lower electron temperatures during hybrid welding compared to arc welding.[14] However, the line intensities were not deconvoluted in that work and as a result, the true value of the electron temperature at the laser beam axis during hybrid welding was never evaluated.[14] In addition, the electron temperatures[14] obtained from the line of sight data are less accurate than electron temperatures calculated using deconvoluted spectral intensities.[23, 32]

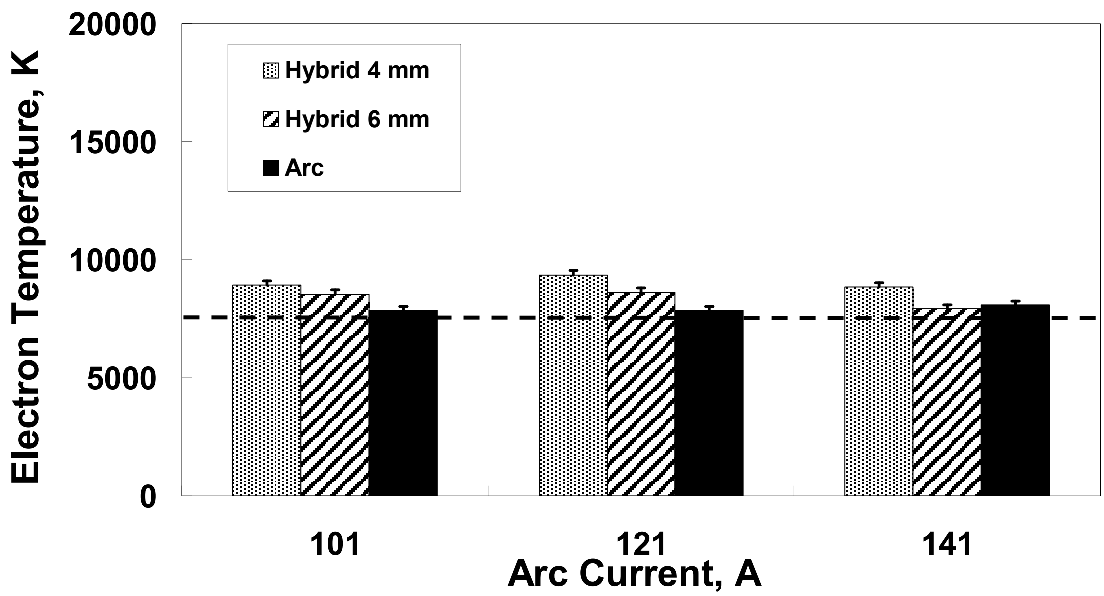

Fig. 4.8: Time-average electron temperatures calculated from spectral measurements for arc, laser, and hybrid welding plasmas as a function of arc current. The data were obtained from the laser beam symmetry axis during laser and hybrid welding and the arc symmetry axis during arc welding. The dashed line is the calculated laser welding plasma time-average electron temperature. Heat source separation distances were 4 mm and 6 mm during hybrid welding. The error bars are based on a 2% standard deviation in the data.

Since electron temperature establishes the equilibrium species densities and electrical conductivity of the plasma, it is important to know the temperature variation along the plasma radius.[1, 13, 15, 53] Calculated time-average electron temperatures are plotted as a function of horizontal location for various heat sources in Fig. 4.9. During hybrid welding, electron temperatures near the laser beam symmetry axis were higher than radially further away. In the case of laser welding, the laser welding plasma electron temperatures shows negligible radial variation in electron temperature due to the approximately uniform power distribution. During arc welding, electron temperatures were highest at the arc symmetry axis for 101 A and 121 A currents. When increasing the arc current from 101 A to 121 A, the electron temperature at the arc symmetry axis were similar for arc welding. However, with increasing radial distance from the symmetry axis, the electron temperatures decreased much more quickly for 101 A arc current than for 121 A.

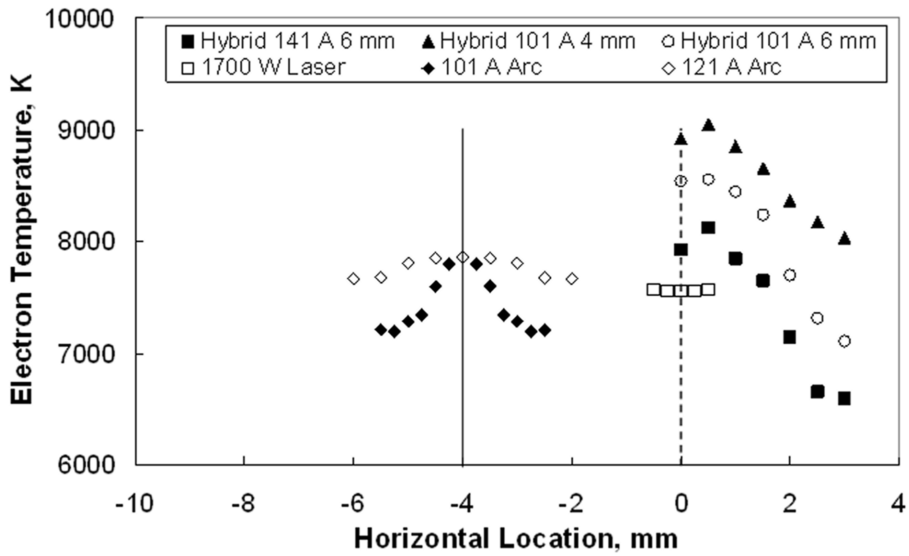

Fig. 4.9: Calculated arc, laser, and hybrid welding plasma electron temperatures from spectral measurements as a function of horizontal location relative to the laser focal point. The laser symmetry axis is at 0 mm and the arc symmetry axis is at – 4 mm. The hybrid welding was performed with a 1700 W laser and 101 A or 141 A arc current. The hybrid welding heat source separation distance was varied from 4 mm to 6 mm using a constant arc current.

4.4.3 Atom, ion, and electron densities

Atom, ion, and total electron densities calculated for argon hybrid welding plasma as a function of electron temperature are shown in Fig. 4.10. The highest electron temperature determined for hybrid welding was 9357 K. At this or lower temperatures, the concentrations of the doubly or multiply ionized species are negligible. Only at much higher temperatures, the concentrations of doubly charged ions become important. For example, Boumans[23], and Glowacki[54] found the second ionization to become important above 15,000 K for various non-metallic species. Tix and Simon[55] found that “Doubly ionized iron atoms become important only for electron temperatures greater than about 1.6 eV.” (= 18,567 K). In addition, singly ionized metallic species in the plasma contribute a significant fraction of the total electron number density for hybrid and laser welding plasmas. Singly ionized metallic species can be produced at plasma temperatures as low as approximately 500 K. Plasma atomic species densities decrease with increasing electron temperatures due to ionization and volume expansion. The number density singly ionized species and the electrons they contribute to the plasma increase with increasing electron temperature up to a critical point. With increasing temperature, volume expansion becomes increasingly significant relative to ionization and the singly ionized species densities increase at a lower rate. When electron temperatures are higher than 10,200 K, volume expansion causes most singly ionized metallic species densities to decrease. In the case of argon and nickel, the critical temperatures are 17,000 K and 11,360 K, respectively. The number densities of chromium, manganese, and iron ions are relatively greater than nickel due to their ionization potentials and vaporization rates. Nickel has the second highest[42] ionization potential (7.64 eV) of iron (7.9 eV), chromium (6.77 eV), manganese (7.43 eV) and nickel. However, since the vaporization rate of nickel is lowest of all the alloying elements considered, the concentration of singly ionized species is lower. The amount of atomic argon is greater than the other elements due to relatively higher concentration in the plasma. The argon atom and ion species lines intersect at a higher temperature than the other elements in the plasma due to argon's relatively higher ionization potential.

Table 4.5 shows calculated total electron densities for arc, laser, and hybrid welding plasmas. Total electron densities calculated using the analytical equations are of the same order of magnitude as those calculated using iron spectra Stark broadening for hybrid welding plasma. However, the arc and laser plasma total electron densities determined via the analytical method are lower than those calculated from Stark broadening, which may occur because Stark broadening is not predominant[56] when the electron density of the plasma is less than the order of 10^{22} m^{-3}.

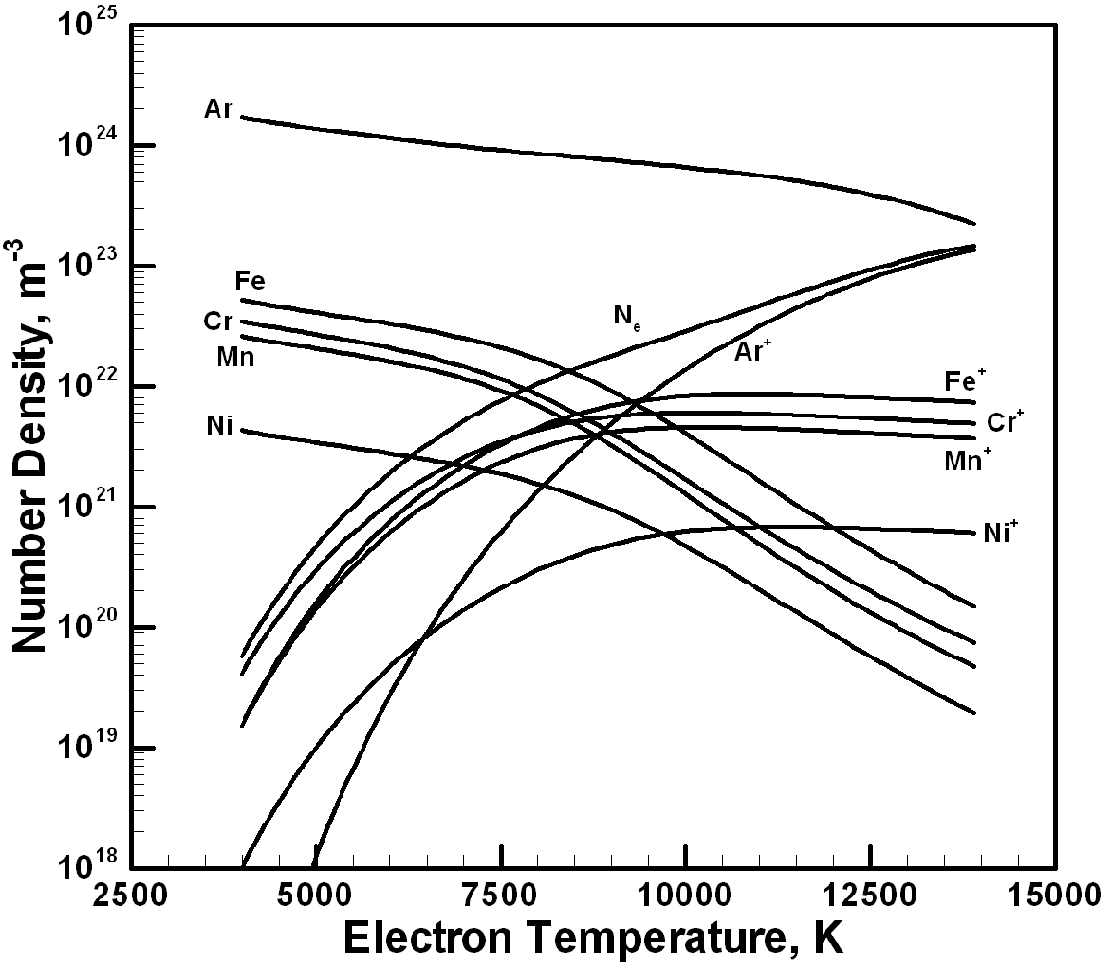

Fig. 4.10: Calculated atom, ion, and total electron densities for hybrid welding argon plasma containing metal vapors as a function of electron temperature. The arc current and heat source separation distance were 121 A and 4 mm. The data were obtained at the laser beam symmetry axis and the laser power was 1700 W. The total electron density of the plasma is given by N_e.

Table 4.5: Arc, laser, and hybrid welding plasma total electron densities calculated via Stark broadening and the analytical method. The data were obtained from the laser beam symmetry axis during laser and hybrid welding and the arc symmetry axis during arc welding for various arc currents and heat source separation distances. The laser power in all cases was 1700 W.

Process	Arc current (A)	Separation distance (mm)	Electron temperature (K)	Electron density using analytical method (m^{-3})	Electron density using iron Stark broadening (m^{-3})
Arc	101		7861	1.20×10^{21}	1.00×10^{22}
	121		7865	1.22×10^{21}	1.30×10^{22}
	141		8081	1.66×10^{21}	1.67×10^{22}
Hybrid	101	4	8924	2.19×10^{22}	1.58×10^{22}
	121	4	9357	2.56×10^{22}	1.35×10^{22}
	141	4	8838	2.12×10^{22}	1.76×10^{22}
	101	6	8540	2.02×10^{22}	1.66×10^{22}
	121	6	8623	1.39×10^{22}	1.52×10^{22}
	141	6	7927	1.69×10^{22}	1.86×10^{22}
Laser			7558	6.92×10^{21}	2.00×10^{22}

In Table 4.5, the total electron densities calculated using the analytical equations are greater for hybrid welding than for arc or laser welding, which agrees with previous research.[11, 14] Plasma total electron densities calculated from the analytical method increase with increasing plasma temperature within the range of electron temperatures studied. The analytical results show that the total electron density for the laser welding plasma is higher than that for the arc welding plasma due to greater concentrations of metal vapors. Calculated laser welding plasma total electron density (using the analytical method) and electron temperature were about double and within 6% difference, respectively, compared to values reported in the literature.[57] The literature reported values for 1000 W Nd:YAG pulsed laser welding of A316L stainless steel calculated using Stark broadening of the 538.3 nm Fe I spectral line.[57] The electron temperatures and total electron densities ranged from 4500 K to 7150 K and 3×10^{22} m^{-3} to 6.5×10^{22} m^{-3} for various locations in the plasma and pulse durations. The calculated Stark broadening total electron densities from Table 4.5 and in the literature differed by approximately 33% to 150%. The calculated total electron densities for hybrid welding plasmas were higher than those for laser and arc welding due to higher vaporization rates and higher plasma temperatures. High density of electrons in the hybrid welding plasma can increase plasma electrical conductivity and improve arc stability.

Results presented in Table 4.5 do not show any clear effect of increasing arc current during hybrid welding on the total electron densities calculated using the analytical method. This means that hybrid welding arc stability may not be affected by increasing arc current within the narrow range of arc currents evaluated. However, increasing heat source separation distance during hybrid welding decreases the total number density of electrons. As the arc moves further from the laser beam focal point, the arc radius increases which results in a lower arc peak power density[11, 27, 30, 51] If the heat source separation increases so that the arc can no longer bend and root within close proximity of the laser focal point, the arc heat flux near the keyhole can decrease and lower the plasma total electron density.

Errors in the values of electron density and electrical conductivity in the plasma may result from possible inaccuracy of the computed weld pool temperatures and the imperfect mixing of the metal vapors with the argon shielding gas. These potential sources of errors are critically examined. In keyhole mode welding, most of the vaporization of alloying elements occurs from within the keyhole, since the vaporization rate depends strongly on temperature. The surface temperature in the keyhole is the boiling point of the alloy, i.e., the temperature at which the sum total of the equilibrium pressures of all alloying elements equals the local pressure. This pressure is the ambient pressure, since the keyhole is open to its environment. The boiling point depends on the alloy composition and since the alloying elements follow ideal behavior (activity = mole fraction) near the boiling point, its uncertainty is equal to the uncertainty in the available vapor pressure data which is small. On the other hand, the temperature field on the weld pool surface outside the keyhole has some uncertainty because it is numerically computed. However, the minimum (solidus temperature) and the maximum values (boiling point) in the field are known with certainty. Calculations show that only about 11% of the metal vapors originate from outside of the keyhole and is susceptible to some errors. Even an unrealistically large error in the vaporization rate outside the keyhole such as 25% will only contribute 2.7% error in the overall vaporization rate from the weld pool.

The impact of imperfect mixing of the metal vapors with the argon shielding gas on electron density and electrical conductivity can be understood from a study of the effect of metal vapor concentrations on plasma properties. Three hypothetical cases were examined. First, the electron density was calculated by assuming perfect mixing of metal vapors with the argon shielding gas. Second, the vaporization rates of each metallic element, i.e., Fe(g), Cr(g), Mn(g), and Ni (g) were each reduced by 10%, keeping the argon flow rate constant and the electron density was determined for the new composition of the species mixture. Third, the vaporization rates of each alloying elements were increased by 10%, again keeping the argon shielding gas constant. The computed results, presented in Table 4.6, show that the variation of computed electron density was about 7.3% when the vaporization rates were changed by 10%. Similarly, plasma electrical conductivity varied 1.6% or less when the vaporization rate was changed by 10%. In summary, it may be concluded that imperfect mixing in the plasma will have some errors in the electron density and electrical conductivity calculations. However, the sensitivity analysis shows that the errors in the calculations are relatively small.

The plasma compositions combined with the pure single element equilibrium species densities calculated using Saha's equation provide a good approximation of the total electron densities in arc, laser, and hybrid welding plasmas. These calculated total electron densities agree with the previous literature in terms of hybrid welding electron densities being greater than those during arc welding[11, 14] and captures the effect of heat source separation distance on electron densities during hybrid welding.

Table 4.6: Analysis of imperfect mixing on hybrid welding plasma total electron density for an arc current and heat source separation of 101 A and 4 mm, respectively. The metal vaporization rates were varied by ± 10%. The percentages in parenthesis are the relative error to the total electron density when perfect mixing is assumed.

		Fe	Cr	Ni	Mn	Ar
Variation of total molar flow rate for entire weld (10^{-4} mol s^{-1})	original	3.19	2.11	0.264	1.59	103
	-10%	2.88	1.90	0.237	1.43	103
	+10%	3.51	2.32	0.290	1.75	103
Variation of species mole fractions	original	0.0291	0.0192	0.0024	0.0145	0.9348
	-10%	0.0264	0.0174	0.0022	0.0131	0.9409
	+10%	0.0318	0.0210	0.0026	0.0158	0.9287
Electron density contribution by each element when T_e = 8924 K (10^{21} m^{-3})	original	6.98	5.68	0.482	4.19	4.50
	-10%	6.34	5.15	0.442	3.79	4.53
	+10%	7.63	6.21	0.523	4.57	4.47
Variation of total electron density (m^{-3})	original	2.18E x 10^{22}				
	-10%	2.02 x 10^{22}(-7.3%)				
	+10%	2.34 x 10^{22}(+7.2%)				
Variation of electrical conductivity (S m^{-1})	original	3328				
	-10%	3274 (-1.6%)				
	+10%	3370 (+1.3%)				

4.4.4 Electrical conductivity

Electrical conductivity of plasma depends on its chemical composition, temperature, and equilibrium total electron density.[11, 26] Calculated electrical conductivities for arc, laser, and hybrid welding plasmas are shown as a function of arc current in Fig. 4.11. Hybrid welding plasmas have relatively higher electrical conductivities compared to arc or laser welding. The combination of an arc and a laser beam enhance plasma electrical conductivity during hybrid welding due to high metal vaporization rates and plasma temperatures. Greater plasma electrical conductivity during hybrid welding improves arc stability compared to arc welding alone.

Fig. 4.11 shows that laser welding results in higher plasma electrical conductivity compared to arc welding which is the result of higher total electron density. With increase in arc current, the arc plasma electron density increases slightly as shown in Table 4.5, resulting in a corresponding increase in electrical conductivity. Hybrid welding plasma electrical conductivity and arc stability decrease with increasing heat source separation distance due to lower total electron densities and electron temperatures. However, increasing arc current does not result in a clear trend for plasma electrical conductivity during hybrid welding within the range of arc currents considered.

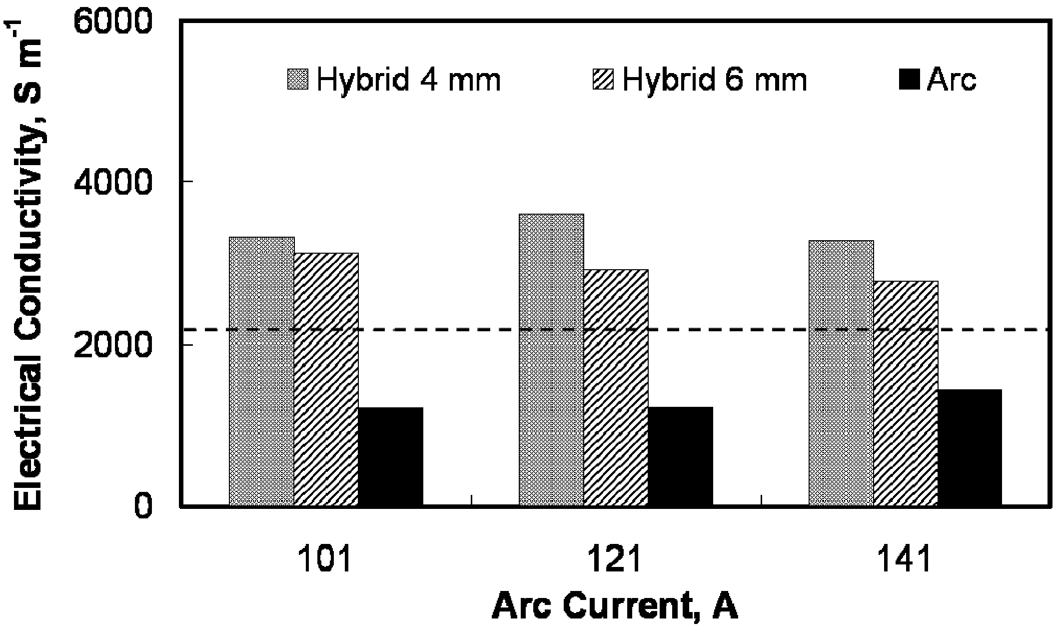

Fig. 4.11: Calculated electrical conductivities for arc, laser, and hybrid welding plasmas as a function of arc current. The electrical conductivity values were obtained from the laser beam symmetry axis during laser and hybrid welding and the arc symmetry axis during arc welding. The laser power was 1700 W. The dashed line shows the electrical conductivity of the laser welding plasma.

4.5 Summary and conclusions

Plasmas generated during GTA, Nd:YAG laser, and Nd:YAG laser/GTA hybrid welding of 304L stainless steel were successfully analyzed for electron temperatures, atom, ion, and electron densities, chemical compositions, and electrical conductivities using optical emission spectroscopy data. A well tested three dimensional heat transfer and fluid flow model was used in order to successfully calculate the temperature profiles and subsequent alloying element vaporization rates for arc, laser, and hybrid welding of 304L stainless steel. The calculated weld depth and width average error compared to the experimentally measured weld dimensions were 6.4% and 8.2% for all of the welding conditions considered, respectively. Using the calculated plasma temperatures from the measured emission spectra with the calculated plasma composition, the total electron density and subsequent electrical conductivity of the plasmas were successfully approximated.

Time-average plasma electron temperatures for arc, laser, and hybrid welding were on average 8000 K, 7500 K, 8950 K for a 4 mm separation distance, and 8350 K for a 6 mm separation distance, respectively. Hybrid welding plasma temperatures were greater than those during arc or laser welding of 304L stainless steel due to the increased heat flux from the addition of two heat sources. The hybrid welding plasmas resulted in higher total electron densities as the result of greater plasma temperatures and higher vaporization rates of alloying elements (Fe, Cr, Mn, and Ni). The total electron densities of arc, laser, and hybrid welding plasmas were approximately 1.4×10^{21} m^{-3}, 7×10^{21} m^{-3}, and 2×10^{22} m^{-3}, respectively. The vaporization rates of iron, chromium, and manganese during hybrid welding were on the order of 1×10^{-4} mol s^{-1} while that of nickel was on the order of 1×10^{-5} mol s^{-1}. The molar flow rate of the argon shielding gas was on the order of 1×10^{-2} mol s^{-1}. Due to the higher heat flux from the addition of two heat sources, hybrid welding resulted in plasma molar percentages of alloying elements approximately 3000 to 4000 times greater than during arc welding and 30% to 100% greater than during laser welding depending upon the alloying element, arc current, and heat source separation distance.

Arc, laser, and hybrid welding plasma average electrical conductivities were 1290 S m^{-1}, 2150 S m^{-1}, and 3000 S m^{-1}, respectively. Higher plasma electrical conductivity can explain why hybrid welding shows better arc stability compared to arc welding. The increase in plasma electrical conductivity and arc stability during hybrid welding arises due to greater heat flux with the addition of a second heat source, higher electron temperatures, metal vapor concentrations, and electron densities relative to during arc or laser welding. Increasing the heat source separation distance from 4 mm to 6 mm reduced hybrid welding plasma electrical conductivity approximately 500 S m^{-1}. Consequently, the reduction in plasma electrical conductivity may have an impact on arc stability. Plasma electrical conductivity decreases as a result of lower heat flux near the laser focal point and lower plasma temperatures. Increasing the heat source separation distance did not have an apparent effect on the vaporization rates of the stainless steel alloying elements considered. Increasing hybrid welding arc current within the range of currents evaluated did not show a clear trend for electron temperature, ion and electron densities, metal vapor concentrations, electrical conductivity, and consequently arc stability for a fixed heat source separation distance.

4.6 References

1. J. Haidar, Journal of Physics D- Applied Physics **43** (16), 165204 (2010).
2. Z. H. Rao, S. M. Liao, H. L. Tsai, Journal of Applied Physics **107** (4), 044902 (2010).
3. G. Xu, J. Hu, H. L. Tsai, Journal of Applied Physics **104** (10), 103301 (2008).
4. M. Schnick, U. Fuessel, M. Hertel, A. Spille-Kohoff, A. B. Murphy, Journal of Physics D- Applied Physics **43** (2), 022001 (2010).
5. A. K. Dasgupta, J. Mazumder, P. Li, Journal of Applied Physics **102** (5), 053108 (2007).
6. M. Beck, P. Berger, H. Hugel, Journal of Physics D- Applied Physics **28** (12), 2430-2442 (1995).
7. J. Dowden, P. Kapadia, Journal of Physics D- Applied Physics **28** (11), 2252-2261 (1995).
8. D. V. Bedenko, O. B. Kovalev, I. V. Krivtsun, Journal of Physics D- Applied Physics **43** (10), 105501 (2010).
9. R. Miller, T. DebRoy, Journal of Applied Physics **68** (5), 2045-2050 (1990).
10. R. Rai, P. Burgardt, J.O. Milewski, T.J. Lienert, and T. DebRoy, Journal of Physics D- Applied Physics **42** (2), 025503 (2009).
11. W. M. Steen, Journal of Applied Physics **51** (11), 5636-5641 (1980).
12. A. Gleizes, J. J. Gonzales, B. Liani, G. Raynal, Journal of Physics D- Applied Physics **26** (11), 1921-1927 (1993).
13. J. J. Gonzalez, A. Gleizes, P. Proulx, M. Boulos, Journal of Applied Physics **74** (5), 3065-3070 (1993).
14. X. Hao, and G. Song, IEEE Transactions of Plasma Science **37** (1), 76-82 (2009).
15. K. Etemadi, G. Y. Zhao, J. Mostaghim, Journal of Physics D- Applied Physics **22** (11), 1692-1696 (1989).

16. G. J. Dunn, T. W. Eager, Metallurgical Transactions A-Physical Metallurgy and Materials Science **17** (10), 1865-1871 (1986).
17. A. B. Murphy, M. Tanaka, K. Yamamoto, S. Tashiro, T. Sato, J. J. Lowke, Journal of Physics D- Applied Physics **42** (19), 194006 (2009).
18. L. M. Liu, X. F. Song, Journal of Physics D- Applied Physics **41** (20), 205202 (2008).
19. S. Canulescu, E. L. Papadopoulou, D. Anglos, Th. Lippert, C. W. Schneider, A. Wokaun, Journal of Applied Physics **105** (6), 063107 (2009).
20. D. L. Crintea, U. Czarnetski, S. Iordanova, I. Koleva, D. Luggenholscher, Journal of Physics D- Applied Physics **42** (4), 045208 (2009).
21. G. Cristoforetti, G. Lorenzetti, P. A. Benedetti, E. Tongnoni, S. Legnaioli, V. Palleschi, Journal of Physics D- Applied Physics **42** (22), 225207 (2009).
22. A. Delserieys, F. Y. Khattak, C. L. S. Lewis, D. Riley, Journal of Applied Physics **106** (8), 083304 (2009).
23. P. W. J. M. Boumans, *Theory of Spectrochemical Excitation*. (Plenum Press, New York, 1966).
24. H. Terasaki, M. Tanaka, M. Ushio, Metallurgical and Materials Transactions A-Physical Metallurgy and Materials Science **33** (4), 1183-1188 (2002).
25. S. Zielinkska, K. Musiol, K. Dzierzega, S. Pellerin, F. Valensi, C. de Izarra, F. Briand, Plasma Sources Science and Technology **16**, 832-838 (2007).
26. Y. B. Chen, Z. L. Lei, L. Q. Li, L. Wu, Science and Technology of Welding and Joining **11** (4), 403-411 (2006).
27. B. Hu, and G. Den Ouden, Science and Technology of Welding and Joining **10** (4), 427-431 (2005).
28. M. Gao, X. Y. Zeng, B. Tan, J. C. Feng, Science and Technology of Welding and Joining **14** (4), 274-281 (2009).
29. L. M. Liu, G. Song, G. Liang, and J. F. Wang, Materials Science and Engineering A-Structural Materials Properties Microstructure and Processing **390**, 76-80 (2005).
30. B. Ribic, R. Rai, T. DebRoy, Science and Technology of Welding and Joining **13** (8), 683-693 (2008).
31. M. M. Collur, T. DebRoy Metallurgical Transactions B-Process Metallurgy **20** (2), 277-286 (1989).
32. W. L. Barr, Journal of the Optical Society of America **52** (8), 885-888 (1962).
33. R. Rai, J. W. Elmer, T. A. Palmer, T. DebRoy, Journal of Physics D- Applied Physics **40** (18), 5753-5766 (2007).
34. H. Zhao, T. Debroy, Journal of Applied Physics **93** (12), 10089-10096 (2003).
35. P. A. A. Khan, T. DebRoy, Metallurgical Transactions B-Process Metallurgy **15** (4), 641-644 (1984).
36. X. He, T. DebRoy, P. W. Fuerschbach,, Journal of Physics D- Applied Physics **36** (23), 3079-3088 (2003).
37. K. Mundra, T. DebRoy, Welding Journal **72** (1), S1-S9 (1993).
38. X. He, T. DebRoy, P. W. Fuerschbach, Journal of Applied Physics **96** (8), 4547-4555 (2004).
39. Y. Ralchenko, A.E. Kramida, J. Reader, and NIST ASD Team (2008), (National Institute of Standards and Technology, Gaithersburg, MD, 2008).

40. J. J. Camacho, L. Diaz, M. Santos, L. J. Juan, J. M. L. Poyato, Journal of Applied Physics **107** (8), 083306 (2010).
41. J. J. Camacho, M. Santos, L. Diaz, J. M. L. Poyato, Journal of Physics D- Applied Physics **41** (21), 215206 (2008).
42. H. R. Griem, *Plasma Spectroscopy*. (McGraw-Hill, New York, 1964).
43. J. Bengoechea, J. A. Aguilera, C. Aragon, Spectrochimica Acta Part B- Atomic Spectroscopy **61** (1), 69-80 (2006).
44. C. Aragon, J. A. Aguilera, Journal of Applied Physics **103** (1), 013310 (2008).
45. R. Konjevic, N. Konjevic, Spectrochimica Acta Part B- Atomic Spectroscopy **52** (14), 2077-2084 (1997).
46. J. S. Cowpe, R. D. Pilkington, J. S. Astin, A. E. Hill, Journal of Physics D- Applied Physics **42** (16), 165202 (2009).
47. K. L. Baluja, A. Gupta, Zeitschrift fur Physik D-Atoms Molecules and Clusters **31** (1-2), 5-11 (1994).
48. H. W. Drawin, Zeitschrift fur Physik **146** (3), 295-313 (1956).
49. W. Williams, J. C. Cheeseborough, and S. Trajmar, Journal of Physics B- Atomic Molecular and Optical Physics **11** (11), 2031-2043 (1978).
50. R. Rai, G. G. Roy, T. DebRoy, Journal of Applied Physics **101** (5), 054909 (2007).
51. B. Ribic, T. Palmer, T. DebRoy, International Materials Reviews **54** (4), 223-244 (2009).
52. B. D. Ribic, R. Rai, T. A. Palmer, T. DebRoy, presented at the Trends in Welding Research, Pine Mountain, GA, USA, 2008 (unpublished).
53. A. E. F. Gick, M. B. C. Quigley, P. H. Richards, Journal of Physics D- Applied Physics **6** (16), 1941-1949 (1973).
54. M. H. Glowacki, Journal of Physics D- Applied Physics **28** (10), 2051-2059 (1995).
55. C. Tix, G. Simon, Physical Review E **50** (1), 453-462 (1994).
56. A. Lesage, J. L. Lebrun, J. Richou, Astrophysical Journal **360** (2), 737-740 (1990).
57. D. Lacroix, G. Jeandel, Journal of Applied Physics **81** (10), 6599-6606 (1997).

Chapter 5

SUMMARY AND CONCLUSIONS

5.1 Summary and conclusions

A critical review of literature[1] on hybrid welding revealed several important areas for further research. (1) The understanding of heat transfer and fluid flow during hybrid welding is still beginning and further research is necessary. (2) Why hybrid welding weld bead width is greater than that of laser or arc welding is not well understood. (3) The influence of arc power and heat source separation distance on cooling rates during hybrid welding are not known. (4) Convection during hybrid welding is not well understood despite its importance to weld integrity. (5) The influence of surface active elements on weld geometry, weld pool temperatures, and fluid flow during high power density laser and laser/arc hybrid welding are not known. (6) Although the arc power and heat source separation distance have been experimentally shown to influence arc stability and plasma light emission during hybrid welding, the influence of these parameters on plasma properties is unknown. (7) The electrical conductivity of hybrid welding plasmas is not known, despite its importance to arc stability and weld integrity.

Hybrid weld bead geometry temperature profiles, cooling rates, and subsequent microstructure and mechanical properties are dependent upon heat transfer and fluid flow, which are influenced by user-controlled process parameters such as arc power, laser power, and laser-arc separation distance. The thermo-fluid transport in the weld pool is also affected by the presence of surface-active elements in the weld metal. At small separation distances (< 5 to 6 mm depending upon the process parameters), the interaction of the laser and arc influence the plasma electrical conductivity which, in turn, affects the arc stability and thermo-fluid transport in the weld pool. Plasma electrical conductivity is influenced by the vaporization of various alloying elements which depend upon the keyhole geometry and weld temperature profiles. In order to better understand hybrid welding, these diverse aspects of the joining process covering the influences of (i) user-specified process parameters, (ii) material composition, (iii) plasma properties, and (iv) the inherent physical processes, were studied in this work.

Heat transfer, fluid flow, and plasma properties were evaluated for laser/GTA hybrid welding of plain carbon and stainless steels. A three-dimensional heat transfer and fluid flow model was developed and successfully validated for the analysis of weld temperatures, fluid velocity profiles, alloying element vaporization rates, and cooling rates during hybrid welding. The model solves the equations of conservation for mass, momentum, and energy in order to iteratively solve for the three dimensional temperature and fluid flow profiles. In addition, the model considers multiple reflections of the laser beam, the influence of sulfur and oxygen content in the weld metal via the Marangoni stress calculation, a pressure balance at the keyhole walls, and the arc energy absorbed inside the keyhole.

Optical emission spectroscopy was successfully used to obtain plasma light emission spectra as a function of wavelength. The measured emission spectra were used to determine plasma temperatures. Calculated temperature profiles from the heat transfer and fluid flow model were used to determine alloying element vaporization rates over the weld pool surface and within the keyhole. Since the species densities and electrical conductivity of the plasma are affected by the composition of the plasma, alloying element vaporization rates and shielding gas mass flow rate were then used to determine the composition of the plasma above the weld pool, assuming that it was well mixed. This assumption was validated successfully by analyzing the influence of imperfect mixing by considering a 10% variation in the molar vaporizations rates of the alloying elements (only Fe, Cr, Mn, and Ni were considered here). Varying the vaporization rates resulted in less than a 2% difference in the plasma electrical conductivity of a 101 A, 4 mm separation hybrid welding plasma at 8924 K. The plasma total electron density varied by less than 7.5%. With the calculated plasma temperatures and plasma composition, the plasma species densities were estimated. Plasma electrical conductivities were calculated using the plasma temperature and total electron density, which provided a means of evaluating the arc stability.

The influence of laser power, arc power and heat source separation distance on weld pool temperatures and fluid flow profiles were successfully evaluated. In order to better understand the hybrid welding process, laser and arc welding were also studied using similar laser powers and arc powers as during hybrid welding. The roles of arc power and heat source separation distance were studied for CO_2 laser/GTA hybrid welding of 321 stainless steel while the influence of laser power for a constant heat source separation was investigated during Nd:YAG laser/GTA hybrid welding of A131 structural steel.

a. For the CO_2 laser/GTA hybrid welding of 321 stainless steel, the calculated weld depth differed from the experimentally measured depth by less than 5%. In the case of Nd:YAG laser/GTA hybrid welding of A131 structural steel, the calculated weld depth and width error compared with the experimental results were 6.5% and 7.7%, respectively.
b. Convection is the dominant mechanism of heat transfer during hybrid welding of steels. The importance of heat transfer by convection is expected to differ for other alloys welded with higher electrical conductivity, such as aluminum and copper alloys. The primary driving forces affecting fluid flow during hybrid welding are the surface tension gradient and the electromagnetic force. The fluid velocities during Nd:YAG laser/GTA hybrid welding of A131 structural steel are on the order of 400 mm s^{-1}.
c. Keyhole mode laser welds result in much deeper weld penetration depth compared to arc welds. Depending upon the welded material and process parameters, the laser weld depths were 0.5 to 5 mm greater than arc weld depths in this study.
d. Penetration depth during laser and hybrid welding is very similar to the keyhole depth (< 0.1 mm difference), which is primarily a function of the focusing optics, laser defocus, and laser power density for a fixed concentration of surface active elements.
e. Increasing the laser power for a fixed focal position and laser optics from 800 W to 4500 W increased the weld depth from approximately 1 mm to 6 mm for Nd:YAG laser/GTA hybrid welding of A131 structural steel. The weld depth was measured as the distance from the weld bead top surface to the bottom of the fusion zone along the weld centerline.

f. Hybrid welding results in wider weld bead widths than laser welding. For Nd:YAG laser/GTA hybrid welding of A131 structural steel, hybrid welds resulted in 1 mm to 2 mm wider welds than Nd:YAG laser welds, depending upon the process parameters. The weld width is defined as the distance from the right hand edge of the weld fusion zone to the left hand edge at the weld bead top surface. The weld width increases due to the addition of a second heat source and increased arc peak power density, and melting efficiency due to arc contraction from the presence of metal vapors in the plasma.
g. Weld pool penetration depth is similar during Nd:YAG laser/GTA hybrid and Nd:YAG laser welding for the same laser power and focusing optics. In the case of laser and hybrid welding of A131 structural steel, the weld depths did not differ by more than 0.7 mm for all of the laser powers considered.
h. When the heat source separation distance was greater than 6.5 mm for 60 A arc, 900 W CO_2 laser/GTA hybrid welding of 321 stainless steel, the cooling rate from 1073 K to 773 K at the centerline of the molten weld pool reduces from approximately 650 K s^{-1} to ~400 K s^{-1}. Beyond the separation distance of 6.5 mm the arc begins to act as more a of a post weld heat treatment process.
i. Increasing arc current from 60A to 120 A and 180 A, for a fixed laser power and heat source separation distance during the CO_2 laser/GTA hybrid welding of 321 stainless steel increases the welding process heat input per unit length and reduces the cooling rate of the weld pool between 1073 K and 773 K to approximately 350 K s^{-1} and 250 K s^{-1}, respectively.

The influence of weld metal oxygen and sulfur concentrations on weld geometry, temperature profiles, and fluid flow during Yb doped fiber laser welding of 0.16 %C, 1.46 %Mn mild steel was successfully investigated experimentally and theoretically.

a. The measured experimental weld depth and width varied for a given sulfur concentration on the order of 1% and 14%, respectively. The calculated and experimental depth and width (when varying the steel sulfur content) differed by an average of 2% and 20%, respectively. Measured experimental weld depth and width, for a given oxygen concentration, varied approximately 6.5% and 11.5%.

Calculated and experimental laser weld depth and width (when varying the weld oxygen content) differed by an average of 12% and 20%, respectively.

b. With increase in concentration of surface active elements in the weld metal, $d\gamma/dT$ may become positive close to the weld pool boundary while remaining negative near the keyhole due to high local temperatures (~3050 K). This results in complex fluid flow patterns with fluid flowing inward from the weld pool boundary and outward from the keyhole walls. As the concentration of surface active elements (both oxygen and sulfur) increases, the radially outward flow diminishes which can lower the weld width. The experimentally measured weld width decreased from 5.2 mm to 3.8 mm as the base metal sulfur concentration was increased for the range of concentrations considered. Increasing the dissolved oxygen content of the weld pool decreased laser weld width from 5.2 to 4 mm for the range of concentrations considered.

c. Sulfur and oxygen differ in terms of their influence of laser weld depth. Increasing the sulfur content of the weld metal from 0.006 wt% to 0.15 wt% resulted in a fairly consistent experimental weld depth of 9.3 mm (variation on the order of about 1%). The increase in weld pool penetration depth due to the influence of surface active elements for laser and hybrid welded mild steel arises from changes in the keyhole depth, not the Marangoni stress as previously theorized. Several reactions were considered involving sulfur to determine its influence on the keyhole pressure balance calculation and keyhole geometry, but none of the reactions resulted in a gaseous species partial pressure above 1×10^{-4} atm. The primary pressures influencing the calculated keyhole geometry were the vapor pressure of the alloy (~0.9 atm), surface tension pressure (~1×10^{-2} atm), and partial pressure of carbon monoxide (~0.1 atm to 0.7 atm).

d. Increased weld penetration observed when increasing the dissolved oxygen concentration in the weld pool from 0.0038 wt% to 0.0257 wt% resulted in the formation of carbon monoxide gas at the surface of the keyhole due to reacting dissolved oxygen and carbon. The partial pressure of carbon monoxide ranged from 0.1 atm to 0.75 atm depending upon the dissolved oxygen concentration. The increase in carbon monoxide pressure resulted in a subsequent deeper keyhole. Depending upon the dissolved oxygen content of the weld metal, the experimental weld depth increased by as much as 1.5 mm.

Hybrid welding plasma temperatures, species densities, and electrical conductivities for various heat source separation distances and arc powers were successfully estimated for GTA, Nd:YAG laser, and Nd:YAG laser/GTA hybrid welding of 304L stainless steel. Arc and laser welding plasmas were evaluated using the same laser and arc power as those during hybrid welding to better understand hybrid welding plasmas. For the experimental conditions considered in this study:

a. In order to determine the vaporization rates needed to calculated the plasma compositions, the three dimensional temperature profiles, weld geometries, and fluid flow profiles for arc, laser, and hybrid welds were calculated. The average error between the experimental and calculated weld bead widths and depths for all welding conditions considered were 6.4% and 8.2%, respectively.
b. The vaporization rates of iron, chromium, and manganese during Nd:YAG laser/GTA hybrid welding of 304L stainless steel were on the order of 1×10^{-4} mol s^{-1}, while that of nickel was on the order of 1×10^{-5} mol s^{-1}. The molar flow rate of the argon shielding gas was on the order of 1×10^{-2} mol s^{-1}.
c. The high power density of the laser beam and presence of the arc during Nd:YAG laser/GTA hybrid welding resulted in molar percentages of alloying elements approximately 3000 to 4000 times greater than those during GTAW for similar arc currents. Compared to Nd:YAG laser welding, the molar percentages of alloying elements in the plasma during Nd:YAG laser/GTA hybrid welding of 340L stainless steel were approximately 30% to 100% greater depending upon the alloying element, arc current, and heat source separation distance.
d. Time-average plasma electron temperatures for arc, laser, and hybrid welding were on average 8000 K, 7500 K, and 8950 K (4 mm separation) and 8350 K (6 mm separation), respectively. Hybrid welding resulted in a high plasma temperature due to the additional heat flux provided from a second heat source.
e. The total electron densities of the GTA, Nd:YAG laser, and Nd:YAG laser/GTA hybrid welding plasmas were approximately 1.4×10^{21} m^{-3}, 7×10^{21} m^{-3}, and

2 x 10^{22} m^{-3}, respectively. The hybrid welding plasma resulted in higher total electron densities due to higher plasma temperatures and higher concentrations of metal vapors in the plasma compared to arc or laser welding.

f. Arc, laser, and hybrid welding plasma electrical conductivities were 1290 S m^{-1}, 2150 S m^{-1}, and approximately 3000 S m^{-1} on average, respectively. Greater plasma electrical conductivity may explain why hybrid welding shows good arc stability. The enhanced plasma electrical conductivity and subsequent arc stability during hybrid welding may arise due to increased heat flux from the addition of second heat source, higher electron temperatures, metal vapor concentrations, and electron densities compared to arc or laser welding.

g. Increasing the heat source separation distance from 4 mm to 6 mm reduced hybrid welding plasma electrical conductivity approximately 500 S m^{-1}. Consequently, this will reduce arc stability due to the lower plasma electrical conductivity resulting from lower heat flux near the laser focal point. Variation of the arc current during hybrid welding showed no clear trend for the range of arc currents evaluated.

5.2 Future work

From the work detailed in the thesis, areas for further research are identified. Modifying the steady state keyhole pressure balance calculation for transient calculations would allow for analysis of heat transfer and fluid flow in ramped keyhole mode laser welding. A transient calculation is important to understand how the pressure terms and keyhole shape vary as a function of time. In addition, the development of this model would provide important insight for evaluating the effect of material composition, and laser power on temperature and fluid velocity profiles, weld bead shape, porosity formation due to unstable keyhole collapse, and cooling rates as a function of time.

Modeling of hybrid welding microstructures remains an area for significant further research. Comprehensive examination of hybrid weld microstructures and mechanical properties for various alloys has been limited. A study of microstructural evolution for several alloys would be a large benefit to better understand the mechanical behavior of hybrid welds.

5.3 References

1. B. Ribic, T. Palmer, T. DebRoy, International Materials Reviews **54** (4), 223-244 (2009).

Appendix A

ANALYSIS OF VARIANCE (ANOVA) CALCULATION

A.1 ANOVA calculation

Details of the analysis of variance (ANOVA) calculations performed are presented in this appendix. An ANOVA analyzes total variance of a dataset between and within groups of observations. The total variance of a dataset can be thought of as the departure of measured values from the grand mean of the dataset. The variance within a group of observations is the deviation of data values from the mean for a particular group of measurements, while the variance between groups is the straying of all group mean values from the grand mean of the entire dataset.

Based upon the variance within a group of observations and variance between groups of observations, a statistical determination as to whether the groups significantly differ in terms of their means can be established with some degree of confidence. The confidence levels for the ANOVA's performed in these studies were all 95%. The ANOVA's performed for these studies consider the modification of only one factor (one-way ANOVA) at a time. By analyzing the difference in means when changing only one factor, the ANOVA is simplified. The analysis of interactions between several factors changing at once is thus avoided.

The ANOVA uses the null hypothesis that there exists no difference between the groups of observations.[1] In order to reject the null hypothesis, the ANOVA must show that the ratio of mean variances between the groups to within the groups is greater than a critical value determined by a statistical probability F distribution table.[1]

The sum of squares evaluates the variation of data within a group, between groups, and for the entire dataset. The sum of squares of variance between groups of observations is given by:[1]

$$SS_B = \sum_{j=1}^{J} n_j (\bar{y}_j - \overline{Y})^2 \tag{A.1}$$

where J is the total number of groups of observations, n_j is the number of observations in the j^{th} group, $\bar{y}_j$ is the mean of the particular j^{th} group of observations, and $\bar{Y}$ is the grand mean for all observations and groups. The grand mean is determined by:[1]

$$\bar{Y} = \sum y_{ij} / N \tag{A.2}$$

where y_{ij} is the ith observed value for a particular group j and N is the total number of observations for all groups. The sum of squares which analyzes the total variation for all observations is defined by:[1]

$$SS_T = \sum_{j=1}^{J} \sum_{i=1}^{n_j} (y_{ij} - \bar{Y})^2 \tag{A.3}$$

where i is the number of observations in group j. The sum of squares for the variance within a group of observations is the difference of the sum of squares for the total variance of the dataset and the sum of squares for the variance between groups of observation and is given by:[1]

$$SS_w = SS_T - SS_B \tag{A.4}$$

The degrees of freedom normalize the calculations based upon their sample size and the number of groups considered and aid in providing a mean variance for the observations. The total degrees of freedom are given by:[1]

$$df_T = N - 1 \tag{A.5}$$

The number of degrees of freedom between groups and within a group of observations are given by:[1]

$$df_B = J - 1 \tag{A.6}$$

$$df_W = N - J \tag{A.7}$$

where df_B is the degrees of freedom for between groups of observations and df_W is the degrees of freedom for within groups of observations.

The mean square is an adjusted measure of the variance within and between groups that considers the number of observations in the group and is used for calculating the ratio F. The mean square between and within groups of observations are given by:[1]

$$MS_B = \frac{SS_B}{J - 1} \tag{A.8}$$

$$MS_W = \frac{SS_W}{N - J} \tag{A.9}$$

where the subscripts B and W stand for between and within the groups of observations. The ratio of the mean squares gives the calculated F value for comparison with the critical F and is given by:[1]

$$F = \frac{MS_B}{MS_W} \tag{A.10}$$

A.2 References

1. P. Dalgaard, *Introductory Statistics with R*. (Springer-Verlag New York, Inc., New York, NY, 2002).

Appendix B

SOURCE CODE FOR ABEL TRANSFORM AND ELECTRON TEMPERATURE CALCULATION

B.1 Source code

The source code presented in this appendix is for the calculation of the plasma electron temperatures using the two line method[1] and the deconvolution of the measured spectral line intensities via an Abel transform.[1-2] The source code performs the calculation for the deconvoluted spectral line intensities and electron temperatures with two user supplied input files. The first input file contains the transition probability, statistical weights, upper energy level potentials, and spectral line wavelength for each of the two spectral lines. A sample of this input is shown by Fig. B.1.

```
!First peak data    Abel Transform program by Brandon Ribic
522.494             !Wavelength of first peak (nm)
2.5E7               !Transition probability of first peak (sec**-1)
11.0                !Statistical weight for first peak (unitless)
46959.0             !Upper energy potential (cm**-1)
!Second peak data
534.581             !Wavelength (nm)
4.9E6               !Transition probability (sec**-1)
5.0                 !Statistical weight (unitless)
26796.0             !Upper energy potential (cm**-1)
```

Fig. B.1: Sample input file for spectral line transition probability, statistical weight, upper energy level potential, and wavelength data.

The second input file contains the location of the spectral measurement relative to the laser beam symmetry axis, a temperature value calculated from non-deconvoluted lines (only read, not later used in the calculation), and measured spectral intensities for two user specified spectral lines. A sample of the second input is given in Fig. B.2.

```
  -0.40000E+01    0.11688E+05    0.25127E+04    0.26182E+04
  -0.45000E+01    0.93897E+04    0.25512E+04    0.48808E+04
  -0.50000E+01    0.10003E+05    0.17457E+04    0.27634E+04
  -0.55000E+01    0.10174E+05    0.12836E+04    0.19350E+04
  -0.60000E+01    0.11711E+05    0.99160E+03    0.10282E+04
```

Fig. B.2: Sample input file for the Abel transform and electron temperature calculation.

The source code calculation procedure is shown by a flow chart in Fig. B.3.

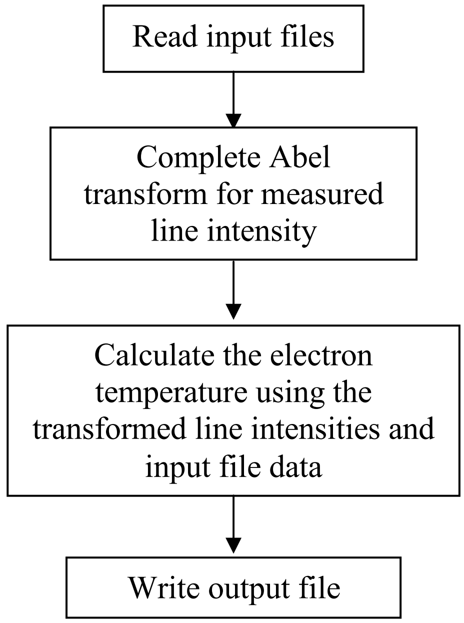

Fig. B.3: Flow chart for measured line intensity deconvolution and calculation of electron temperatures.

The output file contains the plasma light emission sample location relative to the laser beam symmetry axis, the measured spectral line intensities, the deconvoluted line intensities, and the electron temperature calculated using the deconvoluted line intensities.

The source code for the Abel transform and electron temperature calculations is:

```
      program main

      real,dimension(17) :: x, J1, J2, T1
      real,dimension(17) :: A1,A2,TT,AT1,AT2,C, AA
      real B1, B2, G1, G2, V1, V2, L1, L2, term1, term2, term3
      integer i, N

c     Variables used in electron temperature calculation
c     B1 and B2 ....transition probabilities (sec**-1)
c     G1 and G2 ....statistical weights (unitless)
c     V1 and V2 ....upper energy level potential (cm**-1)
c     L1 and L2 ....wavelength of each peak (nm)
      N=5                  !number of data points
      write(*,*) 'Reading Input.txt.'
      open(unit=40, file='input.txt', form='formatted')
      read(40,*)    !comment line
```

```
      read(40,*)L1
      read(40,*)B1
      read(40,*)G1
      read(40,*)V1
      read(40,*)    !comment line
      read(40,*)L2
      read(40,*)B2
      read(40,*)G2
      read(40,*)V2
      write(*,*) 'Done reading input.txt.'

c-----Read the previous calculation set results containing intensity values
      open(unit=10, file='input2.txt')
      do i=1,N
      read(10,22) x(i),T1(i),J1(i),J2(i)
22    format(4(E14.5,1x))
      enddo

      A1=J1
      call Abel(A1,AT1)    !Abel transform of first peak
      write(*,*) 'Completed Abel Inversion of first data set.'

      A2=J2
      call Abel(A2,AT2)    !Abel transform of second peak
      write(*,*) 'Completed Abel Inversion of second data set.'

c-----Electron temperature calculation of transformed data
      write(*,*) 'Starting electron temperature calculation.'
      V1=V1/8065.5 !convert from cm**-1 to eV
      V2=V2/8065.5

      term1=5040.0*(V1-V2)
      term2=log10(G1*B1/(G2*B2))
      term3=log10(L1/L2)


      do i=1,N
      C(i)=log10(AT1(i)/AT2(i))
      TT(i)=term1/(term2-term3-C(i))
      enddo
      write(*,*) 'Finished electron temperature calculation.'
c----------------------------------------------------------
c-----Output of final data
      write(*,*) 'Writing output to OutputAbel.txt.'
      open(unit=20, file='OutputAbel.txt')
      do i=1,N
      write(20,23)x(i),J1(i),J2(i),AT1(i),AT2(i),TT(i)
23    format(6(1x,E14.6))
      enddo
      write(*,*) 'Finished writing data to OutputAbel.txt.'

      close(20)
      close(10)
      close(40)
      end
c-----Abel transformation based upon W.L. Barr's paper in
c-----Journal of optical society of america (Aug. 1962) Vol:52, Iss:8
      Subroutine Abel(A,AT)
      real,dimension(17) :: A,AT

      AT(1)=0.2029*A(1)+0.4439*A(2)+0.1791*A(3)-
      10.5111*A(4)-0.1298*A(5)-0.0095*A(6)-
     20.0237*A(7)-0.0193*A(8)-0.0152*A(9)-
```

```
30.0122*A(10)-0.0099*A(11)-0.0082*A(12)-
40.0069*A(13)-0.0059*A(14)-0.0051*A(15)-
50.0044*A(16)-0.0039*A(17)

  AT(2)=0.1831*A(1)+0.4041*A(2)+0.1778*A(3)-
  10.4342*A(4)-0.1299*A(5)-0.0204*A(6)-
20.262*A(7)-0.203*A(8)-0.0157*A(9)-
30.0125*A(10)-0.0101*A(11)-0.0084*A(12)-
40.007*A(13)-0.006*A(14)-0.0051*A(15)-
50.0045*A(16)-0.0039*A(17)

  AT(3)=0.1239*A(1)+0.2847*A(2)+0.174*A(3)-
  10.2034*A(4)-0.1304*A(5)-0.0531*A(6)-
20.0338*A(7)-0.0235*A(8)-0.0173*A(9)-
30.0134*A(10)-0.0107*A(11)-0.0087*A(12)-
40.0073*A(13)-0.0061*A(14)-0.0053*A(15)-
50.0046*A(16)-0.0045*A(17)

  AT(4)=0.1324*A(2)+0.1936*A(3)+0.0928*A(4)-0.0964*A(5)-
  10.0969*A(6)-0.0501*A(7)-0.0292*A(8)-
  20.0202*A(9)-0.015*A(10)-0.0117*A(11)-
  30.0094*A(12)-0.0077*A(13)-0.0065*A(14)-
  40.0055*A(15)-0.0047*A(16)-0.0041*A(17)

  AT(5)=0.1172*A(3)+0.1523*A(4)+0.0722*A(5)-
  10.0538*A(6)-0.081*A(7)-0.046*A(8)-
  20.026*A(9)-0.0179*A(10)-0.0133*A(11)-
  30.0104*A(12)-0.0084*A(13)-0.0069*A(14)-
  40.0058*A(15)-0.005*A(16)-0.0043*A(17)

  AT(6)=0.1036*A(4)+0.1291*A(5)+0.0636*A(6)-0.0033*A(7)-0.0714*A(8)-
  10.0431*A(9)-0.0236*A(10)-0.0162*A(11)-
  20.012*A(12)-0.0094*A(13)-0.0076*A(14)-
  30.0063*A(15)-0.0053*A(16)-0.0046*A(17)

  AT(7)=0.093*A(5)+0.114*A(6)+0.0586*A(7)-0.0214*A(8)-
  10.0646*A(9)-0.0403*A(10)-0.0217*A(11)-
  20.0148*A(12)-0.0111*A(13)-0.0087*A(14)-
  30.007*A(15)-0.0058*A(16)-0.0049*A(17)

  AT(8)=0.0847*A(6)-0.1032*A(7)+0.0551*A(8)-
  10.0142*A(9)-0.0595*A(10)-0.038*A(11)-
  20.0202*A(12)-0.0138*A(13)-0.0103*A(14)-
  30.0081*A(15)-0.0065*A(16)-0.0054*A(17)

  AT(9)=0.0781*A(7)+0.0951*A(8)+0.0524*A(9)-0.0095*A(10)-
  10.0555*A(11)-0.0359*A(12)-0.0189*A(13)-0.0129*A(14)-
  20.0096*A(15)-0.0075*A(16)-0.0061*A(17)

  AT(10)=0.0727*A(8)+0.0886*A(9)+0.0501*A(10)-0.0063*A(11)-
  10.0522*A(12)-0.0342*A(13)-0.0179*A(14)-
  20.0122*A(15)-0.0091*A(16)-0.0071*A(17)

  AT(11)=0.0682*A(9)+0.0834*A(10)+0.0482*A(11)-
  10.0039*A(12)-0.0495*A(13)-0.0326*A(14)-
  20.017*A(15)-0.0115*A(16)-0.086*A(17)

  AT(12)=0.0644*A(10)+0.079*A(11)+0.0465*A(12)-0.0022*A(13)-
  10.047*A(14)-0.0313*A(15)-0.0162*A(16)-0.011*A(17)

  AT(13)=0.0612*A(11)+0.0752*A(12)+0.045*A(13)-
  10.0009*A(14)-0.045*A(15)-0.0301*A(16)-0.0155*A(17)
```

```
AT(14)=0.0583*A(12)+0.072*A(13)+0.0437*A(14)+
10.0001*A(15)-0.0432*A(16)-0.029*A(17)

AT(15)=0.0558*A(13)+0.0691*A(14)+0.0424*A(15)+
10.0009*A(16)+0.0416*A(17)

AT(16)=0.0536*A(14)+0.0666*A(15)+0.0413*A(16)+0.0015*A(17)

AT(17)=0.0517*A(15)+0.0643*A(16)+0.0402*A(17)
return
end
```

B.2 References

1. P. W. J. M. Boumans, *Theory of Spectrochemical Excitation*. (Plenum Press, New York, 1966).
2. W. L. Barr, Journal of the Optical Society of America **52** (8), 885-888 (1962).

Appendix C

SOURCE CODE FOR CALCULATION OF IONIC AND ATOMIC PURE SPECIES DENSITIES

C.1 Source code

In this appendix, the source code for determining the ion, atom, and electron species densities of pure Ar, Mn, Fe, Cr, Ni, and Mo is presented. The source code determines the species densities either as a function of electron temperature for a range of electron temperatures that is either preset in the code or read from a user supplied input file. The input is determined by a variable called "switch". The preset temperature range is from 4000 K to 14,000 K. The user supplied input file contains measured and deconvoluted spectral lines intensities (not used in calculation, only read), the location of the spectral measurement in the plasma, and the local electron temperature. A sample input file is shown by Table C.1.

Table C.1: Input file sample for species density calculation.

```
0.00000E+00   2.10100E+02   3.63200E+02   2.90516E+03   4.60883E+03   8.00656E+03
0.00000E+00   2.24470E+03   4.72000E+03   3.31798E+03   5.49283E+03   7.91356E+03
0.00000E+00   2.28100E+03   4.61340E+03   3.32535E+03   5.47120E+03   7.92688E+03
```

The first column (far left) is the location of the measured spectra. The second through fifth columns are measured and deconvoluted spectral line intensities (only read, not used in later calculations), and the sixth column (far right) is the calculated electron temperature.

Using the preset electron temperature range or the user provided electron temperature, the equilibrium number densities of pure atomic and ionic Ar, Mn, Cr, Fe, Mo, and Ni are calculated. Fig. C.1 shows a flow chart of the calculation procedure. Upon determining whether to use a preset electron temperature range or user defined data via the switch, the atomic and ionic partition functions for each pure element are calculated. The ionic, atomic, and total species densities for each pure element are then calculated using the electron temperature and calculated partition function value.

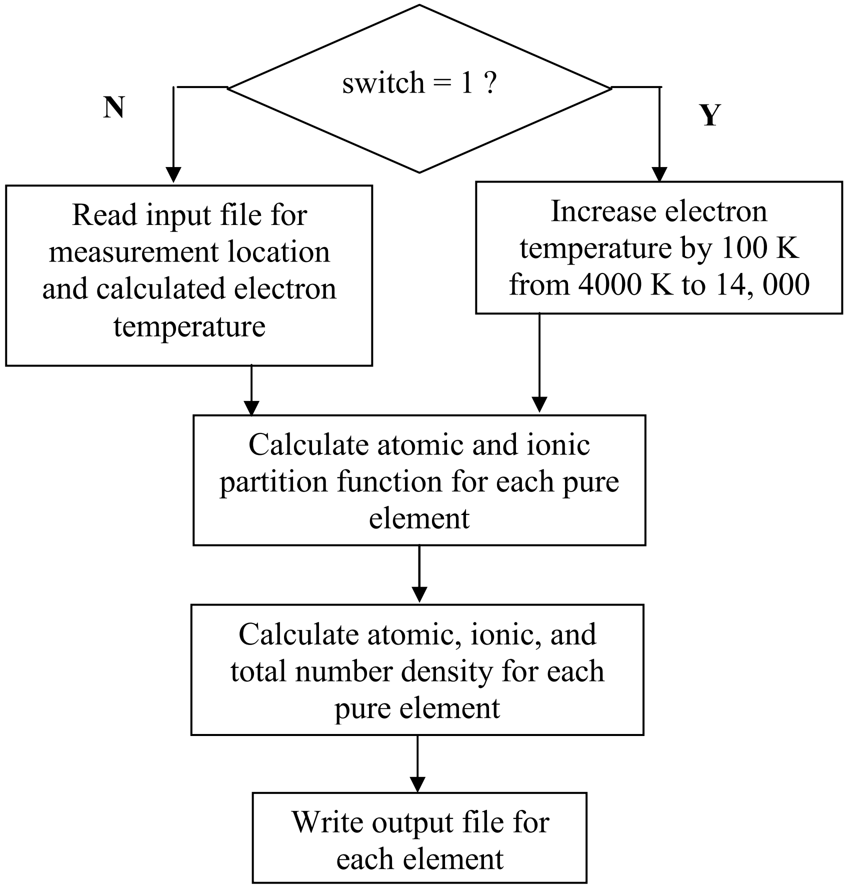

Fig. C.1: Flow chart of species density source code calculation procedure.

The solution of the partition function was completed using the data for chromium, iron, manganese, molybdenum, nickel, and argon given in tables C.2-C.7.[1-5]

Table C.2: Data for atomic and singly charged chromium for calculating the partition function.[2, 4]

Species	Ionization Potential (eV)	Energy Level Potential (cm^{-1})	Statistical Weight
Cr I	6.7665	0	7
		7593.16	5
		7750.78	1
		7810.82	3
		7927.47	5
		8095.21	7
		8307.57	9
Cr II		0	6
		11961.81	3
		12032.58	4
		12147.82	6
		12303.86	8
		12496.44	10

Table C.3: Data for atomic and singly charged iron for calculating the partition function.[2, 4]

Species	Ionization Potential (eV)	Energy Level Potential (cm^{-1})	Statistical Weight
Fe I	7.9024	0	9
		415.932	7
		704.004	5
		888.129	3
		978.072	1
Fe II		0	10
		384.79	8
		667.683	6
		862.613	4
		977.053	2

Table C.4: Data for atomic and singly charged manganese for calculating the partition function.[2, 4]

Species	Ionization Potential (eV)	Energy Level Potential (cm^{-1})	Statistical Weight
Mn I	7.434	0	6
		17052.29	10
		17282	8
		17451.52	6
		17568.48	4
		17637.15	2
Mn II		0	7
		9472.97	5
		14325.86	9
		14593.82	7
		14781.19	5
		14901.18	3
		14959.84	1

Table C.5: Data for atomic and singly charged molybdenum for calculating the partition function.[2-3]

Species	Ionization Potential (eV)	Energy Level Potential (cm^{-1})	Statistical Weight
Mo I	7.0924	0	7
		10768.332	5
		10956.947	1
		11142.784	3
		11454.362	5
		11858.498	7
		12346.28	9
Mo II		0	6
		11783.36	2
		12034.06	4
		12417.28	6
		12900.33	8
		13460.7	10

Table C.6: Data for atomic and singly charged nickel for calculating the partition function.[1-2]

Species	Ionization Potential (eV)	Energy Level Potential (cm^{-1})	Statistical Weight
Ni I	7.6398	0	9
		1332.164	7
		2216.55	5
		204.787	7
		879.816	5
		1713.087	3
Ni II		0	6
		1506.94	4
		8393.9	10
		9330.04	8
		10115.66	6
		10663.89	4

Table C.7: Data for atomic and singly charged argon for calculating the partition function.[2, 5]

Species	Ionization Potential (eV)	Energy Level Potential (cm^{-1})	Statistical Weight
Ar I	15.7596	0	1
		93143.76	5
		93750.5978	3
		94553.6652	1
		95399.8276	3
Ar II		0	4
		1431.5831	2
		108721.53	2
		132327.3621	8
		132481.2071	6
		132630.7281	4
		132737.7041	2

The code produces one output file for each element. Depending upon whether a preset range of electron temperatures is used for the species density calculations or a user provided temperature in the input file, the format of the output files is slightly different. When a user provided input file is implemented, the output will also contain locations from where the measurements were taken within the plasma. If a preset range of temperatures is used, the spectral measurement location will not be provided in the output files. The output files will also contain the electron temperature, the calculated atomic and ionic partition function values, and the ionic, atomic, and total species densities for the pure element.

The species density calculation source code is the following:

```
      program main

      real,dimension(100) :: T, ZAMn, ZiMn, ZAFe, ZiFe, ZAMo, ZiMo
      real,dimension(100) :: ZANi, ZiNi, ZAAr, ZiAr,ZACr, ZiCr
      real,dimension(100) :: DiMn, DAMn, DiFe, DAFe, DAMo, DiMo, DANi
      real,dimension(100) :: DiNi, DiAr, DAAr, DACr, DiCr
      real,dimension(100) :: TNDCr,TNDAr,TNDNi,TNDMo,TNDFe,TNDMn
      real,dimension(100) :: C1Mn,C2Mn,C1Fe,C2Fe,C1Ni,C2Ni,C1Ar,C2Ar
      real,dimension(100) :: C1Cr,C2Cr,C1Mo,C2Mo,x,J1,J2,J3,J4
      integer i,switch


c-----variable definitions
c      ZA- atomic partition function of particular species
c      Zi- ionic partition function of particular species
c      T- electron temperature
c      DA- number density of particular atomic pure species
c      Di- number density of particular ionic pure species
c      TND- total number density of particular pure element
c      C1 and C2- constants for calculations of species densities
c      x- location of measure spectra relative to laser beam symmetry axis
c      J1 through J4- measure and deconvoluted spectral line intensities
c-------------------------------------------------------------------------------

      switch=0 !switch used to either calculate over temp range (1)
                     ! or for specified temp from input file (0)

      if (switch.eq.1) then
      do i=1,100
      T(i)=4000.0+((i-1)*100.0)
      !Partition function for atomic Mn
      !0.695 is 8065.5/8.617E-5 (conversion factor divided by boltzmann const.)
      ZAMn(i)=6.0*exp(0.0)+10.0*exp(17052.29/(0.695*T(i)))+
      18.0*exp(17282.0/(0.695*T(i)))+6.0*exp(17451.52/(0.695*T(i)))+
      24.0*exp(17568.48/(0.695*T(i)))+2.0*exp(17637.15/(0.695*T(i)))
      !Partition function of ionic Mn
      ZiMn(i)=7.0*exp(0.0)+5.0*exp(9472.97/(0.695*T(i)))+
      19.0*exp(14325.86/(0.695*T(i)))+7.0*exp(14593.82/(0.695*T(i)))+
      25.0*exp(14781.19/(0.695*T(i)))+3.0*exp(14901.18/(0.695*T(i)))+
      31.0*exp(14959.84/(0.695*T(i)))
      !Density of ionic Mn species
      C1Mn(i)=2.0*2.41E21*(ZiMn(i)/ZAMn(i))*(T(i)**1.5)*
      1exp(-7.4340/(8.615E-5*T(i)))
      C2Mn(i)=7.34E27/(T(i))

      DiMn(i)=(sqrt(4.0*(C1Mn(i)**2.0)+(4.0*C1Mn(i)*C2Mn(i)))-
      12.0*C1Mn(i))/2.0
      !Density of atomic Mn species
      DAMn(i)=(DiMn(i)*DiMn(i))/C1Mn(i)
```

```
!Total number density of Mn species in plasma
TNDMn(i)=2.0*DiMn(i)+DAMn(i)


!Partition function of atomic Fe
ZAFe(i)=9.0*exp(0.0)+7.0*exp(415.932/(0.695*T(i)))+
15.0*exp(704.004/(0.695*T(i)))+3.0*exp(888.129/(0.695*T(i)))+
21.0*exp(978.072/(0.695*T(i)))
!Partition function of ionic Fe
ZiFe(i)=10.0*exp(0.0)+8.0*exp(384.790/(0.695*T(i)))+
16.0*exp(667.683/(0.695*T(i)))+4.0*exp(862.613/(0.695*T(i)))+
22.0*exp(977.053/(0.695*T(i)))
!Density of ionic Fe species
C1Fe(i)=2.0*2.41E21*(ZiFe(i)/ZAFe(i))*(T(i)**1.5)*
1exp(-7.9024/(8.615E-5*T(i)))

C2Fe(i)=7.34E27/(T(i))

DiFe(i)=(sqrt(4.0*(C1Fe(i)**2.0)+(4.0*C1Fe(i)*C2Fe(i)))-
12.0*C1Fe(i))/2.0
!Density of atomic Fe species
DAFe(i)=(DiFe(i)*DiFe(i))/C1Fe(i)
!Total number density of Fe species in plasma
TNDFe(i)=2.0*DiFe(i)+DAFe(i)


!Partition function of atomic Mo
ZAMo(i)=7.0*exp(0.0)+5.0*exp(10768.332/(0.695*T(i)))+
11.0*exp(10956.947/(0.695*T(i)))+3.0*exp(11142.784/(0.695*T(i)))+
25.0*exp(11454.362/(0.695*T(i)))+7.0*exp(11858.498/(0.695*T(i)))+
39.0*exp(12346.28/(0.695*T(i)))
!Partition function of ionic Mo
ZiMo(i)=6.0*exp(0.0)+2.0*exp(11783.36/(0.695*T(i)))+
14.0*exp(12034.06/(0.695*T(i)))+6.0*exp(12417.28/(0.695*T(i)))+
28.0*exp(12900.33/(0.695*T(i)))+10.0*exp(13460.7/(0.695*T(i)))
!Density of ionic Mo species
C1Mo(i)=2.0*2.41E21*(ZiMo(i)/ZAMo(i))*(T(i)**1.5)*
1exp(-7.0924/(8.615E-5*T(i)))

C2Mo(i)=7.34E27/(T(i))

DiMo(i)=(sqrt(4.0*(C1Mo(i)**2.0)+(4.0*C1Mo(i)*C2Mo(i)))-
12.0*C1Mo(i))/2.0
!Density of atomic Mo species
DAMo(i)=(DiMo(i)*DiMo(i))/C1Mo(i)
!Total number density of Mo species in plasma
TNDMo(i)=2.0*DiMo(i)+DAMo(i)

!Partition function of atomic Ni
ZANi(i)=9.0*exp(0.0)+7.0*exp(1332.164/(0.695*T(i)))+
15.0*exp(2216.550/(0.695*T(i)))+7.0*exp(204.787/(0.695*T(i)))+
25.0*exp(879.816/(0.695*T(i)))+3.0*exp(1713.087/(0.695*T(i)))
!Partition function of ionic Ni
ZiNi(i)=6.0*exp(0.0)+4.0*exp(1506.94/(0.695*T(i)))+
110.0*exp(8393.9/(0.695*T(i)))+8.0*exp(9330.04/(0.695*T(i)))+
26.0*exp(10115.66/(0.695*T(i)))+4.0*exp(10663.89/(0.695*T(i)))
!Density of ionic Ni species
C1Ni(i)=2.0*2.41E21*(ZiNi(i)/ZANi(i))*(T(i)**1.5)*
1exp(-7.6398/(8.615E-5*T(i)))

C2Ni(i)=7.34E27/(T(i))

DiNi(i)=(sqrt(4.0*(C1Ni(i)**2.0)+(4.0*C1Ni(i)*C2Ni(i)))-
```

```
  12.0*C1Ni(i))/2.0
  !Density of atomic Ni species
  DANi(i)=(DiNi(i)*DiNi(i))/C1Ni(i)
  !Total number density of Ni species in plasma
  TNDNi(i)=2.0*DiNi(i)+DANi(i)

  !Partition function of atomic Ar
  ZAAr(i)=1.0*exp(0.0)+5.0*exp(93143.76/(0.695*T(i)))+
  13.0*exp(93750.5978/(0.695*T(i)))+1.0*exp(94553.6652/(0.695*T(i)))+
  23.0*exp(95399.8276/(0.695*T(i)))
  !Partition function of ionic Ar
  ZiAr(i)=4.0*exp(0.0)+2.0*exp(1431.5831/(0.695*T(i)))+
  12.0*exp(108721.53/(0.695*T(i)))+8.0*exp(132327.3621/(0.695*T(i)))+
  26.0*exp(132481.2071/(0.695*T(i)))+
34.0*exp(132630.7281/(0.695*T(i)))+
42.0*exp(132737.7041/(0.695*T(i)))
  !Density of ionic Ar species
  C1Ar(i)=2.0*2.41E21*(ZiAr(i)/ZAAr(i))*(T(i)**1.5)*
  1exp(-15.7596/(8.615E-5*T(i)))

  C2Ar(i)=7.34E27/(T(i))

  DiAr(i)=(sqrt(4.0*(C1Ar(i)**2.0)+(4.0*C1Ar(i)*C2Ar(i)))-
  12.0*C1Ar(i))/2.0
  !Density of atomic Ar species
  DAAr(i)=(DiAr(i)*DiAr(i))/C1Ar(i)
  !Total number density of Ar species in plasma
  TNDAr(i)=2.0*DiAr(i)+DAAr(i)


  !Partition function of atomic Cr
  ZACr(i)=7.0*exp(0.0)+18*exp(17282.0/(0.695*T(i)))+
  15.0*exp(7593.16/(0.695*T(i)))+1.0*exp(7750.78/(0.695*T(i)))+
  23.0*exp(7810.82/(0.695*T(i)))+5.0*exp(7927.47/(0.695*T(i)))+
  37.0*exp(8095.21/(0.695*T(i)))+9.0*exp(8307.57/(0.695*T(i)))
  !Partition function of ionic Cr
  ZiCr(i)=6.0*exp(0.0)+2.0*exp(11961.81/(0.695*T(i)))+
  14.0*exp(12032.58/(0.695*T(i)))+6.0*exp(12147.82/(0.695*T(i)))+
  28.0*exp(12303.86/(0.695*T(i)))+10.0*exp(12496.44/(0.695*T(i)))
  !Density of ionic Cr species
  C1Cr(i)=2.0*2.41E21*(ZiCr(i)/ZACr(i))*(T(i)**1.5)*
  1exp(-6.7665/(8.615E-5*T(i)))

  C2Cr(i)=7.34E27/(T(i))

  DiCr(i)=(sqrt(4.0*(C1Cr(i)**2.0)+(4.0*C1Cr(i)*C2Cr(i)))-
  12.0*C1Cr(i))/2.0
  !Density of atomic Cr species
  DACr(i)=(DiCr(i)*DiCr(i))/C1Cr(i)
  !Total number density of Cr species in plasma
  TNDCr(i)=2.0*DiCr(i)+DACr(i)

  open(unit=20,file='OutputDensityMn.txt')
  open(unit=21,file='OutputDensityFe.txt')
  open(unit=22,file='OutputDensityMo.txt')
  open(unit=23,file='OutputDensityNi.txt')
  open(unit=24,file='OutputDensityAr.txt')
  open(unit=25,file='OutputDensityCr.txt')
  write(20,1011)T(i),ZAMn(i),ZiMn(i),DAMn(i),DiMn(i),TNDMn(i)
  write(21,1011)T(i),ZAFe(i),ZiFe(i),DAFe(i),DiFe(i),TNDFe(i)
  write(22,1011)T(i),ZAMo(i),ZiMo(i),DAMo(i),DiMo(i),TNDMo(i)
  write(23,1011)T(i),ZANi(i),ZiNi(i),DANi(i),DiNi(i),TNDNi(i)
  write(24,1011)T(i),ZAAr(i),ZiAr(i),DAAr(i),DiAr(i),TNDAr(i)
```

```
      write(25,1011)T(i),ZACr(i),ZiCr(i),DACr(i),DiCr(i),TNDCr(i)
1011  format(6(E14.5,1x))
      enddo
      close(20)
      close(21)
      close(22)
      close(23)
      close(24)
      close(25)


      else
      open(unit=10,file='input.txt')

      do i=1,3
c     read(10,*) x(i),T(i),J1(i),J2(i)
      read(10,*) x(i),J1(i),J2(i),J3(i),J4(i),T(i)
c3304 format(6(e14.6,1x))

      !Partition function for atomic Mn
      !0.695 is 8065.5/8.617E-5 (conversion factor divided by boltzmann const.)
      ZAMn(i)=6.0*exp(0.0)+10.0*exp(17052.29/(0.695*T(i)))+
      18.0*exp(17282.0/(0.695*T(i)))+6.0*exp(17451.52/(0.695*T(i)))+
      24.0*exp(17568.48/(0.695*T(i)))+2.0*exp(17637.15/(0.695*T(i)))
      !Partition function of ionic Mn
      ZiMn(i)=7.0*exp(0.0)+5.0*exp(9472.97/(0.695*T(i)))+
      19.0*exp(14325.86/(0.695*T(i)))+7.0*exp(14593.82/(0.695*T(i)))+
      25.0*exp(14781.19/(0.695*T(i)))+3.0*exp(14901.18/(0.695*T(i)))+
      31.0*exp(14959.84/(0.695*T(i)))
      !Density of ionic Mn species
      !2.41E21 is product of (2*3.14*9.11E-31*1.3806E-23)**1.5/(6.626E-34**3.0)
      C1Mn(i)=2.0*2.41E21*(ZiMn(i)/ZAMn(i))*(T(i)**1.5)*
      1exp(-7.4340/(8.615E-5*T(i)))
      C2Mn(i)=7.34E27/(T(i))

      DiMn(i)=(sqrt(4.0*(C1Mn(i)**2.0)+(4.0*C1Mn(i)*C2Mn(i)))-
      12.0*C1Mn(i))/2.0
      !Density of atomic Mn species
      DAMn(i)=(DiMn(i)*DiMn(i))/C1Mn(i)
      !Total number density of Mn species in plasma
      TNDMn(i)=2.0*DiMn(i)+DAMn(i)


      !Partition function of atomic Fe
      ZAFe(i)=9.0*exp(0.0)+7.0*exp(415.932/(0.695*T(i)))+
      15.0*exp(704.004/(0.695*T(i)))+3.0*exp(888.129/(0.695*T(i)))+
      21.0*exp(978.072/(0.695*T(i)))
      !Partition function of ionic Fe
      ZiFe(i)=10.0*exp(0.0)+8.0*exp(384.790/(0.695*T(i)))+
      16.0*exp(667.683/(0.695*T(i)))+4.0*exp(862.613/(0.695*T(i)))+
      22.0*exp(977.053/(0.695*T(i)))
      !Density of ionic Fe species
      C1Fe(i)=2.0*2.41E21*(ZiFe(i)/ZAFe(i))*(T(i)**1.5)*
      1exp(-7.9024/(8.615E-5*T(i)))

      C2Fe(i)=7.34E27/(T(i))

      DiFe(i)=(sqrt(4.0*(C1Fe(i)**2.0)+(4.0*C1Fe(i)*C2Fe(i)))-
      12.0*C1Fe(i))/2.0
      !Density of atomic Fe species
      DAFe(i)=(DiFe(i)*DiFe(i))/C1Fe(i)
      !Total number density of Fe species in plasma
      TNDFe(i)=2.0*DiFe(i)+DAFe(i)
```

```
!Partition function of atomic Mo
ZAMo(i)=7.0*exp(0.0)+5.0*exp(10768.332/(0.695*T(i)))+
11.0*exp(10956.947/(0.695*T(i)))+3.0*exp(11142.784/(0.695*T(i)))+
25.0*exp(11454.362/(0.695*T(i)))+7.0*exp(11858.498/(0.695*T(i)))+
39.0*exp(12346.28/(0.695*T(i)))
!Partition function of ionic Mo
ZiMo(i)=6.0*exp(0.0)+2.0*exp(11783.36/(0.695*T(i)))+
14.0*exp(12034.06/(0.695*T(i)))+6.0*exp(12417.28/(0.695*T(i)))+
28.0*exp(12900.33/(0.695*T(i)))+10.0*exp(13460.7/(0.695*T(i)))
!Density of ionic Mo species
C1Mo(i)=2.0*2.41E21*(ZiMo(i)/ZAMo(i))*(T(i)**1.5)*
1exp(-7.0924/(8.615E-5*T(i)))

C2Mo(i)=7.34E27/(T(i))

DiMo(i)=(sqrt(4.0*(C1Mo(i)**2.0)+(4.0*C1Mo(i)*C2Mo(i)))-
12.0*C1Mo(i))/2.0
!Density of atomic Mo species
DAMo(i)=(DiMo(i)*DiMo(i))/C1Mo(i)
!Total number density of Mo species in plasma
TNDMo(i)=2.0*DiMo(i)+DAMo(i)

!Partition function of atomic Ni
ZANi(i)=9.0*exp(0.0)+7.0*exp(1332.164/(0.695*T(i)))+
15.0*exp(2216.550/(0.695*T(i)))+7.0*exp(204.787/(0.695*T(i)))+
25.0*exp(879.816/(0.695*T(i)))+3.0*exp(1713.087/(0.695*T(i)))
!Partition function of ionic Ni
ZiNi(i)=6.0*exp(0.0)+4.0*exp(1506.94/(0.695*T(i)))+
110.0*exp(8393.9/(0.695*T(i)))+8.0*exp(9330.04/(0.695*T(i)))+
26.0*exp(10115.66/(0.695*T(i)))+4.0*exp(10663.89/(0.695*T(i)))
!Density of ionic Ni species
C1Ni(i)=2.0*2.41E21*(ZiNi(i)/ZANi(i))*(T(i)**1.5)*
1exp(-7.6398/(8.615E-5*T(i)))

C2Ni(i)=7.34E27/(T(i))

DiNi(i)=(sqrt(4.0*(C1Ni(i)**2.0)+(4.0*C1Ni(i)*C2Ni(i)))-
12.0*C1Ni(i))/2.0
!Density of atomic Ni species
DANi(i)=(DiNi(i)*DiNi(i))/C1Ni(i)
!Total number density of Ni species in plasma
TNDNi(i)=2.0*DiNi(i)+DANi(i)

!Partition function of atomic Ar
ZAAr(i)=1.0*exp(0.0)+5.0*exp(93143.76/(0.695*T(i)))+
13.0*exp(93750.5978/(0.695*T(i)))+1.0*exp(94553.6652/(0.695*T(i)))+
23.0*exp(95399.8276/(0.695*T(i)))
!Partition function of ionic Ar
ZiAr(i)=4.0*exp(0.0)+2.0*exp(1431.5831/(0.695*T(i)))+
12.0*exp(108721.53/(0.695*T(i)))+8.0*exp(132327.3621/(0.695*T(i)))+
26.0*exp(132481.2071/(0.695*T(i)))+
34.0*exp(132630.7281/(0.695*T(i)))+
42.0*exp(132737.7041/(0.695*T(i)))
!Density of ionic Ar species
C1Ar(i)=2.0*2.41E21*(ZiAr(i)/ZAAr(i))*(T(i)**1.5)*
1exp(-15.7596/(8.615E-5*T(i)))

C2Ar(i)=7.34E27/(T(i))

DiAr(i)=(sqrt(4.0*(C1Ar(i)**2.0)+(4.0*C1Ar(i)*C2Ar(i)))-
12.0*C1Ar(i))/2.0
```

```
        !Density of atomic Ar species
        DAAr(i)=(DiAr(i)*DiAr(i))/C1Ar(i)
        !Total number density of Ar species in plasma
        TNDAr(i)=2.0*DiAr(i)+DAAr(i)


        !Partition function of atomic Cr
        ZACr(i)=7.0*exp(0.0)+18*exp(17282.0/(0.695*T(i)))+
        15.0*exp(7593.16/(0.695*T(i)))+1.0*exp(7750.78/(0.695*T(i)))+
        23.0*exp(7810.82/(0.695*T(i)))+5.0*exp(7927.47/(0.695*T(i)))+
        37.0*exp(8095.21/(0.695*T(i)))+9.0*exp(8307.57/(0.695*T(i)))
        !Partition function of ionic Cr
        ZiCr(i)=6.0*exp(0.0)+2.0*exp(11961.81/(0.695*T(i)))+
        14.0*exp(12032.58/(0.695*T(i)))+6.0*exp(12147.82/(0.695*T(i)))+
        28.0*exp(12303.86/(0.695*T(i)))+10.0*exp(12496.44/(0.695*T(i)))
        !Density of ionic Cr species
        C1Cr(i)=2.0*2.41E21*(ZiCr(i)/ZACr(i))*(T(i)**1.5)*
        1exp(-6.7665/(8.615E-5*T(i)))

        C2Cr(i)=7.34E27/(T(i))

        DiCr(i)=(sqrt(4.0*(C1Cr(i)**2.0)+(4.0*C1Cr(i)*C2Cr(i)))-
        12.0*C1Cr(i))/2.0
        !Density of atomic Cr species
        DACr(i)=(DiCr(i)*DiCr(i))/C1Cr(i)
        !Total number density of Cr species in plasma
        TNDCr(i)=2.0*DiCr(i)+DACr(i)

        open(unit=20,file='OutputDensityMn.txt')
        open(unit=21,file='OutputDensityFe.txt')
        open(unit=22,file='OutputDensityMo.txt')
        open(unit=23,file='OutputDensityNi.txt')
        open(unit=24,file='OutputDensityAr.txt')
        open(unit=25,file='OutputDensityCr.txt')
        write(20,1012)x(i),T(i),ZAMn(i),ZiMn(i),DAMn(i),DiMn(i),TNDMn(i)
        write(21,1012)x(i),T(i),ZAFe(i),ZiFe(i),DAFe(i),DiFe(i),TNDFe(i)
        write(22,1012)x(i),T(i),ZAMo(i),ZiMo(i),DAMo(i),DiMo(i),TNDMo(i)
        write(23,1012)x(i),T(i),ZANi(i),ZiNi(i),DANi(i),DiNi(i),TNDNi(i)
        write(24,1012)x(i),T(i),ZAAr(i),ZiAr(i),DAAr(i),DiAr(i),TNDAr(i)
        write(25,1012)x(i),T(i),ZACr(i),ZiCr(i),DACr(i),DiCr(i),TNDCr(i)
1012    format(7(E14.5,1x))
        enddo
        close(20)
        close(21)
        close(22)
        close(23)
        close(24)
        close(25)
        close(10)
        endif
        end
```

C.2 References

1. R. H. Page, C. S. Gudeman, Journal of the Optical Society of America B-Optical Physics **7** (9), 1761-1771 (1990).
2. Y. Ralchenko, A.E. Kramida, J. Reader, and NIST ASD Team (2008), (National Institute of Standards and Technology, Gaithersburg, MD, 2008).
3. D. M. Rayner, S. A. Mitchell, O. L. Bourne, and P. A. Hackett, Journal of the Optical Society of America B-Optical Physics **4** (6), 900-905 (1987).

4. J. Sugar, C. Corliss, Journal of Physical and Chemical Reference Data **14** (Supplement 2), 1-664 (1985).
5. I. Velchev, W. Hogerworst, and W. Ubachs, Journal of Physics B- Atomic Molecular and Optical Physics **32** (17), L511-L516 (1999).

VITA

Brandon D. Ribic

Brandon D. Ribic was born in Monroeville, PA on April 16th, 1983. He attained his high school diploma at Norwin High School (North Huntingdon, PA) in 2001. As a high school student, Brandon D. Ribic was recognized for his research in materials science and engineering by organizations such as ASM International, Carnegie Mellon University, the Pennsylvania Junior Academy of Science, and the American Society of Highway Engineers. In August of 2001, he matriculated at the Pennsylvania State University to complete a Bachelors of Science in Materials Science and Engineering. During his undergraduate studies, Brandon D. Ribic was awarded several scholarships for exceptional academic performance including the Harvey Kocher Scholarship (2003-04), Turney Trustee Scholarship (2004-05), Krebs Scholarship (2004-05), and Penn State Metallurgy Alumni Scholarship (2004-05). His undergraduate thesis entitled "*The Crystal Chemistry of Hydrogen in Intermetallic Compounds*" analyzed the relationships between crystallographic geometry of metal hydride structures and hydrogen storage material capacity and hydrogen diffusion patterns. After graduating with his undergraduate degree in December of 2005, Brandon D. Ribic enrolled in graduate school at the Pennsylvania State University under the advisement of Professor Tarasankar DebRoy in January of 2006. His publications during his graduate school experience are the following:

- B. Ribic, R. Rai, and T. DebRoy, "Numerical Simulation of Heat Transfer and Fluid Flow in GTA/Laser Hybrid Welding", Science and Technology of Welding and Joining, 2008, vol. 13(8), pp. 683-693
- B. Ribic, T.A. Palmer, and T. DebRoy, "Problems and Issues in Laser-Arc Hybrid Welding", International Materials Reviews, 2009, vol. 54(4), pp. 223-244.
- B.D. Ribic, R. Rai, T.A. Palmer, and T. DebRoy, "Arc-Laser Interactions and Heat Transfer and Fluid Flow in Hybrid Welding", Trends in Welding Research: Proceedings of the 8th International Conference, Pine Mountain, GA, 2009.
- B. Ribic, P. Burgardt, and T. DebRoy, "Optical Emission Spectroscopy of Metal Vapor Dominated Laser-Arc Hybrid Welding Plasma", Journal of Applied Physics, 2011, vol. 109, Iss. 8, 083301.
- B. Ribic, S. Tsukamoto, R. Rai, and T. DebRoy, "Role of Surface-Active Elements During Keyhole-Mode Laser Welding", Journal of Physics D: Applied Physics, 2011, vol. 44, Iss. 48, 485203.